



Ion currents in diesel engines

A thesis submitted to Monash University as fulfilment for the degree of
DOCTOR OF PHILOSOPHY

Rahul Rao

Laboratory for Turbulence Research in Aerospace & Combustion
Monash University, Australia

Supervised by
Professor Damon HONNERY

2016

Copyright notice

©Rahul Rao, 2016.

Except as provided in the Copyright Act 1968, this thesis may not be reproduced in any form without the written permission of the author.

I certify that I have made all reasonable efforts to secure copyright permissions for third-party content included in this thesis and have not knowingly added copyright content to my work without the owner's permission.

Declaration

This thesis contains no material which has been accepted for the award of any other degree or diploma at any university or equivalent institution and that, to the best of my knowledge and belief, this thesis contains no material previously published or written by another person, except where due reference is made in the text of the thesis.

Rahul Rao

15th September, 2016

Abstract

This thesis documents an experimental and modelling investigation into ion formation in diesel engines, its uses in the field of engine performance and emissions prediction and the mechanisms by which these uses are made possible.

Ion sensors have been employed in engines for a variety of purposes, including estimation of air-fuel ratio, start of combustion and in-cylinder pressure, detection of knock, misfire and combustion resonance, prediction of soot formation, and control of spark advance timing and start of injection. This study presents an experimental setup to measure ion currents in a direct-injection diesel engine and shows further uses of the ion current in engines, including prediction of engine-out torque, peak heat release rate, cumulative heat release and NO_x emissions via the use of statistical correlations. Whilst these correlations are simple to obtain, satisfactory explanations for their existence have not yet been put forward. In-depth analysis of the relationships between the ion current and several species of importance to heat release and emissions formation has been inadequate.

In contrast, ions in flames have been extensively studied by chemical kineticists for decades. The identities of the most abundant ions in flames and the mechanisms for their formation and neutralisation are well known for laminar flames at atmospheric or lower pressure. The physics governing charge transport in gases which is responsible for the development of an ion current from a concentration of charged species is also well established.

This study brings together the two fields of engine research and chemical kinetics in order to provide an understanding of the chemistry underlying the correlations seen previously.

Combustion systems of gradually increasing complexity are studied in order to model ion current trends in engines and establish causal links between the ion current and various measures of engine performance or emissions. Initially, a simple and well understood system is considered; methane combustion with ion formation is studied

in a zero-dimensional model using a perfectly stirred reactor burning a methane-air mixture via the use of a well-known chemical kinetic mechanism augmented with a simplified ionic sub-mechanism. This mechanism is reduced to produce a highly simplified mechanism capable of predicting the ion current for high-pressure methane-air flames at near-stoichiometric mixture fractions. Comparisons of the performance of this mechanism to those of two detailed well-established methane combustion mechanisms show very similar results. A 1-D laminar flame code is used to validate temperature distribution, major species distributions and the laminar flame speed against established experimental data.

Validation of this mechanism is performed in a 2-D CFD simulation of the flame propagation, heat release and ion current developed during the constant-volume combustion of methane in air at different elevated values of initial chamber pressure and near-stoichiometric equivalence ratios. These results predict the same ion current trends as seen in the experiment and give some insight into the relationship between heat release and the ion current in a simple combustion event.

The effects of load, speed or other engine operating parameters on the ion current are difficult to predict when using simple models such as zero-dimensional or constant-volume models. Ion formation in sprays of diesel fuel is therefore studied using a phenomenological diesel engine model with an n-heptane oxidation mechanism to model heat release and species formation. The n-heptane mechanism is augmented with an ionic sub-mechanism based on the ionic methane mechanism developed in this study, and with a reduced NO_x mechanism. The modelled in-cylinder pressure is found to agree well with experimental measurements. The modelled ion current displays the same trends as the measured signal but soot formation is not modelled, leading to inaccuracy in the cycle-minimum value of the ion current.

The reasons for the correlations presented here are investigated in zero-dimensional models and in the phenomenological engine model. Sensitivity analyses are used to identify species important to both heat release and electron production. Heat release is found to be correlated with electron formation due to the temperature dependence of the H-O system radicals, in particular that of OH. A similar study is conducted for NO_x emissions. The NO_x formation rate is also found to be correlated with electrons due to the H-O system radicals, via reactions involving the O radical. The formations of both species in a spray from a diesel injector in an engine are modelled using the same phenomenological model; predictions of their locations in the spray were found to match previous experimental results.

Further uses of the ion sensor in engines are briefly discussed — those of soot prediction

and engine diagnostics for conditions leading to increased soot emissions. Soot is found to affect the sensor response primarily via the deposition of an electrically conductive layer on the sensor and the consequent alteration of the sensor resistance. The ion sensor is found to be able to detect two conditions leading to increased soot emissions, worn injectors and increased backpressure in the exhaust system. Detailed studies into sensor geometry and faulty engine operation are required for these applications to be robust, which are beyond the scope of this study but point out a possible route future ion current studies may take.

Acknowledgements

My deepest gratitude is to my supervisor, Prof. Damon Honnery, whose support has made this PhD at all possible. Quite apart from the frequent guidance Damon gave me on this project, his mentorship has been an invaluable aid to me growing as a person. Damon's warmth and genuine concern for his students' well-being leaves an indelible impression on every student he has had. It has been so with me.

My LTRAC and other PhD colleagues have made the long journey a far from arduous one. Dr. Mahesh Venkataraman, Dr. Lokesh Choudhary, Abel-John Buchner, Edward Kuo, Nick Mason-Smith and Dominic Tan, in particular, have ensured that the PhD office was never boring and spending long hours there never tiresome. Staff at the Mechanical Engineering Workshop, most notably Hugh Venables, Nat Derosé, Ken Sheridan and Mark Symonds have always given freely of their time and knowledge; their contribution to experimental setups has been immense. Helen Frost, Nicole Bodenstaff and Stelios Konstantinidis have dealt admirably with the various administrative issues that cropped up during my candidature.

I have been accompanied on my expedition through student life by as good a body of friends as I could have asked for. Devan Ruben, Ashish Divakaran, Michelle Isaac, Kushagra Jain, Tarun Dhawan, Nick Burris, Randall Bromwich and Neil Patil ensured that I never worked too hard and were always on hand when I wanted to unwind.

From start to finish, my parents Rashmi and Srinivas, and brother Varun have stood by me through thick and thin. They pointed out the silver lining when things looked grim. They celebrated every minor success as if it were their own. Their support and encouragement have been incredible. This thesis is dedicated to them.

Nomenclature

Acronyms

ADC Analogue-to-digital converter

ANN Artificial neural network

DPM Diesel particulate matter

EGA Exhaust gas analyser

FID Flame ionisation detector

ROHR Rate of heat release J/deg

SOC Start of combustion

Greek Symbols

ϵ Compression ratio

μ Species mobility $\text{m}^2 \text{V}^{-1} \text{s}$

ρ_a Air density kg m^{-3}

ϕ Equivalence ratio

ρ_f Fuel density kg m^{-3}

δP Pressure drop across injector Pa

Roman Symbols

$\bar{\nu}$ Momentum transfer collision frequency $\text{s}^{-1} \text{mol}^{-1}$

c_1, c_2 Woschni heat transfer constants

e_P Prediction error in IMEP Pa

e_w	Prediction error in expansion work	J
e_y	Prediction error in torque	Nm
e_{TR}	Training error	
F_G	Ion sensor geometric factor	
K_B	Boltzmann constant	$1.38 \times 10^{-23} \text{ m}^2 \text{ kg s}^{-2} \text{ K}^{-1}$
K_{evap}	Evaporation constant	$\text{m}^2 \text{ s}^{-1}$
m_r	Reduced mass	kg
r	Ratio of length of connecting rod to crank radius	
u	Fuel spray velocity	m s^{-1}
V_S	Voltage applied to ion sensor	V
t_b	Break-up time	s
C_D	Discharge coefficient	
\dot{m}_f	Mass flow rate of fuel	kg s^{-1}
A_n	Nozzle hole area	m^2
d_n	Nozzle hole diameter	m
S	Spray penetration	m
e	Elementary charge	$1.6 \times 10^{-19} \text{ C}$
I	Ion current	A
m	Mass	kg
N	Number of particles of species	

Subscripts

0	Initial value
1	Value during current time step
2	Value during next time step
A,B	Chemical species
b	Burnt zone
u	Unburnt zone

Contents

1	Introduction	1
2	Diesel engine measurements and correlations	6
2.1	Introduction	6
2.2	Background	7
2.3	Laboratory setup	10
2.3.1	Engine parameters	10
2.3.2	In-cylinder parameters	11
2.3.3	Emissions	13
2.4	Experimental results	14
2.4.1	In-cylinder pressure	14
2.4.2	Rate of heat release	16
2.4.3	Ion current	17
2.4.4	NO _x and soot emissions	22
2.5	Relationships between the ion current and other variables	23
2.5.1	In-cylinder pressure and related variables	24
2.5.2	Start of combustion and rate of heat release	25
2.5.3	NO _x emissions	26

2.6	Summary	26
3	Ionic mechanism for methane oxidation	28
3.1	Introduction	28
3.2	Background	29
3.2.1	Ion formation in flames	29
3.2.2	Charge transport in partially ionised gases	36
3.2.3	Methane oxidation mechanisms	37
3.3	Mechanism development	42
3.4	Mechanism validation	44
3.5	Effects of PSR operating conditions on ion current	50
3.6	Summary	53
4	Constant volume chamber: methane oxidation	55
4.1	Introduction	55
4.2	Experiment	56
4.2.1	Setup	56
4.2.2	Results	57
4.3	Modelling	61
4.3.1	Setup	61
4.3.2	Results	62
4.4	Summary	67
5	Phenomenological diesel engine model	70
5.1	Introduction	70

5.2	Background and model formulation	71
5.2.1	Spray division and tip correlations	72
5.2.2	Atomisation & evaporation	74
5.2.3	Air entrainment	75
5.2.4	Heat release and species concentrations	76
5.2.5	Ion current	77
5.2.6	Heat transfer	78
5.2.7	Iterative procedure	79
5.2.8	Calibration and optimisation	81
5.3	Model predictions	82
5.3.1	In-cylinder pressure and rate of heat release	82
5.3.2	Heat transfer	85
5.3.3	Ion current	85
5.3.4	NO _x emissions	88
5.4	Summary	90
6	Heat release, NO_x and the ion current	92
6.1	Introduction	92
6.2	Heat release	93
6.2.1	Introduction	93
6.2.2	Perfectly stirred reactor	93
6.2.3	Premixed auto-igniting flames	96
6.2.4	Flames in diesel engines	98
6.3	NO _x emissions	99

6.3.1	Introduction	99
6.3.2	Perfectly stirred reactor	101
6.3.3	Premixed auto-igniting flames	104
6.3.4	Flames in diesel engines	109
6.4	Summary	112
7	Soot detection	115
7.1	Introduction	115
7.2	State of the art	115
7.3	The ion sensor as a soot mass detection device	116
7.4	Diagnosis of abnormal engine operation	120
7.5	Summary	122
8	Conclusion	124
Appendix A	Further diesel engine measurements	A-1
A.1	Introduction	A-1
A.2	Inputs to model	A-1
A.3	Engine characterisation	A-1
A.3.1	Air and fuel input	A-1
A.3.2	Injection process	A-3
A.3.3	In-cylinder parameters	A-5
Appendix B	Prediction of engine performance	B-1
B.1	Introduction	B-1
B.2	Artificial neural networks	B-1

B.3	Prediction of engine-out torque	B-3
B.4	Prediction of in-cylinder measures of performance	B-6
B.5	Analysis of ANN techniques for engine-related applications	B-7
B.5.1	Effect of ANN topology	B-7
B.5.2	Effect of training error	B-8
B.5.3	Convergence time	B-9
B.6	Summary	B-10
Appendix C Methane reaction mechanism		C-1
Appendix D Sensitivity analysis of CVC model		D-1
Appendix E Further engine modelling results		E-1
E.1	Introduction	E-1
E.2	Outputs from sub-models	E-1
E.2.1	Injection	E-1
E.2.2	Spray	E-2
E.2.3	Air entrainment	E-3
E.2.4	Fuel evaporation	E-4
E.2.5	Combustion & heat release	E-4
E.3	In-cylinder pressure and ion current predictions	E-5
E.4	Sensitivity analysis	E-6
E.4.1	Time step size	E-7
E.4.2	Spray division	E-9
E.4.3	Nozzle discharge coefficient	E-10

E.4.4	Air entrainment constants	E-11
E.4.5	Fuel evaporation constant	E-13
E.4.6	Cylinder wall temperature	E-14

Appendix F	n-Heptane reaction mechanism	F-1
-------------------	-------------------------------------	------------

List of Figures

2.1	Laboratory setup schematic (adapted from Rao [64]).	11
2.2	Ion sensor schematic (adapted from Rao & Honnery [2]).	12
2.3	Pressure in cylinder 1 at different values of engine-out torque at 1600 RPM.	15
2.4	Pressures in cylinders 1 and 4 at 1600 RPM, 140 Nm.	15
2.5	Apparent rates of heat release at 1600 RPM and 80 Nm, 120 Nm and 180 Nm.	16
2.6	Ion current signal at (a) 140 Nm and different engine speeds and (b) 1600 RPM and different engine loads.	17
2.7	Black deposit on the ion sensor.	18
2.8	Ion current signal for 10 consecutive engine cycles at 1600 RPM and 140 Nm.	19
2.9	Ion current signal ensemble-averaged over 20 (a) and 50 (b) consecutive engine cycles at 1600 RPM and 140 Nm.	20
2.10	Average and stochastic components of the ion current (a) and the in-cylinder pressure (b) at 1600 RPM and 100 Nm calculated over 80 engine cycles.	20
2.11	Important measures of the ion current signal.	21
2.12	In-cylinder pressure signal at 1600 RPM and 120 Nm using both AVL and NI systems.	22
2.13	Tailpipe NO _x at 1200 RPM, 1600 RPM and 1800 RPM and various engine loads.	22

2.14	Tailpipe soot mass for varying engine load at 1600 RPM.	23
2.15	Ion current integral versus engine-out torque at 1600 RPM.	24
2.16	Comparison of rate of heat release and ion current at 1600 RPM, 140 Nm.	25
2.17	Ion current integral versus cumulative heat release at 1600 RPM.	25
2.18	Ion current integral versus tailpipe NO_x at 1600 RPM.	26
3.1	Mass spectrometry results for positive ion concentrations in a fuel-lean methane-air flame [57].	32
3.2	Reaction flow diagram for positive ion formation in a fuel-rich methane-air flame [57].	33
3.3	Mass spectrometry results for positive ion concentrations in a fuel-rich methane-air flame [57].	34
3.4	Reaction flow diagram for positive ion formation in a fuel-rich methane-air flame [57].	35
3.5	Temperature, methanol and carbon monoxide concentrations in a stoichiometric methanol-air flame at atmospheric pressure [126].	39
3.6	Concentration profiles for H, O and OH radicals in a stoichiometric methanol-air flame at atmospheric pressure [126].	40
3.7	General simplified methane oxidation scheme [146].	42
3.8	Measured and predicted laminar flame speeds for methane in air at 10 bar and 20 bar.	45
3.9	Measured and predicted temperature and flame composition for an atmospheric laminar methane-air flame, $\phi = 0.86$	46
3.10	Measured and predicted temperature and flame composition for an atmospheric laminar methane-air flame, $\phi = 1.0$. Figure taken from Rao & Honnery [83].	46
3.11	Measured and predicted temperature and flame composition for an atmospheric laminar methane-air flame, $\phi = 1.25$	47

3.12	Main combustion products mole fractions for Leeds mechanism, GRI-Mech 3.0 and current mechanism for varying temperature at reactor operating pressure 20 bar, equivalence ratio 1.0 and residence time 5.57×10^{-3} s.	48
3.13	Main combustion products mole fractions for Leeds mechanism, GRI-Mech 3.0 and current mechanism for varying pressure at inlet temperature 750 K, equivalence ratio 1.0 and residence time 5.57×10^{-3} s. . . .	48
3.14	Main combustion products mole fractions for Leeds mechanism, GRI-Mech 3.0 and current mechanism for varying equivalence ratio at inlet temperature 750 K, reactor operating pressure 20 bar and residence time 5.57×10^{-3} s.	49
3.15	CH and O mole fractions for Leeds mechanism, GRI-Mech 3.0 and current mechanism for varying temperature at reactor operating pressure 20 bar, equivalence ratio 1.0 and residence time 5.57×10^{-3} s.	49
3.16	CH and O mole fractions for Leeds mechanism, GRI-Mech 3.0 and current mechanism for varying pressure at inlet temperature 750 K, equivalence ratio 1.0 and residence time 5.57×10^{-3} s.	50
3.17	CH and O mole fractions for Leeds mechanism, GRI-Mech 3.0 and current mechanism for varying equivalence ratio at inlet temperature 750 K, reactor operating pressure 20 bar and residence time 5.57×10^{-3} s.	50
3.18	Temperature and positive ion concentration profiles for a flat methane-air flame at atmospheric pressure, equivalence ratio 0.513 and temperature at the burner mouth 402 K. Experimental data taken from Wortberg [157].	51
3.19	Predicted ion current at varying values of temperature, pressure, equivalence ratio and residence time. Default values are 298 K, 1 bar, 1.0 and 0.1 s respectively.	52
4.1	Schematic of the constant volume chamber [83].	56
4.2	Schematic of the ion sensor [83].	57
4.3	Experimentally measured ion current and chamber pressure for an equivalence ratio of 0.8 and initial chamber pressures 3 bar and 6 bar. . . .	58

4.4	Experimentally measured ion current and chamber pressure for an equivalence ratio of 1.0 and initial chamber pressures 3 bar and 6 bar. .	58
4.5	Experimentally measured ion current and chamber pressure for an equivalence ratio of 1.2 and initial chamber pressures 3 bar and 6 bar. .	59
4.6	Experimentally measured ion current and chamber pressure for an equivalence ratio of 1.0 and initial chamber pressures 3 bar and 6 bar, with time normalised by total time taken for the combustion event [83].	60
4.7	Experimentally measured ion current and chamber pressure for an equivalence ratio of 1.0 and initial chamber pressure 5 bar with two ion sensors	61
4.8	Charged species concentrations at the centre of the chamber during the combustion event.	62
4.9	Comparison of experimental and modelled ion current and chamber pressure at an equivalence ratio of 0.8 and initial chamber pressure 3 bar [83].	63
4.10	Temperature (top) and electron concentration (bottom) distributions in the chamber at an equivalence ratio of 0.8 and initial chamber pressure 3 bar, $\tau_p = -0.094$ s [83].	64
4.11	Comparison of experimental and modelled ion current and chamber pressure at an equivalence ratio of 0.8 and initial chamber pressure 6 bar [83].	65
4.12	Comparison of experimental and modelled ion current and chamber pressure at an equivalence ratio of 1.0 and initial chamber pressure 6 bar [83].	65
4.13	Comparison of experimental and modelled ion current and chamber pressure at an equivalence ratio of 1.2 and initial chamber pressure 6 bar [83].	66
4.14	Temperature (top) and electron concentration (bottom) distributions in the chamber at an equivalence ratio of 1.2 and initial chamber pressure 6 bar, $\tau_p = -0.130$ s [83].	66
4.15	Concentrations of OH and electrons at the centre of the chamber during the combustion event. Initial pressure 6 bar and equivalence ratio 1.2. .	67

4.16	Concentrations of OH and electrons at the centre of the chamber during the combustion event. Initial pressure 6 bar and equivalence ratio 0.8. . .	68
5.1	Schematic of the interaction of various sub-models.	72
5.2	Schematic of spray division. (a) Cross-section and (b) 3-D.	73
5.3	Relative locations of the piston crown and the injector at 167 CAD. . .	75
5.4	Geometry of the cylinder head with the ion sensor mounted	78
5.5	Weighting function used for optimisation at 1600 RPM, 140 Nm.	82
5.6	Experimental and modelled in-cylinder pressure (a) and heat release (b) at 1600 RPM, 80 Nm.	83
5.7	Experimental and modelled in-cylinder pressure (a) and heat release (b) at 1600 RPM, 180 Nm.	83
5.8	Experimental and modelled in-cylinder pressure (a) and heat release (b) at 1200 RPM, 140 Nm.	84
5.9	Experimental and modelled in-cylinder pressure (a) and heat release (b) at 1800 RPM, 140 Nm.	84
5.10	Modelled heat loss, net heat release and gross heat release at 1600 RPM, 80 Nm (a) and 1600 RPM, 180 Nm (b).	85
5.11	Experimental and modelled ion current at 1600 RPM, 80 Nm (a), 140 Nm (b) and 180 Nm (c).	86
5.12	Trend in normalised ion current integral with changing engine-out torque at 1600 RPM.	87
5.13	Cylinder-average mole fractions of O, OH and CH at 1600 RPM and 140 Nm.	87
5.14	Cylinder-average mole fractions of electrons, H_3O^+ and NO^+ at 1600 RPM and 140 Nm.	88
5.15	Experimental and modelled tailpipe NO_x at 1200 RPM (a), 1600 RPM (b) and 1800 RPM (c).	89

5.16	Predicted evolution of in-cylinder NO_x at 1600 RPM and 80 Nm, 140 Nm and 180 Nm.	89
5.17	Predicted evolution of in-cylinder NO^+ (bold lines) and rate of NO_x production (thin lines) at 1600 RPM and 80 Nm, 140 Nm and 180 Nm.	90
6.1	Evolution of temperature and electron concentration in a perfectly-stirred reactor model with inlet temperature 1450 K, equivalence ratio 0.4 and reactor operating pressure 70 bar.	94
6.2	Important reactions affecting temperature at 1.9×10^{-6} s.	94
6.3	Important reactions affecting electron mole fraction at 1.9×10^{-6} s.	96
6.4	Rate of heat release and concentrations of CH, OH and electrons for a pre-mixed auto-igniting n-heptane flame in air	97
6.5	Rate of heat release and concentration of electrons in two randomly selected packets in the spray at 1600 RPM and 140 Nm. One packet participates in pre-mixed combustion, the other in mixing-controlled.	98
6.6	Evolution of temperature and OH, O, CH and electron concentrations in the diesel spray at 1600 RPM and 120 Nm	100
6.7	Modelled ion current integral and modelled net cumulative heat release at 1600 RPM. $r^2 = 0.94$	101
6.8	Evolution of electron mole fraction (a) and NO mole fraction (b) in a perfectly stirred reactor operating at 70 bar, inlet temperature 1450 K and equivalence ratio 0.4.	102
6.9	Sensitivities of electron production rate (a) and NO production rate (b) to important species.	103
6.10	Sensitivities of production rate of electrons and O (a) and NO, NO_2 and O (b) to important species.	104
6.11	Evolution of NO and electron concentrations in premixed flames of different final temperatures but identical equivalence ratios in a chamber of changing volume.	105
6.12	Evolution of NO production rate, temperature and O concentration during the combustion event.	106

6.13	Evolution of temperature and electron and CH concentrations during the combustion event. Inset: electron and CH concentration peaks. . .	107
6.14	Changes in final NO concentration, peak electron concentration and time integral of electron concentration with different peak mixture temperatures.	107
6.15	Variation in peak electron concentration against final NO concentration.	108
6.16	Evolutions of NO_x and NO^+ in a pre-mixed flame undergoing auto-ignition.	108
6.17	Ion current and NO_x evolution at 1600 RPM, 140 Nm.	109
6.18	Ion current and NO_x evolution in a randomly chosen packet in the spray at 1600 RPM, 140 Nm.	110
6.19	Modelled evolutions of temperature (a), NO_x concentration (b) and electron concentration (c) in a diesel spray at 1600 RPM and 140 Nm. .	110
6.20	Modelled NO_x , ion current integral and ion current peak at 1600 RPM and different engine loads.	111
6.21	Modelled ion current integral and peak against modelled NO_x for different engine loads at 1600 RPM.	112
7.1	Ion current signal at 1200 RPM and different torque settings.	118
7.2	Ion current signal when the engine is cranked with no fuel flow, (a) just after shutdown, (b) after the engine has cooled and (c) after the sensor is removed, cleaned and refit.	119
7.3	Variation of the ion current offset with tailpipe soot.	120
7.4	Ion current signal with injectors in different states of wear at 1200 RPM, 80 Nm (a) and 1200 RPM, 200 Nm (b).	121
7.5	Ion current signal using exhaust systems with and without a DPF at 1200 RPM, 50 Nm (a) and 1200 RPM, 200 Nm (b).	122
A.1	Volumetric flow rate and volumetric efficiency for varying speed at 140 Nm (a) and varying load at 1600 RPM (b).	A-2

A.2	Air-fuel ratio for varying speed at 140 N m (a) and varying load at 1600 RPM (b).	A-3
A.3	Injector needle lift profile at 1600 RPM, 140 Nm with important injection parameters marked.	A-4
A.4	Variation in start of injection and injection duration for 1200 RPM, 1600 RPM and 1800 RPM.	A-4
A.5	Fuel pressure in high pressure line for varying speed at 140 N m (a) and varying load at 1600 RPM (b).	A-5
A.6	Comparison of the original and filtered pressure signals at 1800 RPM and 140 Nm.	A-6
A.7	In-cylinder pressure, rate of heat release and ion current measured at 1600 RPM, 80 Nm.	A-6
A.8	In-cylinder pressure, rate of heat release and ion current measured at 1600 RPM, 100 Nm.	A-7
A.9	In-cylinder pressure, rate of heat release and ion current measured at 1600 RPM, 120 Nm.	A-7
A.10	In-cylinder pressure, rate of heat release and ion current measured at 1600 RPM, 140 Nm.	A-8
A.11	In-cylinder pressure, rate of heat release and ion current measured at 1600 RPM, 160 Nm.	A-8
A.12	In-cylinder pressure, rate of heat release and ion current measured at 1600 RPM, 180 Nm.	A-9
A.13	In-cylinder pressure, rate of heat release and ion current measured at 1200 RPM, 140 Nm.	A-9
A.14	In-cylinder pressure, rate of heat release and ion current measured at 1800 RPM, 140 Nm.	A-10
B.1	Torque prediction error of a four layer, 20 neuron ANN at 1600 RPM, varying engine torque (a) and 140 Nm, varying engine speed (b) [2]. . .	B-4

B.2	Prediction errors of ten artificial neural networks with identical topologies and training errors for 12 Nm, 100 Nm and 180 Nm [2].	B-6
B.3	Error in prediction of engine-out torque, net IMEP and expansion work when a four layer, 20 neuron ANN is used [2].	B-7
B.4	Comparison of prediction performance of ANNs with different topologies at moderate-to-high torque settings. $e_{TR} = 7.0\%$. Figure taken from Rao & Honnery [2]	B-8
B.5	Comparison of prediction performance of four layer, 20 node ANNs topologies at moderate-to-high torque settings with different training errors [2].	B-9
B.6	Comparison of convergence time of ANN topologies over a range of training errors [2].	B-9
D.1	Modelled chamber pressure at 3 bar and equivalence ratio 0.8 for different average cell sizes.	D-1
D.2	Modelled chamber pressure at 3 bar and equivalence ratio 0.8 for different values of time step.	D-2
E.1	Modelled pressure drop across the injector at 1600 RPM, 80 Nm and 1600 RPM, 180 Nm.	E-2
E.2	Spray tip penetration and velocity at 1600 RPM, 80 Nm (a) and 1600 RPM, 180 Nm (b).	E-2
E.3	Spray breakup time and length for 1600 RPM, 80 Nm (a) and 1600 RPM, 180 Nm (b).	E-3
E.4	Air entrainment characteristics for 1600 RPM, 80 Nm (a) and 1600 RPM, 180 Nm (b).	E-4
E.5	Mass of fuel injected and mass of fuel vapour at 1600 RPM, 80 Nm (a) and 1600 RPM, 180 Nm (b).	E-5
E.6	Modelled temperatures of burnt and unburnt zones and cylinder average at 1600 RPM, 80 Nm (a) and 1600 RPM, 180 Nm (b).	E-6

E.7	Measured and predicted in-cylinder pressure and ion current at 1600 RPM, 80 Nm.	E-6
E.8	Measured and predicted in-cylinder pressure and ion current at 1600 RPM, 100 Nm.	E-7
E.9	Measured and predicted in-cylinder pressure and ion current at 1600 RPM, 120 Nm.	E-7
E.10	Measured and predicted in-cylinder pressure and ion current at 1600 RPM, 140 Nm.	E-8
E.11	Measured and predicted in-cylinder pressure and ion current at 1600 RPM, 160 Nm.	E-8
E.12	Measured and predicted in-cylinder pressure and ion current at 1600 RPM, 180 Nm.	E-9
E.13	Measured and predicted in-cylinder pressure and ion current at 1200 RPM, 140 Nm.	E-9
E.14	Measured and predicted in-cylinder pressure and ion current at 1800 RPM, 140 Nm.	E-10
E.15	Sensitivity of in-cylinder pressure predictions to time step size.	E-10
E.16	Sensitivity of NO_x predictions to time step size.	E-11
E.17	Sensitivity of ion current predictions to time step size.	E-11
E.18	Sensitivity of in-cylinder pressure predictions to number of radial zones.	E-12
E.19	Sensitivity of NO_x predictions to number of radial zones.	E-12
E.20	Sensitivity of ion current predictions to number of radial zones.	E-13
E.21	Sensitivity of in-cylinder pressure prediction to air entrainment factor before impingement (a) and after impingement (b).	E-13
E.22	Sensitivity of in-cylinder pressure prediction to evaporation constant.	E-14
E.23	Sensitivity of NO_x prediction to evaporation constant.	E-14
E.24	Sensitivity of ion current prediction to evaporation constant.	E-15

E.25 Sensitivity of in-cylinder pressure prediction to cylinder wall temperature.	E-15
E.26 Sensitivity of NO_x prediction to cylinder wall temperature.	E-16
E.27 Sensitivity of ion current prediction to cylinder wall temperature. . . .	E-16

List of Tables

2.1	Resolution of measurements taken for engine parameters [64].	11
2.2	Statistics of chosen parameters of the ion current curve over 150 consecutive engine cycles at 1600 RPM, 140 Nm.	21
3.1	Predicted properties of the burnt gas in atmospheric pressure methane-air flames by various mechanisms. Table taken from Westbrook & Dryer [126]	38
3.2	Region of interest for methane oxidation mechanism.	43
5.1	Entrainment constants at different values of engine speed.	76
5.2	In-cylinder pressure prediction error at different engine speeds	83
7.1	DPM emissions for old and reconditioned injectors at 1200 RPM (mg m^{-3}).121	
A.1	Model inputs.	A-2
A.2	Injection parameters for different engine-out torque values at 1600 RPM.A-5	
B.1	Engine operating points tested for prediction of engine speed and torque.B-3	

List of Publications

Journal Publications

- Rahul Rao and Damon Honnery. The prediction of torque in a diesel engine using ion currents and artificial neural networks. *International Journal of Engine Research* 15(3): 370-380, 2014.
- Rahul Rao and Damon Honnery. A simplified mechanism for the prediction of the ion current during methane oxidation in engine-like conditions. *Combustion and Flame*, 2015.
- Rahul Rao and Damon Honnery. A study of the relationship between NO_x and the ion current in a direct-injection diesel engine. *Combustion and Flame*, under review.

Conference Publications

- Rahul Rao and Damon Honnery. A reduced ionic mechanism for methane oxidation. *Australian Combustion Symposium*, 6-8 November 2013, University of Western Australia.
- Rahul Rao and Damon Honnery. Modelling of the ion current developed in a direct-injection diesel engine. *Australian Combustion Symposium*, 7-9 December 2015, University of Melbourne.

Chapter 1

Introduction

For the better part of the last century, diesel engines have been recognised as the powerplant of choice when reliability and efficiency have been of paramount importance. Today, they are in use in a variety of applications all over the world. From large ships carrying hundreds of tons of machinery across the world to little generators used to provide electricity in developing countries, it is difficult to think of a facet of today's life that has not been touched by the diesel engine. Rudolf Diesel could hardly have imagined the impact his creation would have on the lives of people living a hundred years later.

Given the ubiquitous nature of the diesel engine, it is hardly surprising that it has been the subject of significant study over the past few decades. Despite these efforts, a full understanding of combustion in diesel engines has not yet been obtained. With the many variables in the fuel spray, air flow and mixing patterns, the motion of the piston, heat loss and effect of combustion chamber geometry, combustion in a diesel engine is an incredibly complex phenomenon.

With this complexity in mind, there are a large number of operational parameters that an engine designer needs to optimise in order to meet some required targets of engine manufacture, performance and emissions. These parameters are all inter-linked, making the design of an engine an expensive and time-consuming affair. Allied to these requirements are the constant redesign required of engines in order to comply with increasingly strict emissions laws, satisfy the end-user's requirements of fuel-efficiency and operability, and take advantage of the invention of new materials and manufacturing processes.

The use of in-cylinder sensors can greatly aid the design process for engines by decoupling parameters of interest. Several different types of in-cylinder sensors have

been developed over the years. In-cylinder pressure transducers are commonly used in laboratories, giving repeatable and reliable signals [1–3]. The in-cylinder pressure, however, is a bulk variable that may not be able to capture fine details of the combustion process. Thermocouples integrated into pistons or cylinder heads can give somewhat spatially resolved temperature measurements of the combustion chamber walls, from which gas temperature can be approximated [4, 5]. Optically accessible engines have one or more transparent windows in the cylinder walls to allow the use of a high-speed camera to record combustion events [6–8] and can give very detailed spatial information on the combustion process. However, the high mixture temperatures in the combustion chamber can make sealing problematic in such engines and, given the modifications required for an engine not specifically designed for optical access, this technique is currently impractical outside the laboratory setting.

When engines are used in the field, different environments, fuels of variable quality and age-related wear often mean the engine is operating well outside its design envelope. Currently, the end-users of engines have little access to in-cylinder data to determine metrics such as engine-out torque or tailpipe emissions, or to detect engine faults such as worn injectors or clogged air filters. A sensor with the ability to achieve this in the field would be of great use to the end-user.

The ion sensor is another instrument that has been used in internal combustion engines. It measures the current carried between two oppositely charged electrodes by charged species which are formed as intermediate compounds during the combustion of hydrocarbon fuels. Since the formation of ions is a direct effect of the combustion process, the ion current may be a useful indicator of combustion. The ion current signal depends on the location of the current path between the electrodes. This dependence adds some complexity to the analysis of the ion current but the spatial information obtained can possibly be of use in engine monitoring.

Ionisation in flames is a field of thermodynamics dating back to the 1950s when the formation of electrons and ions in rocket exhausts and their interference with magnetic waves used for communications were a concern for telecommunications engineers [9]. During this period, the development of magneto-hydrodynamic energy converters was also of interest [10], where an increase in charged particle concentrations was desirable. Since then, ionisation has been linked to both soot formation [11–14] and NO_x formation [15, 16].

Ion sensors have been used extensively in SI engines from the first tailpipe ion detection [17] to more modern in-cylinder studies. In the cylinders of these engines, the ion current has been proven able to predict quantities such as air-fuel ratio [15, 18–21],

peak pressure position [22, 23], and in-cylinder pressure [24]. The ion signal has also been used as an input to the engine control unit to control spark advance timing [20] and to detect and control knock and misfire [25–31]. In SI engines, the spark plug can be used both as the initiator of the combustion process and as an ion sensor. Another style of ion sensor involves one of the electrodes being sandwiched between two insulating materials forming the head gasket of the cylinder [32–34].

In CI engines, a suitable glow plug can be modified to act as an ion sensor. The use of such a sensor has enabled the measurement of the ion current signal in diesel engines, leading to accurate estimations of crank angle at start of combustion [35–38], detection of combustion resonance [39], closed-loop control of injection [40] and estimations of soot formation [41].

Ion currents have not been studied as extensively in CI engines as in SI engines. When the cylinder composition is not uniform, as in conventional diesel engines, the location of the ion sensor greatly affects the signal obtained from it. Multiple injector sprays and in-cylinder air motion make the ion current signal difficult to analyse in a spatial sense. Combined with the effects of shot-to-shot and spray-to-spray variations in injectors, injector spray patterns and geometry of the combustion chamber, the ion current from a CI engine is an inherently complex signal.

Signals as complex as the ion current can often be statistically analysed to produce useful results, albeit with little understanding of the physical or chemical processes underlying ion generation. This is the approach generally taken in studies seeking to make use of the ion current. The present work seeks to redress this shortcoming in the field by approaching the ion current signal from the basics of hydrocarbon chemistry and thereby to provide further insight into ion formation in diesel engines.

Chapter 2 describes the experimental setup developed for the measurement of the ion current and engine performance and emissions parameters of interest in a direct-injection diesel engine. Experimental results are presented for the ion current, in-cylinder pressure, rate of heat release and tailpipe emissions of both NO_x and soot. This chapter also describes relationships between several engine operating parameters of interest and the ion current. Whilst several such relationships exist, there is as yet little understanding of how and why changes in these operating parameters affect the ion current.

Part of the reason for the lack of understanding of ion currents in diesel engines is the difficulty of modelling ion formation in such a complex system. It is necessary to be confident in the mechanisms used to model ion formation, but the large number of

uncontrollable variables inherent to engine operation and the difficulty of measuring ion concentrations in the combustion chamber make detailed validation of these models impractical.

In order to gain a better understanding of the ion generation mechanisms, simple hydrocarbons can be studied in simple experiments initially, with a view to gradually building complexity into the experiments and models. To begin this study, methane is chosen as fuel. Chapter 3 describes the development of a highly simplified ionic mechanism for methane oxidation for use in high temperature, high pressure combustion problems involving CFD modelling. In the absence of experimental data at suitable temperature and pressure values, species concentrations predicted by the mechanism are compared to experimentally measured concentrations in atmospheric laminar flames. The effects of changing system variables on the ion current in a perfectly stirred reactor are examined and the mechanisms by which they operate identified.

Combustion in a constant-volume chamber is studied as an intermediate step between atmospheric laminar flames and diesel engines. Chapter 4 describes the experimental setup and measurements of chamber pressure and ion current during the constant-volume combustion of methane. This experiment is modelled in ANSYS Fluent using the mechanism developed previously. Comparisons of experimental and modelling results are presented. Outputs from the model allow interesting features of the ion current signal measured at different values of equivalence ratio to be explained in the context of findings from Chapter 3.

The constant-volume combustion problem of a fuel, whilst not a trivial phenomenon, still lacks many complex features seen in combustion in a diesel engine. Having developed confidence in the ion generation mechanism, this mechanism needs to be studied in conditions representative of a diesel engine. The inclusion of this mechanism in a phenomenological diesel engine model is described in Chapter 5. Experimental results are compared to predictions from the model. The development of charged species in the diesel flame is investigated and compared to that seen in the constant-volume chamber.

Chapter 6 shows the use of predictions from the ion current mechanism integrated into the diesel engine model to explain some of the correlations presented in Chapter 2. Heat release and tailpipe NO_x are chosen as parameters of interest. The concentrations of species important to the ion current and also to these variables is examined in several combustion modes in order to lay bare the underlying phenomena linking these variables and the common conditions that must exist for their generation.

Chapter 7 describes the use of the ion sensor as a sensor for tailpipe soot and therefore also as a diagnostic tool for engine conditions leading to increased soot emissions. Such studies are currently in their infancy and further investigation is required, involving carefully measured artificially engineered faults in vital engine components such as injectors, piston rings and valves. Whilst this is beyond the scope of this study, Chapter 7 indicates a possible direction ion current studies may take in the near future.

Chapter 2

Diesel engine measurements and correlations

2.1 Introduction

This chapter describes previously-found correlations between the ion current and various engine operating parameters, and presents experimental data corroborating some of these correlations.

The experimental setup used to characterise the diesel engine in which the ion current is measured is described in detail. The methods used to measure engine performance parameters (speed, torque, air flow rate and fuel consumption), in-cylinder parameters (cylinder pressure, injector needle lift, fuel pressure and ion current) and emissions (soot and NO_x) are discussed.

Selected experimental results for the in-cylinder pressure, rate of heat release, ion current, NO_x emissions and soot emissions are shown. Further results for different engine operating conditions and for different engine characteristics can be found in Appendix A.

The ion current signal is analysed in some detail; the profile and the y -offset are shown and possible reasons for these are discussed. A statistical analysis of the ion current is conducted to show its repeatability over a large number of engine cycles.

This signal is then shown to be well correlated to several engine operating parameters of interest. These correlations are simple to obtain, but any detailed insight into the reasons for these correlations has not been presented thus far. Subsequent chapters

in this study describe the interrogation of ion generation mechanisms, beginning with simple fuels in simple flames and terminating with a diesel surrogate fuel in a combusting spray, with the aim of explaining the reasons for these correlations. These reasons are finally presented in Chapter 6.

2.2 Background

Chapter 1 briefly listed a variety of ways in which the ion current is used in engines. This section expands upon these uses and provides an appreciation for the capability of the ion sensor to predict a variety of engine operating parameters.

Ion sensors in SI engines are typically integrated with the spark plug; a relatively small voltage is applied to the ignition coil after the spark is fired. The ion current between the two electrodes of the spark plug is then measured. Several interesting uses for the resulting signal have been found over the years.

Reinmann et al. [15] found that several features of the ion current curve were correlated with the air-fuel ratio in a 1.6 L petrol engine. This study included a rudimentary model for the ion current peak magnitude; the concentration of principal ions was assumed to be inversely proportional to the air-fuel ratio for values above 0.8.

Asano et al. [29] developed an engine control system that used the variation in ion current duration (peak width) to determine and control air-fuel ratio. This control system also used the ion current to detect knock via constant frequency oscillations in the signal. A similar constant frequency oscillation was seen in a diesel engine by Badawy et al. [39], indicating the occurrence of combustion resonance.

Balles et al. [18] observed that the peak value of the ion current, the location of the peak value of the ion current and the integral of the ion current are all strongly correlated with the air-fuel ratio in an SI engine. These correlations were observed experimentally but no further explanation given.

Hellring et al. [42] used neural networks to estimate the air-fuel ratio using the ion current as input. Gazis et al. [24] used a similar technique with thirteen measurements of the ion current curve as input to predict four characteristics of the in-cylinder pressure. The neural network was able to predict peak pressure magnitude and location with fair accuracy.

Hellring and Holmberg [22] presented an algorithm used to estimate peak pressure

position from the ion current, using their observation that peak pressure coincides with a local maximum in the ion current peak. Their observation is not seen in other studies. This algorithm was also used to control the location of peak pressure via spark advance timing [20].

The ion current has also been studied in HCCI and CI engines. Tanaka et al. [43] showed that the ion current was strongly correlated with air-fuel ratio, peak rate of heat release location and magnitude, and peak pressure timing in an HCCI engine. Whilst being of practical use, the reasons for these correlations were not explored.

Glavmo et al. [35] used the ion current to detect the start of combustion in a diesel engine. SOC was deemed to have occurred when the ion current derivative reached a set threshold. This phenomenon was used to control the start of combustion via injector timing. The authors noted that the ability to detect SOC enables the diagnosis of misfire, injectors stuck open or closed, the use of incorrect fuel and incorrect injection timing.

Kubach et al. [36] also detected SOC in a similar manner using the ion current signal in an direct-injection diesel engine. They also used the calculation of ignition delay using the predicted SOC to control the pilot injection quantity in order to reduce the maximum burn rate and control noise.

A number of studies correlating the ion current to various engine operating parameters of interest have emerged from Wayne State University. Badawy et al. [44] characterised the ion current developed in a single-cylinder diesel engine and observed pronounced effects of engine load, injection pressure, injection timing and engine speed on the ion current.

The same group then used the ion current signal to predict and control the peak pressure location via feedback to the ECU. This was achieved by observing that the initial increase in the ion current leads the peak pressure by a fixed temporal value. The ion current was also used with a fuzzy logic control system to control combustion phasing [45].

Badawy et al. [41] also used the ion current to predict tailpipe soot. They noted the lack of understanding of ion formation in diesel engines and hence used non-linear multiple regression with up to four measures of the ion current curve. This model was able to predict tailpipe soot with good accuracy.

Estefanous et al. [16] compared the ion current to NO_x formation in the cylinder. The ion current generated by thermal ionisation of NO was calculated using the Saha

ionisation equation [46]. This was found to be a small fraction of the total ion current measured. The peak ion current was found to be well correlated to in-cylinder NO_x .

A testament to the versatility and utility of the ion sensor is the number of patents it is a part of. Patents exist that integrate the ion sensor into the fuel injector [47] and use the ion sensor to measure engine performance, emissions or in-cylinder parameters [48, 49], modify combustion and reduce emissions [50], and detect and control abnormal combustion [51]. Whilst these patents describe the use of ion sensors for various purposes that would be of interest to OEMs, such applications appear to have been confined to laboratory settings thus far.

Despite the evident appreciation for the utility of the ion sensor, a common thread running through the aforementioned studies is the lack of detailed analysis explaining why the ion sensor can be used in these ways. Statistical or similar models are used which, whilst providing good results, can give little insight into the physical and chemical processes occurring within the combustion chamber leading to ion formation — they are treated as black boxes. Without this understanding, large data sets must be obtained to ensure robustness of predictions. Even when large data sets are available, long-term changes in engine operation or operating conditions not accounted for in the data set make accurate prediction difficult. The use of different fuels makes it necessary to redo the experiments to obtain a data set for each fuel.

This problem can be mitigated somewhat by a greater understanding of the processes leading to ion generation. Given this knowledge, models can be developed to examine the effects of changing operating parameters on the ion current and determine the variables the ion current is most sensitive to, greatly reducing the volume of experimental data needed to be collected.

The development of such models is made easier by advances in the field of chemical kinetics which enable a more accurate estimation of the chemistry within the combustion chamber. To this end, a small number of studies have attacked the problem of ion generation in engines. Some of these studies use chemical kinetics to predict NO_x concentration and calculate an equilibrium between NO and NO^+ [52–54] — in this case, NO^+ is the only positive ion modelled and electrons the only negatively charged particles. These studies, however, ignore a wealth of research on hydrocarbon flames pointing out the importance of the H_3O^+ ion [55–59]. Others use equilibrium models including ions in highly simplified systems [60, 61]. Complexity can be further increased by the use of chemical kinetics in place of equilibrium — Aithal [62] provides one example.

Estefanous [63] presented a modelling study of the ion current in diesel engines which used 3-D CFD techniques with a 120 reaction, 58 species reaction mechanism. Good agreement was obtained between the experimental and modelled in-cylinder pressure and ion current. The complexity of the CFD approach to modelling, however, makes it difficult to perform parametric studies on the ion current due to the computational expense incurred. Such a model is therefore not a suitable candidate for exploring ion generation in a quick and efficient manner.

This study aims to bridge the gap between chemical kinetics research and ion current measurements in engines to explain some of the correlations described above. These correlations are first investigated experimentally on a diesel engine in this chapter. In subsequent chapters, a model of ion generation is developed, first for simple systems and then for a diesel engine. These models are used to develop an understanding of the relationships between the ion current and important engine performance and emissions measurements.

2.3 Laboratory setup

A schematic of the laboratory setup is shown in Figure 2.1. Experiments were conducted on a Hino W04D 4 litre, 4 cylinder naturally aspirated direct-injection diesel engine coupled to a Heenan-Froude eddy current dynamometer. Control of the dynamometer was achieved using a Froude-Hofmann V4 controller. The engine is equipped with a pump-in-line mechanical injection system; the injection process is therefore controlled by the governor and direct control is not achievable by the operator. No external exhaust gas recirculation occurs. It is instrumented with various sensors to measure both in-cylinder and engine parameters as described in the following sections.

2.3.1 Engine parameters

The engine parameters of interest are the engine speed and load, air and fuel flow rates and intake air temperature. The engine speed and load are measured by the Froude-Hofmann V4 dynamometer controller. Fuel consumption is measured by an A&D LC1205-K020 mass balance. K-type thermocouples are used to measure temperatures of the intake air, coolant, engine oil, exhaust and fuel. The volumetric air flow rate is measured using a turbine flowmeter. Manifold pressure is measured using a pressure transducer in the intake.

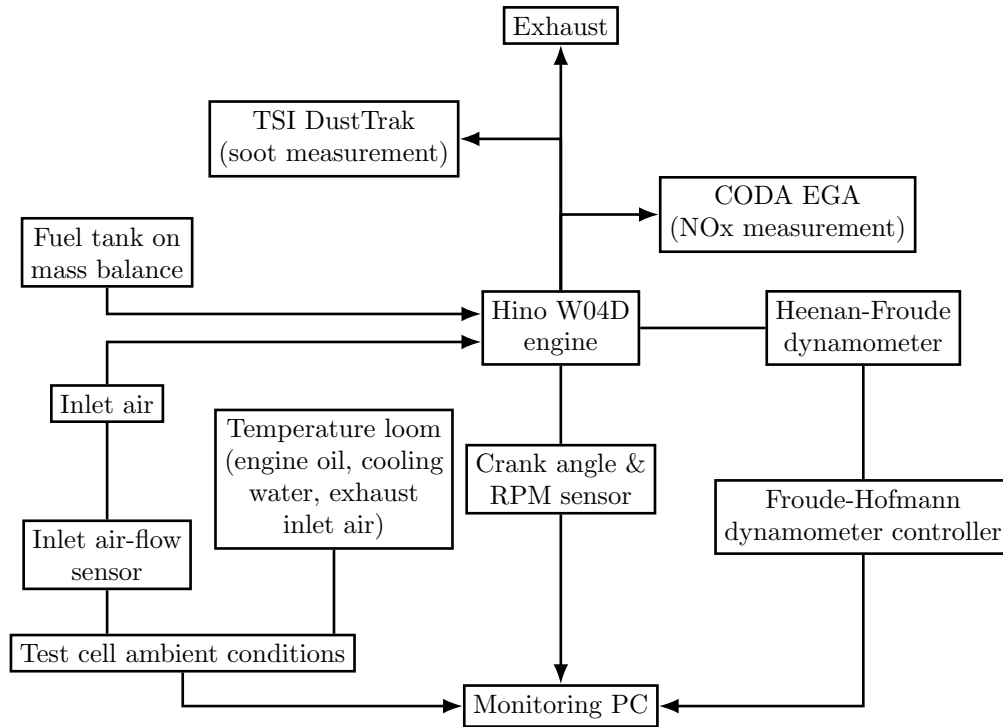


Figure 2.1: Laboratory setup schematic (adapted from Rao [64]).

These sensors are connected to a National Instruments PCI6013 24-bit analogue-to-digital converter. National Instruments Virtual Bench Logger (VBL) is used to acquire and record readings from these sensors at a rate of 1 Hz. The logging period is 60 s. All VBL data is presented as the average over the logging period. Table 2.1 shows the resolution of the sensors used.

Table 2.1: Resolution of measurements taken for engine parameters [64].

Parameter measured	Unit	Resolution
Engine speed	RPM	± 1
Engine-out torque	N m	± 0.1
Temperature	K	± 0.5
Volumetric air flow rate	$\text{m}^3 \text{s}^{-1}$	$\pm 2\%$
Fuel mass	g	± 1

2.3.2 In-cylinder parameters

Cylinders 1 and 4 are instrumented with AVL GU12P high pressure piezoelectric pressure transducers installed in the glow plug ports and located flush with the cylinder head. The range of these sensors is 0–200 bar with a linearity of 0.3% and a frequency of 130 kHz. The fuel line to cylinder 1 is instrumented with an AVL SL31D2000 fuel

pressure transducer capable of measurements in the range 0–2000 bar with a linearity of 0.5% and frequency of 50 kHz. The injector in cylinder 1 is fitted with an AVL needle lift indicator. Crank angle is measured using an AVL 346 angle encoder capable of measurements up to 20,000 RPM.

These sensors are connected through AVL charge amplifiers to an AVL Indimeter 619. AVL Indicom software is used to acquire and record data. The sampling rate used is 0.2 CAD. All AVL data is presented as the average of 80 engine cycles.

The ion current is measured in cylinder 3 using an ion sensor whose schematic is shown in Figure 2.2, adapted from Rao & Honnery [2]. The internal heating element of a Bosch GPH-408 glowplug is replaced by a 3 mm diameter mild steel rod that acts as the positive electrode. Aremco 571 ceramic adhesive is used to electrically insulate the positive electrode from the glowplug casing. The ion sensor is designed to be inserted into the glow plug port of the Hino W04D and to extend the same distance into the cylinder as the factory glow plug.

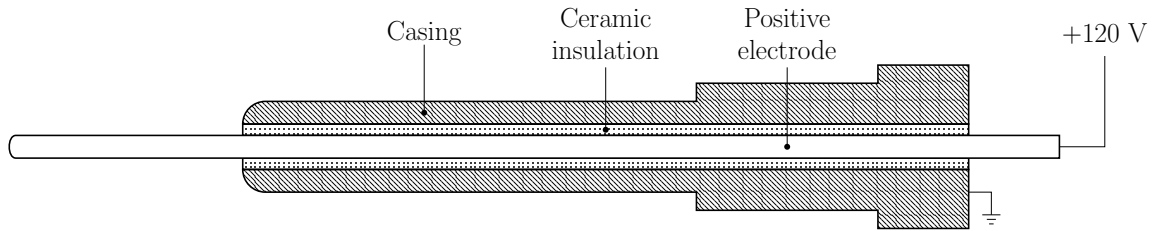


Figure 2.2: Ion sensor schematic (adapted from Rao & Honnery [2]).

The centre electrode is maintained at 120 V relative to the engine block; the current between this electrode and the engine block is measured by a 16-bit National Instruments NI4350 analogue-to-digital converter operating at 80 kHz. The ion current signal is later downsampled to a resolution of 0.2 CAD to match the AVL data.

The location of the ion current signal with respect to piston top dead centre (TDC) is obtained using reflective tape on the engine flywheel and a Honeywell HOA1405 reflective emitter and sensor. The rise and fall time for this sensor is 15 μ s, corresponding to 0.162 CAD at 1800 RPM and 0.108 CAD at 1200 RPM. This enables synchronising of the ion current and pressure signals.

In-cylinder measurements such as those presented here must be used with the proviso that they may not accurately represent the performance of other cylinders not instrumented. This is discussed in more detail in Section 2.4.1.

2.3.3 Emissions

NO_x

The concentration of nitrogen oxides in the exhaust is measured with a CODA automotive 5 gas exhaust analyser (EGA) using a chemiluminescent cell. The measurement range for the NO_x cell in the CODA EGA is 0–5000 ppm and the resolution is 1 ppm. The EGA was calibrated using NATA certified BOC Spectra Seal Gas #29268D; the accuracy of NO_x measurements was $\pm 1.32\%$ after calibration. The exhaust gas is sampled and passed through a condensate trap and particulate filter before entering the EGA.

The CODA EGA measures the sum of concentrations of all three oxides of nitrogen (N₂O, NO and NO₂); however, only mono-nitrogen oxides are considered to be pollutants. The fraction of all nitrogen oxides that is nitrous oxide in any application therefore decides the suitability of a system such as the CODA EGA for measuring NO_x.

Stationary combustion sources typically show N₂O/NO_x ratios of less than 2%; this figure is even lower for automobile engines, approximately 0.3% [65]. A General Motors study in 1992 [66] found the range of N₂O/NO_x ratios to be 0.18%–0.24% for gasoline-fueled vehicles without catalytic converters. Poitras et al. [67] found N₂O to comprise between 0.01% and 0.04% by mass of all nitrogen oxides in a modern turbocharged direct-injection diesel engine with exhaust gas recirculation using commercial ultra-low sulphur diesel. Koebel [68] found that N₂O emissions were below the threshold of detection (≈ 2 ppm) at all values of load applied to a six cylinder direct-injection turbocharged and intercooled MAN diesel engine. Yamada et al. [69] found the N₂O/NO_x ratio to be less than 1% for a 4.8 litre naturally aspirated common rail diesel engine at brake mean effective pressures above 40 kPa.

Due to the low temperature of the exhaust gas between the point of sampling and the point of measurement, it is assumed that no reduction of NO_x occurs. Given the very small amounts of nitrous oxide relative to the other oxides of nitrogen, nitrogen oxide readings from the CODA EGA can therefore be assumed to accurately represent NO_x measurements.

Soot

Soot is measured using a TSI DustTrak DRX8533 aerosol monitor, a laser light scattering photometer that measures the 90° scattering of light by particulate matter in ambient air. The DustTrak is capable of measuring concentrations of particles up to 150 mg m⁻³. The exhaust gas is sampled and cooled before entering the DustTrak.

Calibration of the instrument is performed using the gravimetric method described by Rao & Honnery [3]. An undiluted fraction of the exhaust gas is allowed to flow through Pallflex Fiberfilm T60A20 membrane filters for 120 s. The filters were dried and weighed to an accuracy of 10 μg . The flow rate through the filter is calculated by measuring the pressure drop through an orifice plate. Further details on the calibration method can be found in Rao & Honnery [3].

Several studies have confirmed the suitability of the DustTrak for the measurement of tailpipe soot in diesel engines, with the caveat that it is calibrated specifically for each engine [70–73]. Moosmuller et al. [70] found the performance of the DustTrak to be similar to that of the tapered element oscillating microbalance (TEOM) method. Faghani et al. [72] found measurements from the DustTrak to be proportional to those from TEOM, indicating that the addition of a proportionality constant determined from calibration allows accurate measurements to be made by the DustTrak; in addition, the DustTrak was found to produce more repeatable measurements than TEOMs at low concentrations of particulate matter.

2.4 Experimental results

This section presents experimental results for in-cylinder pressure, rate of heat release and emissions of NO_x and soot from the Hino engine previously described. Only a small subset of results are presented here; additional results are shown in Appendix A, along with characterisation of air flow rate, fuel flow rate and the injection process.

2.4.1 In-cylinder pressure

Figure 2.3 shows the measured pressure in cylinder 1 for different values of load at 1600 RPM. Increasing engine load clearly increases the peak pressure and therefore the maximum average temperature of the contents of the cylinder, from 64.4 bar at 80 Nm to 75.1 bar at 180 Nm.

The engine used in this study is instrumented with pressure transducers in both cylinders 1 and 4. Two cylinders in the same engine do not necessarily show the same performance. Air intake paths, valve wear and piston ring wear are generally not identical for any two cylinders, so volumetric efficiency generally differs between cylinders. Injector wear is another phenomenon that greatly affects cylinder performance and can vary widely between injectors of the same model and of the same age. The locations

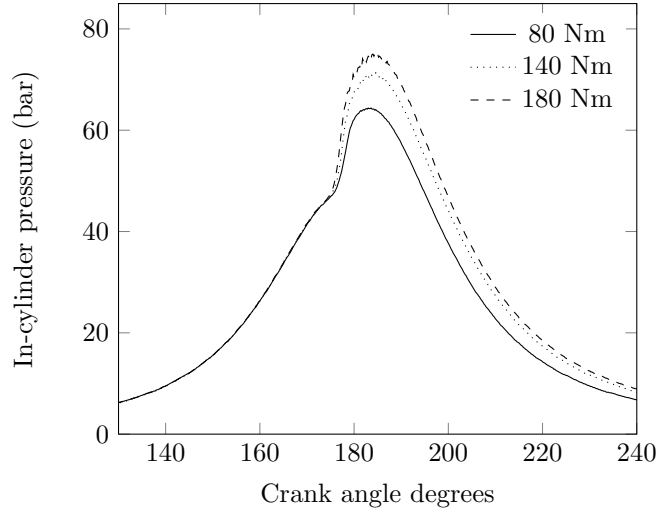


Figure 2.3: Pressure in cylinder 1 at different values of engine-out torque at 1600 RPM.

of cooling jackets and oil galleries may play a role in these differences as well.

Figure 2.4 shows the cylinder pressures measured in cylinders 1 and 4 at 1600 RPM, 140 Nm. The difference between the peak pressures is 13.3%.

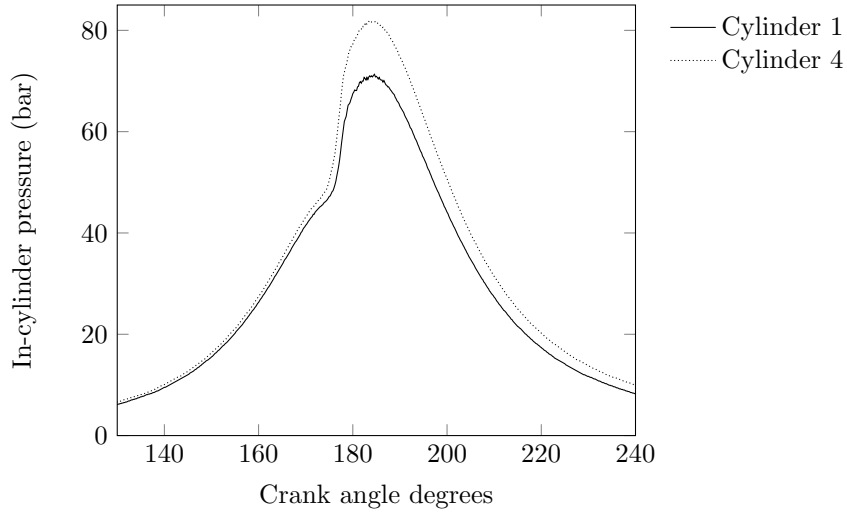


Figure 2.4: Pressures in cylinders 1 and 4 at 1600 RPM, 140 Nm.

For the remainder of this study, in-cylinder variables are presented only for cylinder 1. It is possible for averages to be calculated across the entire engine at considerable expense, but financial constraints limit the instrumentation on the engine.

2.4.2 Rate of heat release

The apparent rate of heat release $\frac{dQ_a}{dt}$ is calculated using the method described by Heywood [74], Equation 2.1.

$$\frac{dQ_a}{dt} = \frac{\gamma}{\gamma - 1} P \frac{dV}{dt} + \frac{1}{\gamma - 1} V \frac{dP}{dt} \quad (2.1)$$

where P and V are the cylinder pressure and volume respectively and γ is the ratio of specific heats of the cylinder contents, assumed to be 1.35 for calculations in this section [1, 74, 75].

A low pass Fourier filter [76] is used to enable the accurate calculation of the derivative of the pressure signal.

The apparent rates of heat release calculated from the filtered pressure signals at 1600 RPM and different values of engine-out torque are shown in Figure 2.5. The region of the heat release curve between ≈ 155 CAD and SOC lies below 0; this indicates heat loss to the cylinder walls and the evaporation of fuel droplets. The sharp increase in the heat release rate at ≈ 174 CAD denotes the start of combustion (SOC). The peak heat release rate increases with increasing engine-out torque.

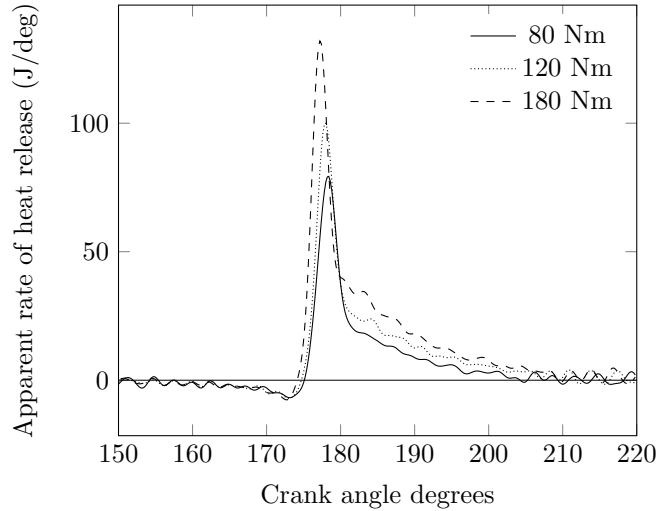


Figure 2.5: Apparent rates of heat release at 1600 RPM and 80 Nm, 120 Nm and 180 Nm.

The earlier occurrence of SOC at higher values of load is partly due to the earlier injection of fuel and partly due to the higher injection pressure at higher torque settings leading to finer atomisation of the spray into smaller fuel droplets, higher spray velocity and greater air entrainment [77–79]. Higher values of load also lead to increased cylinder wall temperatures and therefore decreased ignition delay. A

combination of these phenomena could result in the difference in SOC timing seen in Figure 2.5. Measurements characterising the injection process can be found in Appendix A.

2.4.3 Ion current

Figures 2.6 (a) and (b) show the ensemble-averaged ion current over 80 consecutive engine cycles for changing engine speed at 140 Nm and for changing engine torque at 1600 RPM. The ion current signals at 1600 RPM and 1800 RPM are very similar, while the peak at 1200 RPM is ≈ 3 CAD advanced. This is expected from the earlier SOC at 1200 RPM.

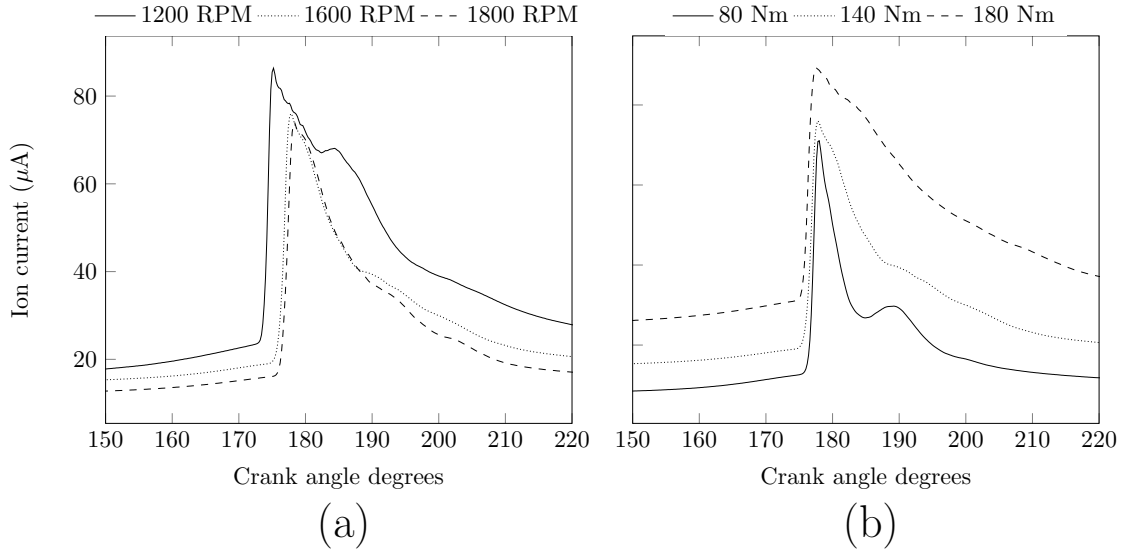


Figure 2.6: Ion current signal at (a) 140 Nm and different engine speeds and (b) 1600 RPM and different engine loads.

Changing the load on the engine can be seen to have a significant effect on the ion current:

- The cycle-minimum value increases monotonically with increasing torque. The non-zero cycle-minimum value of the ion current is believed to be caused by the deposition of a black, electrically conductive layer on the ceramic adhesive between the two electrodes (see Figure 2.7), a phenomenon also observed by Badawy et al. [44]. The deposition of this layer, assumed to be soot, is explored further in Chapter 7. Soot production increases with increasing engine-out torque, leading to a higher value for the cycle-minimum. Lower engine speeds generally also result in higher soot production due to reduced air entrainment

[80, 81]; this can be seen in the increase in cycle-minimum value as engine speed decreases.

- At low values of torque, a second, smaller peak can be seen in the ion current which is absent at higher torque values, while the width of the primary ion current peak increases with increasing torque. Kessler [82] used optical methods to show that the propagation of the flame back out of the piston bowl gives rise to the second peak seen at low values of torque; charge carriers are generated in the flame front and are transported to the vicinity of the ion sensor. At high load, the two peaks merge and give rise to a single, broader peak. Kubach et al. [36] observed the same phenomenon. The exact manifestation of this phenomenon is likely to depend to a great extent on the geometry of the piston crown.



Figure 2.7: Black deposit on the ion sensor.

The ion current shows large cycle-to-cycle variability [2, 40] and therefore has a large stochastic component. Figure 2.8 shows the ion current for 10 consecutive cycles at 1600 RPM and 140 Nm.

The difficulty of dealing with this stochastic component is part of the reason for most studies treating the ion current in a statistical manner. The exceptions are studies concerned with the detection of SOC; these rely on the sharp increase of the ion current shortly before TDC which, as is evident from Figure 2.8, shows excellent repeatability. The 95% confidence interval for SOC as predicted by the thresholding method for the

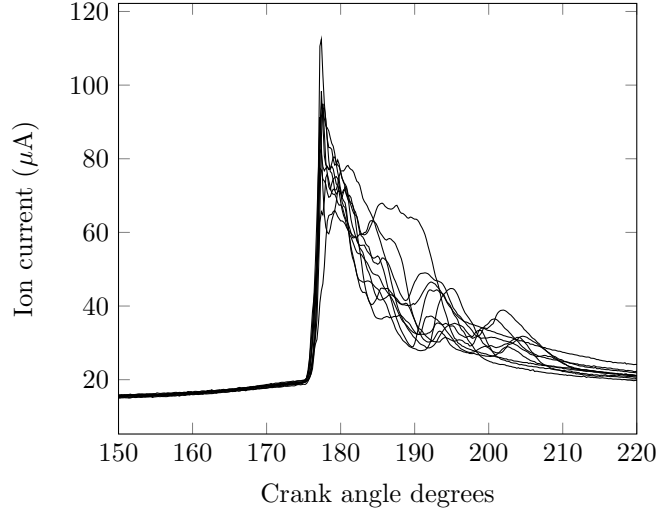


Figure 2.8: Ion current signal for 10 consecutive engine cycles at 1600 RPM and 140 Nm.

conditions in Figure 2.8 is 174.6 ± 0.4 CAD. SOC calculated from the heat release curve is ≈ 174.8 CAD. The relationship between SOC and the initial increase in the ion current depends on the location of the ion sensor in the cylinder; hence it is unique to each engine and must be calibrated for each specific experimental setup.

Figure 2.9(a) shows five ion current curves at 1600 RPM, 140 Nm. Each curve is the ensemble average of 20 consecutive engine cycles. Figure 2.9(b) shows two curves, each of which is the ensemble average of 50 consecutive engine cycles at the same engine operating point. 20 engine cycles are clearly sufficient to ensure a repeatable ensemble-averaged ion current. All subsequent ion current curves are presented as the ensemble average over 80 consecutive cycles to match in-cylinder measurements from the AVL sensors.

Figure 2.10 (a) shows the cycle-averaged ion current over 80 cycles and its coefficient of variance I' at 1600 RPM and 100 Nm.

The high but very narrow peak in I' shortly before TDC indicates that the variability here is due to small variability in the timing of the first ion current peak; Figure 2.8 shows the small range of crank angle over which the ion current climbs to its first peak. The elevated values of I' after TDC indicate significant cycle-to-cycle variability in the ion current — greater than 20% of the average signal over a large crank angle range. This can be qualitatively observed from Figure 2.8.

Figure 2.10 (b) shows the same variables for the in-cylinder pressure signal at 1600 RPM and 100 Nm. The coefficient of variance in the pressure signal is approximately one order of magnitude lower than that in the ion current signal.

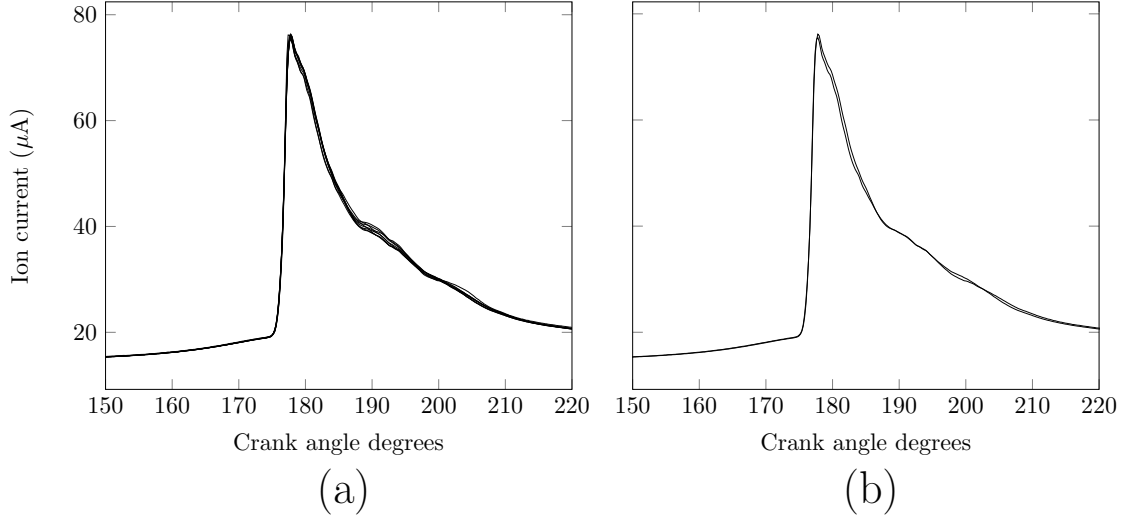


Figure 2.9: Ion current signal ensemble-averaged over 20 (a) and 50 (b) consecutive engine cycles at 1600 RPM and 140 Nm.

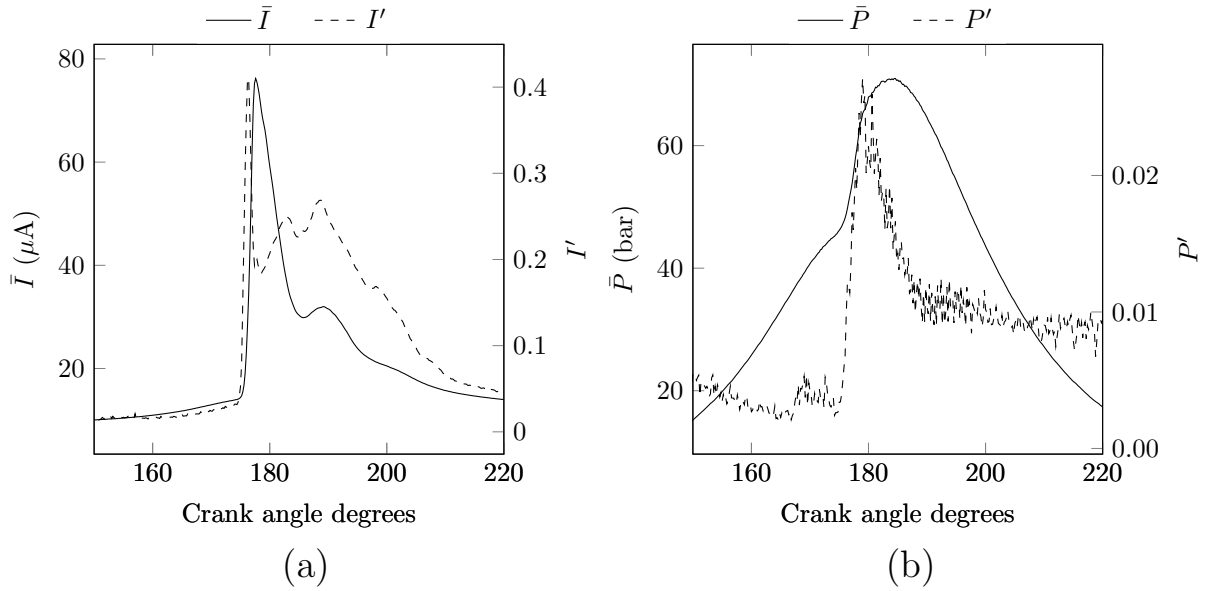


Figure 2.10: Average and stochastic components of the ion current (a) and the in-cylinder pressure (b) at 1600 RPM and 100 Nm calculated over 80 engine cycles.

While single-cycle analysis of the ion current presents some difficulty, some measures of the ion current show remarkable repeatability over several cycles. The measures considered in this study are the minimum, maximum, integral (I_1) and integral with the cycle-minimum value subtracted (I_2). These parameters are depicted in Figure 2.11.

Table 2.2 shows the mean (\bar{x}) and coefficient of variance (c_v) of these measures of interest at an engine speed of 1600 RPM and load of 140 Nm over 150 consecutive

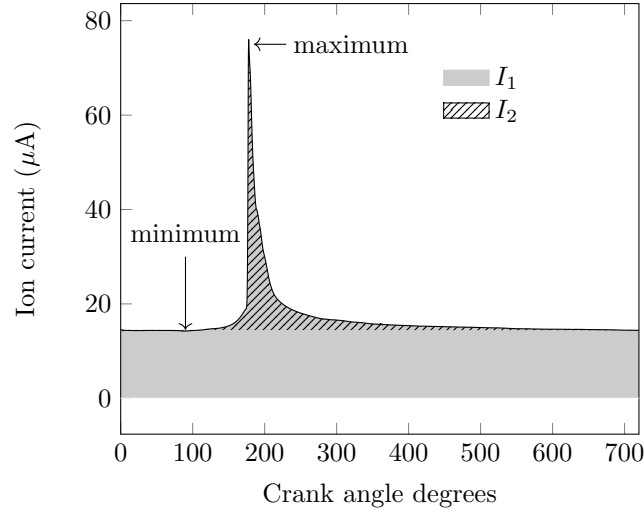


Figure 2.11: Important measures of the ion current signal.

engine cycles. The coefficient of variance of each measure is 0.6% or less of its average over the cycle, indicating that they could be of use even in single-cycle analysis of the signal.

Table 2.2: Statistics of chosen parameters of the ion current curve over 150 consecutive engine cycles at 1600 RPM, 140 Nm.

Variable	\bar{x}	c_v
Minimum	14.234 μA	0.1728 %
Maximum	75.778 μA	0.5468 %
I_1	11.976 mA-deg	0.1933 %
I_2	1.728 mA-deg	0.6024 %

The standard deviation in peak location over these 150 cycles is 0.13 CAD.

The repeatability of these parameters suggest that they may be of use in simple statistical models for the ion current; indeed, the location and magnitude of the ion current peak has been employed in some studies previously described. Simple correlations to these variables are discussed in Section 2.5.

A note on the different measurement systems used: the ion current and pressure signals are measured by NI and AVL systems respectively; as they are both in-cylinder variables and their relative timing is of importance, these are synchronised using an optical sensor and reflective tape on the flywheel of the engine. The accuracy of this method can be evaluated by comparing the pressure signal when measured by the AVL system to that measured by the NI4350 ADC — any horizontal offset indicates calibration is required. Figure 2.12 shows the cylinder pressure signal recorded using

both systems; there is minimal difference.

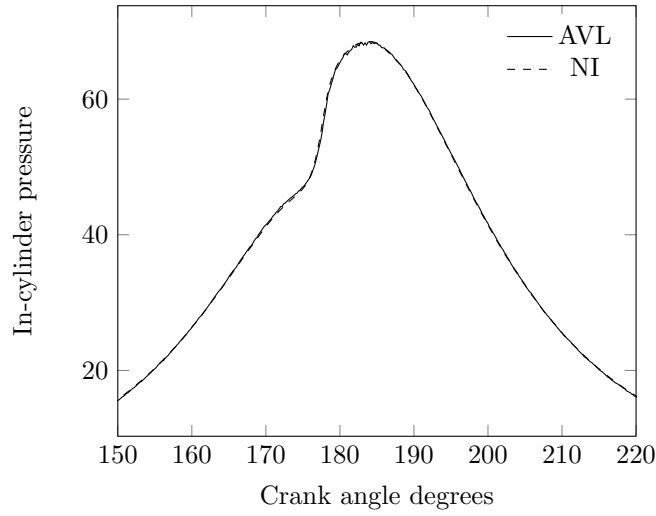


Figure 2.12: In-cylinder pressure signal at 1600 RPM and 120 Nm using both AVL and NI systems.

2.4.4 NO_x and soot emissions

Figure 2.13 shows the measured tailpipe NO_x at 1200 RPM, 1600 RPM and 1800 RPM and at different values of load.

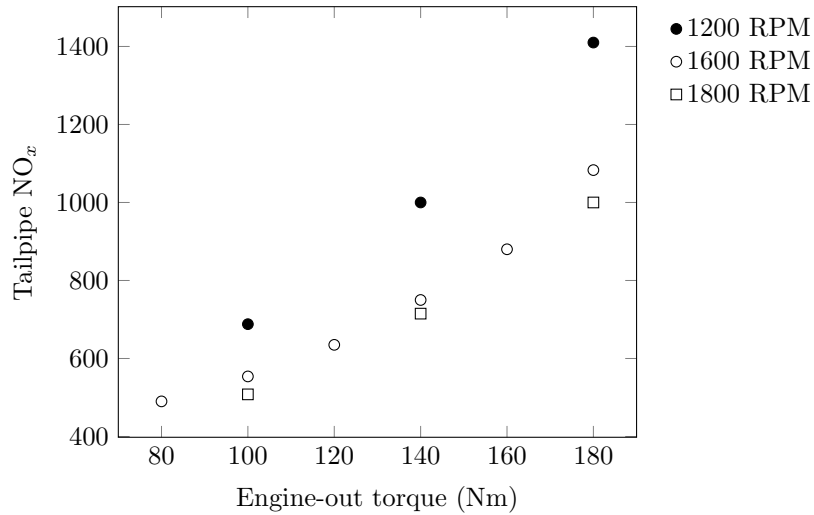


Figure 2.13: Tailpipe NO_x at 1200 RPM, 1600 RPM and 1800 RPM and various engine loads.

NO_x increases monotonically with an increase in load — this is an expected consequence of the higher cylinder-average temperatures generated due to the injection of greater quantities of fuel and greater air entrainment expected as the kinetic energy of the fuel

spray is increased. NO_x also decreases with an increase in engine speed; this is likely due to differing heat transfer rates and/or different entrainment. It is also possible that this is caused by the relative slowness of NO_x reactions; at higher speed, the temperature drop due to expansion causes NO_x reactions to freeze at a relatively early stage. The decrease in NO_x is more marked between 1600 RPM and 1200 RPM than between 1800 RPM and 1600 RPM. There are other significant differences between the 1200 RPM case and the other engine speeds investigated. These differences can be seen in the experimental data presented in Appendix A.

Figure 2.14 shows tailpipe soot mass measurements at 1600 RPM and various load settings. Soot increases monotonically and fairly linearly with engine-out torque, as expected.

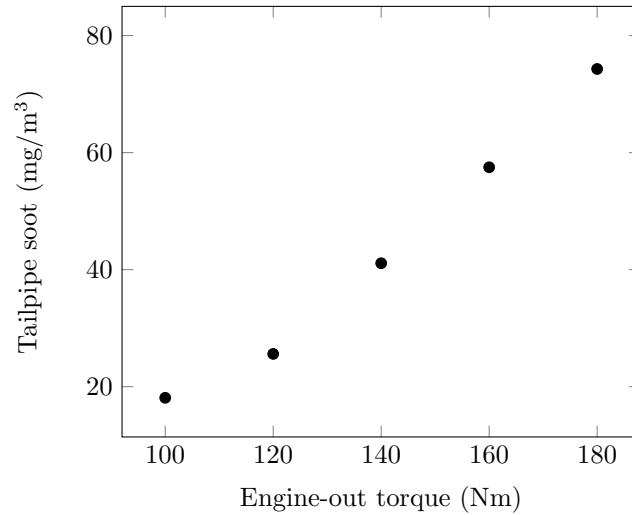


Figure 2.14: Tailpipe soot mass for varying engine load at 1600 RPM.

2.5 Relationships between the ion current and other variables

This section presents examples of relationships between some measures of the ion current and several engine operation parameters of interest. Similar to those found in the studies mentioned before, these relationships are purely statistical and no causality may be assigned to relationships bearing a high correlation coefficient. It is the aim of this study to provide causal links between these variables.

2.5.1 In-cylinder pressure and related variables

The direct result of the in-cylinder pressure is a torque on the crankshaft. This torque is subject to several losses before it appears as engine-out torque — operation of the fuel, water and oil pumps, pumping losses from the transport of gases, driving of the camshaft and the alternator and frictional losses in all moving components. These losses are non-linear and are not a simple function of torque. Given the complexity of this relationship, it appears that a statistical approach may be required to predict torque from the ion current.

Rao and Honnery [2] developed a statistical technique capable of predicting torque on a cycle-by-cycle basis to within 10 Nm RMS error across a wide range of engine loads from 12 Nm to 180 Nm using the ion current as an input. Details of the study can be found in Appendix B.

That study also attempted to predict net IMEP and expansion work from the ion current — these in-cylinder measures of in-cylinder pressure were predicted to generally greater accuracy than the engine-out torque.

If, as postulated earlier, the non-zero cycle minimum value of the ion current is due to soot, this offset is not directly related to engine-out torque. Instead, the integral I_2 is considered, which was earlier shown to be highly repeatable over a large number of cycles. Figure 2.15 shows the correlation of this value with engine-out torque. The trend is linear with $r^2 = 0.94$.

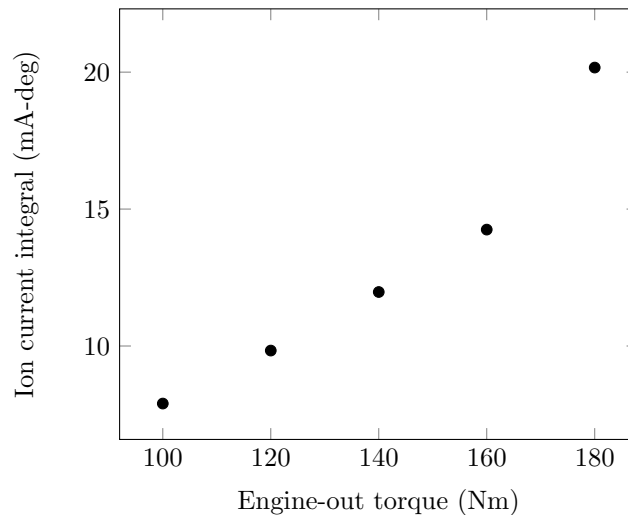


Figure 2.15: Ion current integral versus engine-out torque at 1600 RPM.

2.5.2 Start of combustion and rate of heat release

Figure 2.16 shows the ion current and apparent rate of heat release at 1600 RPM and 140 Nm. The simultaneous increase in both signals at ≈ 175 CAD indicates SOC; the ion current has been used for this purpose previously.

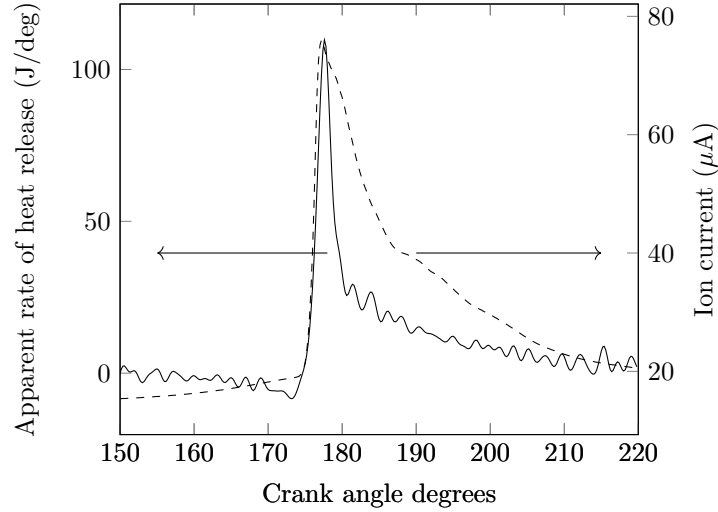


Figure 2.16: Comparison of rate of heat release and ion current at 1600 RPM, 140 Nm.

The ion current integral I_2 over the full engine cycle is also directly correlated to the cumulative heat release at different values of engine-out torque ($r^2 = 0.95$). This is shown in Figure 2.17. Although not shown here, there is also strong correlation between the ion current and the peak rate of heat release with an identical correlation coefficient.

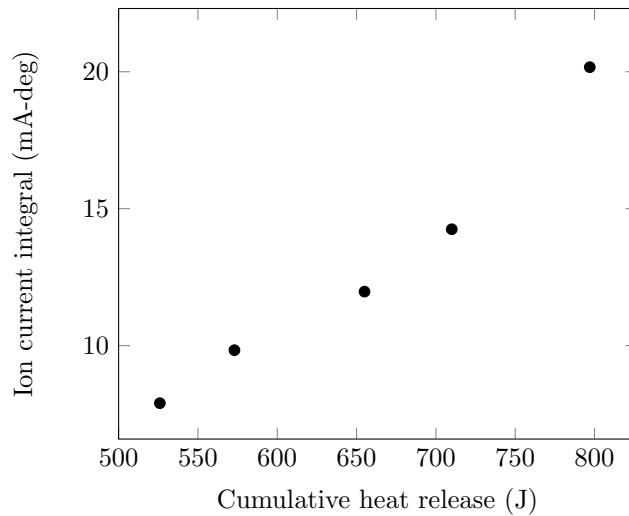


Figure 2.17: Ion current integral versus cumulative heat release at 1600 RPM.

2.5.3 NO_x emissions

Figure 2.18 shows the variation in ion current integral I_2 with tailpipe NO_x at different values of engine-out torque. The correlation is linear with $r^2 = 0.99$. Tailpipe NO_x and peak rate of heat release are positively correlated with each other through their dependence and effect on in-cylinder temperature, respectively. It is therefore not surprising that the ion current integral, being positively correlated with one, behaves similarly with the other.

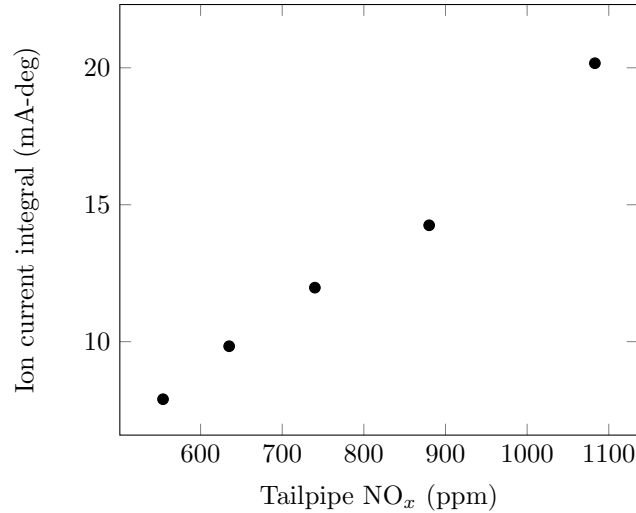


Figure 2.18: Ion current integral versus tailpipe NO_x at 1600 RPM.

2.6 Summary

Literature on ion currents in engines abounds with methods for the prediction of one engine operating parameter or another from one or more measures of the ion current. These predictive methods all rely on statistical manipulation of the ion current signal. Whilst these methods can give useful results, they do not provide much insight into the reasons for which they work. Part of the reason for the use of these models is the stochastic nature of the signal.

This chapter presented a statistical analysis of the ion current signal measured in a direct-injection diesel engine and found five parameters of the ion current curve that are highly repeatable over a large number of engine cycles. These parameters are therefore suitable for cycle-by-cycle statistical analysis.

Examples of correlations that can be derived using these ion current parameters are those for in-cylinder pressure, cumulative heat release, rate of heat release and

emissions of NO_x . High correlation coefficients can be observed for these cases ($r^2 \geq 0.94$).

Given the wide range of uses the ion current can be put to, it is surprising that very few studies have attempted an explanation of the factors affecting it and the mechanisms involved in engine-type situations. Chemical kinetics research has provided several studies that do exactly this for laminar flames at atmospheric or lower pressures and for simple hydrocarbons such as methane. Findings from those studies could be very useful when integrated into engine models; to date, little progress has been made on this front, a shortcoming that this study aims to redress. The initial step to achieving this is the study of ion formation in a simple and generally well-understood system — the laminar methane flame. This is presented in Chapter 3.

Chapter 3

Ionic mechanism for methane oxidation

3.1 Introduction

The laminar methane flame in air is one of the most studied and best understood combustion systems at the present time. This is then a suitable system to study relatively unknown combustion phenomena and is the system chosen for the study of ion formation in hydrocarbon flames.

Ion formation in engines occurs at relatively high temperatures and pressures. The peak motoring temperatures seen in engines range from 750–1000 K and the motoring pressures from 15–50 bar. Any study on ion formation with a view to implementation in engine research requires the formation mechanisms to be studied at these elevated temperatures and pressures. In order to achieve this, an oxidation mechanism is developed for methane that is optimised for accuracy of heat release and major species concentrations under engine-like conditions of pressure and temperature. The equivalence ratios chosen are near 1.0 to mimic those used in the experiment described in Chapter 4. In view of a possible need to use this mechanism in CFD modelling, most existing mechanisms were considered too computationally expensive. Any mechanism developed must be highly simplified.

This oxidation mechanism is required to have an ionic sub-mechanism incorporated into it in order to predict the production and consumption of important ionic species that are generally not of interest in oxidation mechanisms designed for the prediction of laminar flame speed, heat release and major species concentrations.

This chapter describes the development of this mechanism along with its ionic sub-mechanism. The choice of important species and reaction pathways is driven by previous research, a summary of which is included. Identification of important charged species is crucial to the performance of this mechanism; this is entered into in some detail. In the calculation of the ion current generated by these charged species, some knowledge of charge transport in partially ionised gases is required; this is described here briefly.

A lack of experimental data at the requisite temperature and pressure values necessitates the initial validation of this mechanism outside its designed area of interest. This validation is presented here. Also discussed are the effects temperature, pressure, equivalence ratio and stage of completion of the reaction have on the ion current developed and the mechanisms by which these operate.

Some sections of this chapter have previously been published in Rao & Honnery [83]. These have been reproduced here with minimal changes.

3.2 Background

3.2.1 Ion formation in flames

The high electrical conductivity of flames was first observed in the early 1800s when, in 1801, Alessandro Volta, the inventor of the battery, was able to discharge a charged non-conductor in a flame, proving the existence of charge-carriers in the flame [84]. Erman [85] in 1802 recorded the first observation of the ion current when he inserted two wires into a flame. Since those observations, most early explanations presented in the 1920s for the ion current's existence have revolved around the release of electrons from molecules as a result of increased thermal energy [86–88], a process known as thermal ionisation. When this theory is applied, the ion concentrations can quite simply be calculated using the Saha ionisation equation [46] applied to any species with a sufficiently low ionisation energy. Various studies have suggested different species as the source of these charged particles, some notable ones being CO, OH and NO [89, 90]. Polymerised carbon atoms were suggested to have ionisation potentials similar to that of graphite, which is relatively low [90]. The same authors suggested that the cause of ionisation was friction due to gas flow along stationary walls. In 1906, Tufts [91] published the only early study suggesting a non-thermal mechanism of ionisation. This study serves as the first basic description of chemi-ionisation.

The 1950s and 1960s saw a plethora of studies on ion current measurement and identification of the mechanisms by which chemi-ionisation occurs. Calcote [92] presented an analysis of ion concentrations formed via various thermal ionisation pathways: impurities, equilibrium species, non-equilibrium species and carbon particles. He concluded that none of these phenomena produced ions in sufficiently high concentrations to match those measured with a Langmuir probe [93]. His conclusion was that chemi-ionisation was possibly responsible for a large fraction of the ion current observed. In the following years, a plethora of studies on the topic [58, 94–96] were conducted that confirmed that chemi-ionisation was the dominant mechanism by which ions are produced in hydrocarbon flames. It was also observed that the response of a flame ionisation detector (FID) in a hydrocarbon flame was directly proportional to the number of carbon atoms in the parent hydrocarbon [97–99], indicating that the parent hydrocarbon is decomposed into a species with a single carbon atom before it is oxidised. Some early studies [100–102] theorised that that single-carbon species is CH, which initiates chemi-ionisation via Reaction R 3.1.



This reaction was chosen for several reasons [103, 104]:

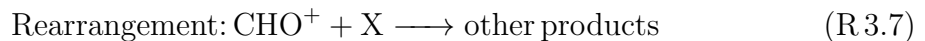
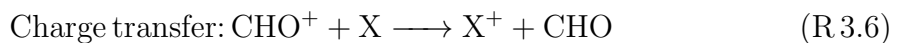
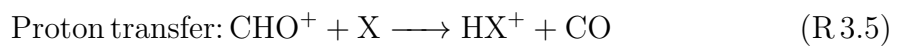
- Presence of C-H bond — some studies [93, 105] have noted very low concentrations of ions in flames where the fuel does not contain a C-H bond. This indicates that a species with a C-H bond may be responsible for ionisation.
- Pressure-dependence — the mole fraction of ions was found to be independent of pressure [102], indicating that the ion formation and the ion recombination reactions must be of the same order. Calcote [102] showed that ion recombination occurred via a second-order reaction, so the ion formation reaction must be second-order too.
- Stoichiometry — ion concentrations were found to be more dependent on mixture composition than on temperature and were found to reach a maximum in stoichiometric mixtures, suggesting that the reaction requires species from both the fuel and the oxidiser.
- Thermochemistry — most reactions that could produce ions in a flame require very high input energy to take place. $\Delta H = 8.4 \text{ kJ mol}^{-1}$ for Reaction R 3.1, making it nearly thermo-neutral.

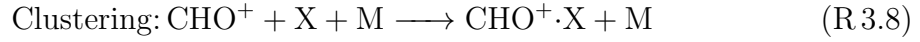
Thus far, experimental measurements of ion concentrations in flames were generally conducted with Langmuir probes. These were unable to provide much information on the individual species present in the flame, apart from their average mobility. Some studies [100, 106] used microwave techniques to measure ion concentration; these methods provided poor spatial resolution. Vanreusel & Delfosse [107] were the first to publish the principle of a method of ion extraction for use in a mass spectrometer. Experimental methods were greatly improved with the use of mass spectrometry in these flames. Initial studies [108–112] were concerned with the profile of molecular weights of ions at a single point in the flame; later studies were able to sample the flame gases at several points along its length, giving more insight into ion production and extinction rates. These early studies all found a significant peak at a molecular mass of 19, indicating an abundance of the hydronium ion H_3O^+ . Knewstubb & Sugden [55] found large concentrations of H_3O^+ and its hydrates, but concluded that hydrate formation was a product of the measurement system rather than the flame itself. DeJaegere et al. [58] published experimental findings of the most abundant ions in $\text{CH}_4\text{--O}_2$ and $\text{C}_2\text{H}_2\text{--O}_2$ flames, finding a slight peak at a mass number of 29, suggesting the CHO^+ ion, and a large peak at a mass number of 19, suggesting the H_3O^+ ion. The H_3O^+ ion was found to represent 70% to 90% of the total positive ion concentration. The C_3H_3^+ ion was also identified in rich $\text{C}_2\text{H}_2\text{--O}_2$ flames and its concentration reported to increase with increasing equivalence ratio. Green & Sugden [59] studied ion formation in a $\text{H}_2\text{--O}_2$ flame with various amounts of CH added and proposed a mechanism for the formation of H_3O^+ from a precursor primary ion and its neutralisation:



Several studies conducted later agreed with this finding [113–115].

Goodings et al. [56, 57] detailed measurements and analysis of the positive ion concentration in a $\text{CH}_4\text{--O}_2$ flame at both lean ($\phi = 0.2$) and rich ($\phi = 2.0$) fuel-air ratios. In the fuel-lean flame, the formation of the ions after Reaction R.3.1 was proposed to occur in one of the following ways:





Reaction R 3.5 was considered the dominant mechanism in the flame front, given the experimental results obtained via mass spectrometry, shown in Figure 3.1. Given the elevated pressures of interest in these studies and the consequent narrowing of the reaction zone, ions briefly existing in the flame front but not persisting downstream of the flame were not considered. Of interest in Figure 3.1 are the relative concentrations of CHO^+ and H_3O^+ . The much lower concentration of CHO^+ as compared to H_3O^+ indicates that Reaction R 3.10, a proton transfer reaction, operates on CHO^+ . This reaction is inherently faster than Reaction R 3.1, leading to the rapid conversion of CHO^+ to H_3O^+ .

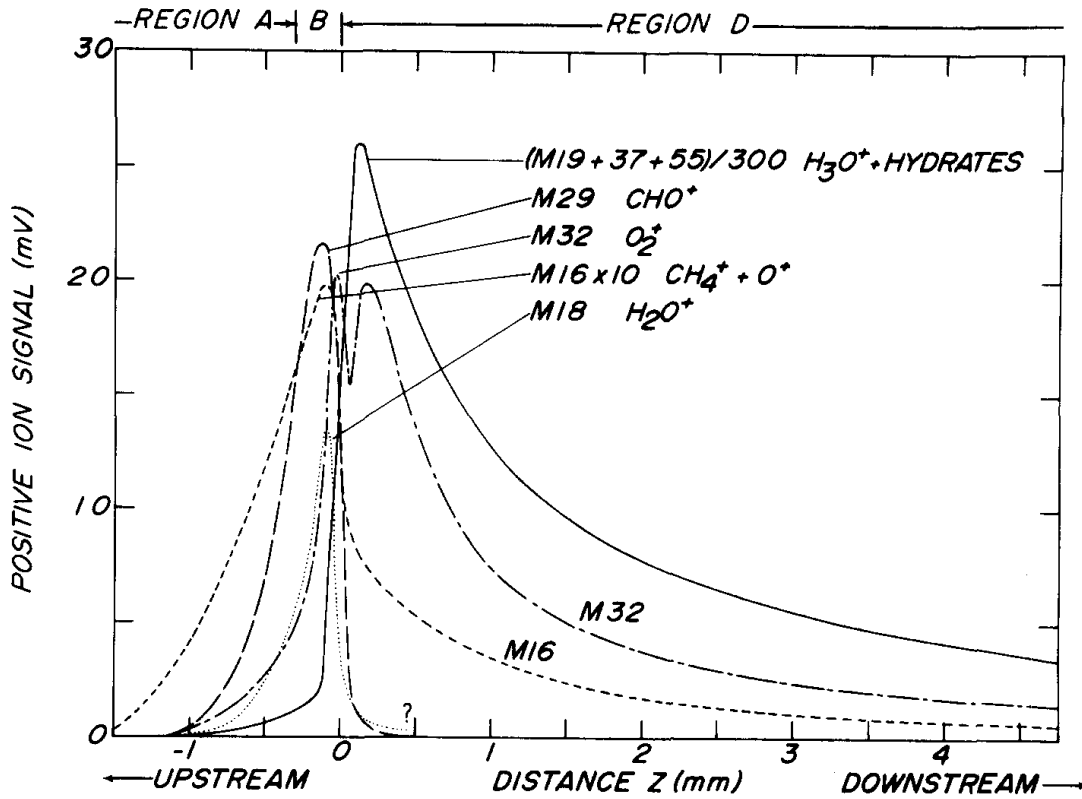


Fig. 5. Selected positive ion profiles, including those persisting far downstream in the fuel-lean flame.

Figure 3.1: Positive ion profiles for ions persisting downstream of the flame front in a fuel-lean atmospheric pressure methane-air flame ($\phi = 0.2$). Figure taken from Goodings et al. [57].



The presence of other charged particles in the flame front, such as $\text{C}_2\text{H}_3\text{O}^+$ and CH_5O^+

led the authors to suggest Figure 3.2 as a reaction flow diagram for the positive ion chemistry in the fuel lean flame. Importantly, the dominant positive ion is seen to be H_3O^+ ; its peak concentration is reported as approximately six times that of the next most abundant ion ($\text{C}_2\text{H}_3\text{O}^+$) and its integral concentration approximately 26 times.

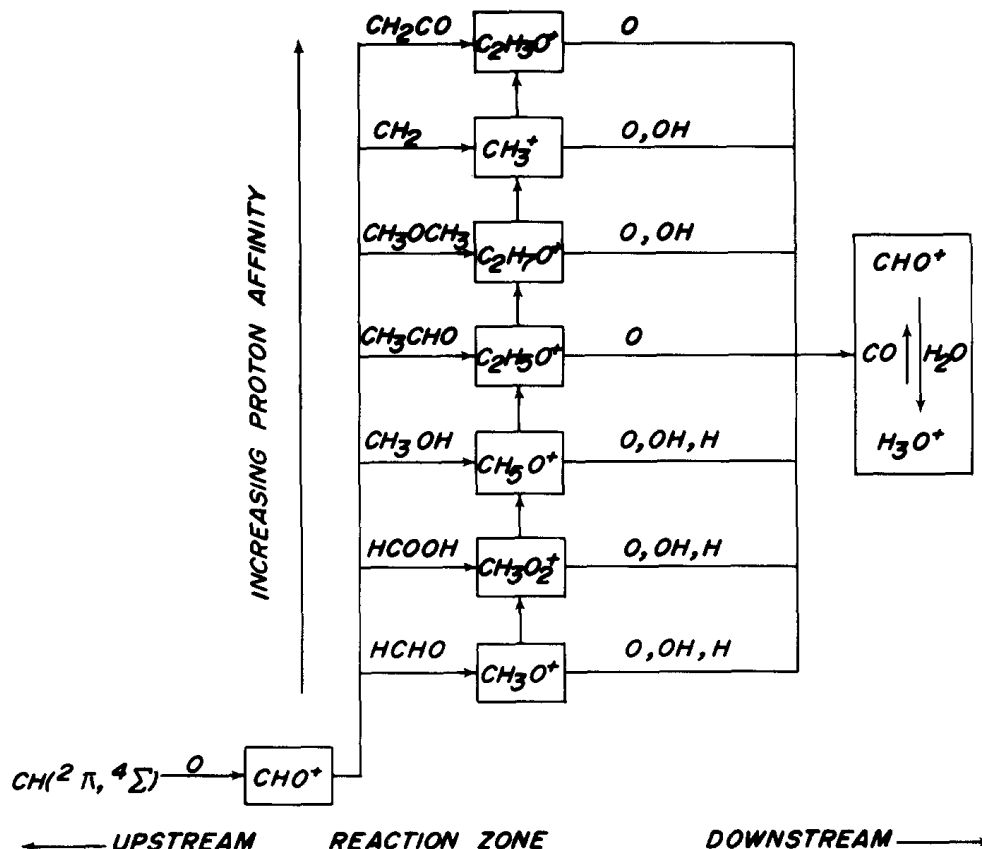


Figure 3.2: Reaction flow diagram showing the formation of large C_nH_x^+ ions in a fuel-rich atmospheric pressure methane-air flame ($\phi = 2.0$). Figure taken from Goodings et al. [57].

The region upstream of the flame front was found to be similar for the fuel-rich flame, dominated by proton transfer reactions. However, the flame front shows markedly different chemistry, with the C_3H_3^+ ion producing a peak ion signal comparable to that of H_3O^+ . This peak, however, decays quickly, leaving H_3O^+ as the most abundant ion in the downstream region — selected ion profiles are shown in Figure 3.3. Of particular interest in these results is the formation of a hydrate of H_3O^+ . This has been postulated to be a spurious measurement resulting from the sampling technique, which is discussed below. The reaction flow diagram for the formation of large C_nH_x^+ ions formed in this case is suggested in Figure 3.4, which shows the development of species with higher molecular weights. It has been postulated that these species are precursors to soot [11–14].

The same authors also investigated negative ion chemistry in the same flames [116].

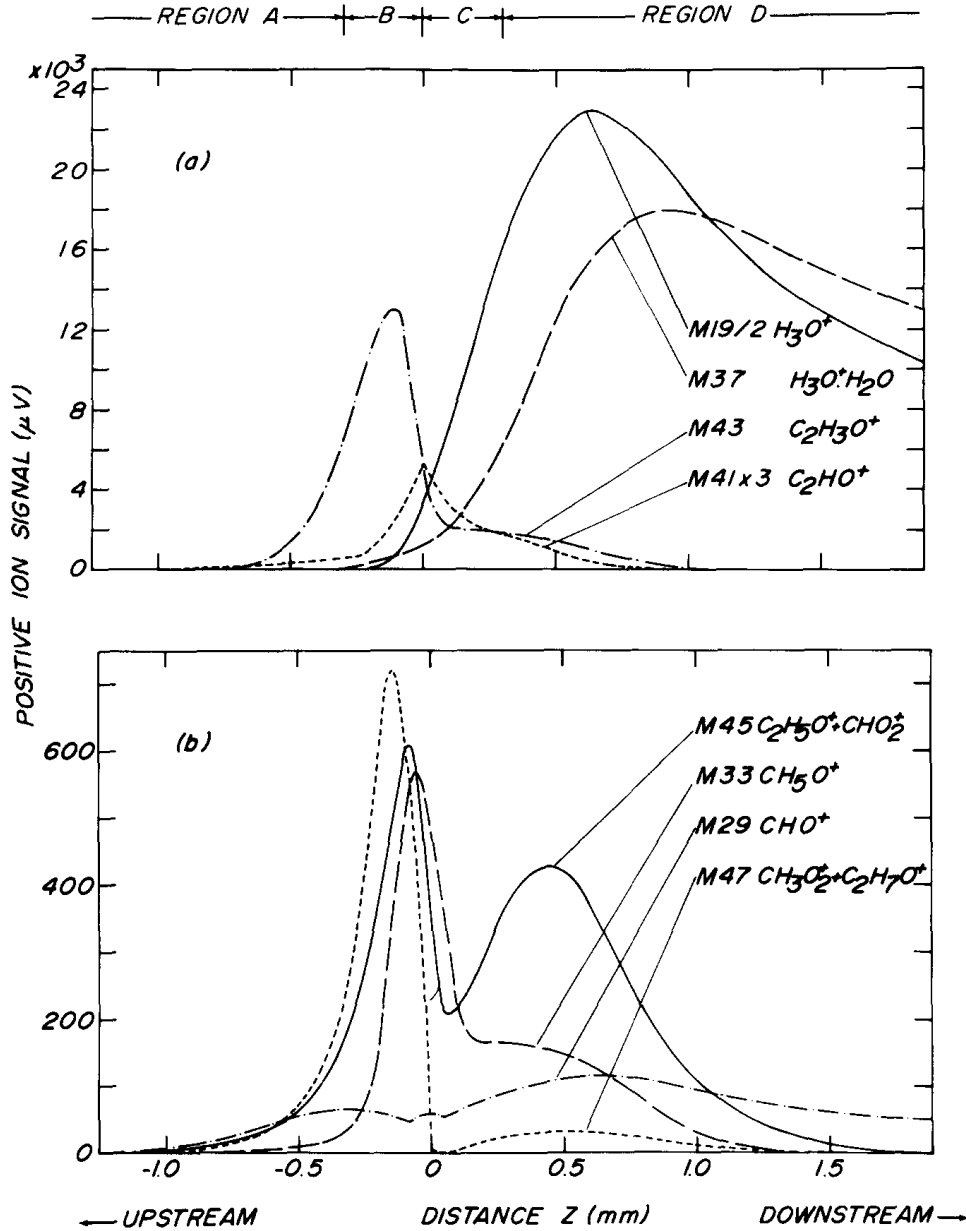
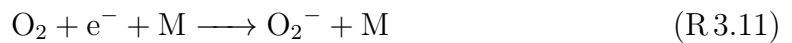


Figure 3.3: Positive ion profiles for ions persisting downstream of the flame front in a fuel-rich atmospheric pressure methane-air flame ($\phi = 2.0$). Figure taken from Goodings et al. [57].

It was found that the dominant charge carrier in the fuel-lean flame was electrons, formed via Reaction R 3.1. Electrons attach to molecular oxygen via the three-body Reaction R 3.11, establishing O_2^- as the primary negative ion. Although Reaction R 3.11 results in the concentration of O_2^- being comparable to that of electrons, the large difference in their mobilities results in much greater current flow due to electrons.



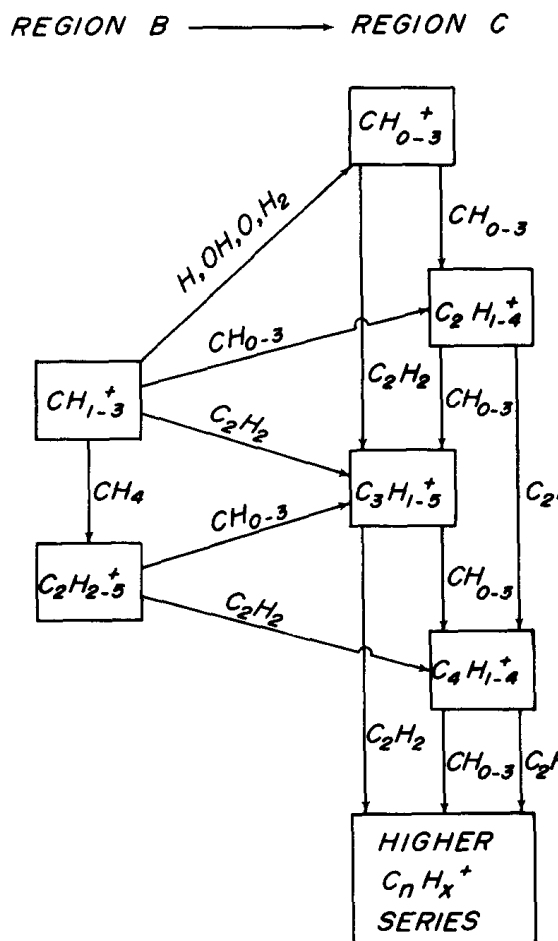


Figure 3.4: Reaction flow diagram showing the formation of large $C_nH_x^+$ ions in a fuel-rich atmospheric pressure methane-air flame ($\phi = 2.0$). Figure taken from Goodings et al. [57].

Several ions were found further downstream in the flame, most abundantly CHO_2^- , CO_3^- , CHO_3^- and OH^- . These ions are all formed from O_2^- via charge transfer and proton transfer reactions. In the fuel-rich flame, CHO_2^- , O_2^- , C_2H^- and C_4H^- were the most abundant negative ions. Electrons were found to contribute an even higher fraction of the total ion current due to negatively charged particles.

While these studies have contributed immeasurably to the understanding of ion formation in flames, a note must be made of the limitations of the mass-spectrography measurement technique. Most studies of ion composition have been performed on atmospheric-to-low pressure (≈ 0.01 – 1 atm) flames due to the effect of pressure on flame thickness. At higher pressures, the reaction zone becomes very thin, leading to large concentration changes over small distances. Lower pressure flames are studied in order to widen the reaction zone, giving greater spatial resolution in the ion profiles measured. The ion collection chambers used were maintained at 10^{-9} – 10^{-8} atm. Sampled flame gas was allowed to expand and cool upon entry via an orifice plate into

the collection chamber, possibly leading to a shift in the equilibria present between ions [117]. The formation of hydrates of H_3O^+ is attributed to this cooling.

Hayhurst et al. [118] also note the effect of the formation of a layer ('sheath') of positive ions at the orifice into the collection chamber. A thicker sheath results in the collection of a greater fraction of the ions present in the sheath, which is not representative of the composition of the flame. The sheath thickness is roughly proportional to the Debye length [119–122], a measure of the distance over which the electrostatic effect due to a charge carrier persists, and varies roughly as $\Delta\phi^n$, $0.5 < n < 1$, where $\Delta\phi$ is the potential difference between the orifice plate of the collection chamber and the burner [123]. A lower concentration of electrons, which occurs if there are significant concentrations of negative ions in the flame, results in an increased Debye length and therefore a thicker sheath. A decrease in the voltage of the orifice plate with respect to the burner also results in a thicker sheath. Either or both of these events occurring leads to an over-estimation of the positive ion concentration in the flame.

Although these limitations mean that some inaccuracies will be present in any mass-spectrometry measurement of the ion composition in flames, the results of the previously-mentioned studies are still useful in indicating the reaction mechanism responsible for ion formation, the important species involved in the mechanism, and the major ions formed. These results are used in the development of the ionic sub-mechanism of the methane oxidation mechanism presented in this chapter.

3.2.2 Charge transport in partially ionised gases

In the calculation of ion current from charged species concentration, some understanding of charge transport in gases subjected to an electric field is required. The relations shown here are used later in this chapter, and also in Chapters 4 and 5 to calculate the ion current developed in a constant-volume chamber and a diesel engine respectively.

An electric field applied to an ionised gas produces a force on charged species in or opposite to the direction of the electric field, depending on their charge. This force, however, does not cause an indefinite increase in the average particle velocity due to the effect of particle-particle collisions. Instead, the net effect on charged particles is a diffusion either parallel or anti-parallel to the electric field. The eventual neutralisation of the particles at the electrodes that is a consequence of this diffusion produces the ion current.

Particle-particle collisions reduce the net diffusion speed by reducing ion mobility. The

frequency of these collisions therefore is an important variable in the calculation of the ion current. The frequency of particle-particle collisions (termed the momentum transfer collision frequency) \bar{v}_{AB} for any two species A and B is given by Equation 3.1 [124].

$$\bar{v}_{AB} = N_A N_B (r_A + r_B)^2 \sqrt{\frac{8\pi K_B T}{m_{r,AB}}} \quad (3.1)$$

N and r denote the number of particles and the radius respectively, of species A or B. K_B is the Boltzmann constant and $m_{r,AB}$ is the reduced mass, calculated from Equation 3.2.

$$m_{r,AB} = \frac{m_A m_B}{m_A + m_B} \quad (3.2)$$

m refers to the mass of either species.

The mobility of any charged species A, μ_A , is then given by Equation 3.3.

$$\mu_A = \frac{e_A}{m_A \sum_{i=1}^N \bar{v}_{iA}} \quad (3.3)$$

where e_A denotes the charge on species A and \bar{v}_{iA} the momentum transfer collision frequency of A and species i .

The ion current for a specific sensor geometry and applied electric field strength can be calculated using Equation 3.4 [60, 125].

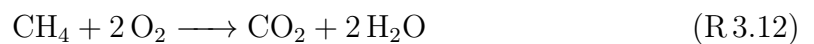
$$I = F_G V_S \sum_{j=1}^N e_j N_j \mu_j \quad (3.4)$$

F_G is a geometric factor depending on the sensor geometry and V_S is the voltage difference across the sensor electrodes.

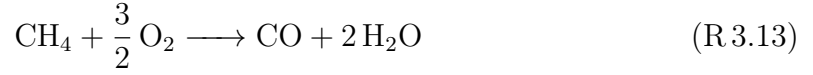
3.2.3 Methane oxidation mechanisms

This section reviews existing mechanisms for methane oxidation to use as a base for the ionic mechanism developed.

The simplest oxidation mechanism for methane is a one-step process:



While single-step mechanisms are able to predict laminar flame speeds reliably over a range of conditions, they suffer from well-known flaws [126], including neglecting the CO₂-CO equilibrium. Two-step reaction models introduce a second step to account for the presence of CO [127]:



These provide more accurate estimations of flame parameters than the one-step mechanism. Table 3.1 reproduced from Westbrook & Dryer [126] shows predicted properties of the burnt gas in atmospheric pressure methane-air flames for detailed, single step and two-step mechanisms. While the two-step mechanism shows significant error in the prediction of the CO-CO₂ equilibrium, its predictions of the adiabatic flame temperature are far closer than the one-step mechanism to those of the detailed mechanism [128].

Table 3.1: Predicted properties of the burnt gas in atmospheric pressure methane-air flames by various mechanisms. Table taken from Westbrook & Dryer [126]

ϕ	Detailed mechanism			One-step mechanism	Two-step mechanism	
	T_{ad}	$\frac{[\text{CO}]}{[\text{CO}_2]}$	$\frac{[\text{H}_2]}{[\text{H}_2\text{O}]}$		T_{ad}	$\frac{[\text{CO}]}{[\text{CO}_2]}$
0.8	1990	0.03	0.005	2017	1975	0.08
1.0	2220	0.11	0.02	2320	2250	0.14
1.2	2140	0.69	0.15	2260	2200	0.43

A natural extension to this mechanism is the inclusion of other equilibria such as H₂-H₂O. As more reactions are added, the equilibrium concentrations of more species can be estimated. Edelman & Fortune [129] used this approach to formulate a quasi-global reaction mechanism for hydrocarbon oxidation; this involved a single-step conversion of fuel to CO and H₂ and a detailed reaction mechanism for the oxidation of these two species. Figures 3.5 and 3.6, reproduced from Westbrook & Dryer [126], compare the performance of this mechanism to that of the detailed mechanism mentioned in Table 3.1 in a stoichiometric methanol-air flame at atmospheric pressure. The profiles of temperature and fuel concentration agree well between the models, but there are large differences in the concentrations of CO, H and O in the pre-flame and the flame regions and the point at which the radicals disappear is markedly different (near $x = 0$ mm for the detailed mechanism and near $x = 0.6$ mm for the quasi-global mechanism). Westbrook & Dryer [126] suggest that ignoring the reactions between these radicals and

fuel molecules as in the quasi-global mechanism results in high radical concentrations, leading to the early oxidation of CO, indicating that the one-step mechanism for the production of CO and H₂ is not sufficient to model processes in the flame region. The formation of radicals from the H₂-O₂ system is hence a crucial part of any hydrocarbon oxidation model seeking to model species concentrations in the flame region. Reaction rates for the H₂-O₂ system have been well documented and experimentally verified [130–132].

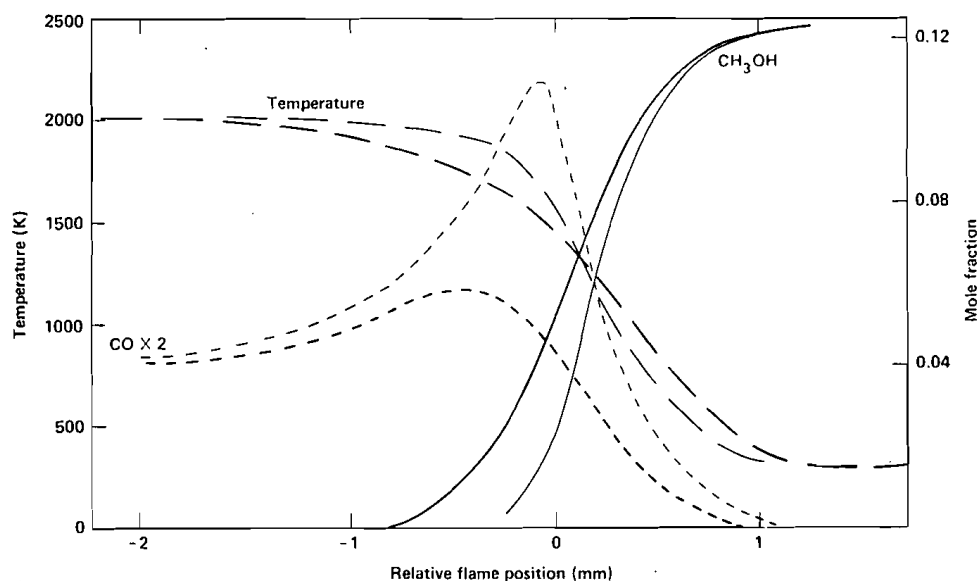


Figure 3.5: Temperature, methanol and carbon monoxide concentrations in a stoichiometric methanol-air flame at atmospheric pressure. The detailed mechanism is shown by light lines and the quasi-global mechanism by heavy lines. Figure taken from Westbrook & Dryer [126].

These observations have led to the formulation of very detailed reaction mechanisms for the oxidation of methane, the most well-established being GRI-Mech [133], which was maintained by the Gas Research Institute until 2000. The initial releases, GRI-Mech 1.1 and 1.2 [134], released in 1995, had 177 reversible reactions and 32 species; later releases built upon this with new experimental data and theoretical understanding. GRI-Mech 2.1 [135] contained 277 reversible reactions and 49 species. The last release of GRI-Mech, designated GRI-Mech 3.0, contains 325 reversible reactions and 53 species. The mechanism is optimised for the ranges 1000 K to 2500 K, 0.01 atm to 10 atm and $\phi = 0.1$ to 5.0 for pre-mixed systems. Importantly, it contains mechanisms for NO formation and reduction, which make it useful in the study of high-temperature methane flames.

Hughes et al. [136] developed a similar mechanism containing 351 irreversible reactions and 37 species. This mechanism was formulated using only experimental rate data available for elementary reactions — no optimisation was performed. The authors

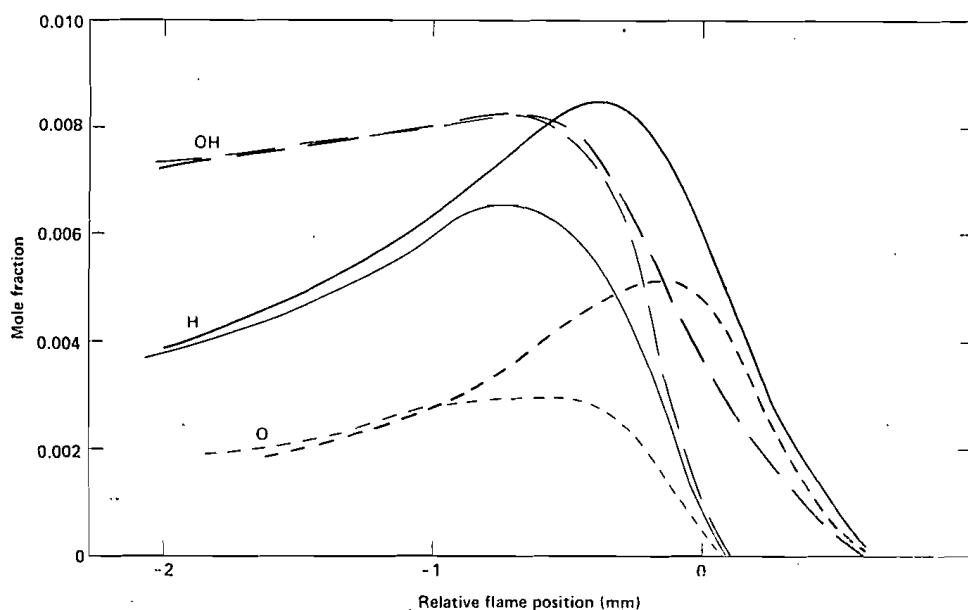


Figure 3.6: Concentration profiles for H, O and OH radicals in a stoichiometric methanol-air flame at atmospheric pressure. The detailed mechanism is shown by light lines and the quasi-global mechanism by heavy lines. Figure taken from Westbrook & Dryer [126].

argue that this makes their mechanism more general than GRI-Mech 3.0, where optimisation leads to changes in experimental reaction rates, producing inaccuracies at points where operating conditions are not similar to experimental data used in optimisation. A further consequence of optimisation is the interdependence of reaction rates; if new experimental data indicates a different reaction rate to that in the mechanism, the new rate must be changed and the mechanism optimised again. When comparing their mechanism to GRI-Mech 3.0, the mechanism of Konnov [137] and that of Chevalier [138] the authors found that, of the 44 most sensitive reactions common to both mechanisms, 14 had significantly different reaction rates. In spite of this, the performance of the mechanisms was similar, indicating that, even with such detailed mechanisms, the chemistry of hydrocarbon oxidation is still not well characterised at the elementary reaction level or that only a very small number of controlling reactions exist.

The mechanisms described above are strictly neutral — they do not model the formation and extinction of charged species. However, some ionic mechanisms for methane have also been developed over the years. Pedersen & Brown [139] formulated an ionic mechanism for pre-mixed methane flames that contained 86 reversible reactions. They were able to predict the concentrations of major neutral species with reasonable accuracy but the concentrations of ions proved difficult to match to experimental data.

Dautov & Starik [140] proposed a detailed mechanism for methane oxidation that

contained 392 reactions and 59 species that was found to perform well against experimental values for ignition delay. Starik & Titova [141] later added 214 ionic and neutral reactions to the same mechanism to model ion formation in methane-air flames. Their findings were similar to the experimental results described in Section 3.2.1 — H_3O^+ was the most important positive ion in stoichiometric flames and electrons were important negatively charged particles. They additionally found that the CO_3^- ion was abundant in the post-flame region. Given the high molecular weight and therefore low mobility of this ion, however, it is unlikely to contribute significantly to the ion current.

Rodrigues et al. [142] extended the kinetics of ionic species from the model of Starik & Titova to predict the ion current in propane-air flames. Their predictions were consistent with experimental results, with $\text{C}_2\text{H}_3\text{O}^+$ present in a narrow zone in the flame and thereafter H_3O^+ and electrons dominating the ion signature. Prager et al. [143] added ion chemistry to a mechanism previously developed by Warnatz et al. [144] and found similar results. Their mechanism, however, predicted incorrect widths of the ion peaks and incorrect peak mole fractions of the ions when compared to experimental results.

A key limitation of most of the above studies comes from the lack of experimental data for higher pressure flames for reasons discussed in Section 3.2.1. Many reactions in the mechanisms mentioned above show a dependence on pressure, making it difficult to extrapolate results to higher pressure flames, which are of primary interest to engine modellers. In these experiments, flame fronts may be vanishingly narrow and measurements difficult to conduct; hence, the ion current may be measured instead of individual ion profiles.

Additionally, the complexity of these mechanisms make them difficult to validate in systems more complex than a laminar flame. Phenomena such as constant-volume combustion or combustion in an engine are vastly more complicated to model and computational times for these combustion events can be prohibitively high. For these situations, simplified mechanisms or equilibrium models must be used.

Some studies have validated equilibrium models using engine-like conditions. Aithal [60] developed an equilibrium model of ionisation during the combustion of a methane-air mixture at constant volume. This model included 20 neutral and 7 charged species. He found H_3O^+ ions to be the most important positive ions except at very lean conditions, when NO^+ ions were abundant. The peak ion current calculated was found to match experimental results but the ion current decay was observed to occur earlier in the numerical simulation. The same author later used a similar equilibrium model

to predict the voltage signature in an HCCI engine fuelled with propane and acetylene to achieve fair agreement between experimental and modelled results. A significant limitation of equilibrium models for engine modellers is the unavoidable inaccuracy when computing the concentrations of species involved in slow reactions in quickly changing conditions [145]. The reactions responsible for NO_x production in a diesel engine are important examples of these. In order to model these reactions accurately, a chemical kinetics mechanism is required.

Figure 3.7, reproduced from Turns [146] shows a typical simplified chemical kinetics mechanism for methane oxidation. Bold lines show the main pathway, through which the majority of fuel molecules are oxidised. Thin lines show secondary pathways that play smaller roles in oxidation. Of particular interest in this scheme is the presence of the CH radical in the left branch — this radical is important for ion formation through Reaction R 3.1 as described in Section 3.2.1. Both CH and CH_2 are also responsible for NO formation via the prompt NO_x mechanism [147, 148]. While prompt NO_x forms a much smaller fraction of total NO_x emissions than does thermal NO_x , it may become important as emissions targets are lowered in the future or when oxygenated fuels such as biodiesel are used.

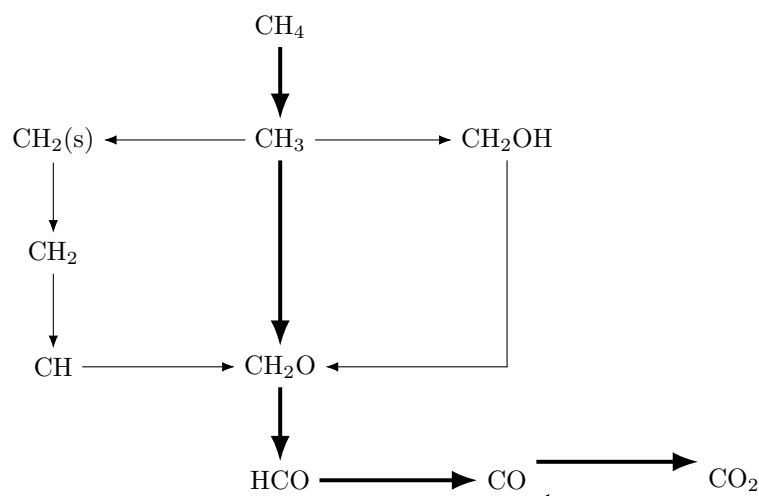


Figure 3.7: General simplified methane oxidation scheme showing the main pathway (bold arrows) and secondary pathways (light arrows). Figure taken from Turns [146].

3.3 Mechanism development

The mechanism developed here for methane oxidation comprises a neutral mechanism with an ionic sub-mechanism. The ionic sub-mechanism is designed to be able to be applied to any mechanism for hydrocarbons, providing the concentrations of the CH

Table 3.2: Region of interest for methane oxidation mechanism.

Parameter	Unit	Minimum	Maximum
Pressure	bar	20	50
Temperature	K	700	2500
Equivalence ratio		0.9	1.1

and O radicals are predicted with sufficient accuracy — as discussed in Section 3.2.1, these species are required for ion generation. The neutral mechanism developed here is based on that of Turns [146] (see Figure 3.7).

It is well known that the first step in the oxidation of methane is the production of CH_3 by reaction with O, H or OH radicals. The bulk of the CH_3 radical is oxidised directly via CH_2O , HCO and CO to CO_2 . These steps occur via reactions with O, OH and H radicals, H_2 molecules and third-body reactions.

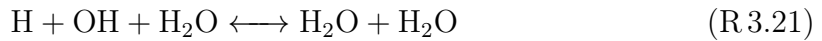
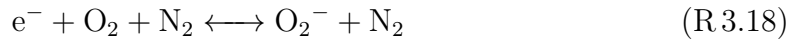
Alternate pathways include oxidation via CH_2OH to CH_2O and the CH_2 branch. This branch involves the oxidation of CH_3 to CH_2 in the singlet configuration via OH or H_2 . The singlet state has higher energy than the triplet state; rapid conversion to the triplet state occurs via collisions with N_2 and H_2O molecules. Oxidation of CH_2 by OH and H radicals forms CH, which then reacts with H_2O to form CH_2O .

The region of interest for this mechanism is shown in Table 3.2 and was chosen to be indicative of the operating regime of the constant-volume chamber experiments presented in the next chapter, where this mechanism is used to predict the experimentally observed ion current during methane oxidation.

A sensitivity analysis was performed on this mechanism using the perfectly stirred reactor code in CHEMKIN and the sensitivity of the mole fractions of major species O_2 , CH_4 , CO and CO_2 to each reaction was examined. Those reactions with little or no effect on the concentrations of these major species were removed in order to make the mechanism as computationally inexpensive as possible. While removal of these reactions may increase inaccuracy of the mechanism under certain conditions, accuracy is required only in the region of interest.

Four ionic reactions (Reactions R 3.15–R 3.18) and three H-O system reactions (Reactions R 3.19–R 3.21) were added to this neutral mechanism to produce a mechanism comprising 21 reactions and 21 species, of which four are charged. Rates for these reactions were obtained from various sources [56, 149, 150]. Thermodynamic data for all species was obtained from Burcat & Ruscic [151]. Transport data for most species was obtained from the CHEMKIN transport database [152]. Data was not available

for some species; their coefficients were estimated from similar species. The complete mechanism can be found in Appendix C.



To investigate the effect of the addition of this ionic sub-mechanism on the performance of the parent mechanism, methane oxidation in a perfectly stirred reactor was modelled within the region of interest as described in Table 3.2. The residence time was chosen to be 5.57×10^{-3} s, typical of a spark-ignition engine operating at 1800 RPM [74]. No deviation in final temperature or the mole fractions of major species and negligible deviation in the mole fractions of CH and O was found.

3.4 Mechanism validation

The mechanism was validated against established experimental data using CHEMKIN. Figure 3.8 shows the measured laminar flame speed for methane at 10 atm and 20 atm and at various equivalence ratios. This data is obtained from the studies of Rozenchan et al. [153], Gu et al. [154] and Lowry et al. [155]. Also shown is the laminar flame speed predicted by GRI-Mech 3.0 [133] and that predicted by the mechanism developed here. The equivalence ratio region of interest is indicated. The laminar flame speed is predicted with good accuracy within the region of interest; outside this region the predictions are similar to those of GRI-Mech 3.0, with significant inaccuracy at equivalence ratios of 0.8 and 1.2. The average error in laminar flame speed compared to the data of Rozenchan et al. is 15.8% in the equivalence ratio range 0.8–1.2 at 20 atm; this decreases to 5.8% in the range 0.9–1.1, which compares favourably to predictions of GRI-Mech 3.0 in the same ranges.

The inaccuracy at values of equivalence ratio far from 1.0 decreases as the pressure

is increased from 10 atm (17.1% average error) to 20 atm (15.8% average error), indicating that the mechanism is well suited to higher pressure applications.

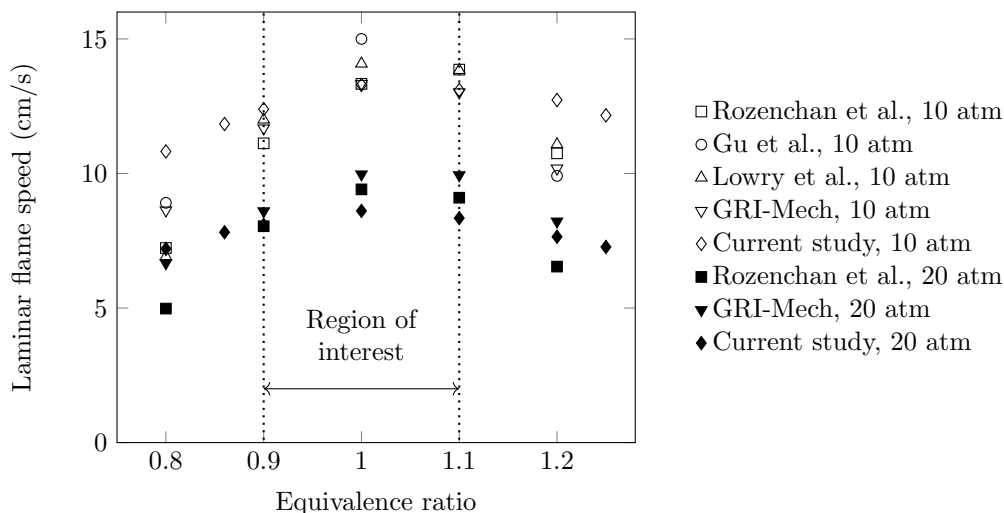


Figure 3.8: Measured and predicted laminar flame speeds for methane in air at 10 bar and 20 bar.

The methane mechanism was further validated using experimental data on species concentrations in a laminar methane-air flame at atmospheric pressure. The experimental data is taken from Bechtel et al. [156]. Whilst the pressure at which the experimental data was obtained is far outside the region of interest, some indication of the performance of the mechanism can be obtained from the comparison. Figures 3.9, 3.10 and 3.11 show this comparison at equivalence ratios of 0.86, 1.0 and 1.25 respectively. In each figure, subfigure (a) shows the variation of temperature and mole fractions of CH_4 , CO_2 and O_2 axially along the flame. Subfigure (b) shows the variation of temperature, CO , H_2 and H_2O axially along the flame.

There is good agreement between experimental measurements and model predictions at an equivalence ratio of 0.86 for most species; the CO mole fraction decays quicker in the experiment and the H_2 mole fraction decay is not seen in the model at all. Excellent agreement can also be seen along the entire length of the flame at an equivalence ratio of 1.0, apart from the decay in H_2 mole fraction which is not predicted well. At an equivalence ratio of 1.25, predictions of species mole fractions are accurate.

Given the lack of experimental observations at the pressures of interest for reasons discussed in Section 3.2.1, validation of the performance of the mechanism at elevated temperatures and pressures is conducted using two comprehensive methane oxidation mechanisms: GRI-Mech 3.0 [133] which contains 325 reactions and 53 species, and the Leeds mechanism developed by Hughes et al. [136] which contains 351 reactions and 37 species.

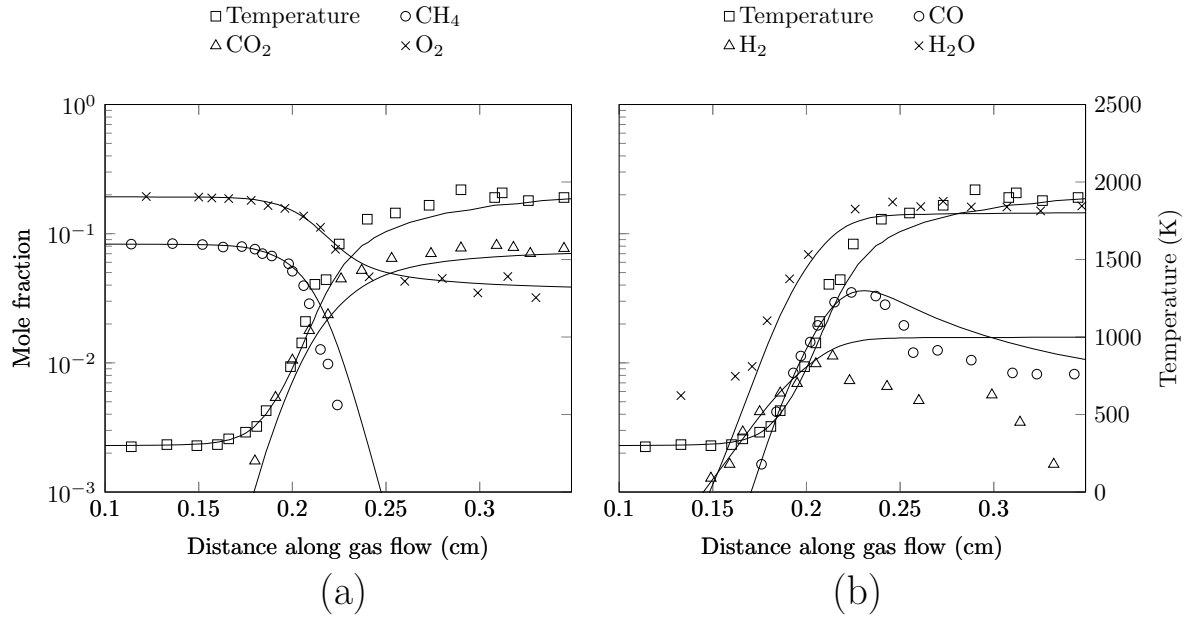


Figure 3.9: Measured and predicted temperature and flame composition for an atmospheric laminar methane-air flame, $\phi = 0.86$.

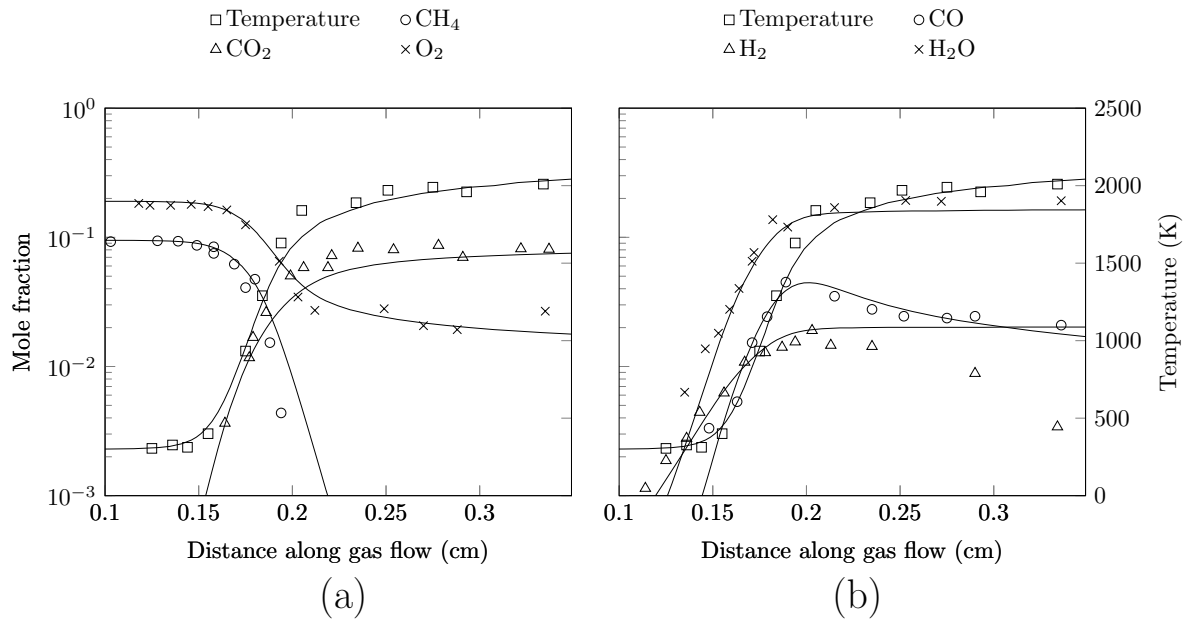


Figure 3.10: Measured and predicted temperature and flame composition for an atmospheric laminar methane-air flame, $\phi = 1.0$. Figure taken from Rao & Honnery [83].

Methane oxidation was modelled using all three mechanisms operating in a perfectly stirred reactor at various values of pressure, temperature and equivalence ratio. As described above, Table 3.2 shows the region of interest. The residence time is chosen to be 5.57×10^{-3} s which, for a diesel engine operating at 1600 RPM, is typically after all heat release has occurred as seen in Chapter 2.

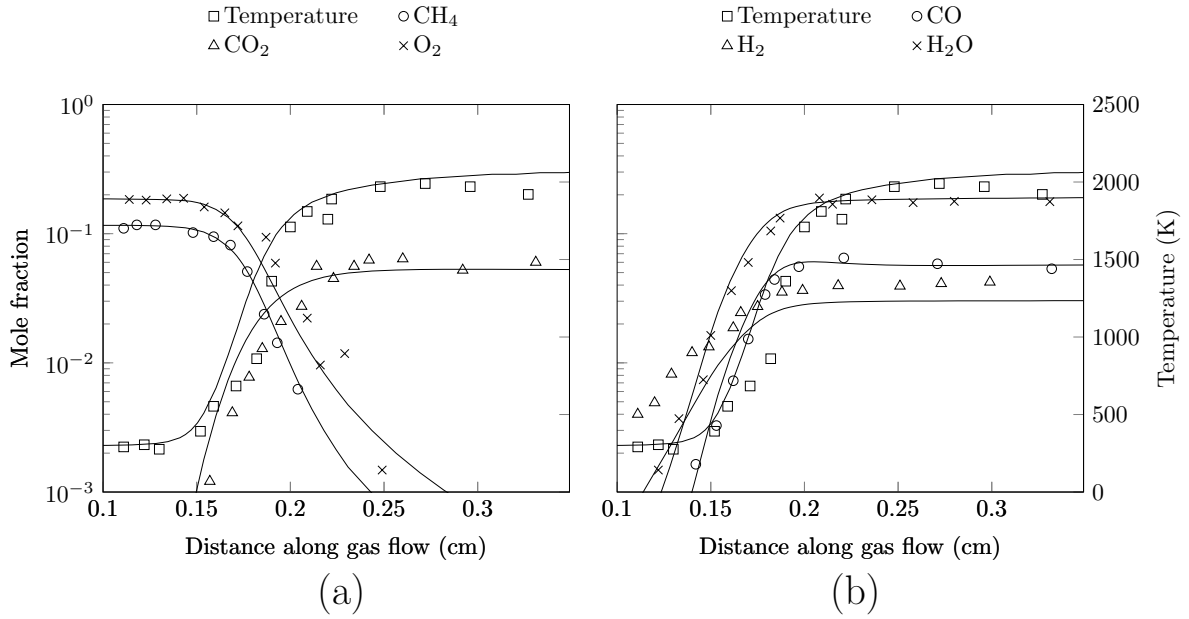


Figure 3.11: Measured and predicted temperature and flame composition for an atmospheric laminar methane-air flame, $\phi = 1.25$.

Heat release in hydrocarbon oxidation mechanisms depends heavily on the concentrations of the main combustion products viz. H_2O , CO_2 and CO . Figures 3.12, 3.13 and 3.14 compare the mole fractions of these major species across different values of inlet temperature, reactor operating pressure and equivalence ratio.

With varying inlet temperature (Figure 3.12), the predictions of CO_2 and CO clearly agree well between the three mechanisms. The ionic mechanism developed here under-predicts the mole fraction of H_2O by $\approx 6\%$ over the temperature range, a phenomenon observed under all configurations of perfectly stirred reactor tested. The same observations can be made when varying reactor pressure (Figure 3.13).

As the equivalence ratio is increased beyond 1.1, the ionic mechanism begins to favour the formation of CO_2 over CO . Consequently, CO_2 is over-predicted by 10% at an equivalence ratio of 1.1 and 18% at an equivalence ratio of 1.2. It is likely that this error will increase further as the equivalence ratio is increased, leading to significant inaccuracy.

The performance of the ionic sub-mechanism depends heavily on the mole fractions of CH and O , as these species are involved in Reaction R.3.15, the first reaction leading to ion production. Whilst these mole fractions are typically small, of the order of 10^{-9} – 10^{-4} , they have a significant effect on the ion formation rate. Thus, further validation specifically for the ionic sub-mechanism must be performed. The same operating conditions were used as in validation of the neutral sub-mechanism. Figures 3.15, 3.16

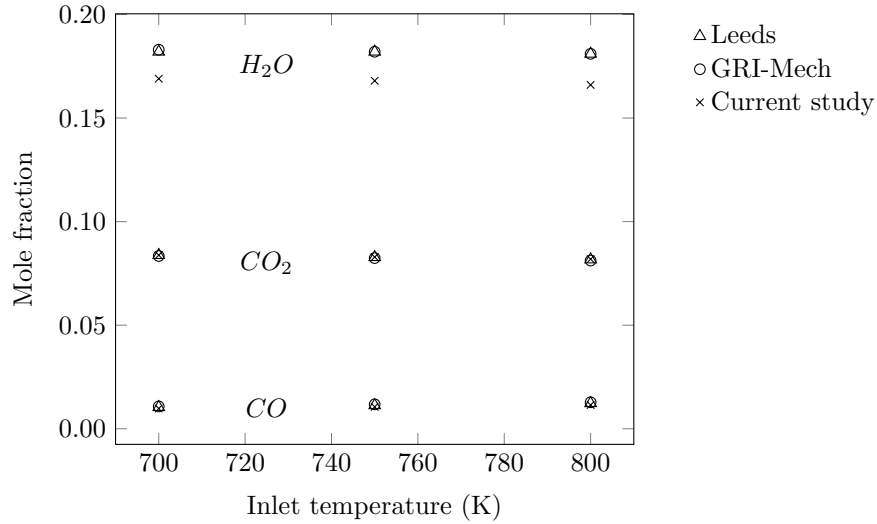


Figure 3.12: Main combustion products mole fractions for Leeds mechanism, GRI-Mech 3.0 and current mechanism for varying temperature at reactor operating pressure 20 bar, equivalence ratio 1.0 and residence time 5.57×10^{-3} s.

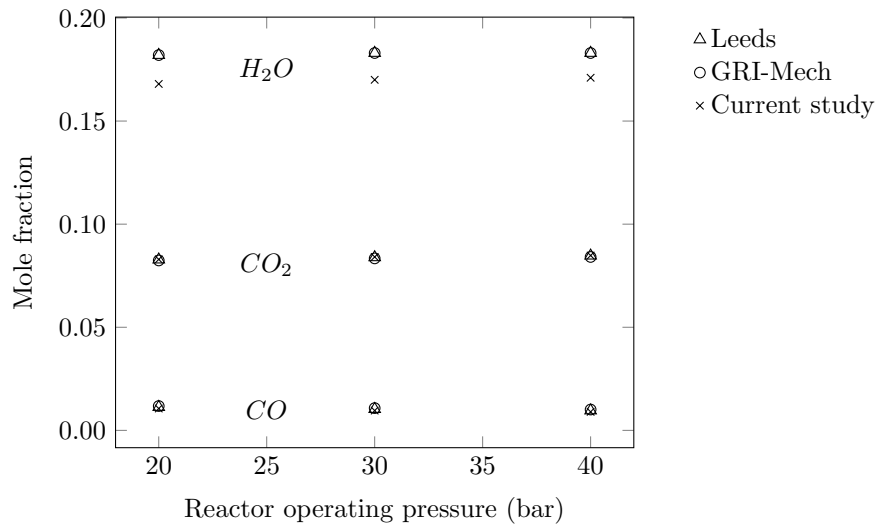


Figure 3.13: Main combustion products mole fractions for Leeds mechanism, GRI-Mech 3.0 and current mechanism for varying pressure at inlet temperature 750 K, equivalence ratio 1.0 and residence time 5.57×10^{-3} s.

and 3.17 show these comparisons. The predictions from the ionic mechanism can be seen to match those from GRI-Mech 3.0 closely; the Leeds mechanism consistently predicts a lower mole fraction of CH at equivalence ratios under 1.1.

Further validation of the spatial ion species profiles is hampered by the paucity of experimental measurements, particularly at the equivalence ratios and pressures of interest. Figure 3.18 shows a comparison of measurements and predictions of total positive ion concentration for a flat methane-air flame at atmospheric pressure with

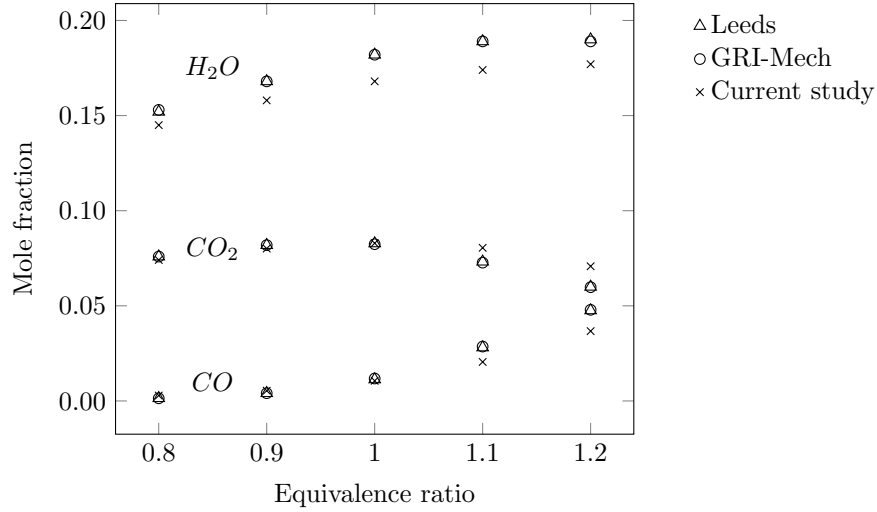


Figure 3.14: Main combustion products mole fractions for Leeds mechanism, GRI-Mech 3.0 and current mechanism for varying equivalence ratio at inlet temperature 750 K, reactor operating pressure 20 bar and residence time 5.57×10^{-3} s.

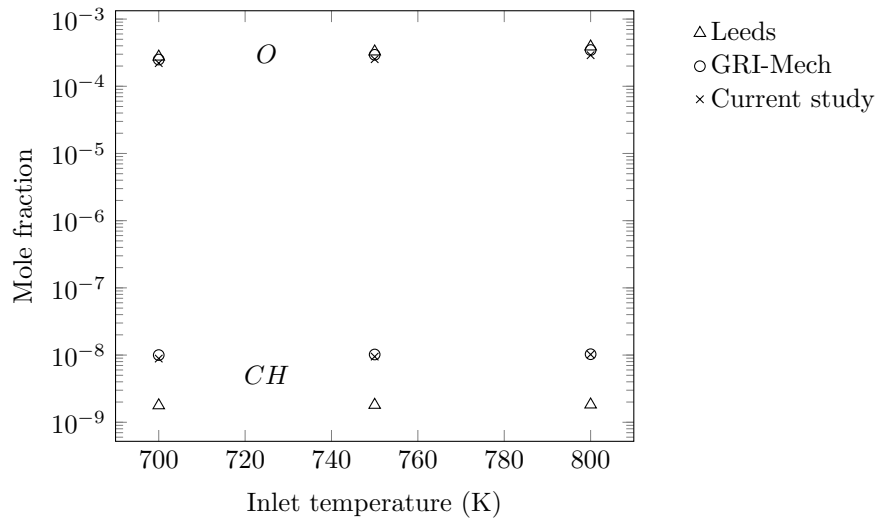


Figure 3.15: CH and O mole fractions for Leeds mechanism, GRI-Mech 3.0 and current mechanism for varying temperature at reactor operating pressure 20 bar, equivalence ratio 1.0 and residence time 5.57×10^{-3} s.

a gas temperature at the burner mouth of 402 K and an equivalence ratio of 0.513. The experimental data is taken from Wortberg [157]. Although the parameters of this experiment are well outside the region of interest, there is reasonable agreement between the experimental and predicted peak positive ion concentration. The increased width of the curve seen in the predictions is expected; this is due to the higher laminar flame speed predicted at low values of equivalence ratios as seen in Figure 3.8. The laminar flame speed prediction is greatly improved at equivalence ratios close to 1.0 so it is expected that the mechanism will be more accurate within its designed range.

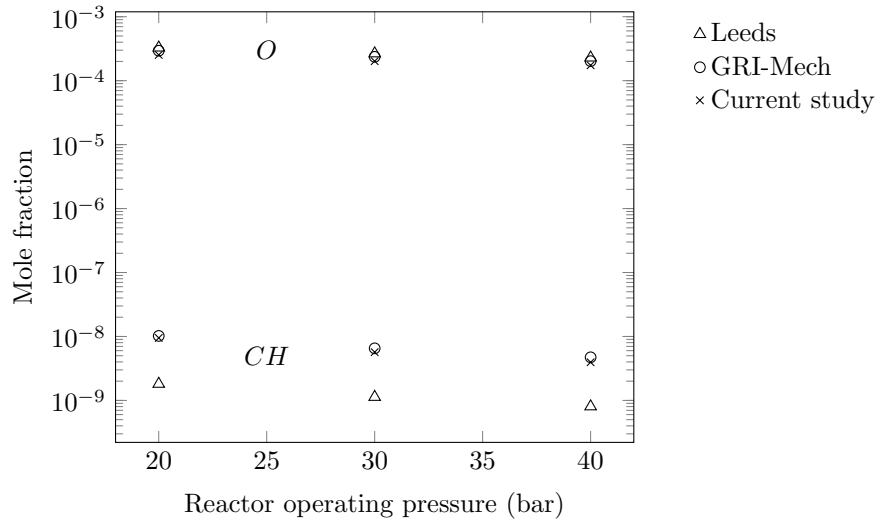


Figure 3.16: CH and O mole fractions for Leeds mechanism, GRI-Mech 3.0 and current mechanism for varying pressure at inlet temperature 750 K, equivalence ratio 1.0 and residence time 5.57×10^{-3} s.

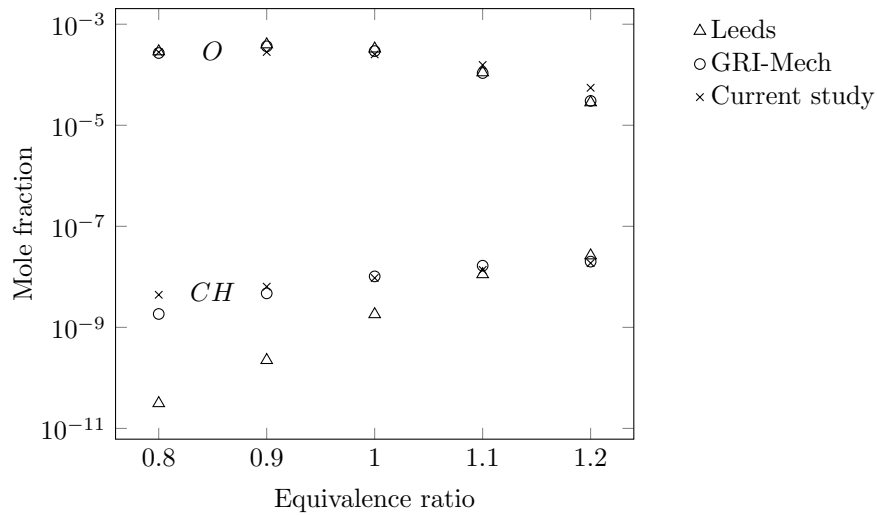


Figure 3.17: CH and O mole fractions for Leeds mechanism, GRI-Mech 3.0 and current mechanism for varying equivalence ratio at inlet temperature 750 K, reactor operating pressure 20 bar and residence time 5.57×10^{-3} s.

3.5 Effects of PSR operating conditions on ion current

This section examines the effects of changing operating conditions in a PSR on predictions of the ion current when using the ionic mechanism developed previously. From knowledge of the species mole fractions and the mass flow rate into the reactor, the ion current can be calculated using Equation 3.4 as described in Section 3.2.2. A

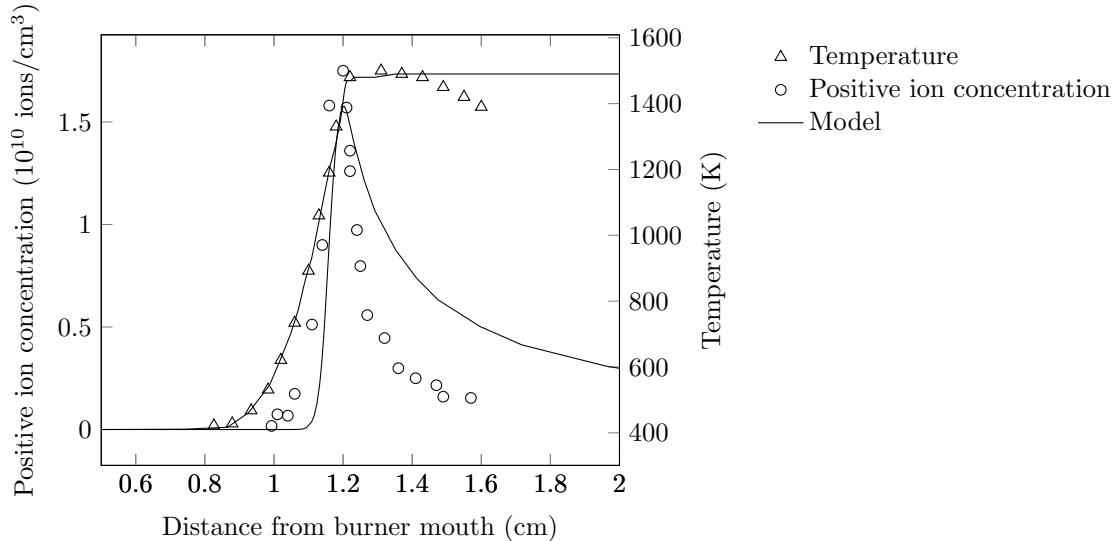


Figure 3.18: Temperature and positive ion concentration profiles for a flat methane-air flame at atmospheric pressure, equivalence ratio 0.513 and temperature at the burner mouth 402 K. Experimental data taken from Wortberg [157].

geometric factor of 1.0 and a sensor voltage of 1 V are assumed for calculation of the ion current in this section.

The ion sensors used in this study all have a smaller positive electrode than negative, so the area for neutralisation of negative ions is smaller by several orders of magnitude than that of positive ions. The concentration of negatively charged species was therefore taken to be the limiting factor in the ion current. Furthermore, the number of electrons was found to be, on average, two orders of magnitude larger than that of O_2^- ions. The radius of O_2^- ions is approximately five orders of magnitude greater than that of electrons and they are also four orders of magnitude heavier. Hence, the mobility of electrons is several orders of magnitude higher than that of O_2^- ions, due to their lower mass. O_2^- ions therefore should contribute negligibly to the total ion current. The total ion current was thus calculated based purely on the concentration of electrons in the mixture.

Figures 3.19 (a)–(d) show predictions of the ion current for varying values of inlet temperature, reactor operating pressure, equivalence ratio and residence time. The default values for these variables are 298 K, 1 bar, 1.0 and 0.1 s respectively. The maximum temperature observed is approximately 2710 K when an inlet temperature of 1400 K is specified.

Increasing the inlet temperature of reactants favours the dissociation of H_2O into H and OH radicals in Reaction R 3.21. The increase in concentration of the H radical shifts the equilibrium between CH_2 and CH towards CH. The concentration of CH_2

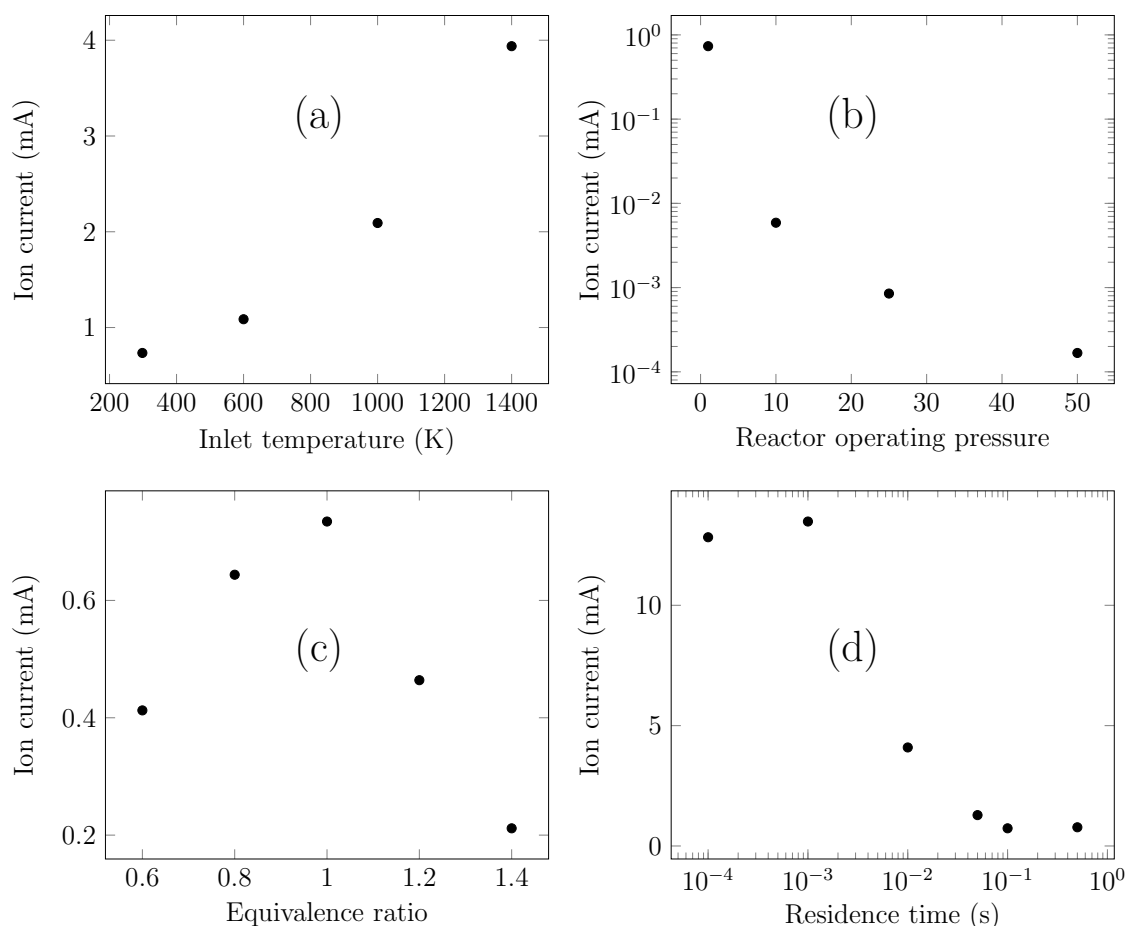


Figure 3.19: Predicted ion current at varying values of temperature, pressure, equivalence ratio and residence time. Default values are 298 K, 1 bar, 1.0 and 0.1 s respectively.

is observed to decrease and that of CH to increase. This favours Reaction R 3.15, increasing the ion concentration and causing an increase in the ion current, shown in Figure 3.19(a). It must be noted, however, that a competing effect is present here — the collision frequency is proportional to the square root of mixture temperature, as seen in Equation 3.1, which means mobility is reduced as temperature is increased. The ion current therefore increases at a slower rate than does the electron concentration.

With increasing reactor pressure, the dissociation of H_2O into H and OH as in Reaction R 3.21 is inhibited. The lower OH mole fraction slows the formation of $\text{CH}_2(\text{s})$ from CH_3 , leading to a lower CH mole fraction and therefore a smaller electron mole fraction. Furthermore, the increase in the number of moles of reactants and products increases the collision frequency for all species; this decreases their mobility drastically and hence the reduction in the ion current is more pronounced than that of electron mole fraction. This trend is shown in Figure 3.19(b).

With increasing equivalence ratio, the shortage of oxygen in the mixture stream leads

to a low concentration of the O radical, which is necessary for Reaction R 3.15 to take place. As the equivalence ratio increases from 1.0, the concentration of the CH radical increases and that of electrons decreases, indicating a leftward shift in the equilibrium of Reaction R 3.15 due to the lower O concentration. The ion current therefore also decreases. With decreasing equivalence ratio, the shortage of CH₄ in the mixture stream leads to a shortage of H atoms in the flow. This causes a reduction in the formation of OH and H radicals, which are required for the conversion of CH₃ to CH₂(s) and CH₂ to CH. The concentration of CH₂(s) is greatly reduced and, while that of CH₂ is relatively unchanged, the concentration of CH is reduced, leading once again to a leftward shift in the equilibrium of Reaction R 3.15 and a decrease in the ion current. Furthermore, maximum heat release and temperature are found at an equivalence ratio of 1.0; these are the conditions most conducive to dissociation of H₂O. The effect of this is to increase the ion current as described above. Any change in equivalence ratio from 1.0 therefore has the effect of decreasing the ion current. These trends are shown in Figure 3.19(c).

Figure 3.19(d) shows the evolution of the ion current as combustion occurs; the ion current can be seen to peak early in the combustion process before reducing to a very low level, indicating that ions will generally be found in or near the flame front. This agrees with previous experimental observations [56, 57].

3.6 Summary

A simplified mechanism for methane oxidation at near-stoichiometric mixture fractions was developed as an initial step towards the understanding of ion formation in engines. The mechanism was validated against experimental results for laminar flame speed and temperature, and species profiles across a laminar flame. Where high pressure experimental data was not available, lower pressure data was used. Good agreement between the modelled and measured values was found for equivalence ratios close to 1.

Mechanisms such as the one presented here can be used in CFD simulations to give spatial information on species compositions in many types of combustion systems, whilst still remaining computationally inexpensive relative to detailed mechanisms such as GRI-Mech or the Leeds mechanism mentioned above. When operating within the range of temperature, pressure and equivalence ratio they are designed for, they are capable of considerable accuracy. Simplified mechanisms are necessarily limited to small sets of conditions for which they are accurate; the mechanism developed here is intended for use at equivalence ratios near 1, moderate-to-high temperatures and

pressures around 20–50 bar. These are chosen to mimic the conditions expected to occur in the experiment described in the next chapter.

Whilst some validation of this mechanism for laminar flames at atmospheric and lower pressures has been presented, experimental data for species concentrations and heat release in engine-like conditions is not presently available. In order to validate the most important aspects of the methane mechanism developed here, viz. heat release and ionic species concentrations, under conditions more representative of those found in engines, the oxidation of methane in a constant volume chamber is studied. The experiment, its results and the performance of this mechanism in engine-like conditions are detailed in Chapter 4.

An important ability of simplified mechanisms is the prediction of the effects of changing system variables on different species concentrations. This chapter explored different values of equivalence ratio, temperature, pressure and residence time in a perfectly stirred reactor and identified the mechanisms by which these system variables affect the ion current. Findings from this chapter are used in the Chapter 4 to provide insight into some aspects of the ion current observed during the oxidation of methane at constant volume. A simplified mechanism for n-heptane is used in Chapter 6 in a similar manner to provide insight into the relationship between the ion current, heat release and NO_x formation in premixed flames and diesel sprays.

Chapter 4

Constant volume chamber: methane oxidation

4.1 Introduction

Constant volume chambers are useful devices in the study of thermodynamics at elevated pressures and/or temperatures. Given maximum chamber pressures in the region of 50 bar, which is similar to the motoring pressure in a CI engine or the peak pressure in an SI engine, constant volume chambers are particularly useful in the field of engine research. These chambers are frequently used in the characterisation of sprays — free jets [158], impinging jets [159] and sprays into porous media [160]. They are also used to characterise fuels, with ignition delay and rate of heat release being of primary interest. The ability to precisely dictate the chamber temperature and geometry and the mixture composition, combined with the ease of including optical access or different sensors means that the constant volume chamber is a valuable tool in the investigation of engine-like conditions.

This chapter describes a study of the ion current produced during methane oxidation in engine-like conditions, using a constant volume chamber to simulate these conditions. The experimental setup and results are presented in Section 4.2. This experiment was modelled using the ionic mechanism for methane oxidation developed in Chapter 3. The model and a comparison of results are presented in Section 4.3.

Some sections of this chapter have been previously published in Rao & Honnery [83] and are reproduced here.

4.2 Experiment

4.2.1 Setup

The constant volume chamber used for this experiment is a hollow stainless steel cylinder of internal height 132 mm and internal diameter 150 mm. Externally, eight faces are machined onto the curved surface with open areas through which sensors, actuators, glass windows or steel blanks can be inserted. The top surface contains a 55 bar pressure relief valve and a manually operated exhaust valve through which the chamber contents can be vented. Needle valves control the flow of both air and methane through a two-way valve entering the chamber from the top in order to produce a uniform gas mixture. A flush line is installed in the bottom surface which allows the entry of compressed air at a high flow rate in order to both flush the chamber of exhaust gases and cool the chamber walls after a combustion event.

Four of the eight sides of the chamber contain instruments: a K-type thermocouple, a GE Druck PMP 4311 pressure transducer, an ion sensor and a spark plug. Schematics of the chamber can be seen in Figure 4.1. The pressure transducer has a range of 0–80 bar and a linearity of 0.1%. Its thermal zero/span shift is $< \pm 1\%$. The ion current is measured by a spark plug with the side electrode removed. The tip of the centre electrode of the ion sensor is located at the centre of the chamber and maintained at +120 V relative to the casing and chamber walls. A schematic of the ion sensor is shown in Figure 4.2.

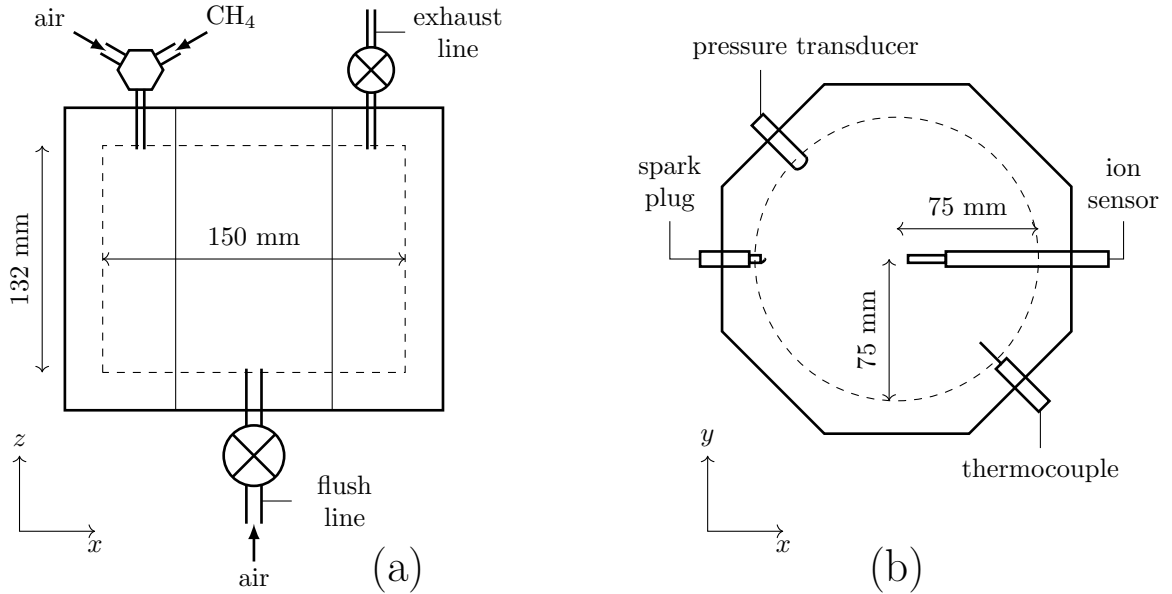


Figure 4.1: Schematic of the constant volume chamber [83].

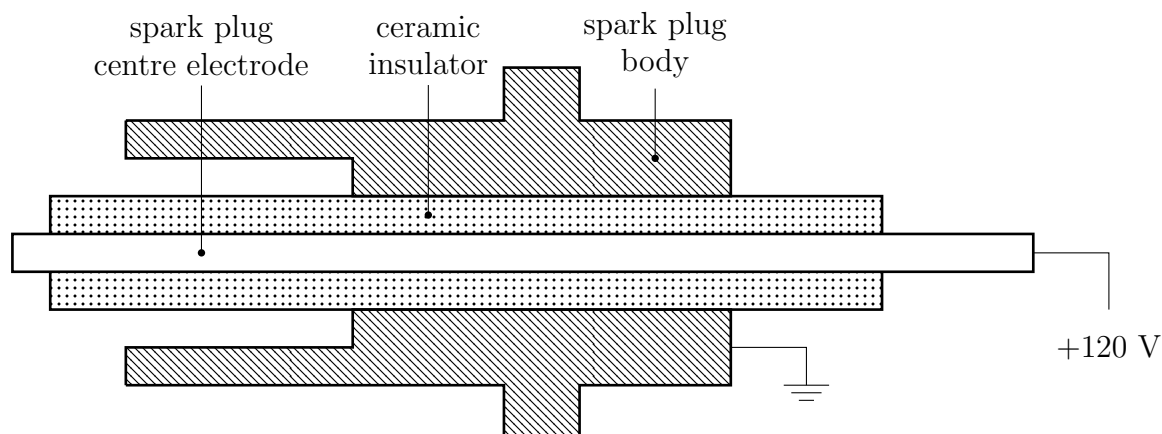


Figure 4.2: Schematic of the ion sensor [83].

The ion current and chamber pressure are sampled at 10 kHz by a National Instruments 24-bit analogue-to-digital converter. The spark plug is activated manually using a momentary switch.

The introduction of gases into the chamber was performed at high flow rates in order to induce turbulent mixing of the two gases. A short time (typically 1 minute) was allowed to elapse for the chamber contents to achieve quiescence. The temperature was noted at this point — due to thorough flushing and cooling of the chamber between consecutive combustion events, the thermocouple recorded the mixture temperature immediately prior to each combustion event to be in the range 300–303 K. The spark plug was then fired and the combustion event recorded. After peak pressure was reached, the exhaust valve was opened and, once the pressure inside the chamber dropped to atmospheric, the flush valve was opened. Flushing continued until the chamber cooled to room temperature.

This procedure was repeated for two values of initial chamber pressure (3 bar and 6 bar) and three values of equivalence ratio (0.8, 1.0 and 1.2). The peak pressure reached in the chamber was approximately 45 bar and the calculated peak temperature from equilibrium approximately 2700 K.

4.2.2 Results

The measured traces of chamber pressure and ion current for varying pressure and constant equivalence ratio are shown in Figures 4.3, 4.4 and 4.5. The time at which the spark is fired is shown as a fine line crossing the pressure curve. Peak pressure is reached at $t=0$ s. Of interest in these plots is the consistent trend of a longer

combustion event at higher values of initial chamber pressure, indicating decreasing flame velocity for increasing pressure — this is a result observed in previous studies and predicted by the ionic mechanism in Section 3.4, albeit for constant pressure flames. This effect is seen to decrease with increasing equivalence ratio; at an equivalence ratio of 1.2, the time taken for the completion of the combustion event is very similar for both values of initial chamber pressure.

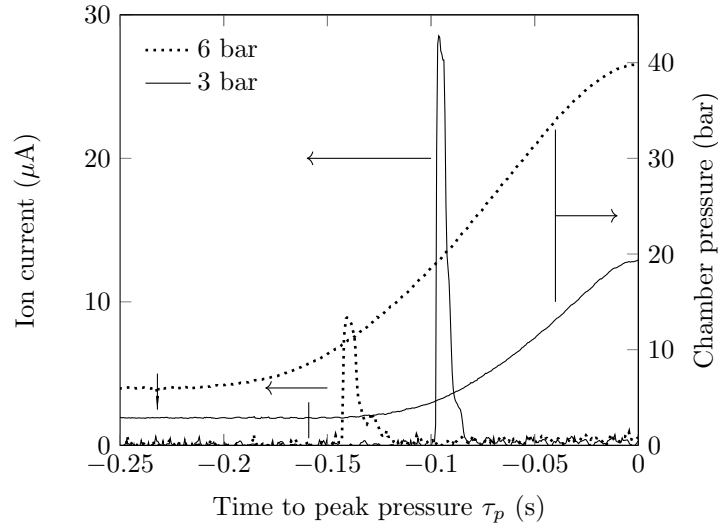


Figure 4.3: Experimentally measured ion current and chamber pressure for an equivalence ratio of 0.8 and initial chamber pressures 3 bar and 6 bar.

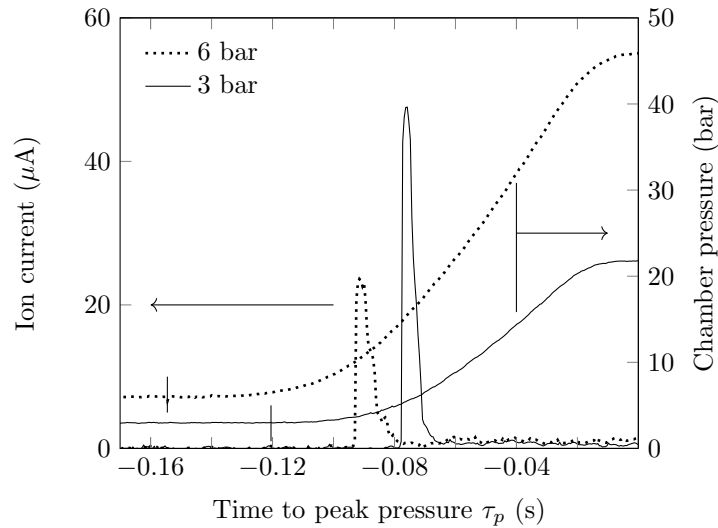


Figure 4.4: Experimentally measured ion current and chamber pressure for an equivalence ratio of 1.0 and initial chamber pressures 3 bar and 6 bar.

The ion current peak is higher at the lower initial chamber pressure value, as predicted in Section 3.5, due both to the greater mole fraction of ions and their increased mobility. The width of the peak is lower at lower values of initial chamber pressure, possibly due

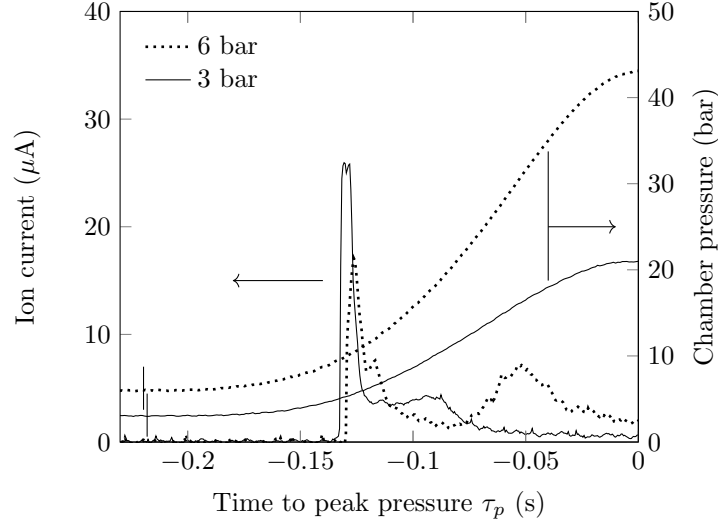


Figure 4.5: Experimentally measured ion current and chamber pressure for an equivalence ratio of 1.2 and initial chamber pressures 3 bar and 6 bar.

to the increased flame velocity leading to a shorter time during which the ion sensor is exposed to the flame front. The ion current quickly decreases to zero, showing the absence of long-lived ionic species.

Of interest in Figure 4.5 is the second peak in the ion current at an equivalence ratio of 1.2. Delfau et al. [161] report the presence of a second peak in the ion current in sooting ethylene and acetylene flames; while the same mechanism may be present in sooting methane flames, the equivalence ratio used here means that any soot formed is likely to be quickly oxidised. A more detailed discussion of the probable cause of this peak is presented in Section 4.3.2.

Time t can be normalised by the time taken for the entire combustion event from spark (τ_s) to peak pressure (τ_p) to obtain τ_n , the normalised time pertaining to the combustion event (Equation 4.1).

$$\tau_n = \frac{t - \tau_s}{\tau_p - \tau_s} \quad (4.1)$$

Figure 4.6 shows the ion current and chamber pressure signals plotted against normalised time for different values of initial chamber pressure at an equivalence ratio of 1.0. The timings of the ion current peaks can be seen to be very similar, both occurring at $\tau_n \approx 0.38$ and at approximately 13% of the total pressure rise. This indicates that the two flames propagate in a similar fashion and both propagate more quickly through the centre of the chamber than on the sides, a result expected due to

quenching of the flame at the cold chamber walls.

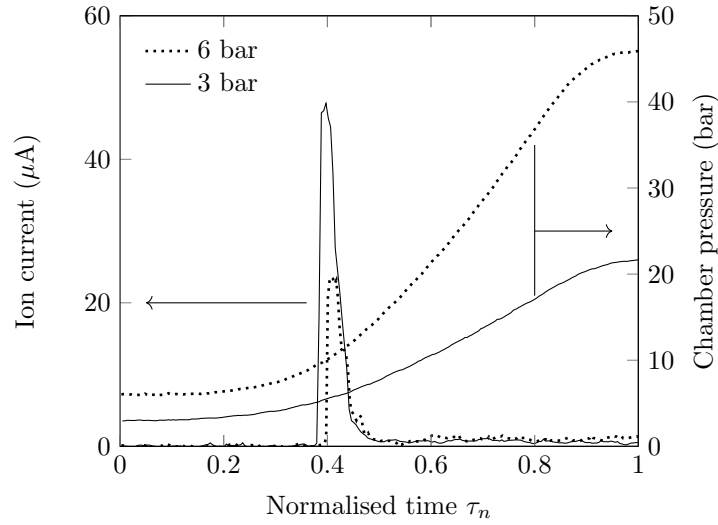


Figure 4.6: Experimentally measured ion current and chamber pressure for an equivalence ratio of 1.0 and initial chamber pressures 3 bar and 6 bar, with time normalised by total time taken for the combustion event [83].

While the locations of the pressure transducer and thermocouple are not of great importance, the relative locations of the spark plug and the ion sensor play a big role in the ion current observed since the ion current is observed mainly in the flame front. The flame front propagates from the spark location spherically outwards, making the timing of the ion current peak highly dependent on the location of the ion sensor. In the region of the walls, heat transfer leads to local cooling and quenching of the flame, leading to lower flame velocity. Figure 4.7 shows the ion current signals from two identical ion sensors for a combustion event at equivalence ratio 1.0 and initial chamber pressure 5 bar. One sensor (A) is located in the centre of the chamber as shown in Figure 4.1 and the other (B) near the wall but at the same values of x and z . The later development of the ion current peak for the sensor B indicates the quenching effect on the flame near the walls. The ion current measurement from sensor B also shows an elevated region well past the peak which is similar to that seen in the high equivalence ratio case.

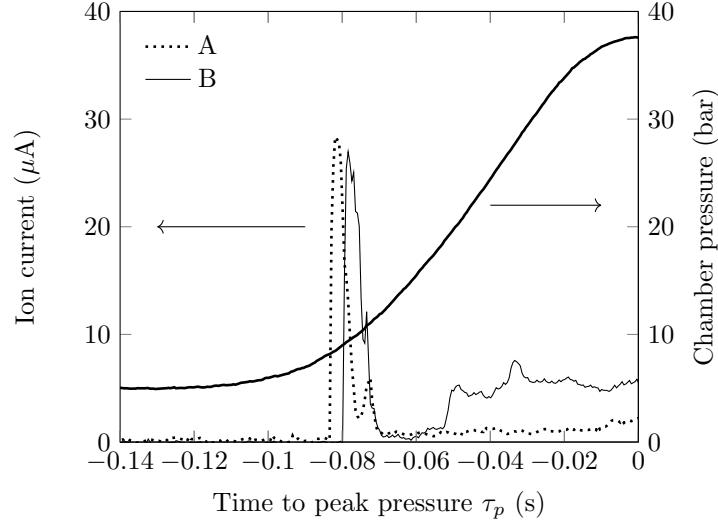


Figure 4.7: Experimentally measured ion current and chamber pressure for an equivalence ratio of 1.0 and initial chamber pressure 5 bar. Two identical sensors A and B are used, A in the centre of the chamber and B near the wall.

4.3 Modelling

4.3.1 Setup

Modelling of the combustion event described in Section 4.2 was performed using ANSYS Fluent with CHEMKIN-CFD, allowing the simulation both of fluid dynamics and of chemical kinetics. Two-dimensional geometry is chosen over three-dimensional in order to reduce computational time, so a horizontal slice of the chamber is used as the fluid domain. To contribute to this reduction, only one half of the chamber is considered and a condition of symmetry imposed on the bisecting axis. Heat loss from the chamber walls is simulated by a constant temperature imposed on the outer surfaces of the walls; experimentally it was determined that the considerable thermal mass of the chamber walls led to no appreciable increase in temperature of the outer surface after a single combustion event. A laminar viscosity model is chosen because, while the flame front is likely to see local turbulence, its propagation is generally laminar. The average cell size is approximately 0.755 mm and the time step chosen is 2.5×10^{-4} s. The Courant number based on the time taken for the entire combustion event is found to be between 0.3 and 0.6 for all initial conditions tested.

The mechanism developed in Chapter 3 is used for the calculation of species concentrations and heat release. The concentration of electrons is taken to be the limiting factor in the production of the ion current for reasons outlined in Section 3.5. Chamber pressure and charged species concentrations are measured at the centre of the chamber,

in the same location as the ion sensor in the experiment. The ion current is calculated from the charged species concentration and the local temperature around the ion sensor as described in Section 3.2.2. The geometric factor is calculated as the ratio of the electrode areas on the shortest current path to the length of the path [162] and was found to be ≈ 0.01 .

Cell size and time-step size sensitivity studies were performed and can be found in Appendix D.

4.3.2 Results

Previous studies and results from Chapter 3 indicate that the dominant charged species in methane oxidation are electrons and H_3O^+ . Figure 4.8 shows the concentrations of electrons, H_3O^+ , HCO^+ and O_2^- at the centre of the chamber for a combustion event beginning at 6 bar and with an equivalence ratio of 0.8. Clearly, HCO^+ and O_2^- ions are found in significantly lower concentrations than are electrons and H_3O^+ . The ion current curve therefore broadly follows those of electron or H_3O^+ concentration. This observation can also be made at all other values of initial chamber pressure and equivalence ratio modelled.

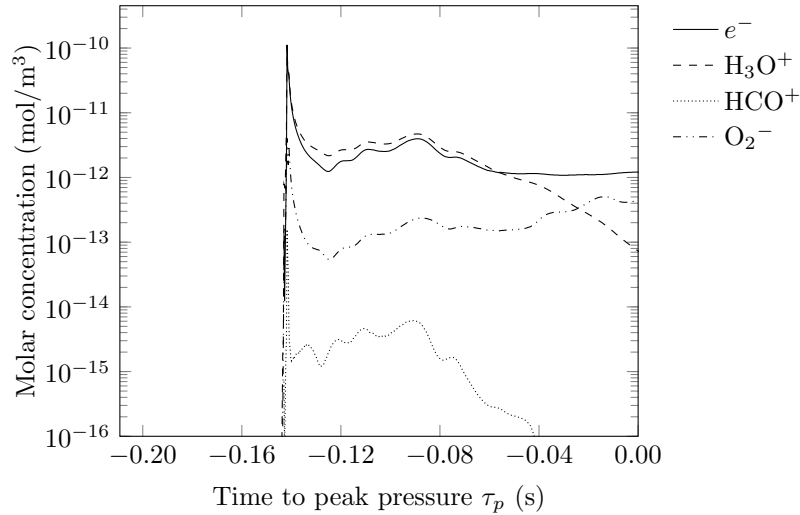


Figure 4.8: Charged species concentrations at the centre of the chamber during the combustion event.

Figure 4.9 compares the modelled and measured ion current and chamber pressure at an equivalence ratio of 0.8 and an initial chamber pressure of 3 bar. The predicted chamber pressure can be seen to follow the measured trace closely. Whilst the ion current occurs at approximately the same time in the model as in the experiment,

the peak is both lower and narrower. It has been suggested that the high voltage of the ion sensor used in the experiment attracts electrons from outside its immediate vicinity, leading to a high ion current even when the ion-rich zone of the flame has passed the sensor [83]. This narrowness of the modelled ion current peak is a feature observed at all values of initial conditions tested in this study.

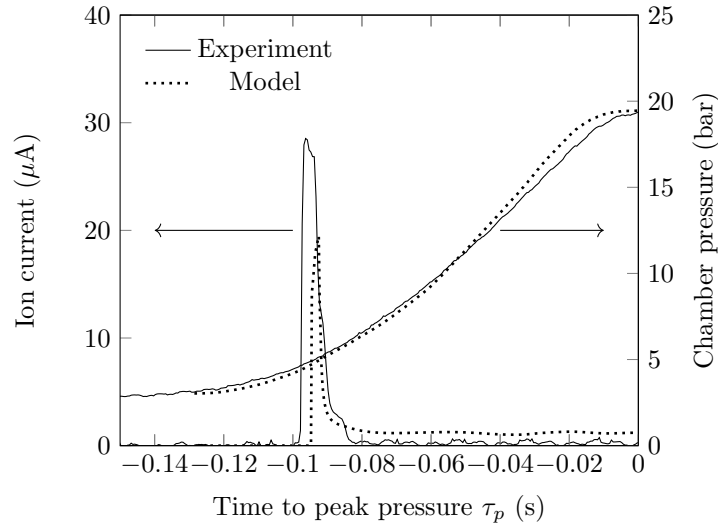


Figure 4.9: Comparison of experimental and modelled ion current and chamber pressure at an equivalence ratio of 0.8 and initial chamber pressure 3 bar [83].

Figure 4.10 shows the temperature and electron distributions within the fluid domain at $\tau_p = -0.094$ s, the time of the ion current peak in the model. The black rectangle shows the location of the ion sensor. Quenching at the walls can be seen to have a significant effect on the propagation of the flame; the penetration of the flame into the unburnt mixture is far deeper in the centre of the chamber than along the sides, explaining the early increase in the ion current seen in the experiment. The presence of electrons is seen to be limited to a thin region near the flame front, with very small concentrations in the burnt zone. This is consistent with the twin requirements of CH and O radicals for electron production. This observation also agrees with Figure 3.19 (d), where the electron concentration is seen to peak early in the combustion event and then decay sharply to nearly zero very shortly after.

The location of electrons near the maximum temperature gradient indicates that they are present in the flame where high rates of heat release occur. As seen in Figure 3.19 (a), electron concentration highly depends on temperature and increases with increasing temperature. These findings suggest that the formation of H-O radicals may be responsible for the correlations seen between heat release and electron formation via the mechanism discussed in Section 3.4. Further exploration of this phenomenon in a more detailed mechanism is presented in Chapter 6.

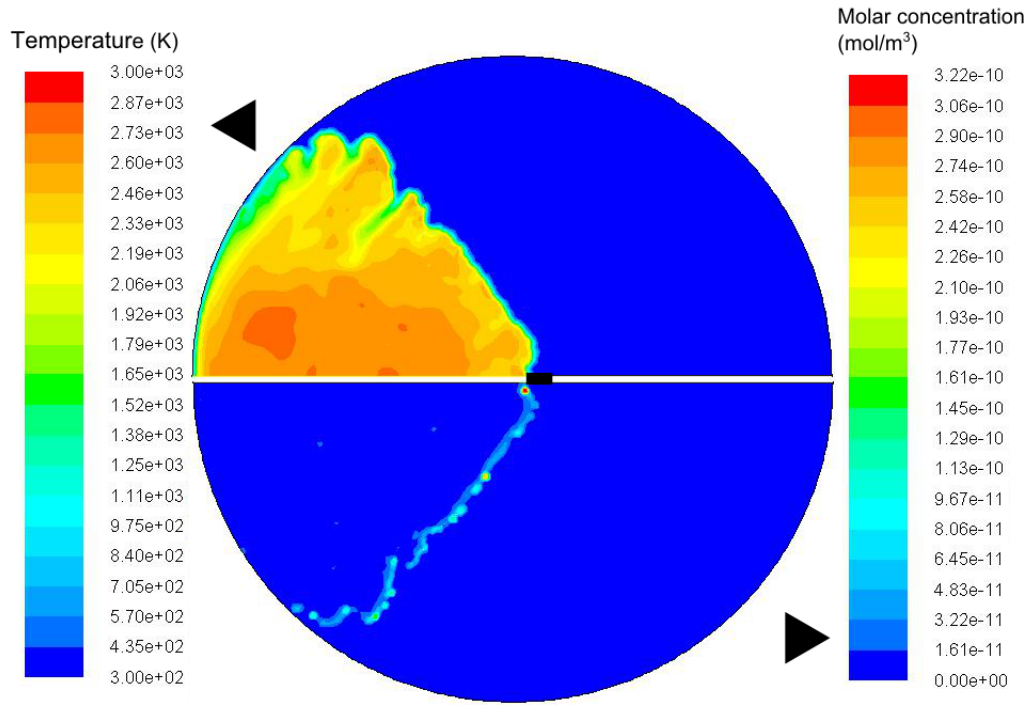


Figure 4.10: Temperature (top) and electron concentration (bottom) distributions in the chamber at an equivalence ratio of 0.8 and initial chamber pressure 3 bar, $\tau_p = -0.094$ s [83].

Figure 4.11 compares experimental and modelling results at an equivalence ratio of 0.8 and initial chamber pressure of 6 bar. The modelled chamber pressure generally follows the experimental curve but chamber pressure is generally under-predicted. Similar to the results in Figure 4.9, the ion current peak is significantly narrower in the model than in the experiment but its magnitude is fairly well predicted.

Similar results are obtained at initial chamber pressure 6 bar and equivalence ratio 1.0, as shown in Figure 4.12. The model predicts a higher flame speed in the initial stage of flame propagation, leading to a more rapid rise in chamber pressure and therefore an early ion current peak. The peak in chamber pressure is well predicted.

Figure 4.13 shows experimental and modelling results at an equivalence ratio of 1.2 and initial chamber pressure of 6 bar. The chamber pressure shows a maximum under-prediction of 9% of the peak pressure. While it is clear that the ion current's first peak is under-predicted in magnitude but accurate in location, the second peak is of particular interest. The second peak seen in the model corresponds well to that seen in experiments. The temperature and electron distributions (Figure 4.14) at the time of the first peak, $\tau_p = -0.13$ s, indicate a region of moderate electron concentration for some distance behind the flame front, in contrast to observations made in fuel-lean

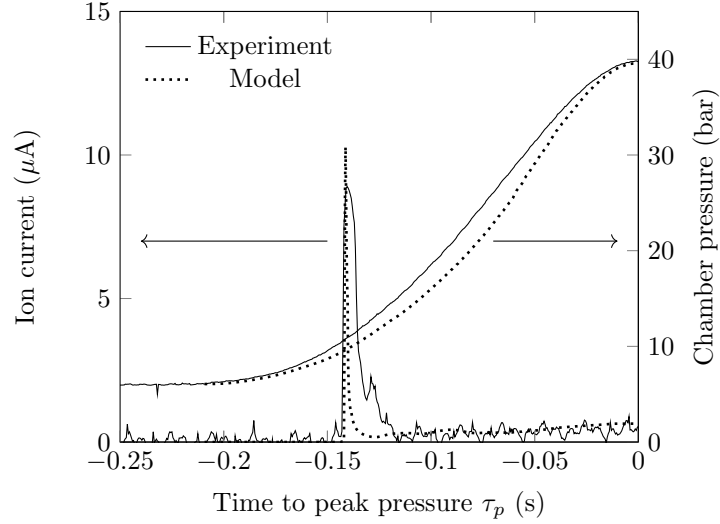


Figure 4.11: Comparison of experimental and modelled ion current and chamber pressure at an equivalence ratio of 0.8 and initial chamber pressure 6 bar [83].

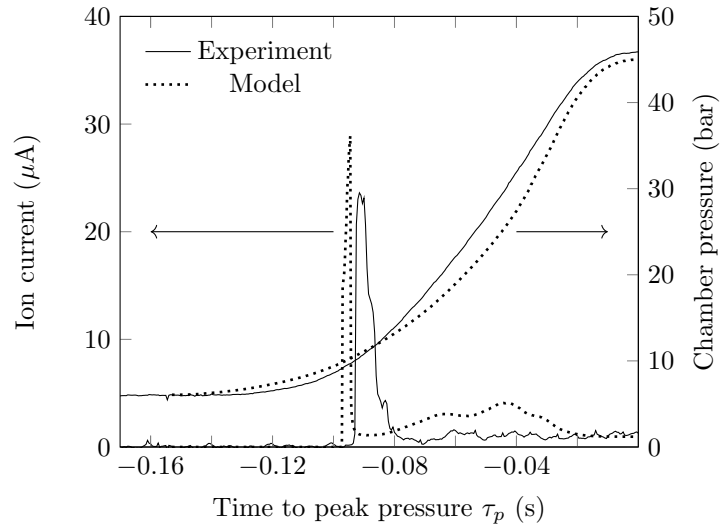


Figure 4.12: Comparison of experimental and modelled ion current and chamber pressure at an equivalence ratio of 1.0 and initial chamber pressure 6 bar [83].

flames.

The production of electrons in this region can be explored by examining the evolution of the concentration of OH radicals at the centre of the chamber during the combustion event, shown in Figure 4.15. The high temperature of the combustion products in the post-flame region leads to dissociation of H_2O and increased production of the OH and H radicals as described in Section 3.5. In fuel-rich flames where the post-flame region contains unburnt hydrocarbons, this results in an increase in CH concentration as described earlier. This is seen clearly in the similarity of the curves in Figure 4.15.

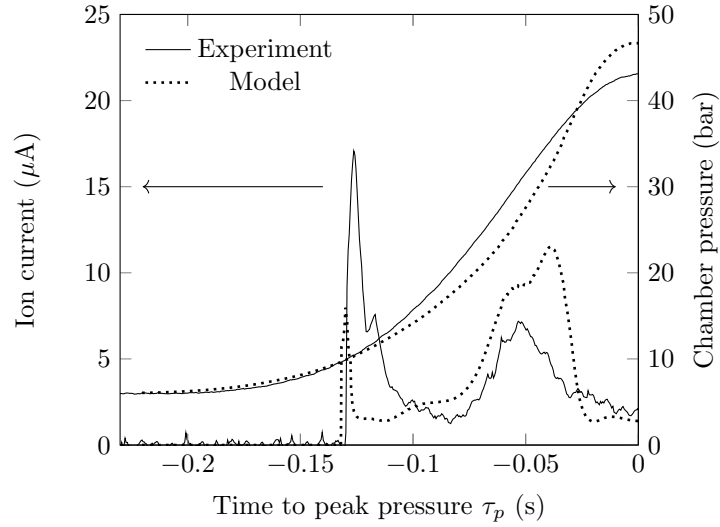


Figure 4.13: Comparison of experimental and modelled ion current and chamber pressure at an equivalence ratio of 1.2 and initial chamber pressure 6 bar [83].

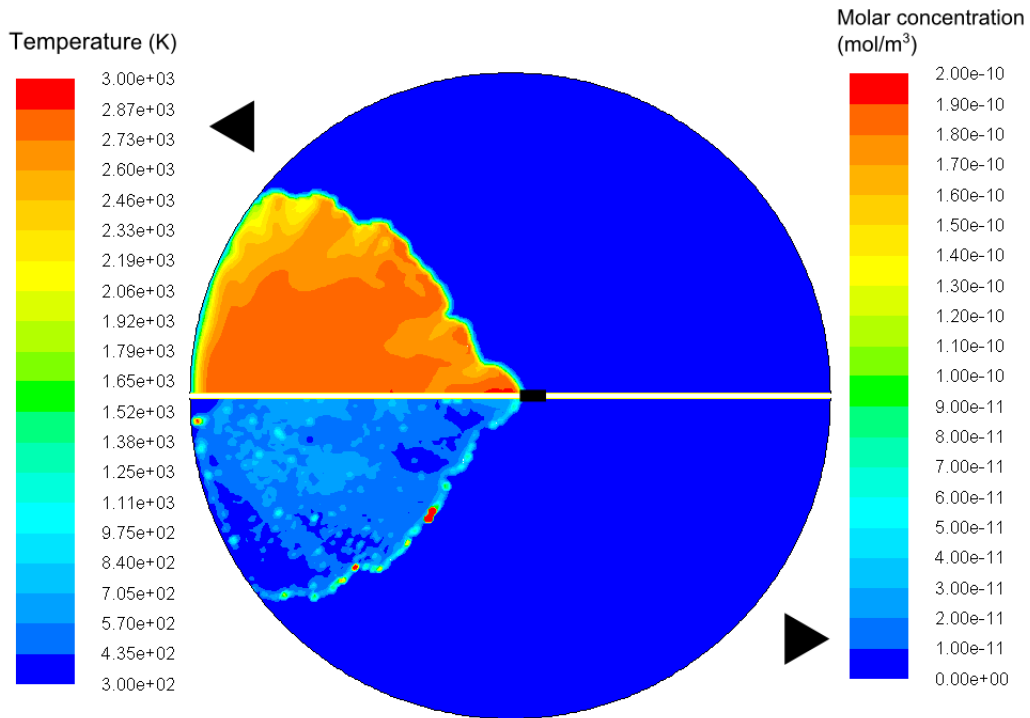


Figure 4.14: Temperature (top) and electron concentration (bottom) distributions in the chamber at an equivalence ratio of 1.2 and initial chamber pressure 6 bar, $\tau_p = -0.130$ s [83].

It is possible that a similar mechanism is responsible for the ion current curve seen for the near-wall sensor (Figure 4.7). Quenching of the flame near the wall may lead to incomplete combustion. Subsequently, the convection of high temperature mixture containing OH and H radicals towards this region may then lead to elevated values of

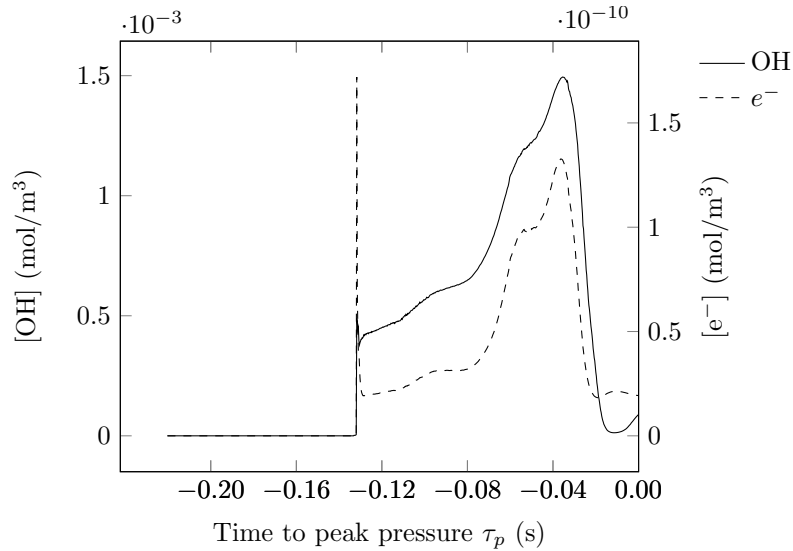


Figure 4.15: Concentrations of OH and electrons at the centre of the chamber during the combustion event. Initial pressure 6 bar and equivalence ratio 1.2.

the ion current.

Large concentrations of the OH radical are seen in the post-flame region even in fuel-lean flames. However, lower equivalence ratios lead to the consumption of nearly all hydrocarbon molecules in the flame front, so the increase in OH concentration has no effect on concentration of the CH radical; electron concentration therefore is generally independent of OH concentration. This can be seen in Figure 4.16 depicting the same variables for a fuel-lean flame at an initial chamber pressure of 6 bar and equivalence ratio of 0.8.

4.4 Summary

This chapter presented experimental and modelling results for the ion current and pressure rise generated during the combustion of a methane-air mixture in a constant volume chamber in engine-like conditions.

Experimental measurements showed lower flame speeds and lower ion current peak magnitudes at higher chamber pressures, as expected from results presented in Chapter 3. Also expected was the greatest ion current peak magnitude at a stoichiometric mixture fraction. An unexpected result was the production of a second ion current peak at an equivalence ratio of 1.2.

CFD modelling of the experiment indicated that the pressure rise was modelled well at

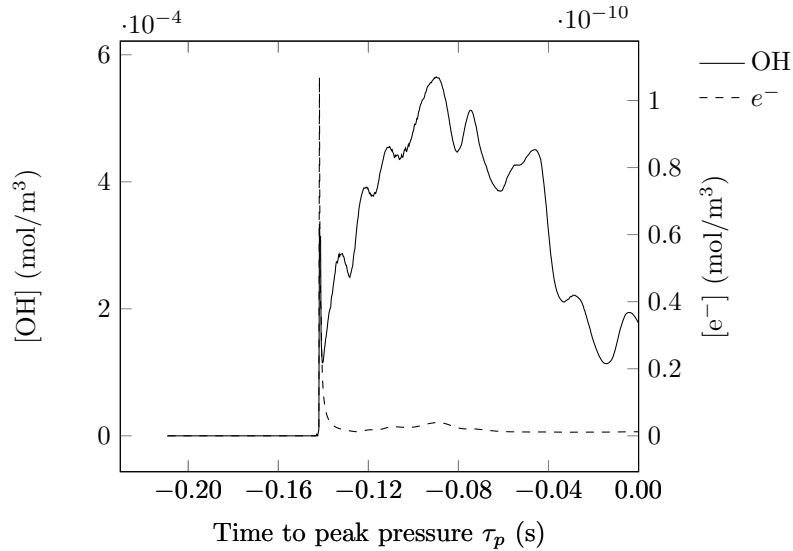


Figure 4.16: Concentrations of OH and electrons at the centre of the chamber during the combustion event. Initial pressure 6 bar and equivalence ratio 0.8.

equivalence ratios of 1 and below; above this value some inaccuracy was noted in the predicted chamber pressure profile. The important charged species were electrons and H_3O^+ as found in previous studies. The ion current peaks were modelled fairly well at equivalence ratios of 1 and below. Electrons were found to be concentrated in the flame front at these equivalence ratios, near where the greatest temperature gradient and highest rate of heat release were located. This observation, in conjunction with predictions presented in Chapter 3, indicates a possible reason for the correlations seen between the ion current and heat release — the formation of H-O radicals in the presence of hydrocarbon molecules.

The experimentally measured second ion current peak at an equivalence ratio of 1.2 was also observed in the model. The concentration of the OH radical was found to be significant in the post-flame region for all initial conditions modelled. The effect of this radical on the concentration of electrons was explored previously in Section 3.5, where it was found that increasing OH concentration generally leads to increased electron concentration via increasing the rate of oxidation of CH_2 to CH ; this results in elevated values of the ion current in the post-flame region. In lean hydrocarbon flames, nearly all hydrocarbon molecules and radicals are consumed in the flame front and increased CH production is not possible; in these cases, no ion current is observed in the post-flame region.

The modelling results indicate that it is possible to predict the ion current developed in the experiment using a highly simplified mechanism. Whilst the predictions show significant inaccuracy, particularly at equivalence ratios greater than 1, the general

trends of the experimental ion current are well captured, including the post-flame peak at high equivalence ratios.

One significant limitation, however, of a CFD model such as this is the computational cost incurred, which is relatively high even for a simplified mechanism. The simulation of a combustion event 0.15–0.2 s long requires approximately 90 CPU hours. The main contributor to this expense is the computation of heat release and species concentrations; were a detailed mechanism to be used, the time taken for the simulation of this event would be unacceptably high.

Therefore, whilst the use of CFD may be appropriate for simple problems such as the one addressed in this chapter, it is unsuited to many problems of a more complex nature. CFD simulations have previously been used to model combustion in diesel engines successfully but, despite improvements in processing power and the development of more efficient CFD codes, the complexities of air entrainment, heat loss and chemical kinetics quickly render CFD models impractical for large numbers of simulations or for parametric studies even when simple reaction mechanisms are used to model combustion. Instead, for these types of studies, phenomenological diesel engine models have been widely used. Chapter 5 details the development and validation of such a model for the Hino engine described in Chapter 2.

Chapter 5

Phenomenological diesel engine model

5.1 Introduction

The use of a simplified mechanism for methane in simplified systems such as the perfectly stirred reactor and the constant volume chamber as detailed in Chapters 3 and 4 respectively enables the identification of the effects of changing system variables on the ion current and the mechanisms by which these effects are produced. Chapter 3 indicated that the electron concentration peaks early in the combustion event and strongly depends on temperature due to the production of the H-O radicals; Chapter 4 corroborated this observation by noting that electrons were present in the flame front where heat release is highest and CH radicals are present in appreciable quantities.

Flames in diesel engines are vastly more complex than the systems modelled thus far. They contain large and constantly changing gradients of equivalence ratio and temperature and are subject to phenomena such as evaporation and heat transfer. Thus, the effect of changing load, speed or any other engine operating parameter on the ion current is difficult to predict using simplified systems such as those presented in previous chapters.

In order to achieve this, an engine model must be developed. Historically, diesel engine modelling has followed either of two styles: CFD- and thermodynamic-based models. CFD-based models are computationally expensive but capable of providing detailed information on the flow-field in the cylinder. Whilst such information may be useful in predicting the ion current given its spatial dependence, it may not be required for studies more concerned with ion current trends, such as the study presented here. The thermodynamic style of modelling is therefore chosen for this study and a

thermodynamic model specially developed.

This chapter describes the sub-models used in the model developed for this study and presents validation of the model when used to predict in-cylinder pressure, NO_x emissions and the ion current developed in the Hino diesel engine described in Chapter 2.

5.2 Background and model formulation

Phenomenological models are based on the conceptualisation of each sub-process observed to occur during the process being modelled. The equations governing each sub-process are based partly on theory and partly on experimental results. This approach means that any sub-model obtained is particular to the experiment it was designed around and may not provide accurate results for a different experimental set-up. Hence, phenomenological models use empirical constants in most sub-models that must be optimised for each application. A relevant example of a phenomenological model is that for soot formation and oxidation developed by Tao et al. [163]. The phenomena thought to govern soot formation and oxidation such as inception, surface growth, surface oxidation and coagulation are each modelled using partially empirical equations.

Thermodynamic phenomenological models can be broadly divided into two categories: zero-dimensional single-zone models and quasi-dimensional multi-zone models. Zero-dimensional single-zone models (eg. [164–166]) assume the entire cylinder volume is uniform in temperature and composition at all times in the cycle. When calibrated and validated correctly, these models are capable of predicting bulk performance parameters, such as fuel consumption and cylinder temperature and pressure, with accuracy and at a very low computational cost. Due, however, to their inability to account for spatial variations in temperature and composition, emissions prove difficult to predict with reliability.

This issue can be resolved by the use of two or more zones in the cylinder, with different composition and temperature attributed to each zone. Initial studies (eg. [167–170]) used two zones, one for fuel (the burnt zone) and one for air (the unburnt zone). Air entrainment was realised by the transfer of mass from the unburnt zone to the burnt zone. The burnt zone therefore experienced a different time history of composition and temperature to the unburnt zone. Later multi-zone studies (eg. [75, 171–176]) extrapolated this concept and divided the fuel mass into several zones, generally

termed ‘packets’. Thus, each packet possessed its own time history of temperature and composition, enabling more detailed spatial information to be obtained. It must be noted that, while packets can be unambiguously defined in a temperature-equivalence ratio space, their spatial location can be found only through empirical means, eg. simple spray models [177, 178]. This limitation is generally not of concern since the most important parameters affecting performance and emissions predictions are the temperature and equivalence ratio in each packet. The multi-zone approach is taken in this study.

Figure 5.1 shows the various sub-models considered in this model and their interaction with each other. Outputs within the dotted line are calculated using the SENKIN routine from CHEMKIN using an n-heptane mechanism described below. The following sections describe the sub-models used.

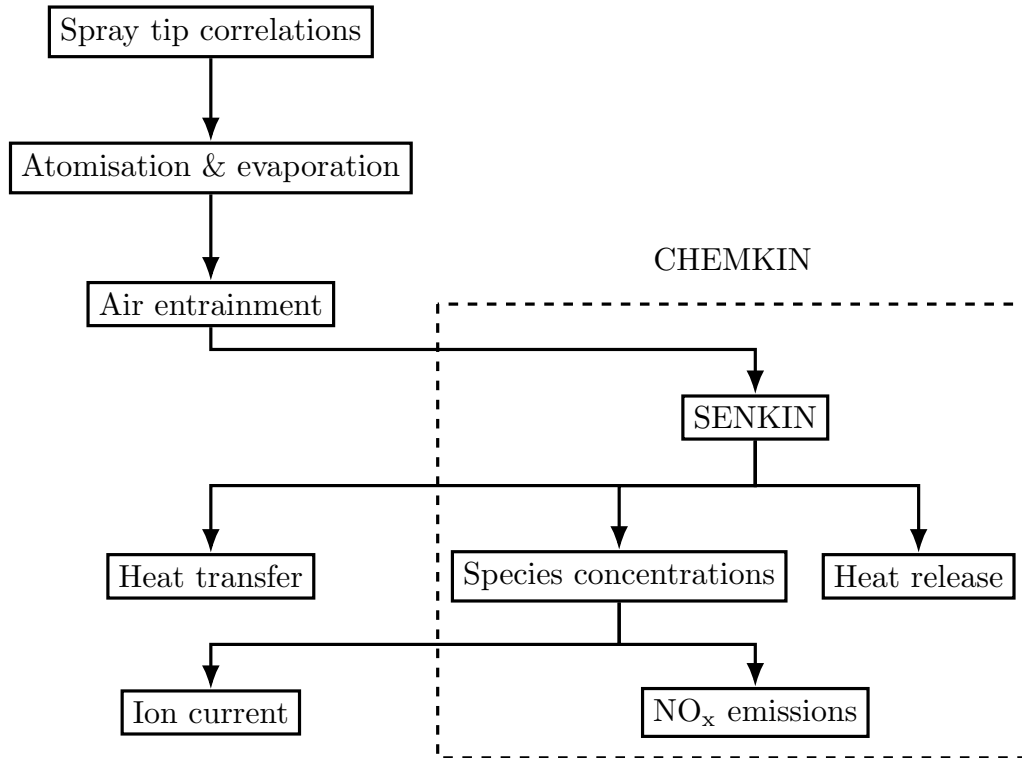


Figure 5.1: Schematic of the interaction of various sub-models. Some feedback processes have been ignored for simplicity.

5.2.1 Spray division and tip correlations

The spray is divided into axial and radial packets as depicted in Figure 5.2. The number of radial packets is chosen to be 9 in this study. The number of axial packets is fixed by the time step and the injection period; for every time step within the injection

period, one set of 9 radial packets is injected. The time step in this study is set to be 0.2 CAD. Sensitivity analyses of model predictions to the choice of time step and number of radial packets can be seen in Appendix E, along with those to several other assumptions made in the model.

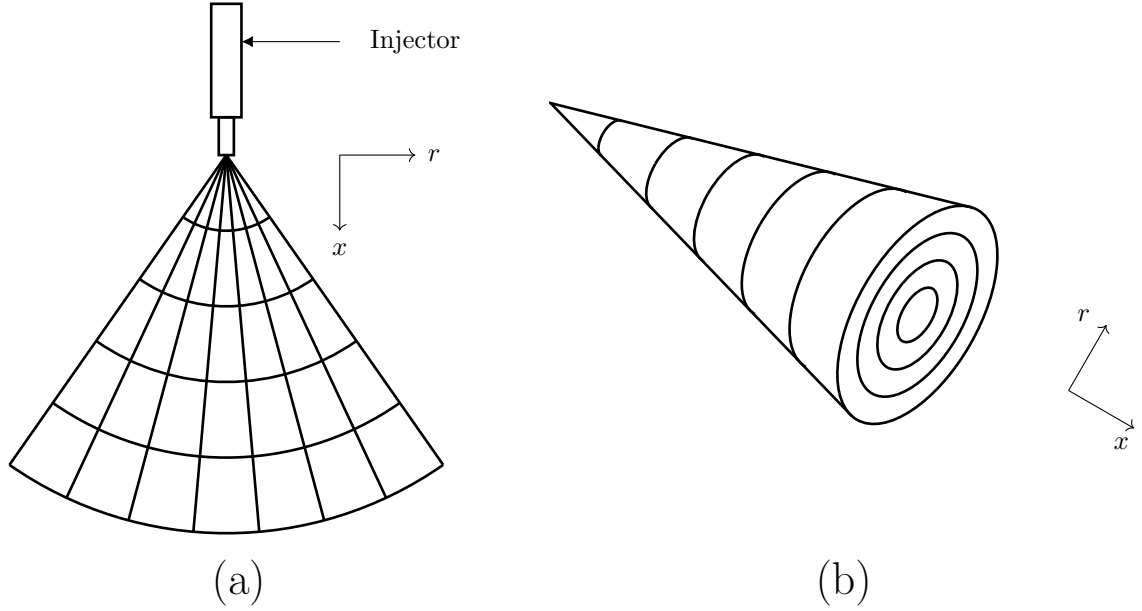


Figure 5.2: Schematic of spray division. (a) Cross-section and (b) 3-D.

The Hiroyasu spray correlations [178] (Equations 5.1, 5.2 and 5.3) with some modifications by Jung & Assanis [176] for modern injector nozzles are ubiquitous in phenomenological diesel engine modelling [175, 176, 178–180] and are used here.

$$S = \begin{cases} C_D \left(\frac{2\delta P}{\rho_f} \right)^{0.5} t & \text{if } 0 < t < t_b \\ 2.95 \left(\frac{\delta P}{\rho_a} \right)^{0.25} \sqrt{d_n t} & \text{if } t \geq t_b \end{cases} \quad (5.1)$$

where S is the spray centre-line penetration, C_D is the nozzle discharge coefficient, ρ_f is the fuel density, ρ_a is the air density and d_n is the nozzle hole diameter.

t_b is the break-up time and is obtained by setting the two possible values for S equal to each other, giving Equation 5.2:

$$t_b = 4.351 \frac{\rho_f d_n}{C_D^2 \sqrt{\rho_a \delta P}} \quad (5.2)$$

The radial variation in penetration is accounted for by the use of Equation 5.3 [178]. $i = 1$ refers to a packet on the spray centreline and $i = n_R$ to one at the spray edge.

$$S_i = S_0 \times e^{-8.557 \times 10^{-3} q^2} \quad (5.3)$$

where $q = 10i/n_R - 1$.

While these relations have been obtained from observation of isothermal sprays, they have been used to good effect in several phenomenological models listed above.

5.2.2 Atomisation & evaporation

The size of droplets after atomisation influences the rate of evaporation and therefore the combustion process. While several researchers [181–185] have studied size distributions of droplets formed by atomising diesel sprays, in a phenomenological engine model droplet size is important only for the determination of the evaporation rate. Some simple models for droplet evaporation use a linear relationship between droplet surface area and evaporation time [186]; others are more complex [171, 175, 185].

The utility of such a model for diesel fuel is debatable when used to predict heat release. Jung & Assanis [176] found the rate of evaporation to be significantly higher than that of combustion, and that evaporation was not a rate-limiting step. In a later model developed by the same authors [187], the fuel was assumed to be injected as a vapour and the evaporation sub-model was eliminated entirely with no effect on model performance. It is possible that evaporation will have a more substantial effect on the combustion process for other fuels or when soot emissions are predicted, so a constant evaporation rate model such as that used by Nguyen et al. [186] is used in this study (Equation 5.4). The initial droplet diameter is calculated in a similar manner as done by Kouremenos et al. [185].

$$\Delta d^2 = K_{evap} \Delta t \quad (5.4)$$

where Δd is the change in diameter of the fuel droplets. The choice of K_{evap} only affects the performance of the model when it is chosen to be very small. It is chosen to be 5.0 in this study. The evaporation rate of fuel, shown in Appendix E, is similar to that seen in previous modelling studies [3, 64].

5.2.3 Air entrainment

The entrainment of air into the fuel spray is modelled in a similar way to previous studies [1, 3, 176, 177, 188]. The decrease in momentum of any fuel packet is assumed to be due to momentum transfer to entrained air. Therefore, air entrainment in diesel engines should be a simple momentum conservation problem and the cumulative mass of entrained air from injection to any time t in a given fuel packet should be given by Equation 5.5.

$$m_a = m_f \left(\frac{u_0}{u_t} - 1 \right) \quad (5.5)$$

where m_a is the air mass entrained, m_f is the mass of fuel in the packet, u_0 is the velocity of the packet at the injector nozzle and u_t is the velocity of the packet at time t .

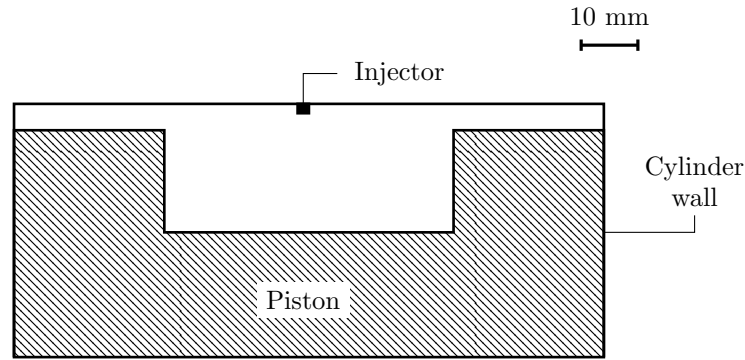


Figure 5.3: Relative locations of the piston crown and the injector at 167 CAD.

In reality, many researchers have found the conservation of momentum an inadequate source for air entrainment [1, 3, 189–192] and have used entrainment factors, empirical constants to enhance air entrainment. A similar approach is taken in the present study. Previous studies, however, have not taken into account the effect of impingement on air entrainment. The geometry of the piston crown of the particular engine modelled in this study (Figure 5.3) and its location relative to the injector shows that impingement on the piston must occur.

Bruneaux [193] suggests that for low injection pressures (below 150 MPa), air entrainment is lower for an impinging spray than for a free spray of diesel fuel from a single hole injector. Furthermore, given that the sprays from each of the five holes in the injectors used in the experiment must enter the bowl in the piston crown, the likelihood of spray-spray interaction increases greatly a short time after impingement. This decreases the likelihood of spray-air interaction and hence entrainment. Therefore, in this study two different entrainment factors are used — one before impingement and one after. At any time step i , the mass of air present in a packet is found from

Equation 5.6.

$$m_{a,i} = F_e(m_{a,i-1} + m_f) \frac{u_{i-1}}{u_i} - m_f \quad (5.6)$$

where F_e is the entrainment factor; $F_e = F_{e,1}$ before impingement and $F_{e,2}$ after. These values for different engine speeds are listed in Table 5.1, as determined from calibration against the experimental cylinder pressure curve. The calibration method is described in Section 5.2.8.

Table 5.1: Entrainment constants at different values of engine speed.

Engine speed	$F_{e,1}$	$F_{e,2}$
1200 RPM	1.7	1.0
1600 RPM	1.9	1.0
1800 RPM	2.0	1.1

5.2.4 Heat release and species concentrations

Heat release and major species concentrations in most phenomenological models is calculated by the use of empirical burning constants and the assumption of quasi-equilibrium. In order to predict the ion current, however, a chemical kinetic mechanism is required to compute the concentrations of the various species that affect the production of ions. It was therefore decided to use a reduced chemical reaction mechanism for a common diesel surrogate fuel to model heat release and species concentrations.

N-heptane is chosen as the surrogate fuel as it has been used by many previous studies with good results [194–199]. It is also one of the most widely studied heavy hydrocarbons and its combustion chemistry is therefore well understood [200–202]. Several mechanisms for n-heptane have been developed, of differing complexities [203–207]. The mechanism chosen for this study is one developed by Patel et al. [205] as it is highly simplified (containing just 52 reactions and 29 species) and has been validated in KIVA/CHEMKIN against experimental data from a diesel engine operating under HCCI-like conditions. It has also been used in the prediction of the ion current in a CFD-based diesel engine model [63].

The NO_x mechanism of Kong et al. [208] was appended to Patel’s mechanism to enable the prediction of NO_x . Kong et al. used XSENKPLOT to reduce the NO_x mechanism from GRI-Mech 3.0 [133] from 22 species and 101 reactions to four additional species and nine additional reactions. Importantly, the prompt NO_x mechanism was found to not contribute significantly to NO_x due to the lack of oxygen in the fuel.

The SENKIN routine in CHEMKIN was used to model ignition delay, heat release and species concentrations. Each time step is modelled at constant pressure both in SENKIN and in the heat loss sub-model, which is considered standard practice in these types of engine models [1, 3, 75, 176, 187].

5.2.5 Ion current

To evaluate the ion current, ten ionic reactions based on the ionic sub-mechanism developed in Chapter 3 were added to the n-heptane mechanism. Given the importance of NO_x in engine-related applications, and the determination by Estefanous [16] that, along with H_3O^+ , NO^+ is an important charge carrier in engines, ionic reactions for N^+ and NO^+ were added to the previously developed ionic sub-mechanism. The rates for these reactions were obtained from Hansen [209] and Albritton [210]. Thus, the charged species considered were electrons, O_2^- , HCO^+ , H_3O^+ , N^+ and NO^+ . The complete mechanism used can be found in Appendix F.

The ion sensor used in the experiment (Figure 2.2) is similar to the ion sensor used in Chapter 4 in that the area for neutralisation of negatively charged species is the surface area of the centre electrode. The area for neutralisation of positive ions is that of the sensor casing and the cylinder walls, which is several orders of magnitude higher than that of negative ions. The concentration of negatively charged species is therefore taken to be the limiting factor in the development of the ion current. As described in Section 3.5, the contribution of O_2^- ions to the ion current is negligible compared to that of electrons; only electrons are therefore considered in the ion current calculation. With these assumptions, the ion current is calculated as in Section 3.2.2.

The geometric factor F_G is simply determined as the ratio of cross-sectional area to length of the current path for simple cylindrical geometry [125]. However, in this case the geometry of the current path is complex due to the construction of the cylinder head. Figure 5.4 shows the ion sensor mounted in the cylinder head; the tip of the sensor which, presumably, has the greatest contact with the charged gas has no simple geometry similar to that of a cylindrical path. The proximity of the piston bowl to the sensor near TDC may also affect the geometric factor.

When a radial current path between the centre electrode and the cylinder head is assumed, which represents the grid region in Figure 5.4 (b), the geometric factor obtained is 12.7×10^{-3} . When a simple conical current path centred around the sensor tip is assumed, which represents the dotted region in Figure 5.4 (b), the geometric factor is estimated to be 3.7×10^{-3} . In addition to the complexity introduced by the

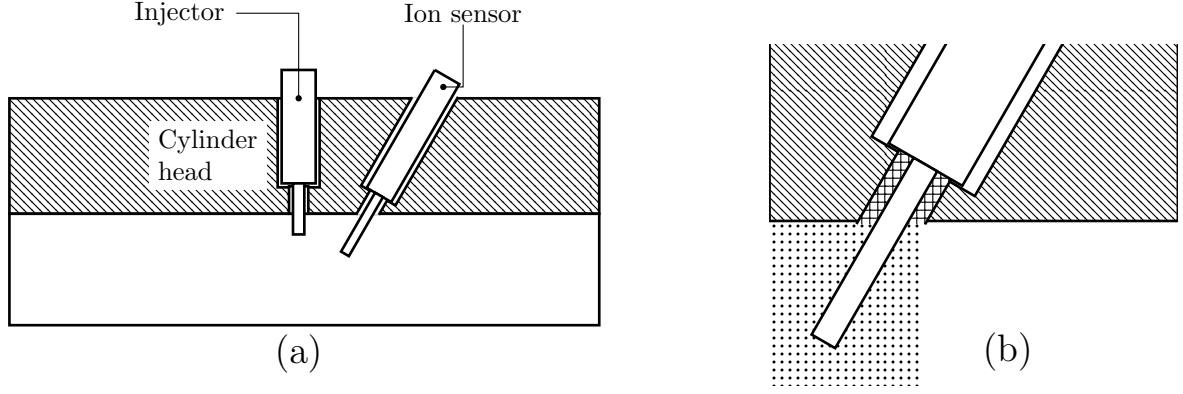


Figure 5.4: Geometry of the cylinder head with the ion sensor mounted. Relative location of the ion sensor to the injector (a) and magnified view of the interaction between the ion sensor and the cylinder head (b).

complex interface between the sensor and the cylinder head, not all of the electrons in the combustion chamber contribute to the ion current; some electrons are located far away from the sensor and are not neutralised on the centre electrode. Identifying the packets whose electrons contribute to the ion current involves several assumptions about spray, impingement and splash dynamics, and swirl and tumble in the charge air and is beyond the scope of this study. The geometric factor in this study was thus empirically calculated to minimise the error in ion current peak prediction $e_{I,p}$ (Equation 5.7).

$$e_{I,p} = \sqrt{\sum_{i=1}^N \frac{(I_{p,m} - I_{p,e})^2}{N}} \quad (5.7)$$

where N is the number of engine operating points tested, $I_{p,m}$ is the modelled ion current peak and $I_{p,e}$ is the experimental ion current peak.

Using this calibration process, F_G was found to be 2.9×10^{-3} , which is similar to that calculated above assuming a conical current path centred around the sensor tip. The ion current predicted is necessarily sensitive to the choice of F_G .

5.2.6 Heat transfer

Heat transfer in this model is based on the Woschni correlations for the in-cylinder convective heat transfer coefficient. The mean gas velocity v in the cylinder is given by Equation 5.8.

$$v = c_1 \bar{S}_p + c_2 \frac{V_d T_r}{P_r V_r} (P - P_m) \quad (5.8)$$

where c_1 and c_2 are defined in Equation 5.9, V_d is the displaced volume of the cylinder, P_r , T_r and V_r are a reference pressure, temperature and volume of the cylinder respectively, P is the instantaneous in-cylinder pressure and P_m is the motoring pressure assuming isentropic compression.

$$c_1, c_2 = \begin{cases} 2.28, 0 & \text{if } \theta \leq 180 \\ 2.28, 3.24 \times 10^{-3} & \text{otherwise} \end{cases} \quad (5.9)$$

With knowledge of the mean gas velocity, the instantaneous overall heat transfer coefficient h can be calculated via Equation 5.10.

$$h = 3.26 B^{-0.2} P^{0.8} T^{-0.55} v^{0.8} \quad (5.10)$$

where B is the cylinder bore.

The heat transfer from the cylinder contents to the walls is then given by Equation 5.11.

$$\dot{Q}_{out} = h A_w (T_{cyl,avg} - T_w) \quad (5.11)$$

where A_w is the exposed area of the interior of the cylinder, $T_{cyl,avg}$ is the average temperature of the mixture in the cylinder and T_w is the cylinder wall temperature, assumed to be 450 K in this study. This is consistent with previous modelling studies [1, 3, 5, 211].

The Woschni heat transfer model takes into account radiation from soot; this is therefore not explicitly modelled.

5.2.7 Iterative procedure

Phenomenological engine models that use empirical burning rates to model heat release generally use iterative methods to solve for the temperature of each fuel packet after combustion. The reason for this is the temperature rise of the fuel packet depends to a great extent on the specific heat capacity of the mixture in the packet. The specific heat capacity of the mixture is a function of its temperature, and depends on the temperature rise. The final temperature of the packet therefore cannot be deduced analytically but must be solved for iteratively.

In this model, this computation is performed by the SENKIN routine of CHEMKIN. There is, however, some iteration required to establish the in-cylinder pressure at the

beginning of a new step. Heat transfer is calculated at the end of the combustion process, leading to a decrease in temperature. Given that each step is modelled as a constant pressure process, this necessitates a decrease in the cylinder volume. The cylinder volume, however, is fixed by the engine geometry and the crank angle. Therefore, after heat transfer has been calculated and the temperature of the cylinder contents reduced, the sum of the volumes of the burnt (V_b) and unburnt zones (V_u) must equal the instantaneous cylinder volume (V) given by the crank angle. This follows the work of Rakopoulos et al. [188]. The volumes of the burnt and unburnt zones are given by Equations 5.12 and 5.13 respectively.

$$V_b = \sum_{i=1}^n \frac{m_i R_i T_i}{P} \quad (5.12)$$

$$V_u = \frac{m_{a,u} R_a T_u}{P} \quad (5.13)$$

where m , R and T refer to the mass of gaseous compounds, gas constant and temperature respectively and the subscripts i and u refer to a fuel packet and the unburnt zone respectively. The gas constant for each fuel packet is calculated for each iteration as it depends on the composition of the packet, which depends on the pressure at which the reactions occur. The specific heat for each packet is also calculated as it depends not only on the composition but also on the temperature of the packet. This is calculated using the polynomial coefficients from the NASA thermodynamic database [212] and from Burcat et al. [151].

The total cylinder volume is given by Equation 5.14.

$$V_t = \frac{1}{4} \left(\frac{V_d}{\epsilon - 1} + \frac{V_d}{2} (1 + r - \cos\theta - \sqrt{r^2 - \sin^2\theta}) \right) \quad (5.14)$$

where V_d is the displaced volume, ϵ is the compression ratio, r is the length of the connecting rod to the radius of the crank and θ is the crank angle. The value of r for the Hino engine modelled is 3.08.

The cylinder pressure based on the calculated burnt and unburnt zone volumes is then:

$$P_2 = P_1 \frac{V_b + V_u}{V_t} \quad (5.15)$$

If $|P_2 - P_1| > e$, further iteration is required for convergence. e is the maximum acceptable error, set to 0.1%. For further iterations, the new value of cylinder pressure,

$P_{1,new}$ is calculated from Equation 5.16.

$$P_{1,new} = P_1 + F_r(P_2 - P_1) \quad (5.16)$$

where F_r is a relaxation factor used to speed convergence. For the first seven iterations, F_r is set to 0.7, after which it is reduced to 0.3. In practice, three iterations were found to be sufficient for most cases.

5.2.8 Calibration and optimisation

Calibration of empirical constants is an important part of phenomenological engine modelling. The air entrainment constants described in Section 5.2.3 are optimised for a chosen output over a desired range of engine operating conditions. Some outputs that can be chosen against which to calibrate these models are in-cylinder pressure, heat release rate or NO_x emissions.

The optimisation approach taken in this study for the air entrainment constants is based on that taken in a previous study on the same engine [64] — the weighted root mean square difference between the experimental in-cylinder pressure and the predicted in-cylinder pressure is minimised. The weight at any time step i , w_i is given by Equation 5.17. w at 1600 RPM, 140 Nm is plotted in Figure 5.5 between 130 CAD and 240 CAD.

$$w_i = \frac{P_{exp,i}}{P_{exp,max}} + v \frac{\left(\frac{dP_{exp}}{d\theta}\right)_i}{\left(\frac{dP_{exp}}{d\theta}\right)_{max}} \quad (5.17)$$

Rao [64] reports negligible sensitivity to the value chosen for v and uses a value of 40; the same value is chosen here.

The root mean square difference, e_P , is then calculated via Equation 5.18.

$$e_P = \frac{1}{N_{dp}} \sqrt{\sum_{i=1}^N (P_{exp,i} - P_{mod,i})^2 w_i} \quad (5.18)$$

where N_{dp} is the number of data points (which depends on the time step) and $P_{exp,i}$ and $P_{mod,i}$ refer to the experimental and the modelled in-cylinder pressure at time step i respectively.

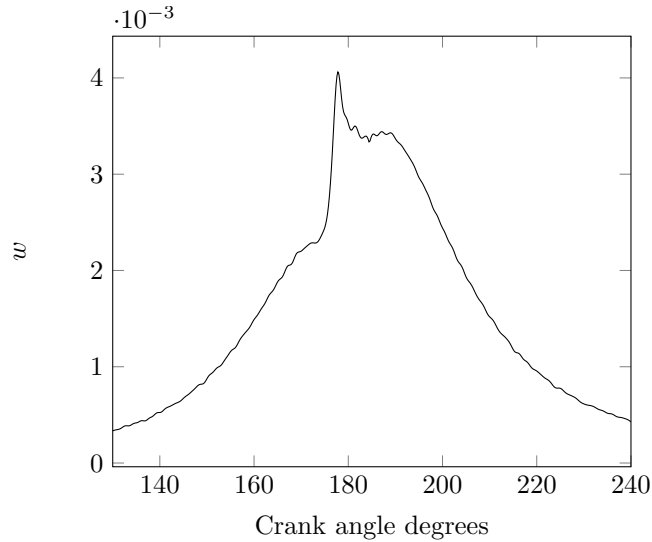


Figure 5.5: Weighting function used for optimisation at 1600 RPM, 140 Nm.

5.3 Model predictions

This section presents comparisons of experimental and modelled in-cylinder pressure, rate of heat release, ion current, NO_x emissions and heat transfer. Model predictions for engine operating points not shown here as well as those of various other phenomena such as spray penetration, air entrainment and fuel evaporation can be found in Appendix E.

5.3.1 In-cylinder pressure and rate of heat release

Figures 5.6, 5.7, 5.8 and 5.9 show the measured and modelled in-cylinder pressure and heat release at various values of engine speed and load.

At 1600 RPM and 1800 RPM, the in-cylinder pressure is predicted well at higher values of engine-out torque. At low torque values the peak is overpredicted and slightly delayed. At 1200 RPM, the cylinder pressure is modelled well at all values of torque. Error statistics of the peak pressure point are shown in Table 5.2.

At 1600 RPM the peak heat release rate (ie. in the premixed burn regime) is generally under-predicted by $\approx 15\%$. At higher values of engine load, the model shows a pronounced and clearly delineated diffusion burning phase; the experiment shows significant overlap between the premixed and diffusion burning regimes. This has been observed previously in another modelling study on the same engine [64]. In that study, the discrepancy was attributed to the use of the Hardenberg-Hase model for ignition

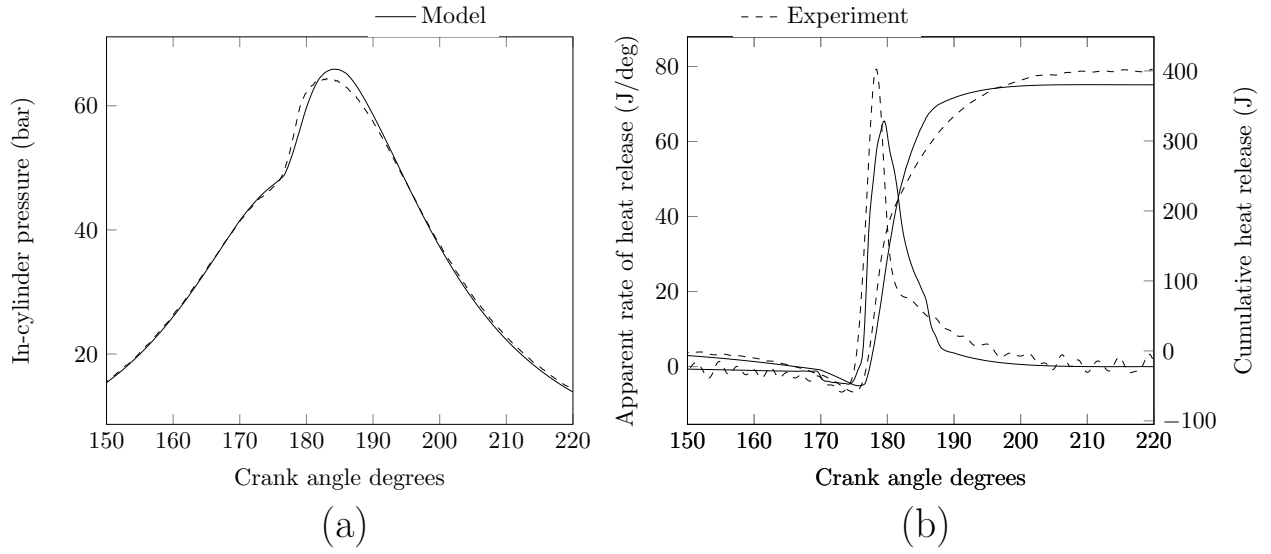


Figure 5.6: Experimental and modelled in-cylinder pressure (a) and heat release (b) at 1600 RPM, 80 Nm.

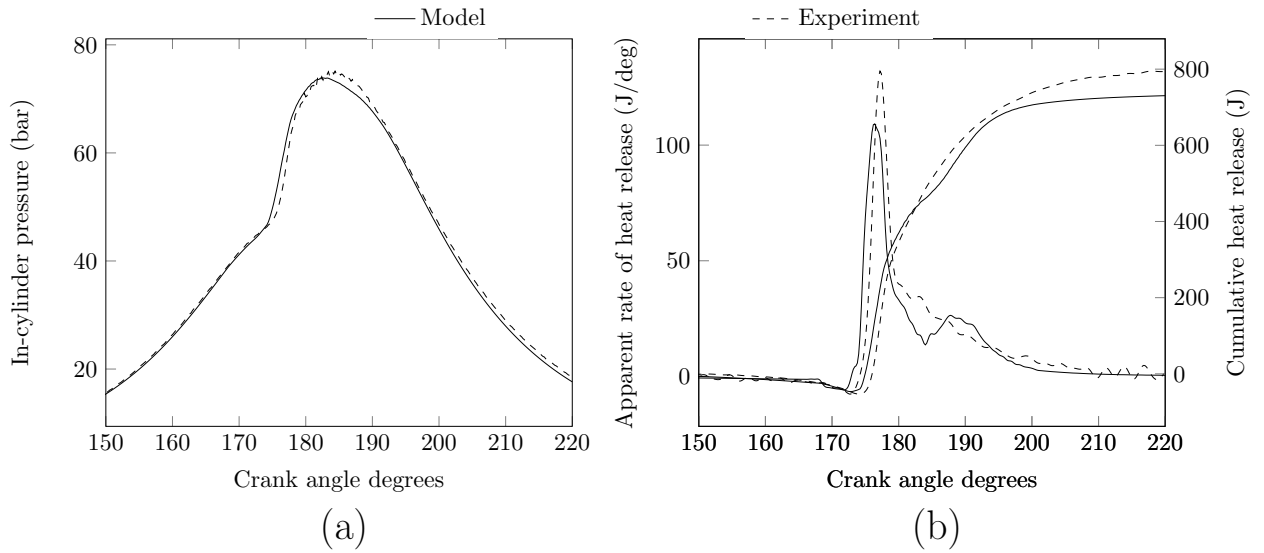


Figure 5.7: Experimental and modelled in-cylinder pressure (a) and heat release (b) at 1600 RPM, 180 Nm.

Table 5.2: In-cylinder pressure prediction error at different engine speeds

Speed (RPM)	Peak pressure position (CAD)	Peak pressure magnitude (%)
1200	0.66	1.09
1600	1.00	1.34
1800	1.20	1.48

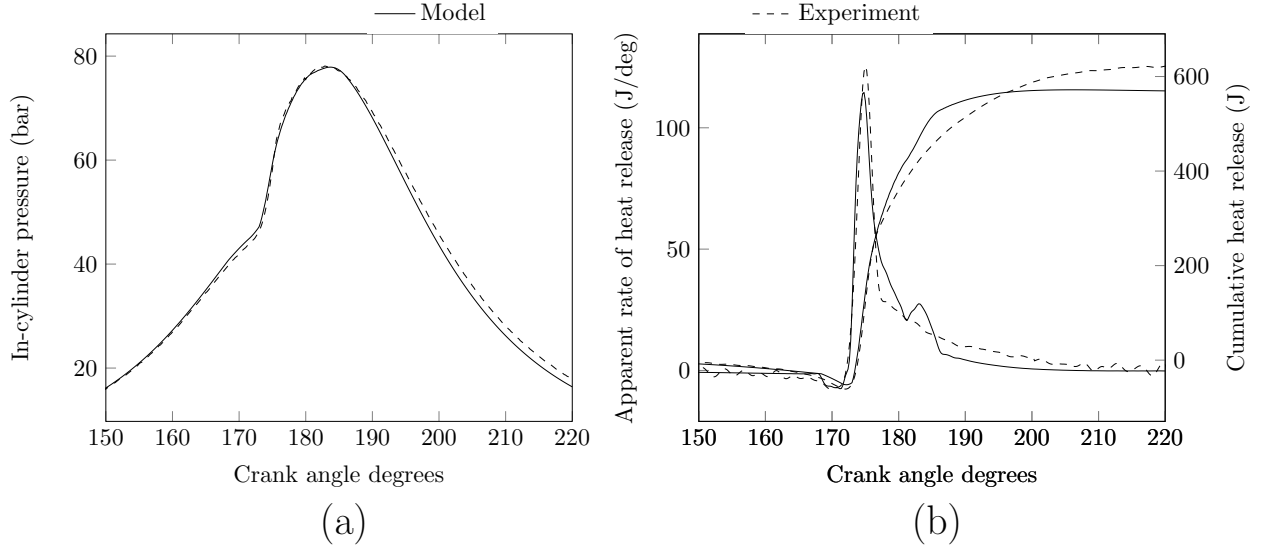


Figure 5.8: Experimental and modelled in-cylinder pressure (a) and heat release (b) at 1200 RPM, 140 Nm.

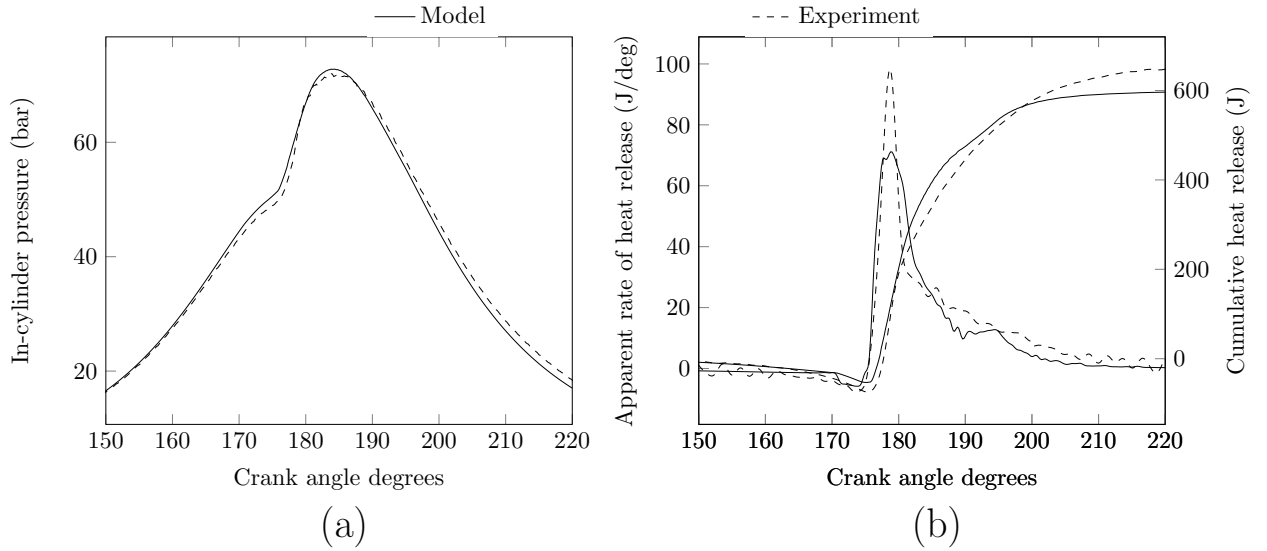


Figure 5.9: Experimental and modelled in-cylinder pressure (a) and heat release (b) at 1800 RPM, 140 Nm.

delay; as this study uses chemical kinetics to model ignition delay, non-realistic air entrainment is the likely cause. The heat release rate is well predicted at 1200 RPM but is under-predicted at 1800 RPM.

The final cumulative heat release is generally under-predicted to an error of $\approx 6\%$ at all speeds, indicating good agreement with the experiment. Some deviation from the experimental curve is seen, particularly in the region where the premixed and mixing-controlled regimes overlap in the experiment.

5.3.2 Heat transfer

Figure 5.10 shows the gross heat release, net heat release and heat transferred to the cylinder walls at 1600 RPM, 80 Nm (a) and 1600 RPM, 180 Nm (b). Heat transfer is 15.2% of the gross heat release at 80 Nm and 13.1% at 180 Nm. Heywood [74] notes the difficulty of measuring this quantity accurately and cites 16–35% as a typical range. Previous experimental studies on this engine approximated this value at 2200 RPM, 150 Nm to be 13% [213]. Previous modelling studies on this engine found heat loss at 1600 RPM to be 13.7% of the gross heat release at 100 Nm and 10.5% at 200 Nm [64].

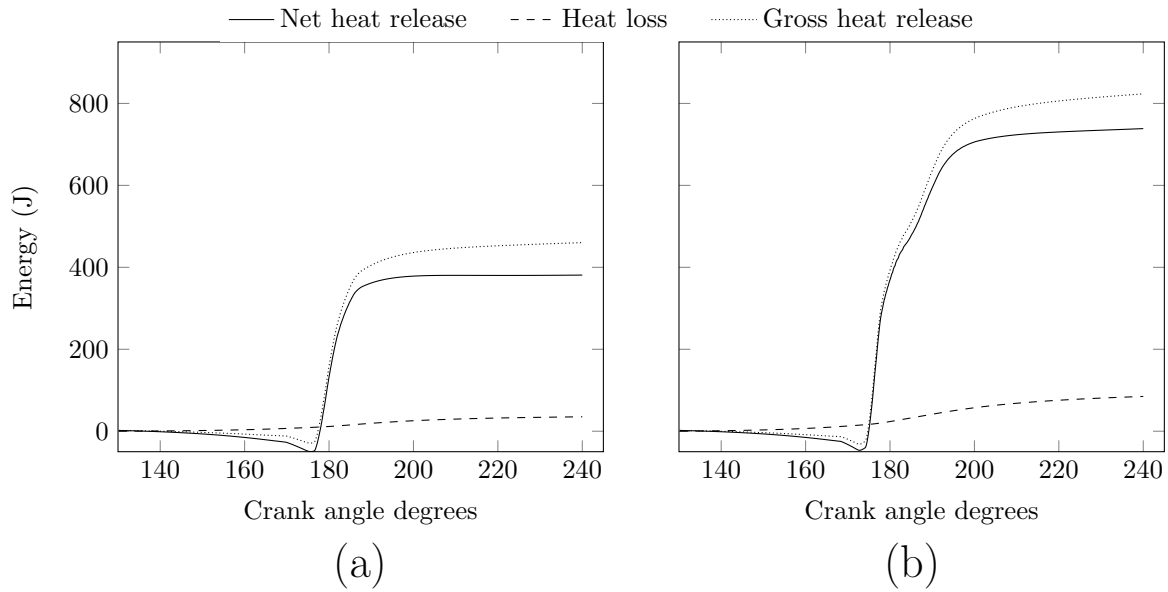


Figure 5.10: Modelled heat loss, net heat release and gross heat release at 1600 RPM, 80 Nm (a) and 1600 RPM, 180 Nm (b).

5.3.3 Ion current

Predictions of the ion current at 1600 RPM and three values of engine-out torque — 80 Nm, 140 Nm and 180 Nm — are shown in Figure 5.11. The cycle-minimum value of the ion current is subtracted from the experimental curves as soot formation, deposition and conductivity are not modelled here.

The width of the peak is under-predicted at high values of torque but this prediction improves at lower loads. However, the secondary peak seen at lower load settings is not predicted. As described in Chapter 2, these phenomena are likely caused by the propagation of material and the flame back out of the piston bowl, which is not modelled in this study. Furthermore, the model assumes that all five sprays begin

to combust in the vicinity of the ion sensor simultaneously. In reality, hole-to-hole variation in injectors causes combustion of the sprays to occur at different times and hence leads to a lower and broader ion current peak.

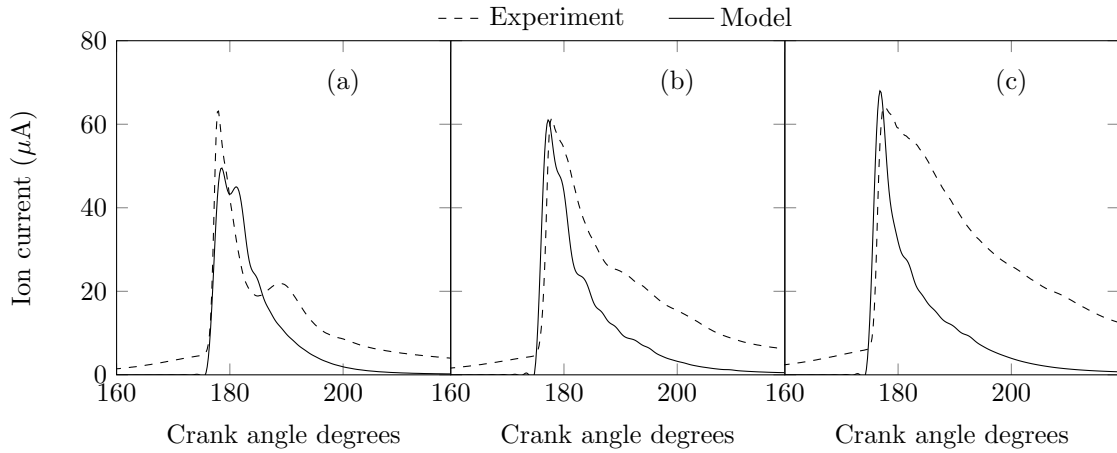


Figure 5.11: Experimental and modelled ion current at 1600 RPM, 80 Nm (a), 140 Nm (b) and 180 Nm (c).

The ion current peak magnitude is similar to that seen in the experiment at higher load values. At low values of load, the peak magnitude is under-predicted. The trend of increasing peak magnitude with increasing load is well captured.

Figure 5.12 shows the trends in ion current integral normalised by the maximum ion current integral for both modelled and experimental signals. Whilst the experimental integral clearly shows a greater variation over torque settings (the minimum normalised value for the experiment is 42% of the maximum while that for the model is 84%), the trend of increasing ion current integral is clearly replicated in the model.

Cylinder-average mole fractions of some neutral species important to ion formation are shown in Figure 5.13 at 1600 RPM and 140 Nm. Both O and OH are present in large quantities, with the OH concentration approximately 13 times greater than that of O, but following the same trend. These peak at the point where cylinder temperature is near its maximum (see Figure E.6) and then decay gradually.

The concentration of CH, however, shows a peak around 175 CAD, where SOC occurs. After the conclusion of the pre-mixed burning phase, CH can still be found in small quantities during the mixing-controlled phase. These concentrations are approximately 5–6 orders of magnitude lower than those of O and OH.

The overlap between the concentrations of O and CH show the region where electron production is possible and an ion current may be observed. This overlap can be seen to occur very close to the start of combustion, indicating the reason why the ion current

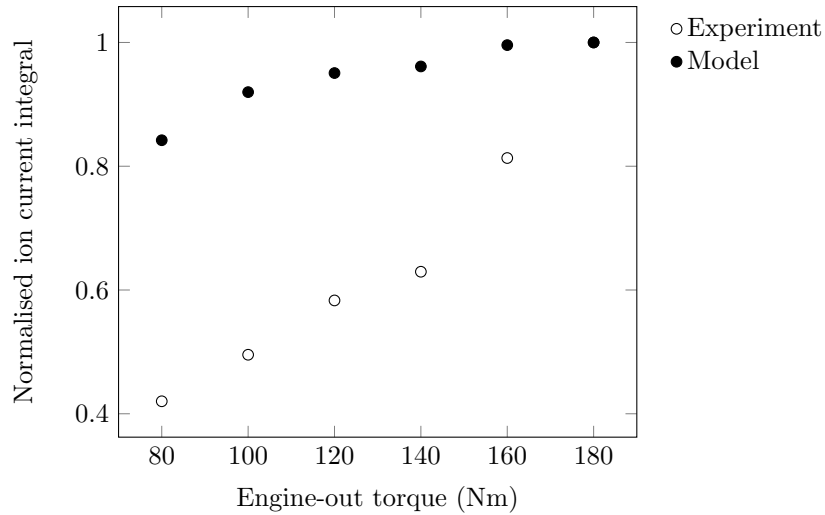


Figure 5.12: Trend in normalised ion current integral with changing engine-out torque at 1600 RPM.

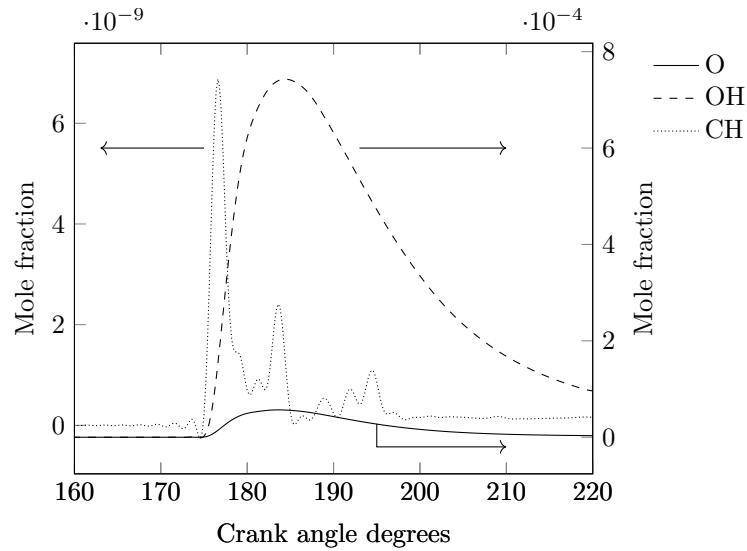


Figure 5.13: Cylinder-average mole fractions of O, OH and CH at 1600 RPM and 140 Nm.

may be used to detect SOC.

Figure 5.14 shows the cylinder-average mole fractions of the most important charged species — electrons, H_3O^+ and NO^+ . Electrons and H_3O^+ show very nearly the same concentration over the entire combustion event. As would be assumed from the ion current curve, both show a large increase around 175 CAD, when the CH mole fraction shows a sharp increase. These then decay gradually but from 178–195 CAD there is significantly less H_3O^+ than electrons due to the formation of NO^+ .

The peak NO^+ concentration is approximately one order of magnitude lower than that of electrons or H_3O^+ . NO^+ increases in concentration later than do the other charged

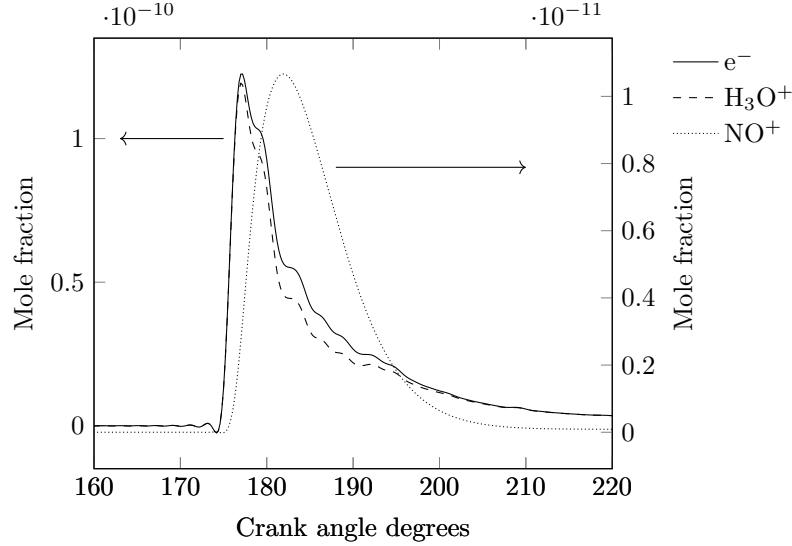


Figure 5.14: Cylinder-average mole fractions of electrons, H_3O^+ and NO^+ at 1600 RPM and 140 Nm.

species and its climb is more gradual, indicative of the slowness of NO_x reactions. After the peak temperature is reached, its concentration gradually decreases to virtually zero.

5.3.4 NO_x emissions

Figure 5.15 shows the experimental and modelled tailpipe NO_x over a range of engine-out torque values at 1200 RPM (a), 1600 RPM (b) and 1800 RPM (c). NO_x is generally overpredicted, with average errors of $\approx 20\%$ at 1600 RPM and 1800 RPM and a significantly higher error of 40% at 1200 RPM. These values compare favourably to the prediction accuracy of the extended Zeldovich mechanism commonly used in phenomenological models [64]. The trend of increasing NO_x with an increase in load mirrors that seen in the experiment.

NO_x emissions presented in this section are those predicted by the model at 240 CAD. By 220 CAD, the temperature of the burnt zone is 1500–1600 K; at 240 CAD, 1200–1300 K. NO_x reactions are well known to “freeze” at temperatures below approximately 2000 K [214]. It is therefore assumed that the NO_x concentration found in the cylinder at this time remains constant through the exhaust to the tailpipe exit where the experimental measurements are made. Figure 5.16 shows the evolution of NO_x in the cylinder at 1600 RPM and 80 Nm, 140 Nm and 180 Nm; NO_x production begins shortly after SOC and continues till approximately 210 CAD. After this time, there is little change in NO_x concentration in the cylinder, indicating the freezing of

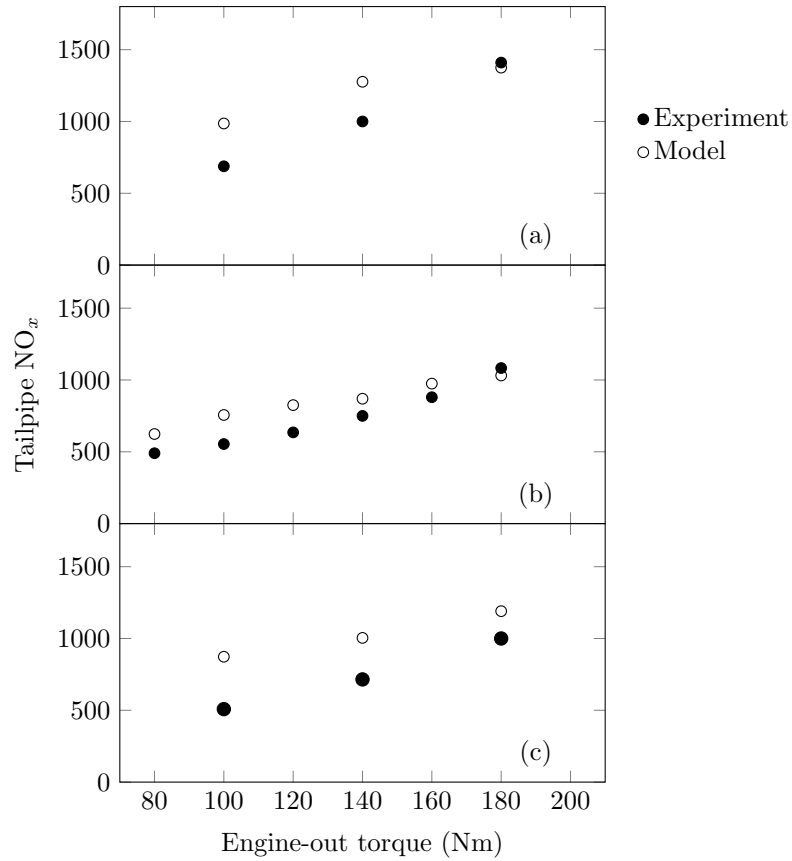


Figure 5.15: Experimental and modelled tailpipe NO_x at 1200 RPM (a), 1600 RPM (b) and 1800 RPM (c).

NO_x reactions as temperature reduces while expansion occurs. This is consistent with other studies using the extended Zeldovich mechanism for NO_x [1, 64].

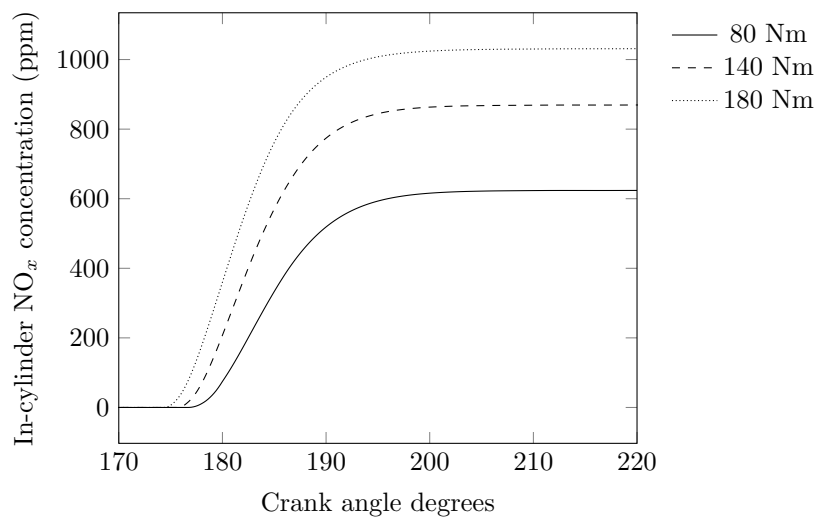


Figure 5.16: Predicted evolution of in-cylinder NO_x at 1600 RPM and 80 Nm, 140 Nm and 180 Nm.

A comparison of the evolution of NO^+ mole fraction and the rate of NO_x production is shown in Figure 5.17. Bold lines refer to NO^+ mole fraction whilst thin lines refer to the rate of NO_x production. There is significant similarity between the two curves at all values of load, indicating that NO^+ is present when NO_x formation is occurring. There is also a consistent trend of increasing peak NO^+ concentration with an increase in steady-state NO_x concentration as load is increased. Possible reasons for these observations are explored in Chapter 6.

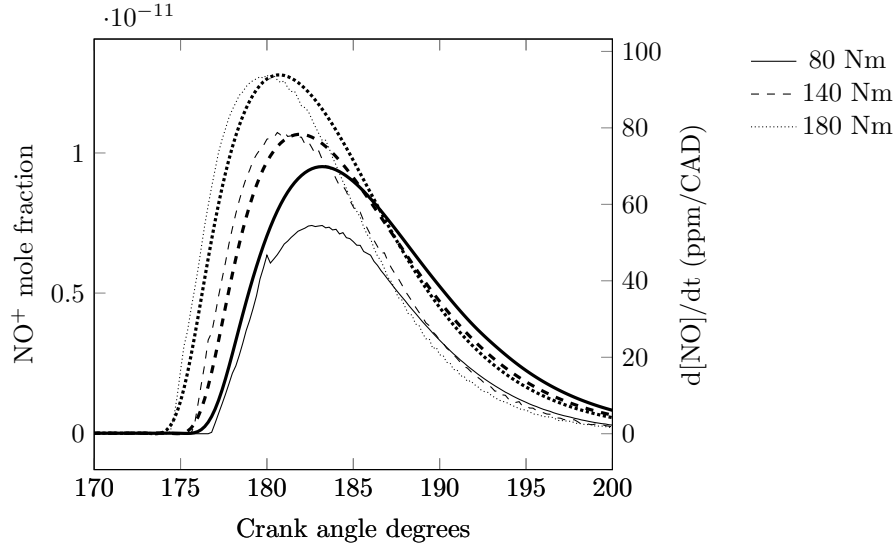


Figure 5.17: Predicted evolution of in-cylinder NO^+ (bold lines) and rate of NO_x production (thin lines) at 1600 RPM and 80 Nm, 140 Nm and 180 Nm.

5.4 Summary

The constant-volume chamber used to measure and model the ion current developed in a laminar flame is a useful tool for a preliminary study on ion formation in diesel engines but the mechanisms by which changes in engine operating parameters affect the ion current cannot be modelled in a simple system such as that presented in Chapter 4. In order to do so, a model must be developed that more closely represents the operation of a diesel engine. This chapter presented the development and validation of such a model.

The model developed was chosen to be phenomenological rather than CFD-based for reasons of computational expense. Well-established relations were used for the sub-models affecting the spray, air entrainment and heat transfer. CHEMKIN was used to model heat release and species concentrations with an n-heptane mechanism that has previously been used in HCCI and diesel engine models. These concentrations were

then used to calculate the ion current using collision theory in a manner introduced in Chapter 3.

The predicted in-cylinder pressure and heat transfer were found to compare well to those seen in the experiment and in previous modelling studies on the same engine. The peak rate of heat release was generally under-predicted by 15% at 1600 RPM and cumulative heat release was within 6% of value calculated from experimental data.

The ion current peak magnitude is predicted fairly well at high values of torque but is under-predicted at low values. The timing of the first ion current peak is predicted accurately. The second peak at low load and increased peak width at high load were not seen in the model, as expected from the modelling style chosen. Trends for the ion current time integral followed those seen in the experiment.

An examination of the concentrations of CH and O, the species involved in ion formation, showed that the only time when appreciable amounts of these species can be found is in the pre-mixed combustion phase between SOC and approximately TDC. This corresponds to the region where electrons and H_3O^+ are formed, giving rise to the ion current. The dominant positive ion seen was H_3O^+ , with NO^+ concentrations peaking at one order of magnitude lower. The importance of H_3O^+ seen here is consistent with previous studies and with that found in the constant-volume chamber in Chapter 4.

NO_x emissions were generally over-predicted; average errors of approximately 20% were seen at 1600 RPM and 1800 RPM; this was 40% at 1200 RPM. Trends in tailpipe NO_x were well captured. NO_x formation is predicted to begin after SOC and NO_x reaches a steady-state concentration at approximately 210 CAD. NO^+ appears to be strongly linked to the NO_x formation rate both in magnitude and in timing, a phenomenon that is investigated in the next chapter.

The accurate representation of trends in the ion current seen here and in Chapter 4 suggest that the ion generation mechanism is modelled well. This mechanism may then be useful in deeper interrogation of the relationships between the ion current and important engine operating parameters. The next chapter uses the n-heptane mechanism detailed above in several combustion systems including the engine model developed here to describe two such relationships.

Chapter 6

Heat release, NO_x and the ion current

6.1 Introduction

Chapter 2 described correlations between the ion current signal and several engine operating parameters of interest in engine design and monitoring but also noted the lack of adequate explanations for the existence of these correlations. In subsequent chapters, an ion generation mechanism was developed and confidence in it gained through its application to several different types of high temperature, high pressure combustion systems with the ultimate aim of using it to correct this gap in knowledge.

The preceding chapter has established the ability of a reduced diesel surrogate mechanism to predict heat release, NO_x emissions and the ion current from a diesel engine when integrated into a phenomenological model. This chapter uses the same mechanism in three different models — a perfectly stirred reactor, a pre-mixed flame undergoing auto-ignition and the diesel engine model described in the preceding chapter — to investigate the link between the ion current and these parameters and identify species and reactions important to both. The identification of common mechanisms affecting these quantities will allow more robust and generalised use of the ion sensor.

Presented in this chapter are results from a single value of equivalence ratio, initial temperature and initial or operating pressure; the conclusions made from this chapter remain unchanged over a range of operating conditions similar to those occurring in diesel engines.

6.2 Heat release

6.2.1 Introduction

An important parameter in evaluating engine performance and combustion quality is heat release. This is also a quantity that appears to be closely linked to the ion current, as evidenced by the production of the ion current in regions of high heat release, seen in Chapter 4, and by the temperature dependence of the ion current, seen in Chapter 3. It would therefore seem that a causal link between the heat release and the ion current may exist.

6.2.2 Perfectly stirred reactor

The n-heptane mechanism used in the engine model described in Chapter 5 was used with the PSR code from CHEMKIN to examine the evolution of both temperature, as a direct consequence of heat release, and electron concentration in a perfectly stirred reactor. An equivalence ratio of 0.4 was used, which is similar to that measured in the Hino engine at 140 Nm. The inlet temperature was chosen to be 1450 K, to give an outlet temperature of 2325 K, similar to the peak temperatures seen in diesel engines. The reactor operating pressure was chosen to be 70 bar, slightly below the peak pressure seen in the engine. The evolution of these two variables as the reaction progresses towards completion is shown in Figure 6.1.

The temperature and electron concentration can be seen to sharply increase at 1.9×10^{-6} s. The electron concentration decreases shortly after, while the temperature gradually climbs to its maximum of 2325 K. This indicates that electrons are found predominately in the flame front, an observation also made in Chapter 4 (see Figures 4.10 and 4.14) during the constant-volume combustion of methane.

Using KINALC [215], a sensitivity analysis of important reactions and species affecting these two variables was conducted at the point where the net production rate of electrons and rate of increase of temperature are the highest, 1.9×10^{-6} s. A sensitivity analysis with respect to reaction rates is achieved in KINALC by determining the change in concentration of a given species, or parameter such as temperature, for a very small change in the rate of each reaction. Figure 6.2 shows the reactions whose rates have the greatest effect on mixture temperature at this time.

The oxidation of CO to CO₂ is responsible for a large fraction of the heat released in

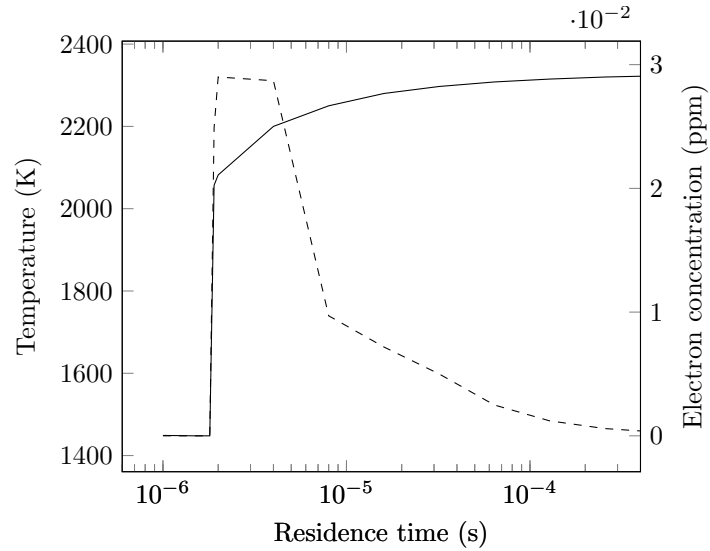


Figure 6.1: Evolution of temperature and electron concentration in a perfectly-stirred reactor model with inlet temperature 1450 K, equivalence ratio 0.4 and reactor operating pressure 70 bar.

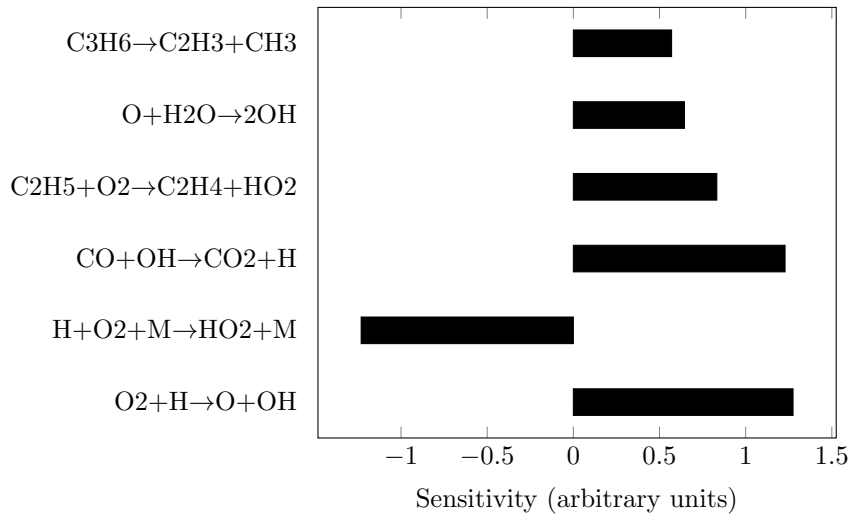


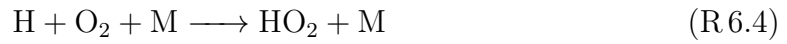
Figure 6.2: Important reactions affecting temperature at 1.9×10^{-6} s.

hydrocarbon combustion [216]; 66.1% of CO₂ formation at this time is due to Reaction R 6.1.

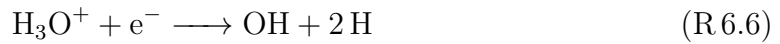


At this time, 64.4% of the OH required for the oxidation of CO to CO₂ is produced by Reactions R 6.2 (46.7%) and R 6.3 (17.7%). The concentrations of the primary radicals of the H-O system in hydrocarbon flames — H, OH and O — are known to increase with increasing temperature [217] and are linked by the well known chain branching reactions. The progress of Reaction R 6.4 retards that of Reaction R 6.3 via

competition for H radicals and O₂ molecules and so reduces the mixture temperature, leading to negative sensitivity of temperature to this reaction.



Reactions R 6.5–R 6.7 are the primary reactions affecting electron formation and consumption at this time. 100% of electron formation occurs via Reaction R 6.5, whilst Reactions R 6.6 and R 6.7 account for 77.1% and 22.4% of electron consumption respectively. The only region where CH and O radicals are both present in high concentrations is in the flame front, limiting electron formation to this region. Clearly, any increase in the concentration of the OH or H radicals retards the consumption of electrons.



This suggests that there may be some similarity between the reactions affecting both heat release and electron concentration due to their mutual dependence on the radicals in the H-O system. The reactions whose rates have the greatest effect on electron mole fraction are shown in Figure 6.3. The similarity between these reactions and those shown in Figure 6.2 is remarkable; five out of six reactions are common to both figures and their sensitivities have the same sign.

Sensitivity analysis with respect to species concentrations is performed in KINALC by determining the change in concentration of a given species to a small perturbation in concentration of each species in the mechanism. The species whose concentrations were found to affect those of CH and O to the greatest degree, and therefore to most significantly affect electron production at this stage in the reaction are H, H₂O, OH, CH₂ and O₂. The effects of the first three species are expected; due to H-O system kinetics, the concentrations of species O, H, OH and H₂O are closely linked. Increased dissociation of H₂O results in greater concentrations of the three radicals. As seen in the engine model in Section 5.3, the concentrations of OH and O show identically-shaped profiles.

The oxidation of CH₂ by H radicals (Reaction R 6.8) is responsible for nearly all the

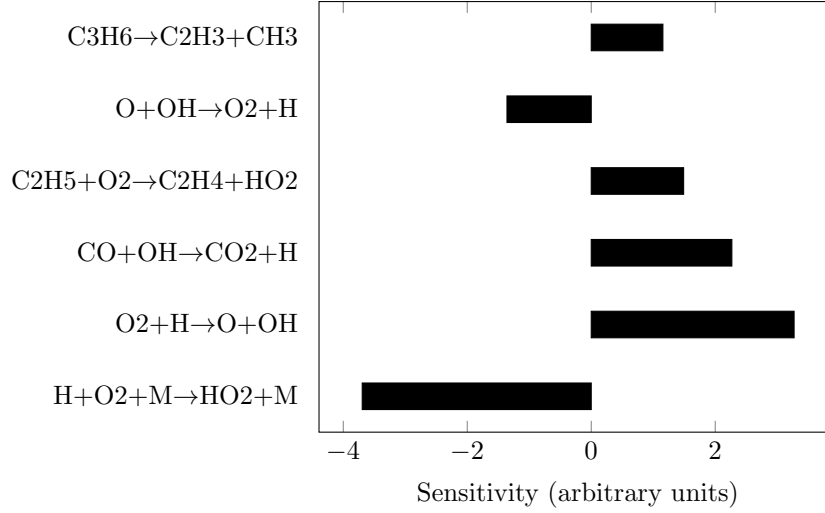


Figure 6.3: Important reactions affecting electron mole fraction at 1.9×10^{-6} s.

production of CH and the reaction between CH and H₂O (Reaction R.6.9) nearly all the consumption. Therefore, any shift in the H-O system equilibrium towards dissociation of H₂O — and therefore increased OH and H production — results in a shift in the CH₂-CH equilibrium towards CH.



Increased production of OH therefore favours increased electron production through increasing the concentrations of both CH and O. It also retards electron neutralisation with H₃O⁺. This radical is therefore important to both heat release and electron concentration and is proposed to be the reason for the correlation presented previously. Previous studies have used CH and OH as indicators of heat release [218–221] — since electron concentration depends to a great degree on these radicals, it could conceivably also be used in a similar manner.

6.2.3 Premixed auto-igniting flames

This relationship is explored further in premixed flames undergoing auto-ignition. The SENKIN routine of CHEMKIN was used with the same n-heptane mechanism in a chamber of varying volume, calculated as a function of time in order to simulate the changing cylinder volume of the Hino engine described previously when operated at 1600 RPM. Simulation was begun at 5 CAD BTDC at a pressure of 70 bar and

continued for 0.003 s, corresponding to a 28.8 CAD simulation duration. The maximum temperature observed was 2364.7 K, similar to the peak temperatures seen in diesel engines. The equivalence ratio chosen was 0.4, identical to that chosen in the PSR model. Figure 6.4 shows the rate of heat release (normalised by the maximum rate of heat release) and the evolution of electrons, CH and OH during this combustion event.

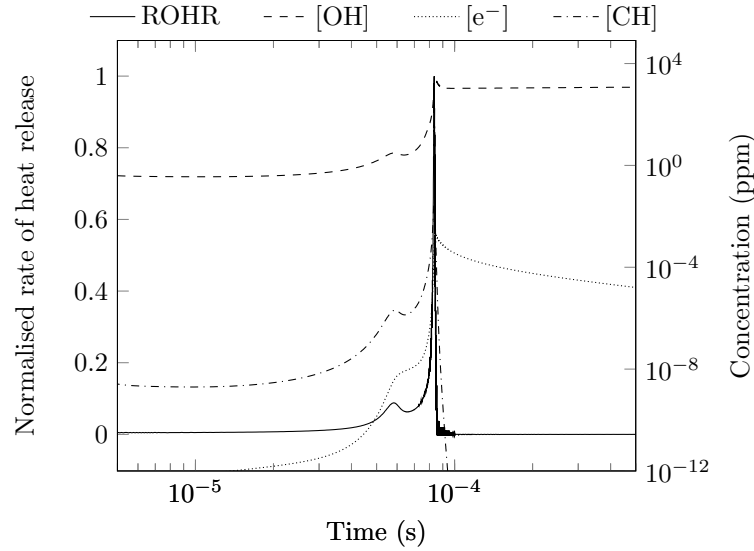


Figure 6.4: Rate of heat release and concentrations of CH, OH and electrons for a pre-mixed auto-igniting n-heptane flame in air

Clearly, in the initial stages of the combustion event where CH is abundant, electron concentration follows the same trends as OH concentration. The peaks in both concentrations occur at the same time as the peak heat release rate. After the maximum heat release rate is reached, the concentration of CH drops sharply, while that of OH declines very gradually. The concentration of electrons reduces at a moderate rate.

These results are consistent with the known dependence of electrons on both oxidiser and fuel concentrations. When there is a sufficient amount of fuel, as before the peak rate of heat release, electron concentration follows the same trends as OH concentration due to the relationship shared by OH and O radicals. During heat release, CH is consumed, and after, there is an insufficient amount of CH in the mixture and electron neutralisation dominates.

Given that electron concentration is linked to OH concentration for reasons discussed in Section 6.2.2 and demonstrated here, and that OH is an important species for heat release, electron concentration and therefore the ion current would appear to be valid indicators for the heat release process.

6.2.4 Flames in diesel engines

The flames presented in the above two sections represent highly simplified versions of flames in a diesel engine — they do not consider the influence of changing chemistry as more air is entrained into the spray, temperature and composition gradients or heat loss to the cylinder walls. Furthermore, the effects of changing engine load on chemistry of the mixture are complex and difficult to model in simplified models such as those presented above. The phenomenological engine model developed in Chapter 5 is therefore used for further investigation into the use of the ion current as an indicator of the heat release process.

The heat release and ion current for randomly selected packets in the spray participating in both pre-mixed and mixing-controlled combustion are shown in Figure 6.5 for engine operating conditions of 1600 RPM and 140 Nm. Electron formation occurs at approximately the same time as the heat release peak for both packets, which is consistent with findings in Sections 6.2.2 and 6.2.3. The lower rate of heat release in the packet participating in mixing-controlled combustion is reflected in the lower electron peak concentration.

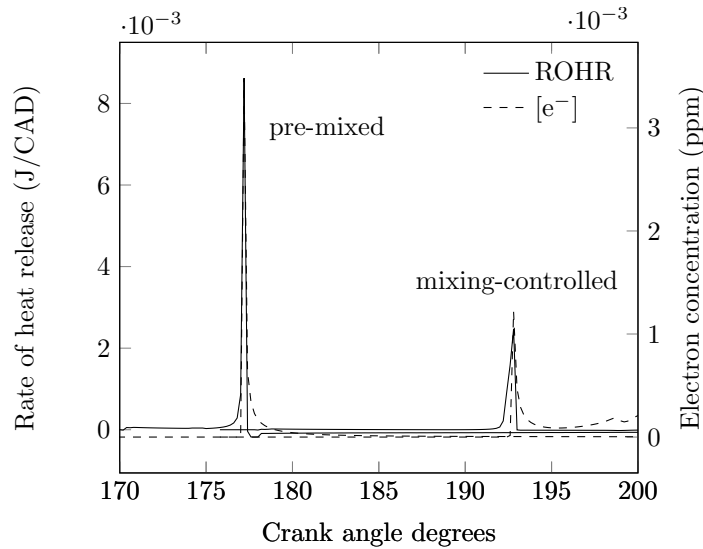


Figure 6.5: Rate of heat release and concentration of electrons in two randomly selected packets in the spray at 1600 RPM and 140 Nm. One packet participates in pre-mixed combustion, the other in mixing-controlled.

The evolutions of temperature and concentrations of OH, O, CH and electrons in the entire diesel spray at 1600 RPM, 120 Nm are presented in Figure 6.6. Pre-mixed combustion begins shortly after 175 CAD where slightly fuel-rich packets first begin to burn. These packets are located on the spray edge where air entrainment is maximum. As the temperature in the chamber rises, combustion spreads to additional fuel-rich

packets. Entrainment of air as the spray decelerates leads to reducing equivalence ratios of the packets as the combustion event proceeds. The highest temperatures are seen in the packets that initiate pre-mixed combustion. At this value of torque, no clear mixing-controlled regime of combustion can be observed.

The OH radical concentration increases simultaneously with the temperature at SOC and remains high in the hot, moderately lean areas of the spray for some time after. The contours of OH concentration can be seen to follow the flame front closely. There are also small concentrations of the OH radical in fuel-rich areas of the flame. The O radical is generally found in the same areas as the OH radical with the exception of fuel-rich areas of the flame front where very little O is seen.

CH is seen in high concentrations in the flame front, both at SOC and later, up to approximately 7 CAD ATDC. It can also be found in moderate concentrations in the fuel-rich area of the post-flame region. It is completely absent in lean areas of the flame, where it would be expected to be completely oxidised. The location of CH seen here is consistent with its use as a marker of the flame front.

Electrons are produced in their highest concentrations at SOC and remain abundant for a very short time after. Thereafter, they are found in diminishing concentration in the hot post-flame region at equivalence ratios near 1, where their decay is slow.

Figure 6.7 shows the variation in modelled ion current integral with modelled cumulative heat release as engine-out torque is varied. The correlation coefficient is 0.94. The modelled ion current integral is also correlated to the modelled peak rate of heat release ($r^2 = 0.90$) but this is not shown here.

These strong correlations are similar to those seen in the experiment ($r^2 = 0.95$ for both cumulative heat release and peak rate of heat release) and indicate that the ion current is a valid indicator of heat release in engines.

6.3 NO_x emissions

6.3.1 Introduction

Mono-nitrogen oxides (NO_x) have, together with diesel particulate matter (DPM), been the main focus of evolving emissions standards the world over. European emissions standard Euro 3 was the first to limit NO_x emissions in diesel-powered passenger vehicles, allowing 0.5 g km⁻¹ in 2000. By 2014, Euro 6 allowed only 0.08 g km⁻¹ — a

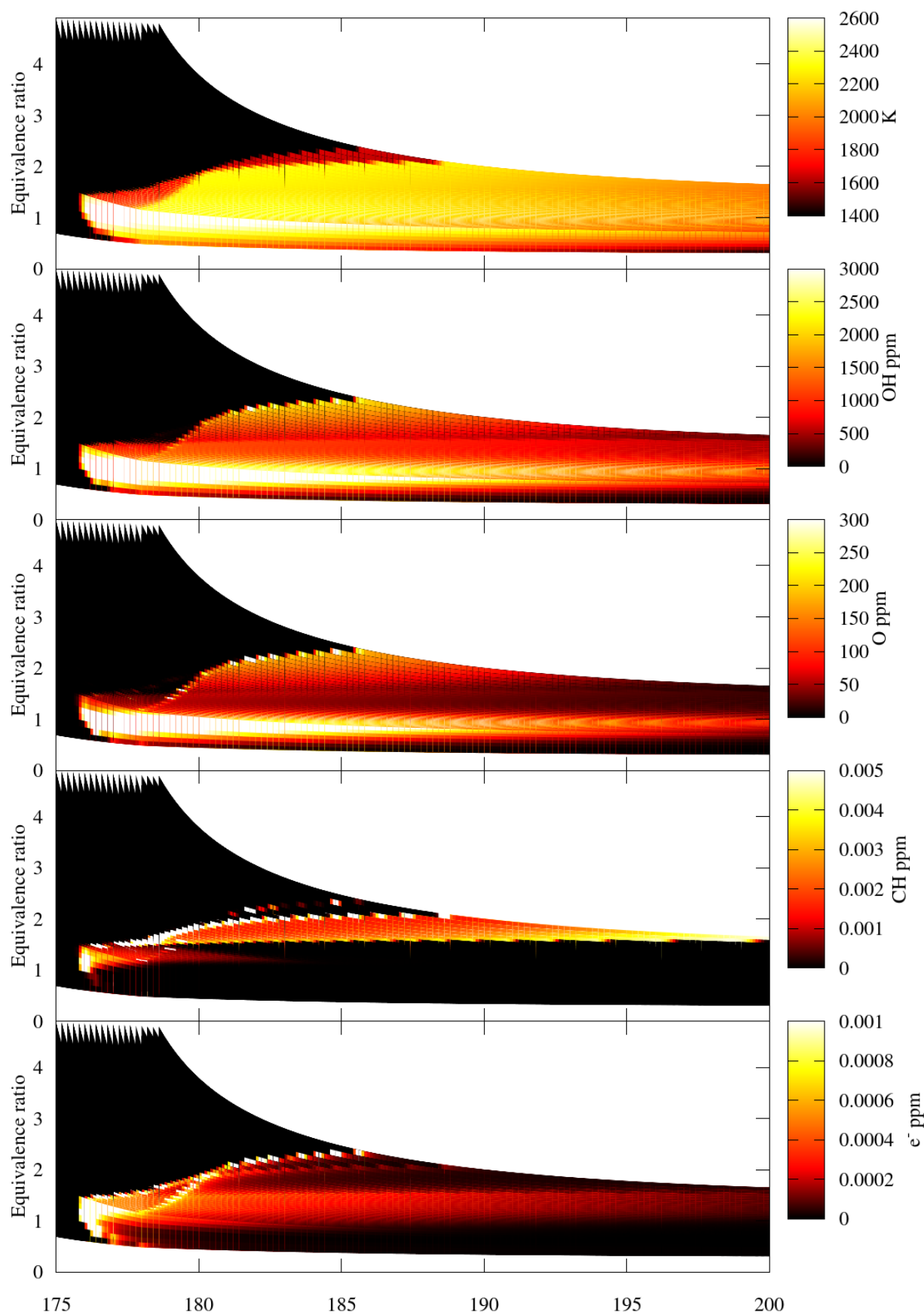


Figure 6.6: Evolution of temperature and OH, O, CH and electron concentrations in the diesel spray at 1600 RPM and 120 Nm

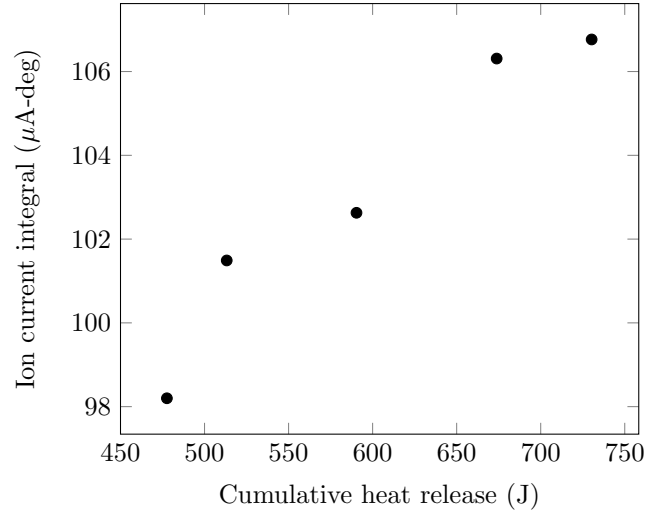


Figure 6.7: Modelled ion current integral and modelled net cumulative heat release at 1600 RPM. $r^2 = 0.94$.

six-fold decrease in fourteen years.

NO_x emissions are measured in laboratories and testing centres using exhaust gas analysers such as the CODA instrument used in this study. Whilst good accuracy can be achieved using this method, it is time-consuming and inconvenient to test vehicles on an annual or similar basis to ensure NO_x emissions are kept within the legal limits. When wear occurs, or the engine falls out of tune or aftermarket modifications are made to the engine, NO_x emissions can increase beyond permissible limits. Detection of unacceptable NO_x emissions relies upon testing and is likely only in countries where mandatory emissions testing is performed. The ability of an in-cylinder sensor to measure NO_x emissions in-situ increases the chance of detection.

Chapter 2 showed that the ion current integral in diesel engines bears a strong correlation to tailpipe NO_x emissions. This correlation may be of use in the prediction of NO_x emissions but the lack of sufficient understanding of the relationship between these two variables precludes its use. The reasons for this correlation are explained in the following sections.

6.3.2 Perfectly stirred reactor

The same methodology used in Section 6.2.2 is used here to investigate the link between the ion current and NO_x. The operating conditions of the PSR chosen are identical to those in Section 6.2.2. As NO₂ was found to constitute approximately 1% of NO_x under all conditions modelled here, it is ignored; NO is assumed to be the only constituent

of NO_x in the sensitivity analysis presented here. As described in Chapter 5, the NO_x sub-mechanism in the n-heptane mechanism used here contains only reactions that generate NO_x via the thermal pathway; Kong et al. [208] found prompt NO_x to be insignificant. For oxygenated fuels this pathway may assume greater importance.

Figure 6.8 shows the evolution of both electron and NO mole fractions as the residence time is varied. The peak electron concentration is seen in the flame front, as observed in Section 6.2.2 and in Chapter 4 (see Figures 4.10 and 4.14), while NO begins to form in the post-flame region.

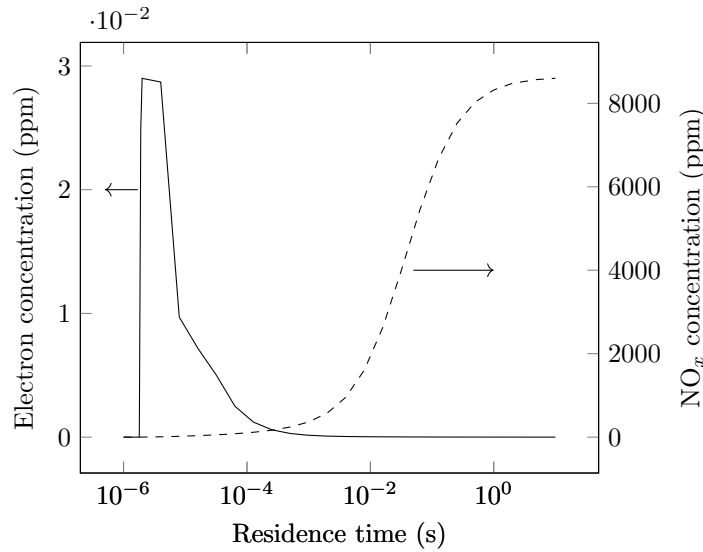


Figure 6.8: Evolution of electron mole fraction (a) and NO mole fraction (b) in a perfectly stirred reactor operating at 70 bar, inlet temperature 1450 K and equivalence ratio 0.4.

As discussed in Chapter 2, from the engine data a strong correlation can be shown between the ion current and tailpipe NO_x, suggesting the possibility that there is a common cause for elevated electron and NO_x production. A sensitivity analysis was conducted on the PSR combustion process using KINALC to determine species important to the production of both electrons and NO_x. Figure 6.9 shows the six species whose concentrations most strongly affect the electron production rate (a) and the NO production rate (b). For Figure 6.9 (a), the residence time is 1.9×10^{-6} s, near the point where the electron production rate is the highest. For Figure 6.9 (b), the residence time is 0.05 s, near where the NO production rate is maximum. The units on the x -axis are arbitrary and cannot be compared between different graphs.

The electron production rate depends to a great extent on the CH and O radicals, as described in Section 6.2.2. Predictably, there is also dependence on H₃O⁺; this is quickly formed from CHO⁺ after Reaction R 3.1 via Reaction R 3.10. There is also a weak dependence on NO⁺, H and CHO⁺. The important reactions affecting the

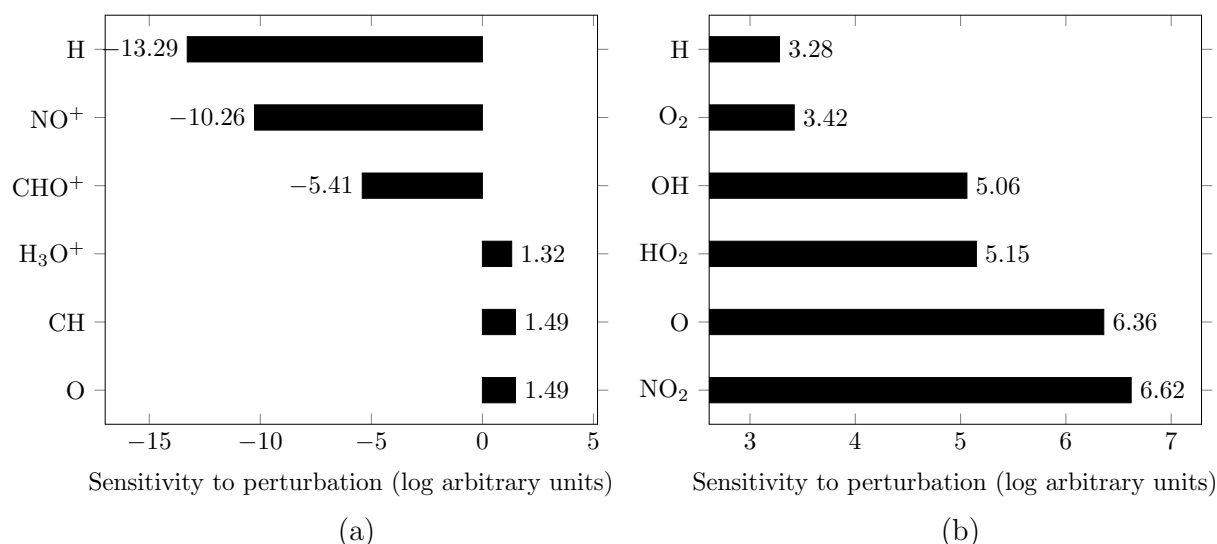


Figure 6.9: Sensitivities of electron production rate (a) and NO production rate (b) to important species.

concentration of electrons at this instant are as found in Section 6.2.2.

The production rate of NO depends heavily on the concentrations of NO₂ and O and, to a smaller extent, HO₂, OH, O₂ and H. NO production at this time is split between Reactions R 6.10 and R 6.11 in equal proportions.



Of interest is the common radical O. The O radical is one of the top two radicals affecting the production rates of both electrons and NO, suggesting that it is of particular importance in linking the two species. To investigate this link further, the sensitivities of two groups of species to concentrations of all other species were evaluated. One group of species was electrons and O, and the other was NO, NO₂ and O.

These results are shown in Figure 6.10 (a) and (b). Remarkable similarity is seen between the species on both graphs — no fewer than four of the top five species are shared, indicating the strong dependence of electron and NO_x concentration on a very similar set of conditions.

The O radical is produced primarily by Reaction R 6.12.



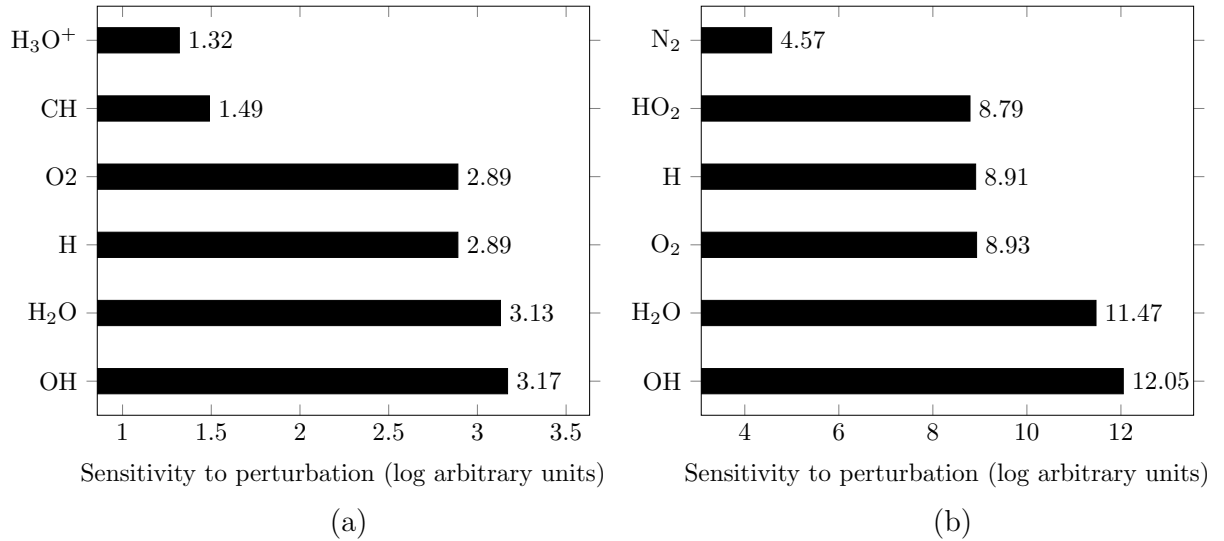
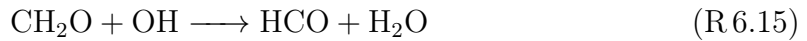


Figure 6.10: Sensitivities of production rate of electrons and O (a) and NO, NO₂ and O (b) to important species.

73.2% of the H radical required for this reaction is produced via Reactions R 6.13 and R 6.14.



HCO required for Reaction R 6.13 is mainly formed via Reaction R 6.15.



Clearly, as described in Section 6.2.2 the concentrations of the H, OH and O radicals are all closely linked. The temperature dependence of the concentrations of these species indicates that the electron concentration is also highly temperature dependent, an observation made in Chapter 3 (Figure 3.19 (a)) and in Section 6.2.2. It is well known that the reactions producing NO_x also heavily depend on temperature, suggesting that temperature plays a key role in the formation of both electrons and NO_x.

6.3.3 Premixed auto-igniting flames

The formations of NO_x and electrons were also investigated in premixed auto-igniting flames using the same methodology as in Section 6.2.3. The initial temperature was varied to give different maximum temperatures representative of the maximum temperatures in diesel engines.

Figure 6.11 shows the evolutions of electrons and NO for maximum temperatures of 2278.1 K and 2446.7 K. Similar to the results from Section 6.3.2, electrons are produced early in the combustion event, with NO rising and reaching a steady state much later. Since both electron and NO formation are highly temperature-dependent, both species are present in appreciably higher concentrations in mixtures whose final temperatures are only ≈ 170 K apart — a peak temperature difference of 6.95% results in changes in final NO and peak electron concentrations of 97.75% and 92.97% of the higher values respectively. The location of electrons with respect to the flame front agrees with that found previously in this study (see Chapter 4); that of NO_x with respect to the flame front agrees with findings by Dec & Canaan [222] using PLIF imaging in a diesel engine.

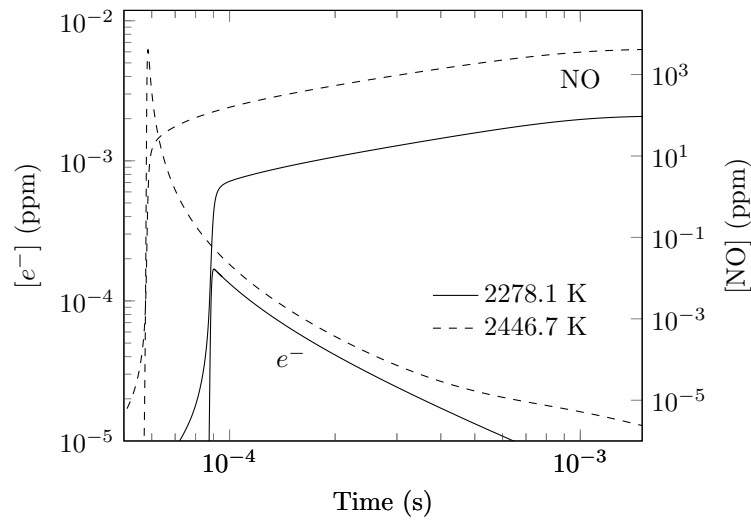


Figure 6.11: Evolution of NO and electron concentrations in premixed flames of different final temperatures but identical equivalence ratios in a chamber of changing volume.

A detailed examination of the dependence of both NO and electrons on temperature, O and CH was conducted using a moderate mixture peak temperature of 2364.7 K. Figure 6.12 shows the evolutions of temperature, NO production rate and O concentration during the combustion event. The initial peak in NO production follows the start of ignition and the consequent sudden increase in temperature. The peak O concentration also occurs simultaneously. Peak temperature is reached at $t = 0.5$ ms. The concentration of O and the NO production rate both begin to fall to zero at this point; NO reactions begin to freeze and NO reaches a steady state concentration.

At 5×10^{-4} s, NO is produced at its maximum rate of $5.79 \text{ mol cm}^{-3} \text{ s}^{-1}$. 45.2% of this is generated via Reaction R 6.10 and 43.2% via Reaction R 6.11.

Reaction R 6.11 is also responsible for 85.6% of the consumption of N₂ at this time and 95.7% of the production of the radical N required for Reaction R 6.10. The O

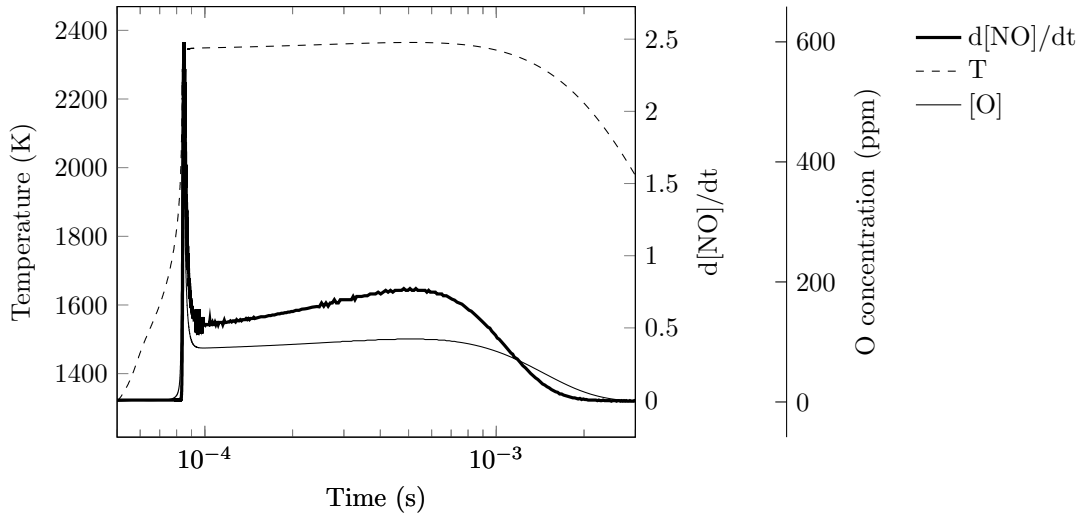


Figure 6.12: Evolution of NO production rate, temperature and O concentration during the combustion event.

radical can therefore be seen to be integral to the production of NO.

This is in contrast to the evolution of electrons in the same flame, shown in Figure 6.13. The inset plot shows the electron and CH concentration peaks. The CH concentration curve leads the electron concentration curve by 5×10^{-7} s. The concentration of O also reaches a peak in this region, as shown in Figure 6.12. As expected, the electron concentration only rises when CH and O are abundant; electron formation ceases when both CH and O concentrations drop a short while later. The concentration of electrons decays relatively rapidly and, even though the temperature is high in the latter stages of the combustion event and there are approximately 100 ppm of O, there is insufficient CH remaining to produce electrons via Reaction R 3.1.

The peak rate of electron production occurs at 8.35×10^{-5} s, with negligible consumption occurring at this time. 100% of production occurs via Reaction R 6.5. The CH required for this reaction is primarily produced via Reaction R 6.8. A large fraction of CH consumption occurs via Reaction R 6.9. Clearly, any increase in H production promotes the formation of CH and inhibits its consumption. Given the chain branching reactions, this implies that an increase in O concentration results in an increase in CH concentration when unburnt hydrocarbons are abundant.

Given the similar relationships of NO and electrons to temperature and the O radical, some correlation is expected between the concentrations of these two species. Figure 6.14 shows the steady-state NO concentration, peak electron concentration and integral of the electron concentration over time over a 3 ms period for different peak temperatures of the mixture. The integral of electron concentration was found to be

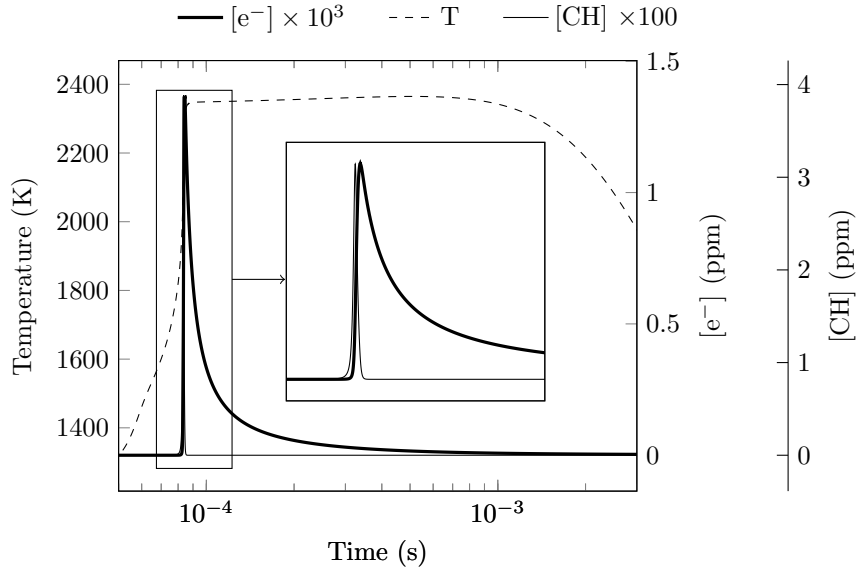


Figure 6.13: Evolution of temperature and electron and CH concentrations during the combustion event. Inset: electron and CH concentration peaks.

unchanged for time periods over 2 ms. All three variables monotonically increase with increasing peak temperature. The electron peak concentration is highly correlated with steady-state NO concentration ($r^2 = 0.995$). Both appear to bear a power relationship with maximum temperature, while the time-integral of the electron concentration increases fairly linearly with maximum temperature.

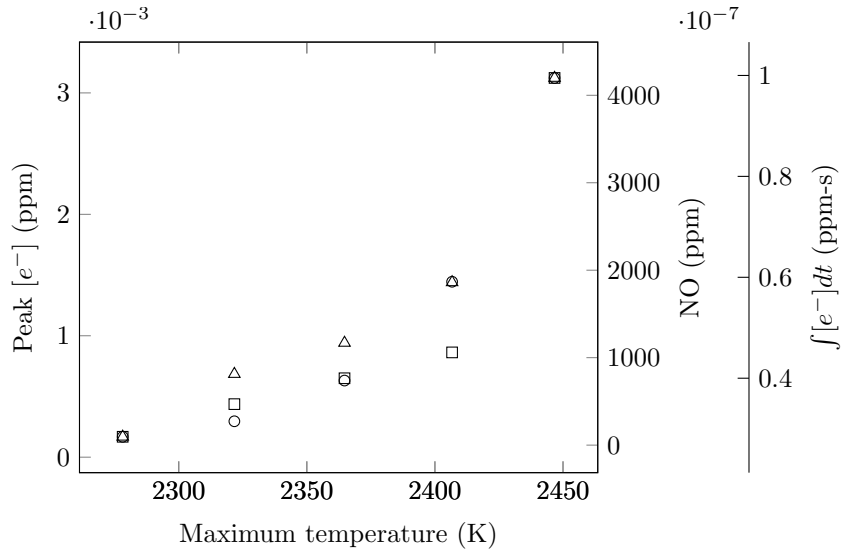


Figure 6.14: Changes in final NO concentration, peak electron concentration and time integral of electron concentration with different peak mixture temperatures.

Figure 6.15 shows the variations of peak electron concentration and integral electron concentration with steady-state NO concentration. There is a strong positive correla-

tion between both measures of electron concentration and NO — the trend is linear with an r^2 value of 0.98 for the peak and 0.95 for the integral.

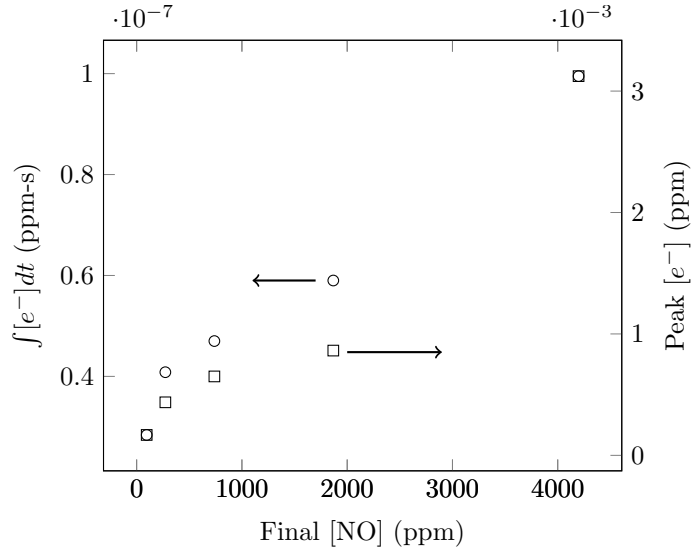


Figure 6.15: Variation in peak electron concentration against final NO concentration.

In Chapter 5, it was noted that the crank angle range where NO_x is formed shows considerable overlap with that where NO⁺ is present. This can also be seen in the combustion of this pre-mixed flame (Figure 6.16).

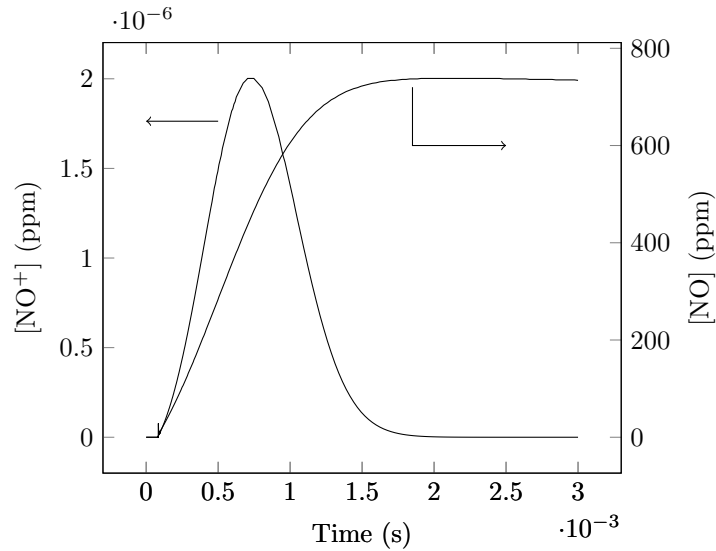


Figure 6.16: Evolutions of NO_x and NO⁺ in a pre-mixed flame undergoing auto-ignition.

At 0.465 ms, when the NO⁺ production rate is maximum, nearly all the NO⁺ present is formed via Reaction R 6.16.



In light of information presented in this chapter, the reasons for this overlap are clear — the presence of the radicals N and O results in the formation of both species. NO⁺ recombines with electrons via Reaction R.6.16 upon cooling, reducing its concentration to nearly zero whilst NO_x reactions freeze and NO concentration reaches a steady state.

6.3.4 Flames in diesel engines

The phenomenological engine model developed in Chapter 5 is used to more closely examine the evolution of NO_x and the ion current in the temperature-equivalence ratio space commonly seen in diesel engines.

Figure 6.17 shows the ion current and NO_x developed during an engine cycle at 1600 RPM, 140 Nm. The ion current peak appears early in the combustion event (at 175 CAD), as seen in the preceding sections, whilst the steady-state value of NO_x is reached over a period of ≈ 20 CAD. The ion current drops to less than 10% of its peak by 195 CAD, by which time 97% of the steady state NO_x has been formed. The regions of elevated ion current and NO_x formation are seen to overlap considerably. Peak NO_x formation is 78.4 ppm/CAD at 181.6 CAD.

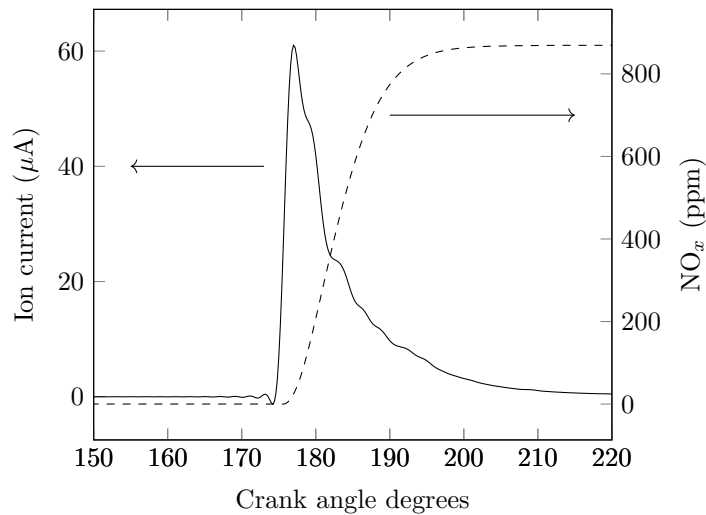


Figure 6.17: Ion current and NO_x evolution at 1600 RPM, 140 Nm.

Figure 6.18 shows the evolutions of electron concentration and NO_x for a randomly selected packet of fuel in the spray. Similar relationships can be seen here.

Evolutions of temperature (a), NO_x (b) and electrons (c) in a combusting diesel spray at 1600 RPM, 140 Nm are shown in Figure 6.19 in a temperature-equivalence ratio space.

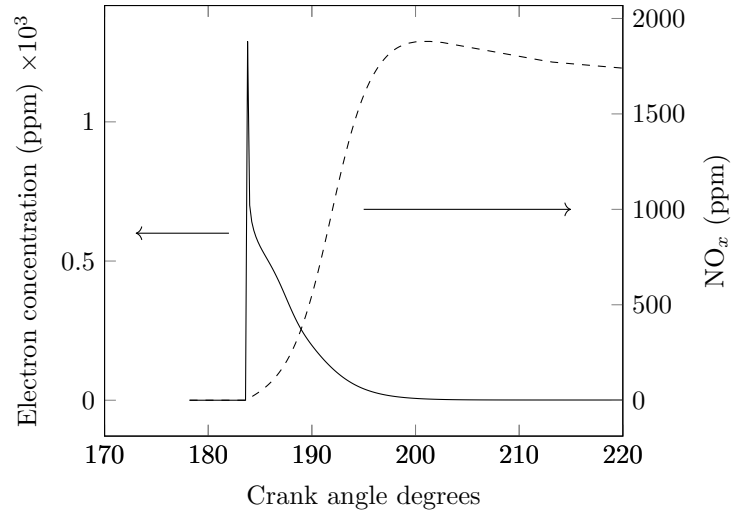


Figure 6.18: Ion current and NO_x evolution in a randomly chosen packet in the spray at 1600 RPM, 140 Nm.

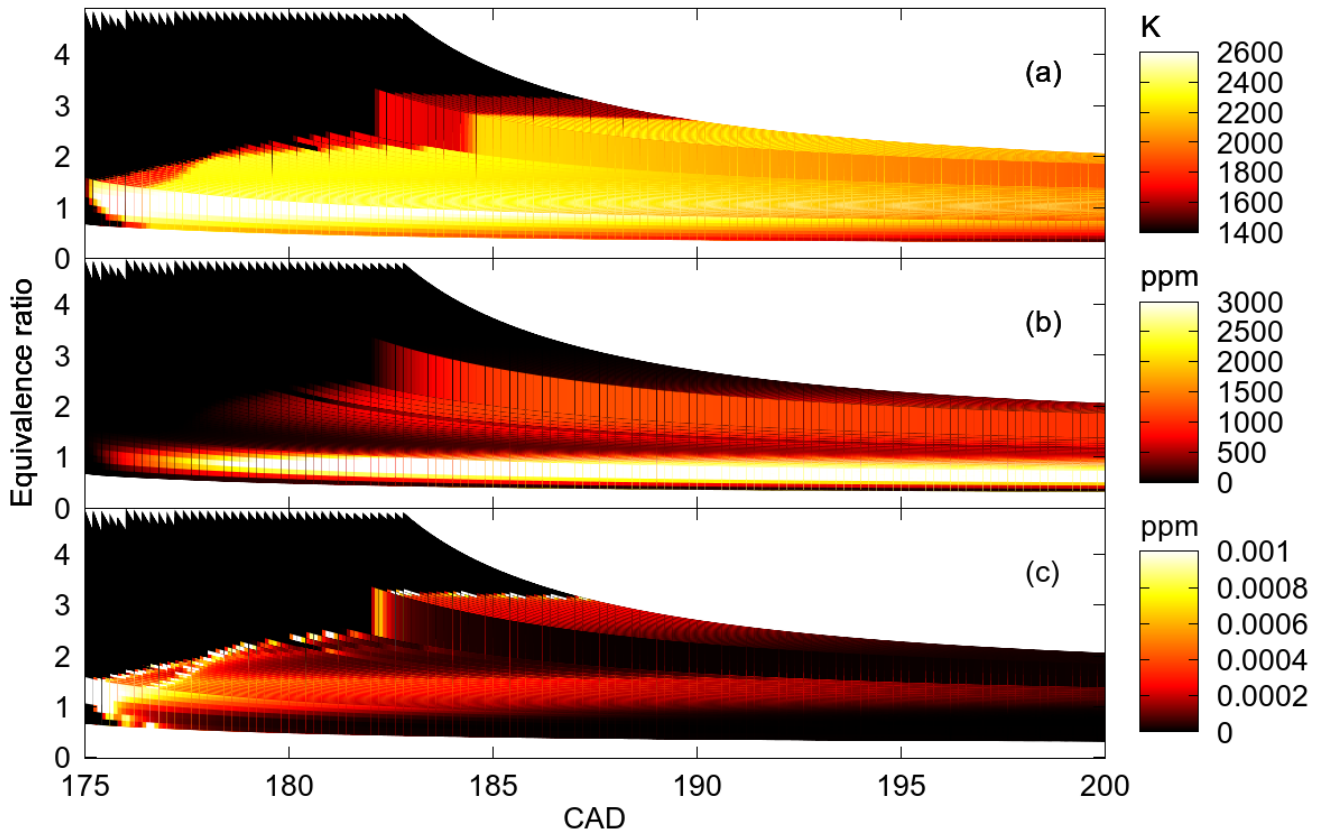


Figure 6.19: Modelled evolutions of temperature (a), NO_x concentration (b) and electron concentration (c) in a diesel spray at 1600 RPM and 140 Nm.

Similar observations to those made in Section 6.2.4 can be made here with respect to the temperature increase at SOC. The pronounced increase in temperature for packets with equivalence ratios greater than 2 around 182 CAD shows the onset of

mixing-controlled combustion — this typically takes place in the interior of the spray where entrainment is low and equivalence ratios are higher than at the spray edges. Similar observations can also be made with respect to the location of electrons in the flame front, for reasons detailed in previous sections.

NO_x formation begins approximately 2 CAD after electrons are formed. At the speed shown here (1600 RPM), this corresponds to 0.2 ms, similar to the delay seen in Figure 6.12. The highest NO_x concentrations are seen in the most fuel-lean areas of the spray, which are typically the fuel packets injected first. These packets also show high electron concentration during premixed combustion. NO_x is also present in smaller concentrations in the packets participating in mixing-controlled combustion.

Figure 6.20 shows the variations in tailpipe NO_x, ion current peak and time integral of the ion current with changing load at 1600 RPM as predicted by the model. All three parameters increase monotonically with engine load. Figure 6.21 plots the ion current peak and integral against NO_x for different engine loads. The r^2 values are 0.90 for the peak and 0.95 for the integral, similar to those seen in Section 6.3.3.

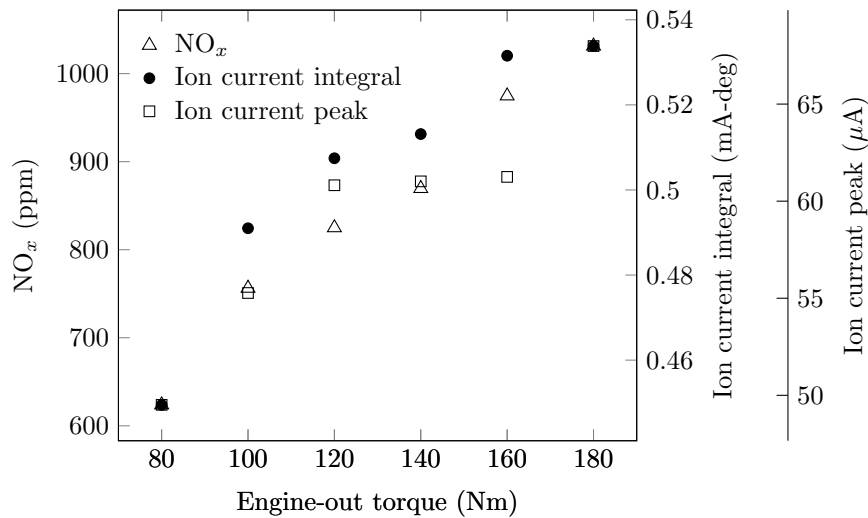


Figure 6.20: Modelled NO_x, ion current integral and ion current peak at 1600 RPM and different engine loads.

The experimental correlation coefficient between the ion current integral and NO_x is 0.99, similar to that seen here. This suggests that the ion current could be used to predict NO_x emissions in diesel engines.

Temperatures of the burnt and unburnt zones predicted by the diesel engine model are presented in Appendix E, along with several predictions by other sub-models not directly relevant to the ion current.

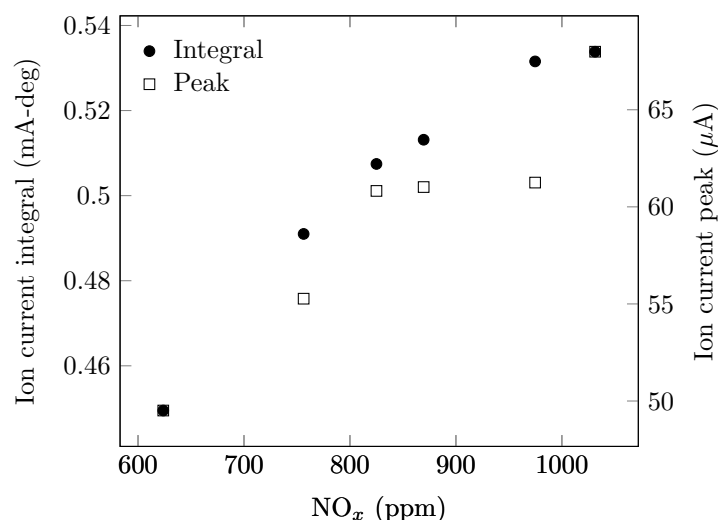


Figure 6.21: Modelled ion current integral and peak against modelled NO_x for different engine loads at 1600 RPM.

6.4 Summary

A study of the relationship between heat release, NO_x and the ion current in models of varying complexity using a reduced n-heptane mechanism with an ionic sub-mechanism has been discussed. For both heat release and NO_x, specific species and mechanisms have been found to be responsible for their correlations with the ion current.

Heat release and electron production were found to occur simultaneously in a perfectly stirred reactor in the region of the flame front. At the point where the peak rate of heat release occurs, heat release depends strongly on the concentration of the OH radical. Due to chain branching reactions, the presence of OH implies that of the H and O radicals as well. In the same flame, electron production was found to depend strongly on CH and O radicals as expected from previous studies. The reactions most strongly affecting both electron production and heat release were found to be very similar.

In pre-mixed auto-igniting flames, the electron concentration was found to mirror OH concentration when a sufficient amount of CH was present and was therefore found to peak in the flame front. After the flame front where CH is oxidised, its concentration decreased sharply, causing a slow decline in the electron concentration via neutralisation.

In the diesel engine spray, OH and O radicals were found in the flame front and in the post flame region where high temperatures were observed. The CH radical was found in the flame front but was oxidised in the post-flame region. Electrons, whose

formation depends on both CH and O radicals, were seen in high concentrations in the flame front with decaying concentration in the post-flame region. The location of peak electron concentration was found to be the same as that of peak heat release.

An investigation of the relationship between NO_x and electron formation in flames was also conducted. In a perfectly stirred reactor operating at conditions similar to those in a diesel engine, electrons and NO_x were found to be most sensitive to a very similar group of species, indicating that for non-oxygenated fuels a high electron concentration implies a high NO_x concentration and vice versa. Temperature and the presence of the O radical were found to be the most important requisites for both species. It must be noted that these findings apply only to thermal NO_x; prompt NO_x formation is small compared to thermal NO_x in diesel engines operating with standard diesel fuel.

In premixed flames, the NO production rate was found to be directly correlated to O concentration. High values of both these variables were found in the flame front and the post-flame region. The bulk of NO was produced in the post-flame region, as PLIF experiments on diesel engines conducted by other researchers have found. Both the electron concentration peak and integral were found to be strongly correlated with final NO concentration, with r^2 values of 0.95 and 0.98 respectively. The radicals N and O were also found to be responsible for the bulk of NO⁺ formation, leading to the formation of NO⁺ at the same time as NO; however, NO⁺ is neutralised shortly after, consistent with results seen in Chapter 5.

In the diesel engine spray, similar results were found for the locations of NO_x and electrons. A study of the evolution of the mixture thermochemistry indicated the areas in the spray responsible for the majority of electron and NO_x production. These were found to agree well with previous experimental results. The ion current integral and peak were strongly correlated with NO_x ($r^2 = 0.95$ and 0.90 respectively).

The agreement between the experiment and the model on the trends shown by these variables indicates a close relationship between the ion current and NO_x. As shown in Chapter 2, the ion current integral shows excellent repeatability over several consecutive engine cycles, suggesting that it could be reliably used in the prediction of tailpipe NO_x.

This chapter delved into the chemical kinetics affecting heat release, NO_x and the ion current in order to explain correlations seen in Chapter 2. A correlation not mentioned in that chapter is that for tailpipe soot mass concentration, which is caused by an entirely different mechanism and is largely beyond the scope of this study. However, a brief overview of the effect soot has on the ion current signal and possible uses of this

effect are discussed in the next chapter.

Chapter 7

Soot detection

7.1 Introduction

Chapter 2 describes the linear relationship between emissions of NO_x and the time-integral of the ion current signal and posits that the ion current can be used to predict NO_x , for reasons explained in Chapter 6. Another emission of interest from diesel engines is DPM, commonly referred to as soot — a generic term for particles of incompletely burnt hydrocarbons in a range of sizes and with no specific chemical composition. Inhalation of soot is well known to be detrimental to human health. This is reflected in changes in particulate matter emissions allowed for passenger vehicles by the European emissions standards — from 0.14 g km^{-1} in 1992 (Euro 1) to 0.005 g km^{-1} in 2009 (Euro 5).

Two characteristics of soot emissions from engines are of particular interest from a human health perspective — total soot mass emitted and soot particle size. Thus far, emissions standards for internal combustion engines have largely ignored the effect of particle size and have only placed restrictions on the total soot mass emitted. This chapter presents a brief outline of the possibility of using an ion sensor as a soot mass detection device in diesel engines.

7.2 State of the art

Several techniques exist to measure soot mass emissions from engines, which broadly fall into three categories: gravimetric, optical and microbalance.

Gravimetric methods

Gravimetric methods require a sample of known quantity of the exhaust to be passed through an appropriate filter. The change in filter weight is then used to calculate the mass concentration of soot in the exhaust. A significant drawback to this method is its time-consuming nature due in part to the repeated disassembly and reassembly of the filter housing for each measurement. Additionally, water vapour in the exhaust gas condenses in the housing, necessitating the drying of the filter. The equipment required for this method makes it unsuitable for use in the field.

Optical methods

Optical methods include scattering and extinction meters. Scattering meters (eg. the DustTrak instrument used in this study) measure the scattering of light incident upon the sampling chamber to provide both size and mass of aerosols in the sample. These instruments are used extensively in the determination of air quality and can, with careful calibration, be used for exhaust soot measurement. Extinction meters such as the opacity meter measure the difference in light measured by a sensor at one end of the chamber and that emitted by a source at the other end. Such sensors have often been used to measure exhaust soot mass but have questionable accuracy [223].

Microbalance methods

Microbalances such as the tapered element oscillation microbalance (TEOM) use the change in resonant frequency of a vibrating element as it accumulates mass from a sample gas flow. Such methods generally give fairly accurate results but their operation in environments like engine exhausts is problematic due to humidity and pressure changes [224]. Furthermore, TEOMs are delicate instruments and are more suited to laboratory work than use in the field.

A common limitation of all three methods discussed above is their requirement for the sample of exhaust gas to be cooled before entry into the instrument, making in-situ measurement of exhaust soot concentration difficult to conduct.

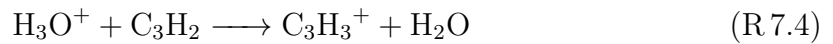
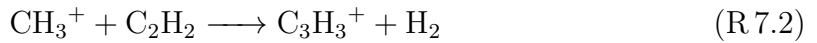
7.3 The ion sensor as a soot mass detection device

An in-cylinder ion sensor has previously been used in conjunction with a non-linear multiple regression model similar to the model described in Appendix B to predict tailpipe soot mass [41]. That study, however, utilised statistical techniques with little understanding of the reasons why soot may affect the ion current. The use of a statistical technique makes it difficult to detect abnormal operation of the engine,

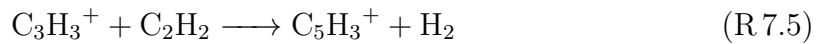
where the measured ion current may be far removed from that seen during ordinary operation. This section presents two mechanisms by which soot may affect the ion current signal observed.

Ions have been linked to soot formation in several studies [11–14, 161]. These studies posit that a charged species is the soot precursor and reactions between this charged species and neutral species such as acetylene produce larger ions. Further reactions with neutral species occur to produce even larger ions, resulting finally in the formation of soot particles. C_3H_3^+ is generally thought to be this precursor species.

Calcote & Keil [13] found that in a pre-mixed acetylene-oxygen flame, soot appearance coincided with a sharp decay in ion concentration. They proposed an ionic mechanism for soot formation beginning with the well-known reaction for the formation of CHO^+ , from which C_3H_3^+ can be formed via several mechanisms, such as those shown here (Reactions R 7.1–R 7.4).



Larger ions are then produced via neutral species (eg. Reactions R 7.5 and R 7.6).



With the addition of low molecular weight neutral species, very heavy ions can be produced in this manner. In another study, Calcote & Keil [225] observed ions up to a mass of 557. Michaud et al. [226] observed ions up to a mass of 265 in low pressure acetylene-oxygen flames.

The ionic mechanism for soot formation has not, however, been universally accepted. Hall-Roberts et al. [227] studied the effect of introducing caesium into a pre-mixed acetylene-oxygen flame. It is believed that caesium removes C_3H_3^+ ions from the flame by undergoing ionisation itself to Ce^+ . It was found, however, that the addition of caesium had little effect on the amount of soot formed early in the flame. The role of ions in soot formation is still the subject of some debate.

A different way in which soot formation may affect the ion current observed is via the deposition of soot on the ion sensor. Soot is electrically conductive and its deposition may therefore change the geometry of the current path between the two electrodes. Depending on the sensor geometry, soot may entirely bridge the electrode gap, leading to the observation of a non-zero ion current even in the absence of ions. Chapter 2 briefly describes the deposition of an electrically conductive substance (presumed to be soot) on the ion sensor leading to a non-zero cycle-minimum value (‘offset’) of the ion current. It is possible that this phenomenon could be used to estimate soot mass emissions. Sensors utilising this principle have previously been developed and placed in the exhaust systems of diesel engines [228, 229].

The two mechanisms described above and the possibility of using the in-cylinder ion sensor to indicate soot emissions are explored here.

To investigate the effect of soot on the ion sensor, the ion current was measured at several engine loads. The engine was first idled at 1200 RPM. The load was then gradually increased to 125 Nm and then to 200 Nm. The ion signals for these three conditions are shown in Figure 7.1.

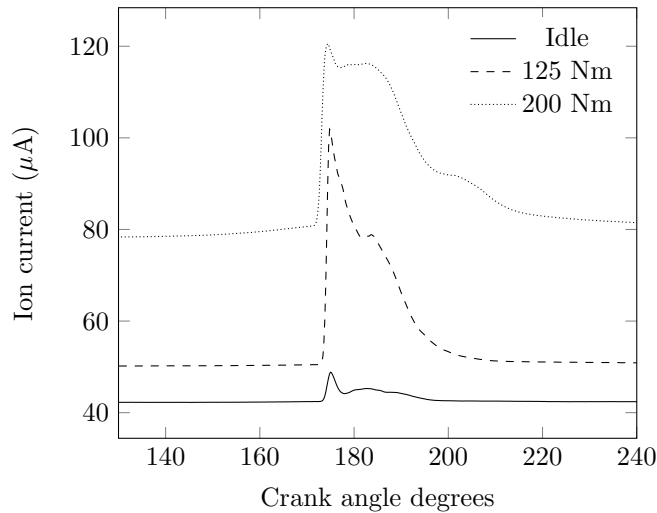


Figure 7.1: Ion current signal at 1200 RPM and different torque settings.

After the engine operation reached steady-state at 200 Nm, the load was quickly reduced to idle and the engine switched off. The offset in the ion current decreased from $\approx 78 \mu\text{A}$ to $\approx 74 \mu\text{A}$ during this process. When switched off, however, the offset persisted. Repeated cranking of the engine without the injection of fuel to flush out any residual exhaust gas did not reduce the offset to zero. In the absence of fuel, any current observed cannot be due to the ions involved in soot formation but must be caused by another electrically conductive material in the cylinder.

While cranking the engine, a small increase in the sensor output was noticed during the compression stroke, indicating that the electrically conductive material causing the offset is sensitive to temperature and/or pressure. This can be seen in Figure 7.2 (a). The peak in the sensor output occurs at TDC.

An hour was allowed for the engine to cool and the same test performed. The ion current offset decreased to $\approx 25 \mu\text{A}$, indicating that the electrical conductivity of the material is temperature-sensitive. The increase in the ion current on the compression stroke was also noticed here. Figure 7.2 (b) shows this.

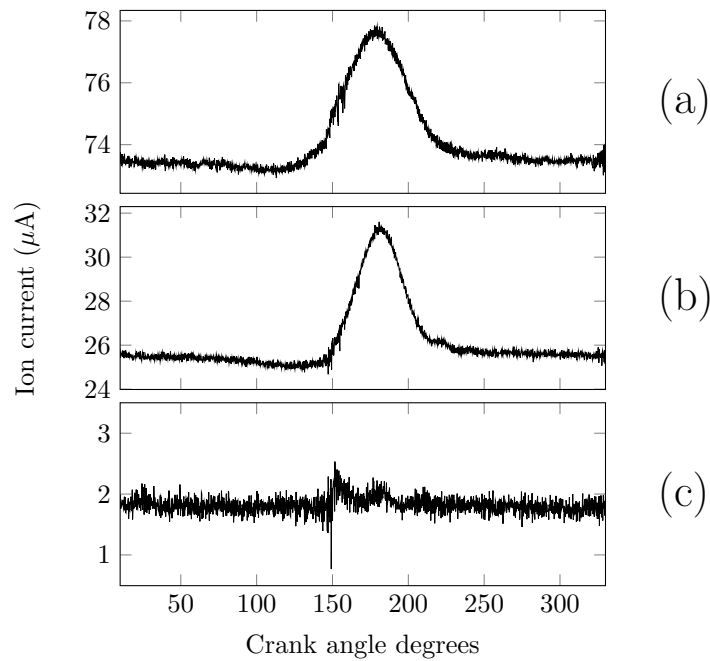


Figure 7.2: Ion current signal when the engine is cranked with no fuel flow, (a) just after shutdown, (b) after the engine has cooled and (c) after the sensor is removed, cleaned and refit.

The sensor was then removed and a black deposit observed on the ceramic adhesive between the casing and the centre electrode (see Figure 2.7). The sensor was cleaned and refit. Figure 7.2 (c) shows the ion sensor output when cranking the engine with the clean sensor installed — the offset drops to nearly zero and the peak during the compression stroke is not observed. The black deposit is postulated to be soot. The mechanism by which soot affects the offset in the ion current is therefore via deposition and is not ionic in nature.

When the ion current offset is plotted against tailpipe soot for varying engine-out torque, a strong correlation ($r^2 = 0.96$) is observed, indicating that the ion current can be used to predict DPM emissions from engines at a single speed. These parameters are plotted in Figure 7.3. A significant limitation of this technique must be mentioned

here: there is little, if any, understanding of the deposition process of soot on the ion sensor. This is likely to depend to a great extent on the sensor and combustion chamber geometry, and may also depend to some extent on the engine speed. A full analysis of the deposition process is beyond the scope of this study.

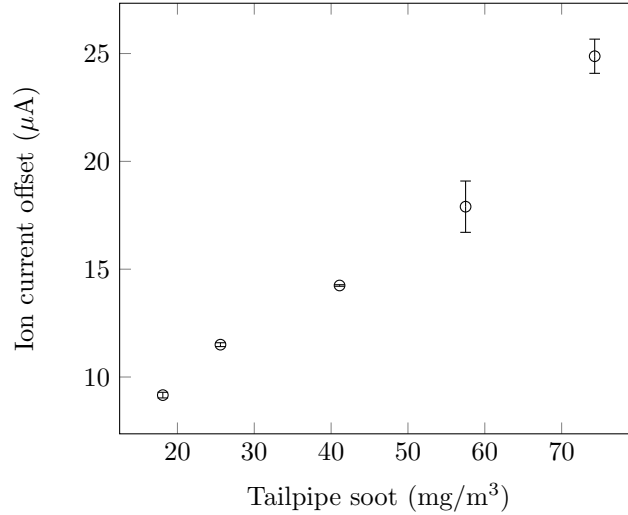


Figure 7.3: Variation of the ion current offset with tailpipe soot.

7.4 Diagnosis of abnormal engine operation

Excessive DPM formation in engines can be indicative of poor health of engine components. Two conditions found in engines are conducive to DPM formation: low temperature and high equivalence ratio. Pockets of high equivalence ratio mixtures can be found in the combustion chamber when air-fuel mixing is poor. A common reason for poor air-fuel mixing is diesel injector wear. Worn injectors display spray patterns that result in inadequate atomisation of the fuel and reduced air entrainment into the spray, causing incomplete combustion of the fuel.

Given the relationship between the ion current offset and DPM emissions from the engine, it is suggested that the ion sensor could be used to diagnose worn injectors. The ion current was measured at 1200 RPM, 80 Nm and 1200 RPM, 200 Nm for injectors in different states of wear. Old injectors were tested on a Bosch EPS200 injector bench tester and found to fail seat leakage and spray pattern tests. These were later reconditioned. The measured DPM emissions for these test conditions are shown in Table 7.1.

Soot emission for old injectors at 200 Nm as predicted by the line of best fit for the correlation between the ion current cycle-minimum value and tailpipe soot at 1600

Table 7.1: DPM emissions for old and reconditioned injectors at 1200 RPM (mg m^{-3}).

Injectors	80 Nm	200 Nm
Old	86.1	$> 150.0^*$
Reconditioned	15.4	81.8

* The DustTrak DRX8533 LLSP has a measurement range of 0 mg m^{-3} to 150 mg m^{-3}

RPM is 295 mg m^{-3} . Given that very little is known about the soot deposition process and that it may depend on engine speed, the use of this relationship may not be valid.

A comparison of the ion current measured when each set of injectors was installed in the engine is shown in Figure 7.4. The difference between the signal offset with old injectors and that with new injectors is clear.

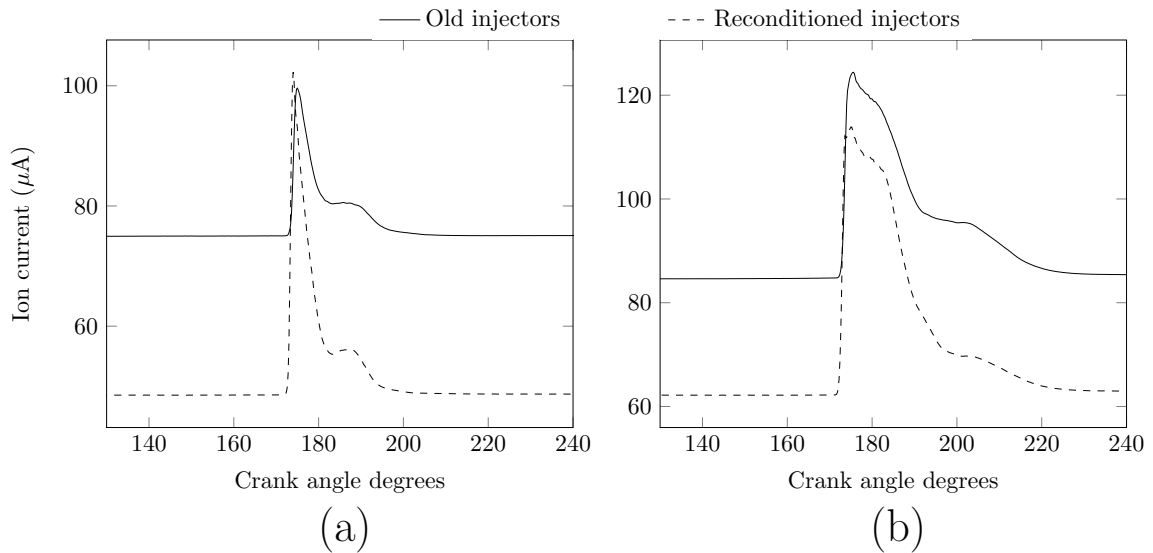


Figure 7.4: Ion current signal with injectors in different states of wear at 1200 RPM, 80 Nm (a) and 1200 RPM, 200 Nm (b).

Another cause of high DPM emissions is decreased volumetric efficiency caused by conditions such as clogged air filters or damaged compressor wheels in turbochargers. The lower effective compression ratio leads to a higher equivalence ratio for the same engine out torque, thereby increasing DPM production. Restrictions in the exhaust system such as damaged turbines in turbochargers lead to increased back-pressure on the cylinder during the exhaust stroke. This increases the residual gas fraction and decreases the oxygen fraction of the mixture before SOC, leading to high equivalence ratios, lower maximum combustion temperatures and the concomitant increase in DPM.

Modern diesel-powered vehicles use diesel particulate filters (DPFs) in the exhaust

system to trap DPM upstream of the exit to atmosphere. The Hino engine used in this study can be fitted with an underground mine-spec diesel exhaust system, consisting of a scrubber and a filter. Exhaust gas is first bubbled through water in the scrubber and then passed through the filter before exiting to the atmosphere. Both the scrubber and the filter contribute to increased back-pressure on the engine compared to the standard exhaust system.

Figure 7.5 shows the measured ion current for the same exhaust system with and without a DPF. The higher offset for the exhaust system with the filter is as expected, indicating that the sensor is able to detect changes in the back-pressure experienced by the engine due to changes in the exhaust system.

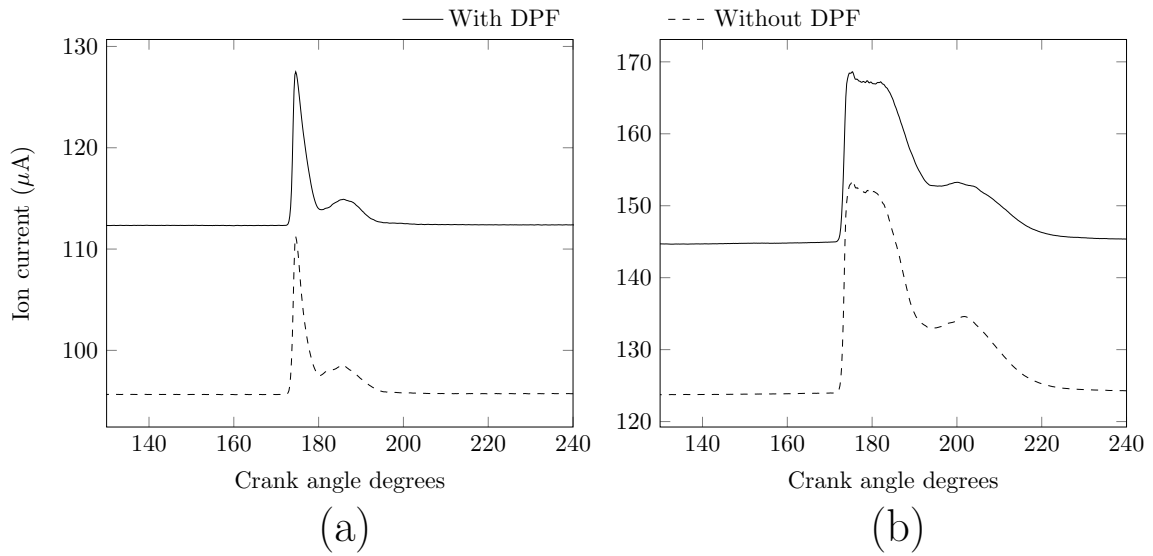


Figure 7.5: Ion current signal using exhaust systems with and without a DPF at 1200 RPM, 50 Nm (a) and 1200 RPM, 200 Nm (b).

7.5 Summary

Ions have been linked to soot formation in studies suggesting the soot precursor may be the ion $C_3H_3^+$. The deposition of electrically conductive soot on the sensor can also alter its response via a change in the current path between the electrodes. These phenomena may allow the ion sensor to predict soot mass formation in diesel engines. Advantages of the ion sensor over currently used methods of measuring soot emissions in engines include robustness and ease of use. The ion current signal has previously been used in a statistical model to predict tailpipe soot mass but no physical basis for the model was presented.

For the engine and sensor used in this study, the deposition of soot was found to be the primary reason for a non-zero cycle-minimum value of the ion current. Sensors relying on the deposition and electrical conductivity of soot have been placed in the tailpipe of engines to measure soot mass in the exhaust. This chapter presented the use of the in-cylinder ion sensor to predict tailpipe soot mass.

The cycle-minimum value of the ion current was found to be strongly correlated to tailpipe soot mass concentration ($r^2 = 0.96$), suggesting the possibility of using the ion sensor to diagnose abnormal engine operating conditions leading to high soot emissions. Two such engine operating conditions, worn injectors and an included diesel particulate filter in the exhaust system, were tested. The ion sensor was found able to detect the soot increase for both these conditions.

The study presented here consists only of preliminary observations of the effect of soot on the ion current signal. For robust use in the detection of abnormal engine operating conditions or for prediction of soot, further and more detailed investigation is required into the mechanism of deposition of soot on the sensor and the effect of the geometry of the sensor–cylinder head interface. The exact geometry of both this interface and the ion sensor itself will likely have a significant effect on the deposition of soot and therefore the ion current. Further study of abnormal engine operating conditions will require the careful engineering of measurable faults in components such as injectors, piston rings and valves, which is well beyond the scope of this study.

Chapter 8

Conclusion

The ion current signal in engines has, over the years, been found to be a useful predictor of many interesting engine operating parameters over a large number of experimental studies, such as engine-out torque, rate of heat release, cumulative heat release, and NO_x and soot emissions. These predictions have generally been made statistically with little understanding of the origins of the signal, conditions under which it is formed and its relationships to the parameters being predicted. The lack of knowledge of the basic mechanisms governing these relationships precludes the robust use of the same statistical relations for different ion sensors in different engines.

In contrast, the formation of ions in flames has been extensively studied for over a century. Mechanisms of ion formation are well established and physical and chemical properties of these ions are well known. Their reaction rate constants have been measured by several researchers using different experimental methods and general agreement has been reached on the identities of the important ions in hydrocarbon flames.

The aim of this study has been to marry these two fields to develop a more thorough understanding of the ion current developed in direct injection diesel engines.

Experimental measurements of the performance and emissions characteristics, including the ion current, of a Hino direct-injection diesel engine, were taken over a range of engine speeds and loads. Several correlations were observed between different characteristics of the ion current curve and important engine operating parameters, such as start of combustion timing, net heat release rate, net cumulative heat release and tailpipe NO_x emissions. Without an understanding of why these relationships exist, use of the ion current for robust prediction of engine operation is difficult.

In order to obtain this understanding, ion formation was studied in progressively more complex systems. The first system studied was methane combustion in a 1-D laminar flame. A simplified chemical kinetic mechanism for high pressure, high temperature methane oxidation was developed and augmented with an ionic sub-mechanism. Comparisons of predictions of this mechanism against experimental data and data from other mechanisms showed good agreement.

To study ion formation in conditions more representative of combustion chambers in engines, the ion current developed during the combustion of a near-stoichiometric methane-air mixture in a constant-volume chamber was measured, along with the chamber pressure rise. This experiment was modelled using ANSYS Fluent with CHEMKIN-CFD to calculate heat release, pressure rise and mixture composition in the chamber. Good agreement was found between experimental and modelled chamber pressure. The ion current peak locations were well predicted; trends in the peak magnitude agreed with experiment but there was significant error in its prediction. Electrons were generally found to be confined to the flame front, except at high equivalence ratios, where a region of moderate electron concentration caused by oxidation of unburnt hydrocarbons was found some distance behind the flame front. This was predicted by the model.

The effects of changing engine operating parameters on the chemistry within the combustion chamber were studied in a phenomenological model of the test engine using a modified n-heptane mechanism to simulate heat release and species concentrations. The predictions from the model showed good agreement with experiment for cylinder pressure and heat release and fair agreement for NO_x emissions. Trends for the ion current integral, an important measure of the signal, were accurately modelled.

The relationship between heat release and the ion current was studied in a perfectly stirred reactor model. The reactions important to both quantities are very similar and their rates were found to depend heavily on the production of radicals of the H-O system. In particular, the OH radical was found to play an important role. The study of these quantities in a pre-mixed flame undergoing auto-ignition and in the diesel engine model showed their simultaneous occurrence. Evolutions of important species in the spray were studied and the relative locations of CH, O and electrons found were consistent with expectations developed from the 1-D flame model.

The relationship between NO_x and the ion current was also studied in the same systems. Both NO and electron concentrations were found to depend heavily on temperature and on a largely similar group of species, indicating that conditions conducive to the formation of one species generally result in the formation of large amounts of the

other. The O radical was found to be necessary for the production of both NO_x and electrons via oxidation of N and N_2 , and CH respectively. The locations of NO_x and electrons differed — electrons were found in the flame front in both zero-dimensional models and the diesel engine model, whilst NO_x was found in the post-flame region, as PLIF experiments on diesel engines have shown — but steady-state NO_x concentration was found to be strongly correlated with electron formation when modelled both in premixed flames and in a diesel engine spray.

Soot emissions and the ion current are also related through the deposition of soot on the surface of the sensor and the consequent increase in the ion current cycle-minimum value. Over a large range of torque values, tailpipe soot and the ion current offset were found to be highly correlated ($r^2 = 0.96$), indicating that the ion current may be able to be used as a measure of soot emissions. This finding suggests the ability to diagnose engine conditions that result in increased soot production. Two such conditions — worn injectors and a DPF in the exhaust system — were tested and the soot increase detected by the ion sensor.

The study of ion generation in engines is a field still largely unexplored. The study described here is an attempt to model the ion current in diesel engines from first principles — the chemistry leading to ion generation in simple flames — and thus enable greater confidence in correlations seen previously. Whilst the chemical kinetics presented here are fairly mature and well known, familiar limitations of phenomenological models apply. These models are, however, useful in indicating avenues that are worth exploring when investigating the impact of changing engine conditions or design on engine performance.

Bibliography

- [1] V. Rao and D. Honnery. A comparison of two NO_x prediction schemes for use in diesel engine thermodynamic modelling. *Fuel*, 107:662–670, 2013.
- [2] R. Rao and D. Honnery. The prediction of torque in a diesel engine using ion currents and artificial neural networks. *International Journal of Engine Research*, 15(3):370–380, 2014.
- [3] V. Rao and D. Honnery. Application of a multi-step soot model in a thermodynamic diesel engine model. *Fuel*, 135:269–278, 2014.
- [4] J. Dent and S. Sulaiman. Convective and radiative heat transfer in a high swirl direct injection diesel engine. *SAE Technical Paper 770407*, 1977.
- [5] C. Rakopoulos, D. Rakopoulos, G. Mavropoulos, and E. Giakoumis. Experimental and theoretical study of the short term response temperature transients in the cylinder walls of a diesel engine at various operating conditions. *Applied Thermal Engineering*, 24(5):679–702, 2004.
- [6] C. Espey and J. E. Dec. Diesel engine combustion studies in a newly designed optical-access engine using high-speed visualization and 2-D laser imaging. *SAE Technical Paper 930971*, 1993.
- [7] R. Reitz and C. Rutland. Development and testing of diesel engine CFD models. *Progress in Energy and Combustion Science*, 21(2):173–196, 1995.
- [8] A. S. Cheng, A. Upatnieks, and C. Mueller. Investigation of the impact of biodiesel fuelling on NO_x emissions using an optical direct injection diesel engine. *International Journal of Engine Research*, 7(4):297–318, 2006.
- [9] H. Pergament and H. Calcote. Thermal and chemi-ionization processes in afterburning rocket exhausts. In *Symposium (International) on Combustion*, volume 11, pages 597–611. Elsevier, 1967.
- [10] T. Sugden. Elementary combustion reactions: charged species. In *Symposium (International) on Combustion*, volume 10, pages 539–544. Elsevier, 1965.
- [11] H. Calcote. Ionic mechanisms of soot formation. In *Soot in Combustion Systems and its Toxic Properties*, pages 197–215. Springer, 1983.
- [12] H. Calcote, D. Olson, and D. Keil. Are ions important in soot formation? *Energy & Fuels*, 2(4):494–504, 1988.
- [13] H. Calcote, D. Keil, et al. The role of ions in soot formation. *Pure Appl. Chem*, 62(5):815–824, 1990.
- [14] H. Calcote, D. Keil, R. Gill, and C. Berman. Modeling Study to Evaluate the Ionic Mechanism of Soot Formation. Technical report, DTIC Document, 1994.
- [15] R. Reinmann, A. Saitzkoff, and F. Mauss. Local air-fuel ratio measurements using the spark plug as an ionization sensor. *SAE Technical Report 970856*, 1997.
- [16] F. A. A. Estefanous, T. Badawy, and N. Henein. Cycle Resolved In-Cylinder NO_x and

- Ion Current Measurements in a Diesel Engine. *SAE Technical Paper 2013-01-0555*, 2013.
- [17] G. Schweimer. Ion probe in the exhaust manifold of diesel engines. *SAE Technical Paper 860012*, 1986.
- [18] E. Balles, E. VanDyne, A. Wahl, K. Ratton, and M. Lai. In-cylinder air/fuel ratio approximation using spark gap ionization sensing. *SAE Technical Paper 980166*, 1998.
- [19] N. Wickstrom, M. Taveniku, A. Linde, M. Larsson, and B. Svensson. Estimating pressure peak position and air-fuel ratio using the ionization current and artificial neural networks. In *Intelligent Transportation System, 1997. ITSC'97., IEEE Conference on*, pages 972–977. IEEE, 1997.
- [20] M. Hellring, T. Munther, T. Rognvaldsson, N. Wickstrom, C. Carlsson, M. Larsson, and J. Nytomt. Spark advance control using the ion current and neural soft sensors. *SAE Technical Paper 1999-01-1162*, 1999.
- [21] H. Klövmark, P. Rask, and U. Forssell. Estimating the air/fuel ratio from Gaussian parameterizations of the ionization currents in internal combustion SI engines. *SAE Technical Paper 2000-01-1245*, 2000.
- [22] M. Hellring and U. Holmberg. An Ion Current Based Peak-Finding Algorithm for Pressure Peak Position Estimation. *SAE Technical Paper 2000-01-2829*, 2000.
- [23] M. Hellring and U. Holmberg. A comparison of ion current based algorithms for peak pressure position control. *SAE Technical Paper 2001-01-1920*, 2001.
- [24] A. Gazis, D. Panousakis, R. Chen, and W.-H. Chen. Computationally inexpensive methods of ion current signal manipulation for predicting the characteristics of engine in-cylinder pressure. *International Journal of Engine Research*, 7(3):271–282, 2006.
- [25] R. L. Anderson. In-cylinder measurement of combustion characteristics using ionization sensors. *SAE Technical Paper 860485*, 1986.
- [26] J. Auzins, H. Johansson, and J. Nytomt. Ion-gap sense in misfire detection, knock and engine control. *SAE Technical Paper 950004*, 1995.
- [27] A. Lee and J. S. Pyko. Engine misfire detection by ionization current monitoring. *SAE Technical Paper 950003*, 1995.
- [28] F. An, G. Rizzoni, and D. Upadhyay. Combustion diagnostics in methane-fueled SI engines using the spark plug as an ionization probe. *SAE Technical Paper 970033*, 1997.
- [29] M. Asano, T. Kuma, M. Kajitani, and M. Takeuchi. Development of new ion current combustion control system. *SAE 980162*, 1998.
- [30] Y. Ohashi, M. Koiwa, K. Okamura, and A. Ueda. The application of ionic current detection system for the combustion condition control. *SAE Technical Paper 1999-01-0550*, 1999.
- [31] J. Förster, A. Günther, M. Ketterer, and K.-J. Wald. Ion current sensing for spark ignition engines. *SAE Technical Paper 1999-01-0204*, 1999.
- [32] P. O. Witze. Cycle-resolved multipoint ionization probe measurements in a spark ignition engine. *SAE Technical Paper 892099*, 1989.
- [33] D. Nicholson and P. Witze. Flame location measurements in a production engine using ionization probes embodied in a printed-circuit-board head gasket. *SAE Technical Paper 930390*, 1993.
- [34] S. Yoshiyama, E. Tomita, N. Tabuchi, K. Matsumoto, and K. Matsuki. Combustion Diagnostics of a Spark Ignition Engine by Using Gasket Ion Sensor. *SAE Technical Paper 2003-01-1801*, 2003.

- [35] M. Glavmo, P. Spadafora, and R. Bosch. Closed loop start of combustion control utilizing ionization sensing in a diesel engine. *SAE Technical Report 1999-01-0549*, 1999.
- [36] H. Kubach, A. Velji, U. Spicher, and W. Fischer. Ion current measurement in diesel engines. *SAE Technical Paper 2004-01-2922*, 2004.
- [37] N. Henein and W. Bryzik. Characteristics of ion current signals in compression ignition and spark ignition engines. *SAE Technical Paper 2010-01-0567*, 2010.
- [38] N. A. Henein, T. Badawy, N. Rai, and W. Bryzik. Ion current, combustion and emission characteristics in an automotive common rail diesel engine. *Journal of Engineering for Gas Turbines and Power*, 134(4):042801, 2012.
- [39] T. Badawy, A. Shrestha, and N. Henein. Detection of combustion resonance using an ion current sensor in diesel engines. *Journal of Engineering for Gas Turbines and Power*, 134(5):052802, 2012.
- [40] T. Badawy, N. Henein, and W. Bryzik. Closed Loop Control Using Ion Current Signal in a Diesel Engine. *SAE Technical Paper 2011-01-2433*, 2012.
- [41] T. Badawy, F. Estefanous, and N. Henein. Cycle-by-Cycle Soot Estimation in Diesel Engines. *SAE Technical Paper 2013-01-0545*, 2013.
- [42] M. Hellring, T. Munther, T. Rognvaldsson, N. Wickstrom, C. Carlsson, M. Larsson, and J. Nytomt. Robust AFR estimation using the ion current and neural networks. *SAE Technical Paper 1999-01-1161*, 1999.
- [43] T. Tanaka, K. Narahara, M. Tabata, S. Yoshiyama, and E. Tomita. Ion current measurement in a homogeneous charge compression ignition engine. *International Journal of Engine Research*, 6(5):453–463, 2005.
- [44] T. Badawy, N. Rai, J. Singh, W. Bryzik, and N. Henein. Effect of design and operating parameters on the ion current in a single-cylinder diesel engine. *International Journal of Engine Research*, 12(6):601–616, 2011.
- [45] T. Badawy, N. Khaled, and N. Henein. Fuzzy Logic Control of Diesel Combustion Phasing using Ion Current Signal. In *ASME 2012 Internal Combustion Engine Division Spring Technical Conference*, pages 645–658. American Society of Mechanical Engineers, 2012.
- [46] M. N. Saha. LIII. Ionization in the solar chromosphere. *The London, Edinburgh, and Dublin Philosophical Magazine and Journal of Science*, 40(238):472–488, 1920.
- [47] F. A. A. Estefanous. Multi-sensing fuel injection system and method for making the same, March 10 2015. US Patent 8,973,553.
- [48] F. A. Estefanous, T. H. Badawy, and N. A. Henein. Using ion current signal for soot and in-cylinder variable measuring techniques in internal combustion engines and method for doing the same, February 28 2012. US Patent App. 14/001,668.
- [49] T. H. Badawy, F. A. Estefanous, and N. A. Henein. Using ion current signal for engine performance and emissions measuring techniques and method for doing the same, October 22 2015. US Patent 20,150,300,278.
- [50] F. A. Estefanous and N. A. Henein. Combustion modification and emissions reduction utilizing an electrically insulated engine member in internal combustion engines, March 28 2013. US Patent App. 14/388,376.
- [51] S. Korenaga, T. Haibara, and S. Miyashita. Abnormal combustion detecting device for internal combustion engine and control device for internal combustion engine, March 31 2010. US Patent App. 12/999,953.
- [52] A. Ahmedi, A. Franke, H. Soyhan, F. Mauss, and B. Sunden. Prediction tool for the ion current in SI combustion. 2003.

- [53] I. Andersson. A comparison of combustion temperature models for ionization current modeling in an SI engine. 2004.
- [54] I. Andersson and L. Eriksson. A parametric model for ionization current in a four stroke SI engine. *Journal of Dynamic Systems, Measurement, and Control*, 131(2):021001, 2009.
- [55] P. Knewstubb and T. Sugden. Mass-spectrometric studies of ionization in flames. I. The spectrometer and its application to ionization in hydrogen flames. In *Proceedings of the Royal Society of London. Series A, Mathematical and Physical Sciences*.
- [56] J. Goodings, D. Bohme, and T. Sugden. Positive ion probe of methane-oxygen combustion. In *Symposium (International) on Combustion*, volume 16, pages 891–902. Elsevier, 1977.
- [57] J. Goodings, D. Bohme, and C.-W. Ng. Detailed ion chemistry in methane-oxygen flames. I. Positive ions. *Combustion and Flame*, 36:27–43, 1979.
- [58] S. De Jaegere, J. Deckers, and A. Van Tiggelen. Identity of the most abundant ions in some flames. In *Symposium (International) on Combustion*, volume 8, pages 155–160. Elsevier, 1961.
- [59] J. Green and T. Sugden. Some observations on the mechanism of ionization in flames containing hydrocarbons. In *Symposium (International) on Combustion*, volume 9, pages 607–621. Elsevier, 1963.
- [60] S. Aithal. Analysis of the current signature in a constant-volume combustion chamber. *Combustion Science and Technology*, 185(2):336–349, 2013.
- [61] P. Mehresh, D. Flowers, and R. Dibble. Experimental and numerical investigation of effect of fuel on ion sensor signal to determine combustion timing in homogeneous charge compression ignition engines. *International Journal of Engine Research*, 6(5):465–474, 2005.
- [62] S. Aithal, A. White, and V. Subramaniam. Kinetic modeling of an ionization sensor for combustion processes. In *AIAA Plasmadynamics and Lasers Conference*, page 3606. American Institute of Aeronautics & Astronautics, 1999.
- [63] F. Estefanous. Modeling of Ion Current Signal in Diesel Combustion. In *ASME 2013 Internal Combustion Engine Division Fall Technical Conference*, pages V002T06A010–V002T06A010. American Society of Mechanical Engineers, 2013.
- [64] V. Rao. *New insights into the phenomenological modelling of diesel engine NO_x and soot emissions*. PhD thesis, Monash University. Faculty of Engineering. Department of Mechanical and Aerospace Engineering, 2015.
- [65] C. T. Bowman. Control of combustion-generated nitrogen oxide emissions: technology driven by regulation. In *Symposium (International) on Combustion*, volume 24, pages 859–878. Elsevier, 1992.
- [66] J. M. Dasch. Nitrous oxide emissions from vehicles. *Journal of the Air & Waste Management Association*, 42(1):63–67, 1992.
- [67] M.-J. Poitras, D. Rosenblatt, T. W. Chan, and G. Rideout. Impact of Varying Biodiesel Blends on Direct-Injection Light-Duty Diesel Engine Emissions. *SAE Technical Paper 2012-01-1313*, 2012.
- [68] M. Koebel, M. Elsener, and T. Marti. NO_x-reduction in diesel exhaust gas with urea and selective catalytic reduction. *Combustion science and technology*, 121(1-6):85–102, 1996.
- [69] H. Yamada, K. Misawa, D. Suzuki, K. Tanaka, J. Matsumoto, M. Fujii, and K. Tanaka. Detailed analysis of diesel vehicle exhaust emissions: nitrogen oxides, hydrocarbons and particulate size distributions. *Proceedings of the Combustion Institute*, 33(2):2895–2902,

- 2011.
- [70] H. Moosmüller, W. Arnott, C. Rogers, J. Bowen, J. Gillies, W. Pierson, J. Collins, T. Durbin, and J. Norbeck. Time-resolved characterization of diesel particulate emissions. 2. Instruments for elemental and organic carbon measurements. *Environmental science & technology*, 35(10):1935–1942, 2001.
 - [71] J. Zhu, B. Aikawa, and R. Pigeon. Measurement of fine particles in diesel emissions using a real-time aerosol monitor. *Journal of the Air & Waste Management Association*, 55(7):978–983, 2005.
 - [72] E. Faghani, B. Patychuk, G. McTaggart-Cowan, and S. Rogak. Soot Emission Reduction from Post Injection Strategies in a High Pressure Direct-Injection Natural Gas Engine. *SAE Technical Paper 2013-24-0114*, 2013.
 - [73] D. C. Quiros, S. Yoon, H. A. Dwyer, J. F. Collins, Y. Zhu, and T. Huai. Measuring particulate matter emissions during parked active diesel particulate filter regeneration of heavy-duty diesel trucks. *Journal of Aerosol Science*, 73:48–62, 2014.
 - [74] J. B. Heywood. *Internal combustion engine fundamentals*, volume 930. McGraw-Hill New York, 1988.
 - [75] C. Rakopoulos, K. Antonopoulos, D. Rakopoulos, and D. Hountalas. Multi-zone modeling of combustion and emissions formation in DI diesel engine operating on ethanol–diesel fuel blends. *Energy Conversion & Management*, 49(4):625–643, 2008.
 - [76] W. H. Press, S. A. Teukolsky, W. T. Vetterling, and B. P. Flannery. *Numerical Recipes: The art of scientific computing*, 1992.
 - [77] T. Kamimoto, H. Yokota, and H. Kobayashi. Effect of high pressure injection on soot formation processes in a rapid compression machine to simulate diesel flames. Technical report, Society of Automotive Engineers, Warrendale, PA, 1987.
 - [78] B. V. Rajalingam and P. V. Farrell. The effect of injection pressure on air entrainment into transient diesel sprays. *SAE Technical Paper 1999-01-0523*, 1999.
 - [79] X. Wang, Z. Huang, O. A. Kuti, W. Zhang, and K. Nishida. Experimental and analytical study on biodiesel and diesel spray characteristics under ultra-high injection pressure. *International journal of heat and fluid flow*, 31(4):659–666, 2010.
 - [80] J. E. Dec and C. Espey. Soot and fuel distributions in a DI diesel engine via 2-D imaging. *SAE Technical Paper 922307*, 1992.
 - [81] A. Uludogan, D. E. Foster, and R. D. Reitz. Modeling the effect of engine speed on the combustion process and emissions in a DI Diesel engine. *SAE Technical Paper 962056*, 1996.
 - [82] M. Kessler. Ionenstromsensorik im dieselmotor. *Fortschritt Berichte-VDI Reihe 12 Verkehrstechnik Fahrzeugtechnik*, 2002.
 - [83] R. Rao and D. Honnery. A simplified mechanism for the prediction of the ion current during methane oxidation in engine-like conditions. *Combustion and Flame*, 162(7):2928–2936, 2015.
 - [84] J. J. Thomson. *Conduction of electricity through gases*. University press, 1903.
 - [85] P. Erman. Ueber die Fähigkeit der Flamme, der Knochen und des luftleeren Raumes, die Wirkung der Voltaischen Säule zu leiten. *Annalen der Physik*, 11:143–168, 1802.
 - [86] W. Garner and S. Saunders. Ionisation in gas explosions. *Transactions of the Faraday Society*, 22:281–288, 1926.
 - [87] S. Saunders and K. Sato. Investigations on gaseous explosions. Part III. Ionisation in explosions of carbon monoxide and oxygen. *Transactions of the Faraday Society*, 23:248–256, 1927.

- [88] W. Garner. Roffey, F. *J. Chem. Soc.*, 1929:1123, 1929.
- [89] K. Bonhoeffer and F. Haber. Band spectroscopy and flame reactions. *Z. physik. Chem. A*, 137:263, 1928.
- [90] B. Lewis and G. Von Elbe. Combustion, flames and explosions of gases, 1951.
- [91] F. Tufts. The Phenomena of Ionization in Flame Gases and Vapors. *Physical Review (Series I)*, 22(4):193, 1906.
- [92] H. Calcote. Mechanisms for the formation of ions in flames. *Combustion and Flame*, 1(4):385–403, 1957.
- [93] H. Calcote and I. King. Studies of ionization in flames by means of Langmuir probes. In *Symposium (International) on Combustion*, volume 5, pages 423–434. Elsevier, 1955.
- [94] T. Kinbara, J. Nakamura, and H. Ikegami. Seventh Symposium (International) on Combustion, 1959.
- [95] P. Knewstubb and T. Sugden. Seventh symposium (international) on combustion. *The Combustion Institute, London*, 1959.
- [96] N. Mukherjee, T. Fueno, H. Eyring, and T. Ree. Eighth Symposium (International) on Combustion. *Williams and Wilkins, Baltimore*, page 1, 1962.
- [97] J. C. Sternberg, W. S. Gallaway, and D. T. Jones. The mechanism of response of flame ionization detectors. *Gas chromatography*, pages 231–267, 1962.
- [98] E. Bulewicz and P. Padley. A cyclotron resonance study of ionization in low-pressure flames. In *Symposium (International) on Combustion*, volume 9, pages 638–646. Elsevier, 1963.
- [99] E. Bulewicz and P. Padley. A study of ionization in cyanogen flames at reduced pressures by the cyclotron resonance method. In *Symposium (International) on Combustion*, volume 9, pages 647–658. Elsevier, 1963.
- [100] E. Bulewicz and P. Padley. Suggested origin of the anomalous line-reversal temperatures in the reaction zone of hydrocarbon flames. *Combustion and Flame*, 5:331–340, 1961.
- [101] C. W. Hand and G. Kistiakowsky. Ionization accompanying the acetylene–oxygen reaction in shock waves. *The Journal of Chemical Physics*, 37(6):1239–1245, 1962.
- [102] H. Calcote. Eighth Symposium (International) on Combustion. *Williams and Wilkins, Baltimore*, page 184, 1962.
- [103] H. Calcote. Fundamental studies of ions and plasmas. In *26th Meeting of Propulsion and Energetics Panel. Agard Conf. Proc. 9*, pages 1–1, 1965.
- [104] J. Franklin. *Ion-molecule reactions*, volume 1. Springer Science & Business Media, 2012.
- [105] I. King. Comparison of ionization and electronic excitation in flames. *The Journal of Chemical Physics*, 31(3):855–855, 1959.
- [106] J. Schneider and F. Hofmann. Absorption and dispersion of microwaves in flames. *Physical Review*, 116(2):244, 1959.
- [107] L. Vanreusel and J. Delfosse. Method for extraction of ions formed in a rapid combustion. *Ann. soc. sci. Bruxelles Ser. I*, 70:67–72, 1956.
- [108] P. Knewstubb and T. Sugden. Mass-spectrometric observations of ions in flames. 1958.
- [109] P. Knewstubb and T. Sugden. Mass-spectrometric observations of ions in hydrocarbon flames. *Nature*, 181:1261, 1958.
- [110] P. Knewstubb and T. Sugden. Mass spectrometry of the ions present in hydrocarbon flames. In *Symposium (International) on Combustion*, volume 7, pages 247–253. Elsevier, 1958.

- [111] J. Deckers and A. Van Tiggelen. Extraction of ions from a flame. *Combustion and flame*, 1(3):281–286, 1957.
- [112] J. Deckers and A. Van Tiggelen. Ion identification in flames by mass spectrometry. *Nature*, 181:1460, 1958.
- [113] H. Calcote. Ion and electron profiles in flames. In *Symposium (International) on Combustion*, volume 9, pages 622–637. Elsevier, 1963.
- [114] J. Lawton and F. Weinberg. Electrical Aspects of Combustion, 1969. *London: Clarendon P. ISBN: 0-19-855341-2*, 1970.
- [115] R. C. Brown and A. N. Eraslan. Simulation of ionic structure in lean and close-to-stoichiometric acetylene flames. *Combustion and Flame*, 73(1):1–21, 1988.
- [116] J. Goodings, D. Bohme, and C.-W. Ng. Detailed ion chemistry in methane-oxygen flames. II. Negative ions. *Combustion and Flame*, 36:45–62, 1979.
- [117] A. Hayhurst. Mass spectrometric sampling of a flame. *Combustion, Explosion, and Shock Waves*, 48(5):516–525, 2012.
- [118] A. N. Hayhurst, J. M. Goodings, and S. G. Taylor. The effects of applying electric fields on the mass spectrometric sampling of positive and negative ions from a flame at atmospheric pressure. *Combustion and Flame*, 161(12):3249–3262, 2014.
- [119] P. C. Clemmow and J. P. Dougherty. *Electrodynamics of particles and plasmas*. Addison-Wesley, 1969.
- [120] P. Smy. The use of Langmuir probes in the study of high pressure plasmas. *Advances in Physics*, 25(5):517–553, 1976.
- [121] J. M. Goodings and N. S. Karellas. Correlated absolute ion density and temperature measurements in a flame plasma. *International journal of mass spectrometry and ion processes*, 62(2):199–218, 1984.
- [122] K. G. Xu. Plasma sheath behavior and ionic wind effect in electric field modified flames. *Combustion and Flame*, 161(6):1678–1686, 2014.
- [123] S. Axford and A. Hayhurst. Electrical effects during the mass spectrometric sampling of ions from hot flame gases at atmospheric pressure. *International journal of mass spectrometry and ion processes*, 110(1):31–65, 1991.
- [124] M. Mitchner and C. H. Kruger. *Partially ionized gases*, volume 8. Wiley New York, 1973.
- [125] S. Aithal. Prediction of Voltage Signature in a Homogeneous Charge Compression Ignition (HCCI) Engine Fueled with Propane and Acetylene. *Combustion Science and Technology*, 185(8):1184–1201, 2013.
- [126] C. K. Westbrook and F. L. Dryer. Simplified reaction mechanisms for the oxidation of hydrocarbon fuels in flames. *Combustion science and technology*, 27(1-2):31–43, 1981.
- [127] F. Dryer and I. Glassman. High-temperature oxidation of CO and CH₄. In *Symposium (International) on combustion*, volume 14, pages 987–1003. Elsevier, 1973.
- [128] C. K. Westbrook and F. L. Dryer. Prediction of laminar flame properties of methanol-air mixtures. *Combustion and Flame*, 37:171–192, 1980.
- [129] R. Edelman and O. Fortune. A quasi-global chemical kinetic model for the finite rate combustion of hydrocarbon fuels. In *AIAA Seventh Aerospace Sciences Meeting*, number 69-86, 1969.
- [130] D. Baulch, D. Drysdale, D. Horne, and A. Lloyd. Evaluated kinetic data for high temperature reactions, Vol. I.
- [131] D. Baulch, D. Drysdale, D. Home, and A. Lloyd. Evaluated kinetic data for high temperature reactions, Vol. 2.

- [132] D. Baulch and H. Drysdale. Evaluated Kinetic Data for High Temperature Reactions, Vol. 3.
- [133] C. Bowman, R. Hanson, D. Davidson, J. W.C. Gardiner, V. Lissianski, G. Smith, D. Golden, M. Frenklach, and M. Goldenberg. GRI-Mech 3.0, 1995.
- [134] M. Frenklach, H. Wang, C. Yu, M. Goldenberg, C. Bowman, R. Hanson, D. Davidson, E. Chang, G. Smith, D. Golden, et al. GRI-Mech 1.2, An Optimized Detailed Chemical Reaction Mechanism for Methane Combustion. *GRI Tech. Report GRI-95/0058*, 1995.
- [135] C. Bowman, R. Hanson, D. Davidson, J. W.C. Gardiner, V. Lissianski, G. Smith, D. Golden, M. Frenklach, and M. Goldenberg. GRI-Mech 2.11, 1995.
- [136] K. Hughes, T. Turanyi, A. Clague, and M. Pilling. Development and testing of a comprehensive chemical mechanism for the oxidation of methane. *International Journal of Chemical Kinetics*, 33(9):513–538, 2001.
- [137] A. Konnov. Detailed reaction mechanism for small hydrocarbons combustion, Release 0.5, 2000.
- [138] C. Chevalier. *Entwicklung eines detaillierten Reaktionsmechanismus zur Modellierung der Verbrennungsprozesse von Kohlenwasserstoffen bei Hoch- und Niedertemperaturbedingungen*. PhD thesis, Universität Stuttgart, 1992.
- [139] T. Pedersen and R. C. Brown. Simulation of electric field effects in premixed methane flames. *Combustion and Flame*, 94(4):433–448, 1993.
- [140] N. Dautov and A. Starik. On the problem of choosing a kinetic scheme for the homogeneous reaction of methane with air. *Kinetics and Catalysis*, 38(2):185–208, 1997.
- [141] A. Starik and N. Titova. Kinetics of ion formation in the volumetric reaction of methane with air. *Combustion, Explosion and Shock Waves*, 38(3):253–268, 2002.
- [142] J. Rodrigues, A. Agneray, X. Jaffrézic, M. Bellenoue, S. Labuda, C. Leys, A. Chernukho, A. Migoun, A. Cenian, A. Savel'ev, et al. Evolution of charged species in propane/air flames: mass-spectrometric analysis and modelling. *Plasma Sources Science Technology*, 16:161–172, 2007.
- [143] J. Prager, U. Riedel, and J. Warnatz. Modeling ion chemistry and charged species diffusion in lean methane–oxygen flames. *Proceedings of the Combustion Institute*, 31(1):1129–1137, 2007.
- [144] J. Warnatz, U. Maas, and R. W. Dibble. *Verbrennung*. Springer-Verlag, Berlin, Heidelberg, 400:23–50, 1997.
- [145] S. Aithal. Modeling of NO_x formation in diesel engines using finite-rate chemical kinetics. *Applied Energy*, 87(7):2256–2265, 2010.
- [146] S. R. Turns et al. *An introduction to combustion*, volume 287. McGraw-Hill New York, 1996.
- [147] S. M. Correa. A review of NO_x formation under gas-turbine combustion conditions. *Combustion science and technology*, 87(1-6):329–362, 1993.
- [148] A. Konnov. Implementation of the NCN pathway of prompt-NO formation in the detailed reaction mechanism. *Combustion and Flame*, 156(11):2093–2105, 2009.
- [149] J. Warnatz. Rate coefficients in the C/H/O system. In *Combustion chemistry*, pages 197–360. Springer, 1984.
- [150] I. Kossyi, A. Y. Kostinsky, A. Matveyev, and V. Silakov. Kinetic scheme of the non-equilibrium discharge in nitrogen-oxygen mixtures. *Plasma Sources Science and Technology*, 1(3):207, 1992.
- [151] A. Burcat and B. Ruscic. *Third millenium ideal gas and condensed phase thermochemical*

- database for combustion with updates from active thermochemical tables.* Argonne National Laboratory Argonne, IL, 2005.
- [152] R. Kee, G. Dixon-Lewis, J. Warnatz, M. Coltrin, and J. Miller. The Chemkin transport database. *Sandia Report# SAND*, pages 86–8246, 1986.
- [153] G. Rozenchan, D. Zhu, C. Law, and S. Tse. Outward propagation, burning velocities, and chemical effects of methane flames up to 60 atm. *Proceedings of the Combustion Institute*, 29(2):1461–1470, 2002.
- [154] X. Gu, M. Haq, M. Lawes, and R. Woolley. Laminar burning velocity and Markstein lengths of methane–air mixtures. *Combustion and flame*, 121(1):41–58, 2000.
- [155] W. Lowry, J. de Vries, M. Krejci, E. Petersen, Z. Serinyel, W. Metcalfe, H. Curran, and G. Bourque. Laminar flame speed measurements and modeling of pure alkanes and alkane blends at elevated pressures. *Journal of Engineering for Gas Turbines and Power*, 133(9):091501, 2011.
- [156] J. Bechtel, R. J. Blint, C. J. Dasch, and D. A. Weinberger. Atmospheric pressure premixed hydrocarbon-air flames: Theory and experiment. *Combustion and Flame*, 42:197–213, 1981.
- [157] G. Wortberg. Ion-concentration measurements in a flat flame at atmospheric pressure. In *Symposium (International) on Combustion*, volume 10, pages 651–655. Elsevier, 1965.
- [158] C. Edwards, D. L. Siebers, and D. H. Hoskin. A study of the autoignition process of a diesel spray via high speed visualization. *SAE Technical Paper 920108*, 1992.
- [159] N. Katsura, M. Saito, J. Senda, and H. Fujimoto. Characteristics of a diesel spray impinging on a flat wall. *SAE Technical Paper 890264*, 1989.
- [160] N. Shahangian, D. Honnery, and J. Ghojel. The Role of Porous Media in Homogenization of High Pressure Diesel Fuel Spray Combustion. *Journal of Energy Resources Technology*, 136(1):012202, 2014.
- [161] L. Delfau, P. Michaud, and A. Barassin. Formation of small and large positive ions in rich and sooting low-pressure ethylene and acetylene premixed flames. *Combustion Science and Technology*, 20(5-6):165–177, 1979.
- [162] R. Rao and D. Honnery. A reduced kinetic mechanism for methane oxidation. In *Proceedings of the Australian Combustion Symposium*, volume 13, pages 373–380. Combustion Institute, 2013.
- [163] F. Tao, V. I. Golovitchev, and J. Chomiak. A phenomenological model for the prediction of soot formation in diesel spray combustion. *Combustion and Flame*, 136(3):270–282, 2004.
- [164] B. Krieger and G. Borman. The computation of apparent heat release for internal combustion engines ASME paper 66 WA, 1966.
- [165] D. E. Foster. An overview of zero-dimensional thermodynamic models for IC engine data analysis. *SAE Technical Paper 852070*, 1985.
- [166] D. N. Assanis and J. B. Heywood. Development and use of a computer simulation of the turbocompounded diesel system for engine performance and component heat transfer studies. *SAE Technical Paper 860329*, 1986.
- [167] N. D. Whitehouse and B. K. Sareen. Prediction of heat release in a quiescent chamber diesel engine allowing for fuel/air mixing. *SAE Technical Paper 740084*, 1974.
- [168] S. Shahed, W. Chiu, and W. Lyn. A mathematical model of diesel combustion. In *Combustion in Engines*, pages 119–128. Inst. Mech. Engrs, 1975.
- [169] W. Chiu, S. Shahed, and W. Lyn. A transient spray mixing model for diesel combustion.

- SAE Technical Paper 760128*, 1976.
- [170] D. Kouremenos, C. Rakopoulos, and D. Hountalas. Thermodynamic analysis of indirect injection diesel engines by two-zone modeling of combustion. *Journal of engineering for gas turbines and power*, 112(1):138–149, 1990.
- [171] F. Payri, J. Benajes, and F. Tinaut. A phenomenological combustion model for direct-injection, compression-ignition engines. *Applied mathematical modelling*, 12(3):293–304, 1988.
- [172] C. Rakopoulos, D. Hountalas, G. Taklis, and E. Tzanos. Analysis of combustion and pollutants formation in a direct injection diesel engine using a multi-zone model. *International journal of energy research*, 19(1):63–88, 1995.
- [173] D. Kouremenos, C. Rakopoulos, and D. Hountalas. Multi-zone combustion modelling for the prediction of pollutants emissions and performance of DI diesel engines. *SAE Technical Paper 970635*, 1997.
- [174] C. D. Rakopoulos and D. Hountalas. Development and validation of a 3-D multi-zone combustion model for the prediction of DI diesel engines performance and pollutants emissions. *SAE Technical Paper 981021*, 1998.
- [175] Z. Gao and W. Schreiber. A multizone analysis of soot and NO_x emission in a DI diesel engine as a function of engine load, wall temperature, and intake air O_2 content. *ASME Paper*, (2000-ICE):314, 2000.
- [176] D. Jung and D. N. Assanis. Multi-zone DI diesel spray combustion model for cycle simulation studies of engine performance and emissions. *SAE Technical Paper 2001-01-1246*, 2001.
- [177] H. Hiroyasu and M. Arai. Fuel spray penetration and spray angle in diesel engines. *JSAE Transactions*, 21(5):11, 1980.
- [178] H. Hiroyasu, T. Kadota, and M. Arai. Development and Use of a Spray Combustion Modeling to Predict Diesel Engine Efficiency and Pollutant Emissions: Part 1 Combustion Modeling. *Bulletin of JSME*, 26(214):569–575, 1983.
- [179] S. Kyriakides, J. Dent, and P. Mehta. Phenomenological diesel combustion model including smoke and NO emission. *SAE Technical Paper 860330*, 1986.
- [180] Z. Bazari. A DI diesel combustion and emission predictive capability for use in cycle simulation. *SAE Technical Paper 920462*, 1992.
- [181] H. Hiroyasu and T. Kadota. Droplet size distributions in diesel engines. *SAE Transactions*, 4(342):672–684, 1974.
- [182] K. Takeuchi, J. Senda, and M. Shikuya. Transient characteristics of fuel atomization and droplet size distribution in diesel fuel spray. *SAE Technical Paper 830449*, 1983.
- [183] T. Kamimoto, S. K. Ahn, Y. J. Chang, H. Kobayashi, and S. Matsuoka. Measurement of droplet diameter and fuel concentration in a non-evaporating diesel spray by means of an image analysis of shadow photographs. *SAE Technical Paper 840276*, 1984.
- [184] J. Hodges, T. Baritaud, and T. Heinze. Planar liquid and gas fuel and droplet size visualization in a DI diesel engine. *SAE Technical Paper 910726*, 1991.
- [185] D. Kouremenos, C. Rakopoulos, and E. Yfantis. A FORTRAN program for calculating the evaporation rates in diesel engine fuel sprays. *Advances in Engineering Software*, 15(1):67–71, 1992.
- [186] D. Nguyen, D. Honnery, and J. Soria. Measuring evaporation of micro-fuel droplets using magnified DIH and DPIV. *Experiments in fluids*, 50(4):949–959, 2011.
- [187] D. Jung and D. N. Assanis. Reduced quasi-dimensional combustion model of the direct injection diesel engine for performance and emissions predictions. *KSME international*

- journal*, 18(5):865–876, 2004.
- [188] C. Rakopoulos, K. Antonopoulos, and D. Rakopoulos. Development and application of multi-zone model for combustion and pollutants formation in direct injection diesel engine running with vegetable oil or its bio-diesel. *Energy conversion and management*, 48(7):1881–1901, 2007.
- [189] S. R. Bell and J. A. Caton. Numerical simulation of a coal-fuelled compression-ignition engine. *Fuel*, 67(4):474–481, 1988.
- [190] H. Salem, S. El-Bahnasy, and M. Elbaz. Prediction of the effect of injection parameters on NO_x emission and burning quality in the direct injection diesel engine using a modified multizone model. *Proceedings of the Institution of Mechanical Engineers, Part D: Journal of Automobile Engineering*, 212(5):427–436, 1998.
- [191] M. Andersson, B. Johansson, A. Hultqvist, and C. Nöhre. A Real Time NO_x Model for Conventional and Partially Premixed Diesel Combustion. Technical report, 2006.
- [192] G. J. Rad, M. Gorjiinst, M. Keshavarz, H. Safari, and S. Jazayeri. An investigation on injection characteristics of direct-injected heavy duty diesel engine by means of multi-zone spray modeling. *Oil & Gas Science and Technology—Revue de l'IFP Energies nouvelles*, 65(6):893–901, 2010.
- [193] G. Bruneaux. Mixing process in high pressure diesel jets by normalized laser induced exciplex fluorescence part II: wall impinging versus free jet. *SAE Technical Paper 2005-01-2097*, 2005.
- [194] K. Sahetchian, N. Blin, R. Rigny, A. Seydi, and M. Murat. The oxidation of n-butane and n-heptane in a CFR engine: isomerization reactions and delay of autoignition. *Combustion and flame*, 79(3):242–249, 1990.
- [195] K. Sahetchian, R. Rigny, and S. Circan. Identification of the hydroperoxide formed by isomerization reactions during the oxidation of n-heptane in a reactor and CFR engine. *Combustion and Flame*, 85(3):511–514, 1991.
- [196] W. R. Leppard. The autoignition chemistries of primary reference fuels, olefin/paraffin binary mixtures, and non-linear octane blending. *SAE Technical Paper 922325*, 1992.
- [197] N. Blin-Simiand, R. Rigny, V. Viossat, S. Circan, and K. Sahetchian. Autoignition of hydrocarbon/air mixtures in a CFR engine: experimental and modeling study. *Combustion science and technology*, 88(5-6):329–348, 1993.
- [198] A. Cavaliere, A. Ciajolo, A. D’anna, R. Mercogliano, and R. Ragucci. Autoignition of n-heptane and n-tetradecane in engine-like conditions. *Combustion and flame*, 93(3):279–286, 1993.
- [199] H. J. Curran, P. Gaffuri, W. J. Pitz, C. K. Westbrook, and W. R. Leppard. Autoignition chemistry of the hexane isomers: An experimental and kinetic modeling study. *SAE 952406*, 1995.
- [200] D. Vermeer, J. Meyer, and A. Oppenheim. Auto-ignition of hydrocarbons behind reflected shock waves. *Combustion and Flame*, 18(3):327–336, 1972.
- [201] A. Burcat, R. F. Farmer, and R. A. Matula. Shock initiated ignition in heptane-oxygen-argon mixtures. Technical report, DTIC Document, 1981.
- [202] H. Ciezki and G. Adomeit. Shock-tube investigation of self-ignition of n-heptane-air mixtures under engine relevant conditions. *Combustion and Flame*, 93(4):421–433, 1993.
- [203] H. Curran, P. Gaffuri, W. J. Pitz, and C. K. Westbrook. A comprehensive modeling study of n-heptane oxidation. *Combustion and flame*, 114(1):149–177, 1998.
- [204] M. Mehl, W. J. Pitz, C. K. Westbrook, and H. J. Curran. Kinetic modeling of gasoline surrogate components and mixtures under engine conditions. *Proceedings of*

- the Combustion Institute*, 33(1):193–200, 2011.
- [205] A. Patel, S.-C. Kong, and R. D. Reitz. Development and validation of a reduced reaction mechanism for HCCI engine simulations. *SAE Technical Paper 2004-01-0558*, 2004.
- [206] S. Liu, J. C. Hewson, J. H. Chen, and H. Pitsch. Effects of strain rate on high-pressure nonpremixed n-heptane autoignition in counterflow. *Combustion and flame*, 137(3):320–339, 2004.
- [207] R. Seiser, H. Pitsch, K. Seshadri, W. Pitz, and H. Gurran. Extinction and autoignition of n-heptane in counterflow configuration. *Proceedings of the Combustion Institute*, 28(2):2029–2037, 2000.
- [208] S.-C. Kong, Y. Sun, and R. D. Rietz. Modeling diesel spray flame liftoff, sooting tendency, and NO_x emissions using detailed chemistry with phenomenological soot model. *Journal of Engineering for Gas Turbines and Power*, 129(1):245–251, 2007.
- [209] C. Hansen. Ionization of NO at high temperature. Technical report, NASA Grant NAG-1-1200, CR-188798, 1991.
- [210] D. Albritton. Ion-neutral reaction-rate constants measured in flow reactors through 1977. *Atomic data and nuclear data tables*, 22(1):1–89, 1978.
- [211] C. Rakopoulos, D. Rakopoulos, and D. Kyritsis. Development and validation of a comprehensive two-zone model for combustion and emissions formation in a DI diesel engine. *International journal of energy research*, 27(14):1221–1249, 2003.
- [212] B. J. McBride, M. J. Zehe, and S. Gordon. *NASA Glenn coefficients for calculating thermodynamic properties of individual species*. National Aeronautics and Space Administration, John H. Glenn Research Center at Lewis Field, 2002.
- [213] J. Ghojel, D. Honnery, and K. Al-Khaleefi. Performance, emissions and heat release characteristics of direct injection diesel engine operating on diesel oil emulsion. *Applied Thermal Engineering*, 26(17):2132–2141, 2006.
- [214] K. Mollenhauer and H. Tschöke. Handbook of Diesel Engines. *Handbook of Diesel Engines, Edited by K. Mollenhauer and H. Tschöke. Berlin: Springer, 2010.*, 1, 2010.
- [215] T. Turányi. Applications of sensitivity analysis to combustion chemistry. *Reliability Engineering & System Safety*, 57(1):41–48, 1997.
- [216] J. B. Bell, M. S. Day, J. F. Grcar, M. J. Lijewski, J. F. Driscoll, and S. A. Filatyev. Numerical simulation of a laboratory-scale turbulent slot flame. *Proceedings of the Combustion Institute*, 31(1):1299–1307, 2007.
- [217] J. Warnatz. Chemistry of high temperature combustion of alkanes up to octane. In *Symposium (International) on Combustion*, volume 20, pages 845–856. Elsevier, 1985.
- [218] L. C. Haber, U. Vandsburger, W. R. Saunders, and V. K. Khanna. An examination of the relationship between chemiluminescent light emissions and heat release rate under non-adiabatic conditions. In *ASME Turbo Expo 2000: Power for Land, Sea, and Air*, pages V002T02A041–V002T02A041. American Society of Mechanical Engineers, 2000.
- [219] Y. Hardalupas and M. Orain. Local measurements of the time-dependent heat release rate and equivalence ratio using chemiluminescent emission from a flame. *Combustion and Flame*, 139(3):188–207, 2004.
- [220] H. Anders, M. Christensen, B. Johansson, A. Franke, M. Richter, and M. Aldén. A study of the homogeneous charge compression ignition combustion process by chemiluminescence imaging. *SAE Technical Paper 1999-01-3680*, 1999.
- [221] T. Lieuwen and Y. Neumeier. Nonlinear pressure-heat release transfer function measurements in a premixed combustor. *Proceedings of the Combustion Institute*, 29(1):99–105, 2002.

- [222] J. E. Dec and R. E. Canaan. PLIF imaging of NO formation in a DI diesel engine. *SAE Technical Paper 980147*, 1998.
- [223] P. Anyon, S. Brown, D. Pattison, J. Beville-Anderson, G. Walls, and M. Mowle. Proposed Diesel Vehicle Emissions, National Environment Protection Measure: Preparatory Work. In-service emissions performance. Technical report, National Environment Protection Council, 2000.
- [224] B. Giechaskiel, M. Maricq, L. Ntziachristos, C. Dardiotis, X. Wang, H. Axmann, A. Bergmann, and W. Schindler. Review of motor vehicle particulate emissions sampling and measurement: From smoke and filter mass to particle number. *Journal of Aerosol Science*, 67:48–86, 2014.
- [225] H. Calcote and D. Keil. Ion-molecule reactions in sooting acetylene-oxygen flames. *Combustion and flame*, 74(2):131–146, 1988.
- [226] P. Michaud, J. Delfau, and A. Barassin. The positive ion chemistry in the post-combustion zone of sooting premixed acetylene low pressure flat flames. In *Symposium (International) on Combustion*, volume 18, pages 443–451. Elsevier, 1981.
- [227] V. Hall-Roberts, A. Hayhurst, D. Knight, and S. Taylor. The origin of soot in flames: Is the nucleus an ion? *Combustion and flame*, 120(4):578–584, 2000.
- [228] A. Warey and M. J. Hall. Performance characteristics of a new on-board engine exhaust particulate matter sensor. *SAE Technical Paper 2005-01-3792*, 2005.
- [229] T. Ochs, H. Schittenhelm, A. Genssle, and B. Kamp. Particulate matter sensor for on board diagnostics (OBD) of diesel particulate filters (DPF). *SAE International Journal of Fuels and Lubricants*, 3(2010-01-0307):61–69, 2010.
- [230] D. E. Rumelhart, G. E. Hinton, and R. J. Williams. Learning representations by back-propagating errors. *Cognitive modeling*, 5:3, 1988.
- [231] M. Riedmiller and H. Braun. A direct adaptive method for faster backpropagation learning: The RPROP algorithm. In *Neural Networks, 1993., IEEE International Conference on*, pages 586–591. IEEE, 1993.
- [232] J. J. Moré. The Levenberg-Marquardt algorithm: implementation and theory. In *Numerical analysis*, pages 105–116. Springer, 1978.
- [233] P. Shayler, M. Goodman, and T. Ma. Transient air/fuel ratio control of an SI engine using neural networks. *SAE Technical Paper 960326*, 1996.
- [234] J. R. Asik, J. M. Peters, G. M. Meyer, and D. X. Tang. Transient A/F estimation and control using a neural network. *SAE Technical Paper 970619*, 1997.
- [235] U. Lenz and D. Schröder. Air-fuel ratio control for direct injecting combustion engines using neural networks. *SAE Technical Paper 981060*, 1998.
- [236] G. Thompson, C. Atkinson, N. Clark, T. Long, and E. Hanzevack. Technical Note: Neural network modelling of the emissions and performance of a heavy-duty diesel engine. *Proceedings of the Institution of Mechanical Engineers, Part D: Journal of Automobile Engineering*, 214(2):111–126, 2000.
- [237] A. de Lucas, A. Durán, M. Carmona, and M. Lapuerta. Modeling diesel particulate emissions with neural networks. *Fuel*, 80(4):539–548, 2001.
- [238] S. Leonhardt, C. Ludwig, and R. Schwarz. Real-time supervision for diesel engine injection. *Control Engineering Practice*, 3(7):1003–1010, 1995.
- [239] M. Hafner, M. Schöler, O. Nelles, and R. Isermann. Fast neural networks for diesel engine control design. *Control Engineering Practice*, 8(11):1211–1221, 2000.
- [240] M. L. Traver, R. J. Atkinson, and C. M. Atkinson. Neural Network-Based Diesel Engine Emissions Prediction Using In-Cylinder Combustion Pressure. *SAE Technical Paper*

- 1999-01-1532, 1999.
- [241] Y. He and C. Rutland. Application of artificial neural networks in engine modelling. *International Journal of Engine Research*, 5(4):281–296, 2004.
 - [242] S. Nissen. Implementation of a fast artificial neural network library (FANN). *Report, Department of Computer Science University of Copenhagen (DIKU)*, 31, 2003.
 - [243] C. Igel and M. Hüsken. Empirical evaluation of the improved RPROP learning algorithms. *Neurocomputing*, 50:105–123, 2003.
 - [244] N. K. Treadgold and T. D. Gedeon. A cascade network algorithm employing progressive RPROP. In *Biological and Artificial Computation: From Neuroscience to Technology*, pages 733–742. Springer, 1997.
 - [245] I. Ahmad, S. U. Swati, and S. Mohsin. Intrusions Detection Mechanism by Resilient Back Propagation (RPROP). *European Journal of Scientific Research ISSN*, pages 523–531, 2005.
 - [246] B. A. Souza, N. D. Brito, W. L. Neves, K. M. Silva, R. B. Lima, and S. S. da Silva. Comparison between backpropagation and RPROP algorithms applied to fault classification in transmission lines. In *Neural Networks, 2004. Proceedings. 2004 IEEE International Joint Conference on*, volume 4, pages 2913–2918. IEEE, 2004.
 - [247] A. Kantsila, M. Lehtokangas, and J. Saarinen. Complex RPROP-algorithm for neural network equalization of GSM data bursts. *Neurocomputing*, 61:339–360, 2004.
 - [248] J. He, T. Jiang, and Z. Xing. A method of target detection and identification based on RPROP and UWB channel characteristic parameters. In *Globecom Workshops (GC Wkshps), 2012 IEEE*, pages 1460–1463. IEEE, 2012.
 - [249] A. Yule and I. Filipovic. On the break-up times and lengths of diesel sprays. *International journal of heat and fluid flow*, 13(2):197–206, 1992.

Appendix A

Further diesel engine measurements

A.1 Introduction

This appendix contains experimental data collected on the Hino engine used in this study that are not presented in Chapter 2. These measurements are useful in characterising the engine and as inputs to the diesel engine model described in Chapter 5 but are not directly relevant to the measurement of the ion current.

A.2 Inputs to model

Experimental results required as inputs to the engine model described in Chapter 5 are the start and end of the injection period (SOI and EOI), the air-fuel ratio and the pressure at 130 CAD, P_{130} . The inputs for various values of engine speed and load are tabulated in Table A.1.

A.3 Engine characterisation

A.3.1 Air and fuel input

Diesel engines control power generation simply by limiting the fuel mass injected; they therefore have nearly constant volumetric efficiency. Given a constant ambient temperature, this leads to a certain mass of air present in the cylinder when the intake valve closes, irrespective of engine load and speed. Figure A.1(a) shows the volumetric

Table A.1: Model inputs.

Engine speed RPM	Torque Nm	SOI CAD	EOI CAD	AFR	P ₁₃₀ bar
1200	100	166.8	173.4	54.9	6.55
	140	166.6	174.4	41.8	6.54
	180	166.8	176.2	31.1	6.50
1600	80	168.0	177.2	65.4	6.20
	100	168.0	178.0	52.4	6.18
	120	167.6	178.0	46.0	6.16
	140	167.2	178.8	38.8	6.11
	160	166.8	178.8	35.1	6.11
	180	166.6	179.0	31.1	6.19
1800	100	168.8	178.8	51.4	6.55
	140	168.0	180.0	40.1	6.70
	180	167.6	180.8	31.5	6.72

flow rate and the volumetric efficiency over a range of engine speeds at a constant engine-out torque of 140 Nm. Figure A.1(b) shows the same parameters at a constant engine speed of 1600 RPM for varying engine-out torque. The Hino W04D has a fairly constant volumetric efficiency between 91% and 94% across a wide range of engine speeds and loads.

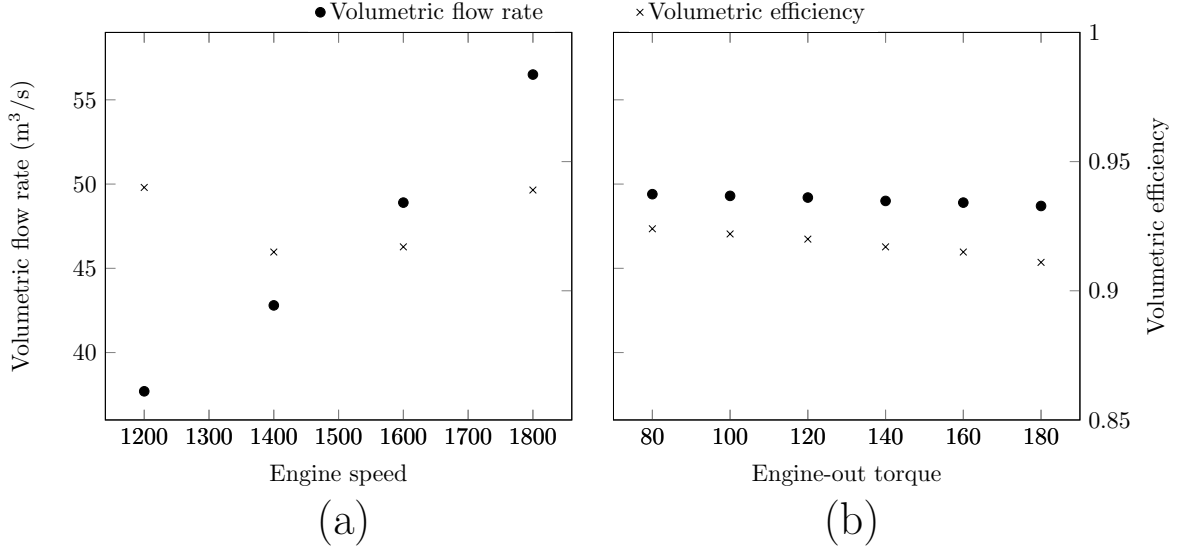


Figure A.1: Volumetric flow rate and volumetric efficiency for varying speed at 140 Nm (a) and varying load at 1600 RPM (b).

The air-fuel ratio by mass for varying engine speed at a constant torque (140 Nm) and for varying engine-out torque at constant speed (1600 RPM) is shown in Figure A.2 (a) and (b). Air-fuel ratio is found to be minimally affected by changes in engine

speed, but to vary linearly with engine-out torque ($r^2 = 0.96$).

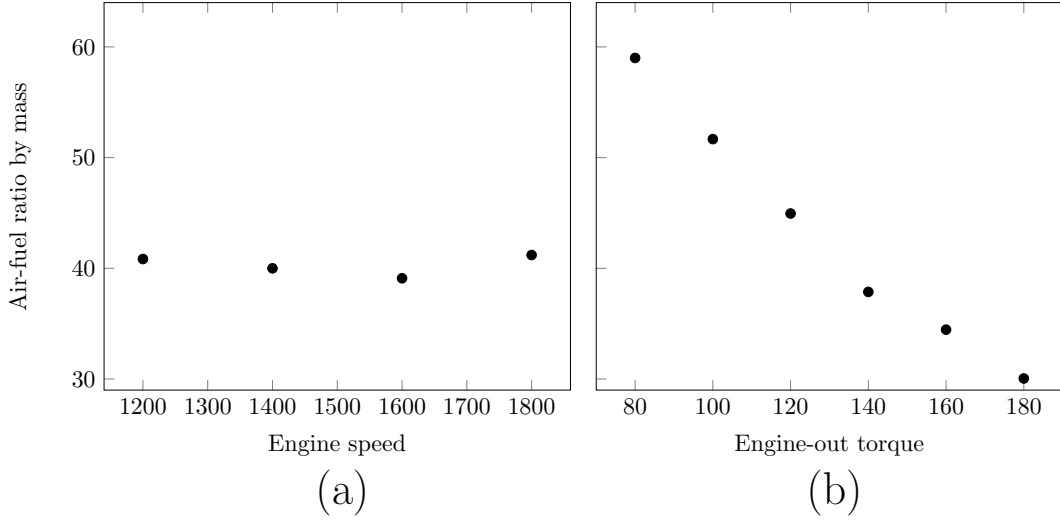


Figure A.2: Air-fuel ratio for varying speed at 140 N m (a) and varying load at 1600 RPM (b).

A.3.2 Injection process

The Hino W04D engine used in this study uses a pump in-line injection system. Injection pressure is not constant as in common-rail fuel injection systems; instead, a camshaft in the injector pump forces an injection cylinder to compress fuel in the fuel line to each cylinder. The pressure wave then travels up the fuel line towards the injector, causing it to open at a specified pressure. The needle opening pressure for the factory injectors specified for this engine is 220 bar.

Figure A.3 shows the profile of injector needle lift at 1600 RPM, 140 Nm. The units on the y -axis are arbitrary. Important points on the profile are marked — start of injection, end of injection and the injection duration.

Figure A.4 shows the variation in start of injection and injection duration over a range of torque values for three different engine speeds. The injector generally opens earlier at lower engine speeds and for a slightly shorter duration. This is seen most clearly in the 1200 RPM case. The 1600 RPM and 1800 RPM cases show more similarity. The injection duration increases significantly as engine-out torque is increased and the start of injection is advanced slightly.

The high pressure fuel line to cylinder 1 is fitted with a pressure transducer. Figures A.5 (a) and (b) show the fuel pressure in the injection line for varying engine speed

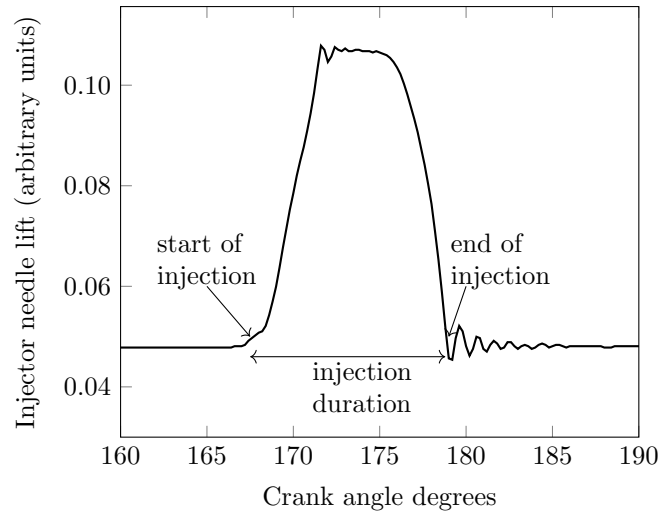


Figure A.3: Injector needle lift profile at 1600 RPM, 140 Nm with important injection parameters marked.

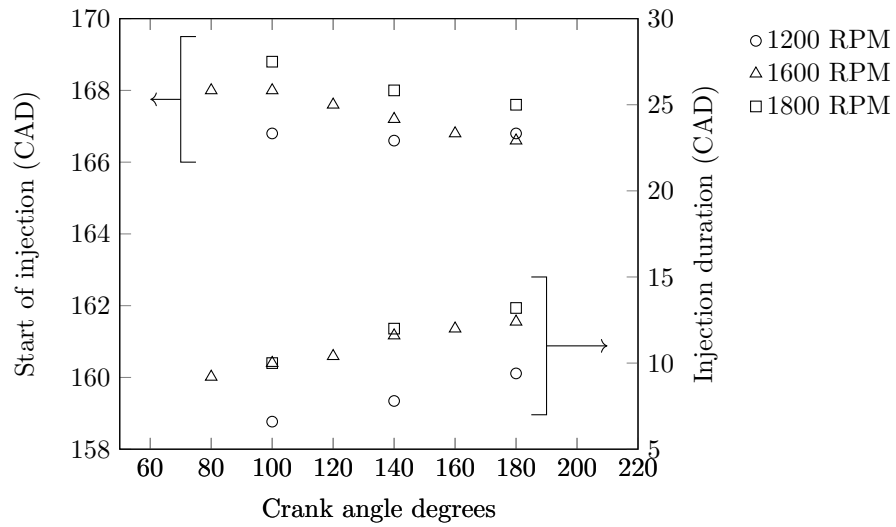


Figure A.4: Variation in start of injection and injection duration for 1200 RPM, 1600 RPM and 1800 RPM.

and torque. The significant increase in peak fuel injection pressure at higher torque values can also be seen in Figure A.5 (b).

The average pressure in the injection line for different values of engine-out torque is shown in Table A.2, along with the crank angle at the start and end of injection. This clearly illustrates the dependence of both injection duration and mean injection pressure on load.

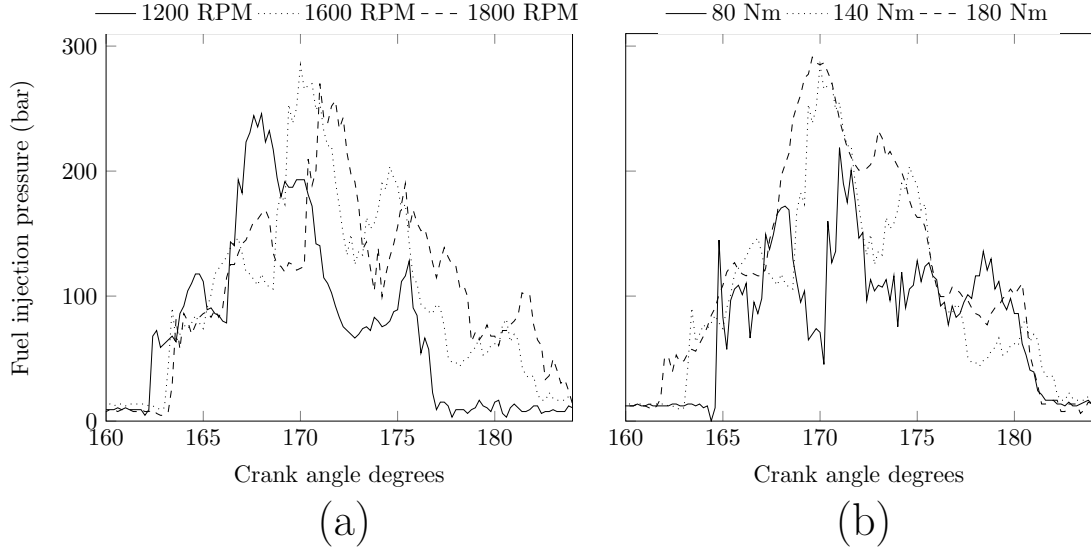


Figure A.5: Fuel pressure in high pressure line for varying speed at 140 N m (a) and varying load at 1600 RPM (b).

Table A.2: Injection parameters for different engine-out torque values at 1600 RPM.

Torque Nm	Start of injection CAD	Injection duration CAD	Mean injection pressure bar
80	168.0	9.2	118.15
140	167.2	11.6	148.09
180	166.6	12.4	185.63

A.3.3 In-cylinder parameters

The in-cylinder parameters of interest are pressure and ion current. Rate of heat release can be calculated from the pressure as described in Chapter 2. The requirement of the time derivative of the pressure signal to calculate heat release presents minor difficulties — the pressure signal is subject to high frequency noise that has significant effects on its derivative. A low pass Fourier filter [76] is therefore used to process the pressure signal for calculation of the heat release rate. Figure A.6 shows a comparison between the original and the filtered pressure signals, indicating that the signal remains generally unchanged by the filtering process.

Figures A.7–A.14 show experimental measurements made of in-cylinder parameters at different engine operating points.

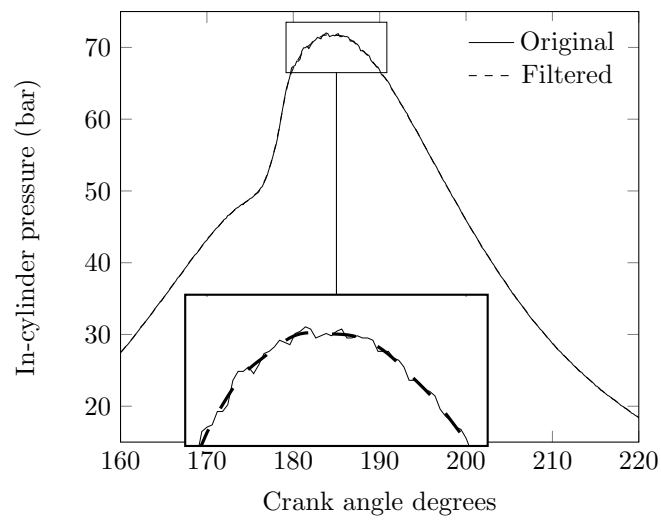


Figure A.6: Comparison of the original and filtered pressure signals at 1800 RPM and 140 Nm.

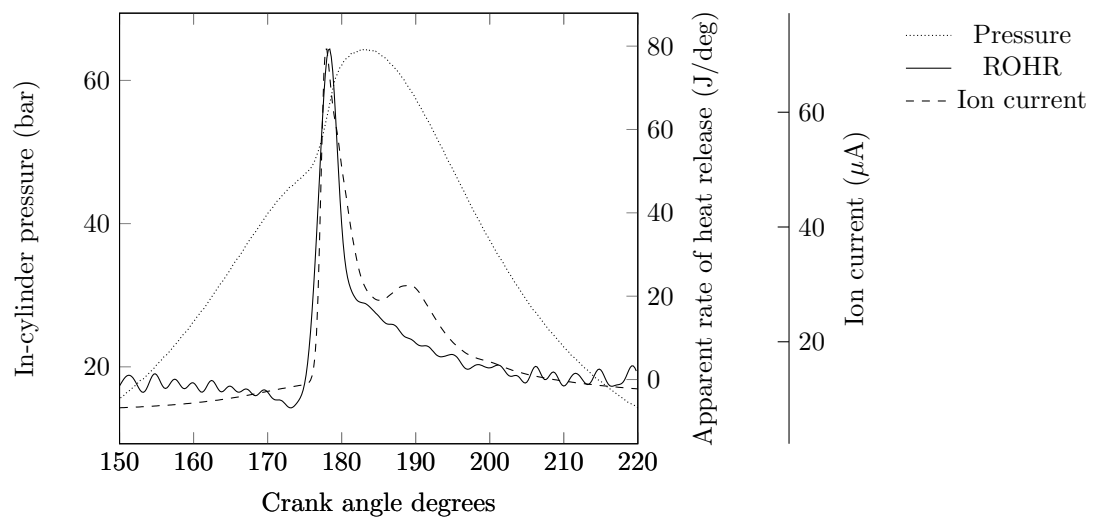


Figure A.7: In-cylinder pressure, rate of heat release and ion current measured at 1600 RPM, 80 Nm.

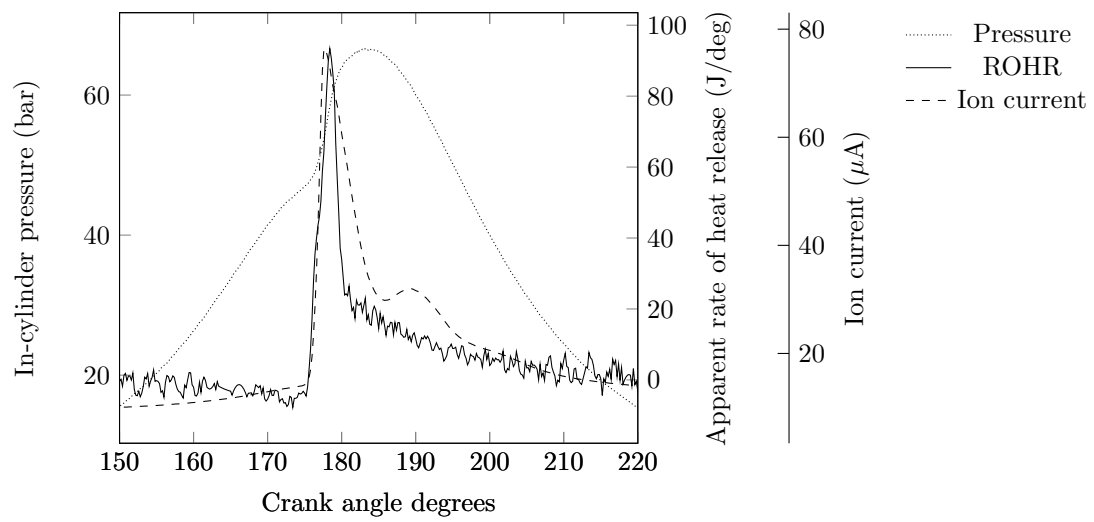


Figure A.8: In-cylinder pressure, rate of heat release and ion current measured at 1600 RPM, 100 Nm.

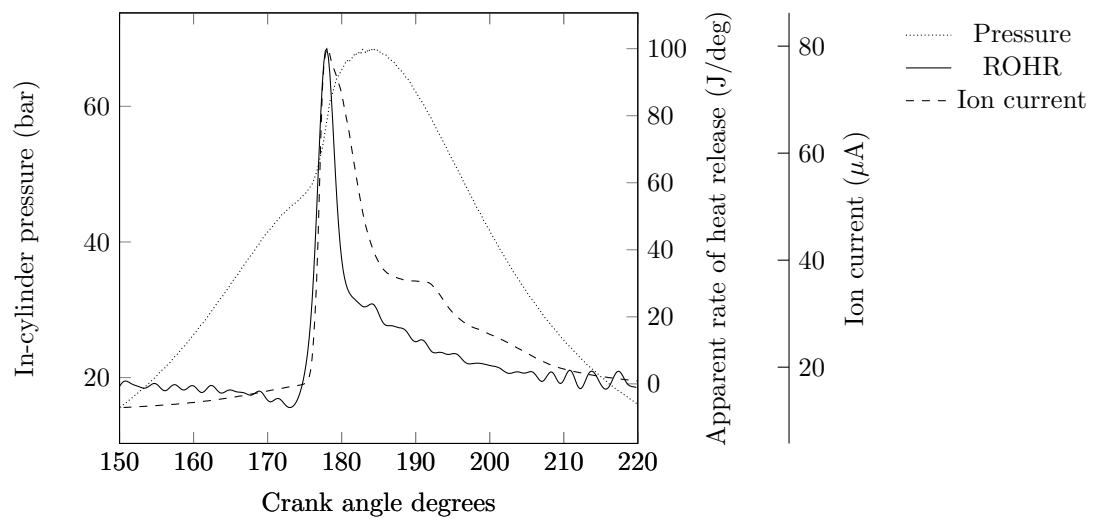


Figure A.9: In-cylinder pressure, rate of heat release and ion current measured at 1600 RPM, 120 Nm.

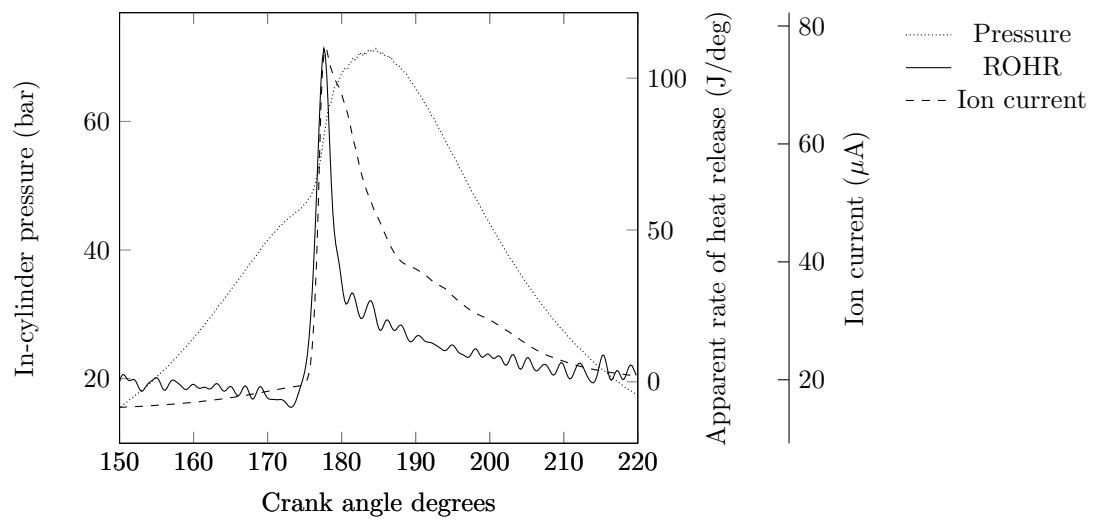


Figure A.10: In-cylinder pressure, rate of heat release and ion current measured at 1600 RPM, 140 Nm.

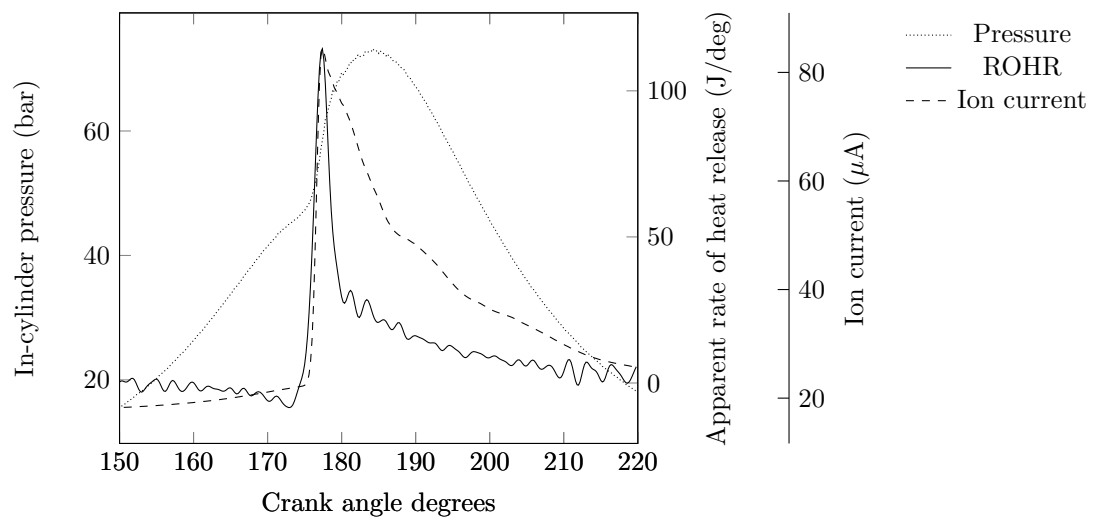


Figure A.11: In-cylinder pressure, rate of heat release and ion current measured at 1600 RPM, 160 Nm.

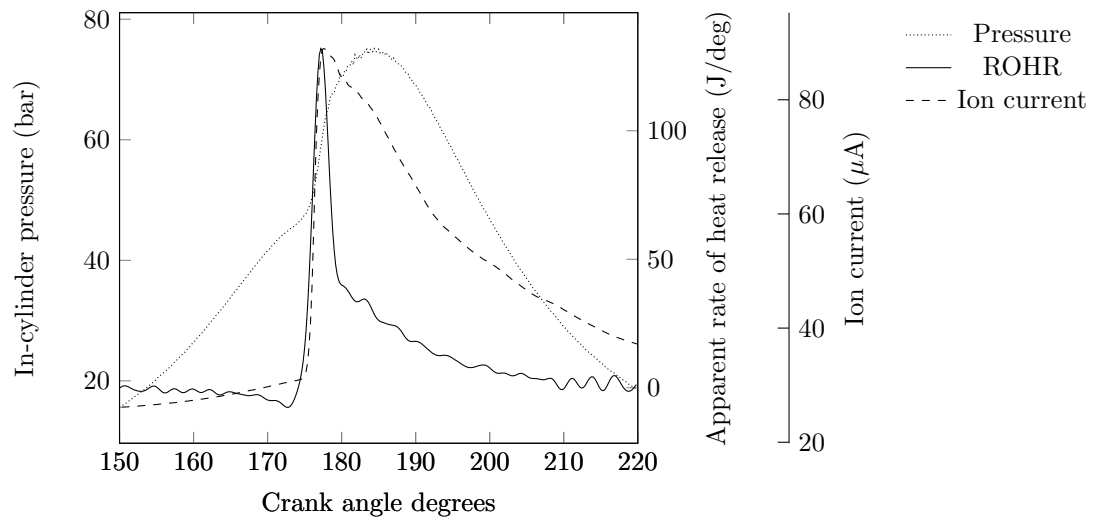


Figure A.12: In-cylinder pressure, rate of heat release and ion current measured at 1600 RPM, 180 Nm.

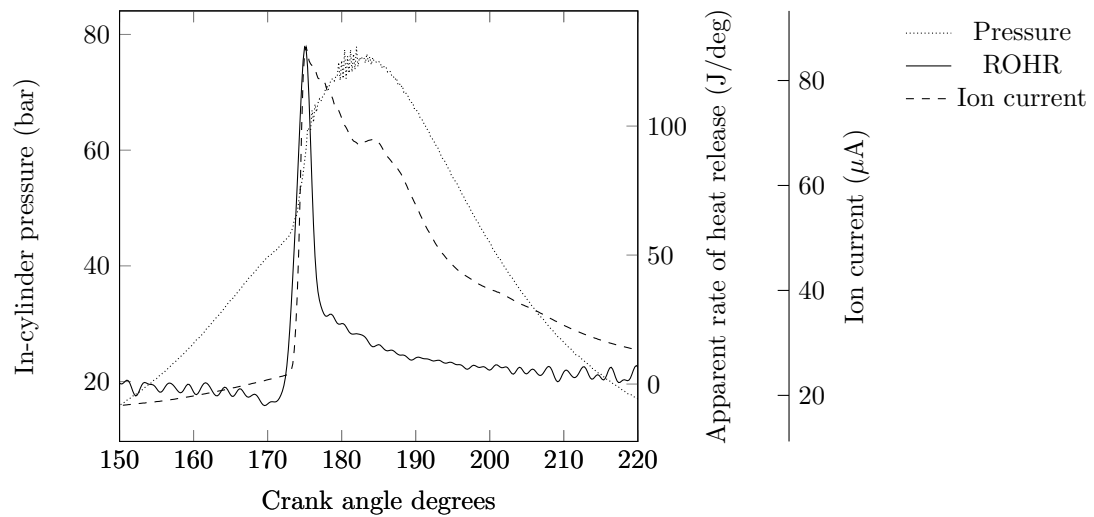


Figure A.13: In-cylinder pressure, rate of heat release and ion current measured at 1200 RPM, 140 Nm.

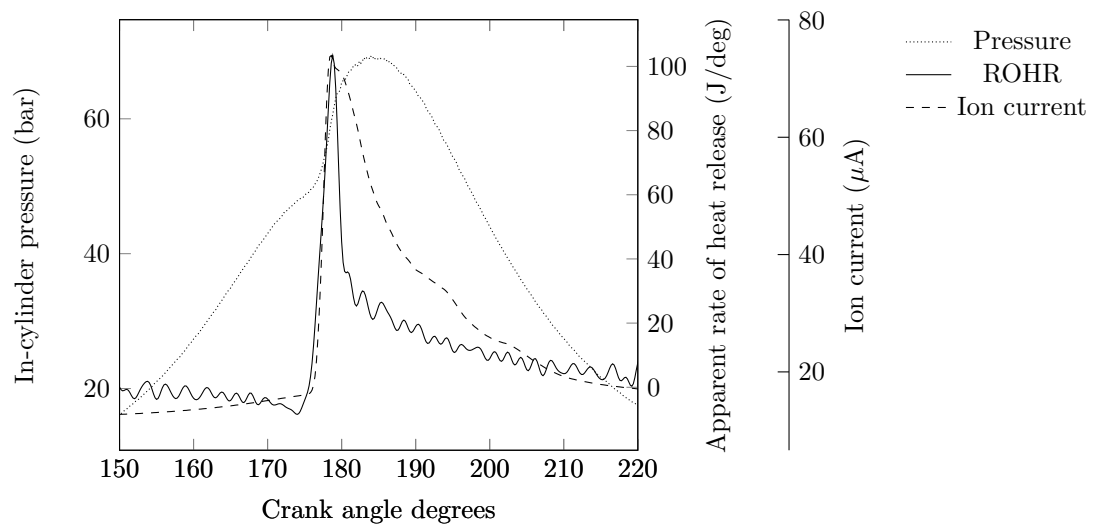


Figure A.14: In-cylinder pressure, rate of heat release and ion current measured at 1800 RPM, 140 Nm.

Appendix B

Prediction of engine performance

B.1 Introduction

The measurement of engine performance parameters is an integral part of engine evaluation. Measures such as engine-out torque, engine speed, peak cylinder pressure, peak rate of heat release, combustion timing and fuel consumption are useful tools in quantifying engine performance. Engine-out torque and engine speed are measured by a dynamometer such as the Heenan Froude unit used in this study. Cylinder pressure is measured by a pressure transducer inserted into the glow plug port in diesel engines, like the AVL instruments used here. Post-processing of these measurements allows the determination of rate of heat release and combustion timing, as described in Chapter 2. Instruments such as a mass balance can be used to measure fuel consumption.

The engine-out torque is of interest in this study; it is closely related to heat release in the engine cylinder during combustion and, given the link between the ion current and heat release shown in Chapter 6, must be related the ion current also. This appendix details the prediction of engine-out torque using the ion current. Aspects of this appendix have been published previously in Rao & Honnery [2] and are presented here mostly unchanged.

B.2 Artificial neural networks

Given the complex nature of losses between heat release and the production of torque, a statistical method may be of use in the prediction of engine-out torque from an in-cylinder variable such as the ion current.

Artificial neural networks (ANNs) are a family of statistical machine learning techniques that have been used widely in the processing of complex data signals and are used here. An ANN consists of two or more layers, each with a set number of nodes ('neurons'). Each node is connected to all nodes in both adjacent layers with a given weighting. This differing weighting gives each node the ability to act as a non-linear summing device. When presented with several samples of the input and the expected output, the weights can be adjusted via a training algorithm. Training allows ANNs to classify objects, recognise patterns, predict values and approximate functions.

Training requires that a set of data (the 'training set') be available whose inputs and outputs are both known. The initial values of the weights w_i are assigned randomly and the outputs for a given set of inputs calculated. These outputs are compared to the known outputs to obtain a least squares cost function. For a training set with N instances, known outputs $y_{m,i}$ and predicted outputs $y_{p,i}$, the least squares cost function $J(\mathbf{w})$ for a given set of weights \mathbf{w} is given by Equation B.1.

$$J(\mathbf{w}) = \sum_{i=1}^N (y_{m,i} - y_{p,i})^2 \quad (\text{B.1})$$

There exist several different training algorithms for ANNs, most based on a gradient descent method to find the minimum of the error between the prediction and the given output. Backpropagation [230] is a popular method used to evaluate the gradient of the error function. Using this method, the gradient of the cost function is evaluated for each instance of input and output in the training set in two steps; first a propagation phase, where the potentials and the outputs of all neurons are calculated moving from input to output; second, a backpropagation phase where the values of the partial cost functions are computed and the total cost function found by summation. Simple gradient descent [230], resilient backpropagation [231] and Levenberg-Marquardt [232] are some of the more popular backpropagation algorithms in use.

Training is considered to be complete when the least squares cost function $J(\mathbf{w})$ drops below a pre-determined value known as the training error. The ANN can then be used to predict outputs from a different set of inputs known as the test set to gauge its performance.

ANNs are employed in this study to predict torque from the ion current. These networks have seen wide use in empirical engine-related applications such as the estimation and control of the air-fuel ratio [233–235]. This has been shown to be possible even during transient engine operation. When used with the ion current, ANNs have been able to predict the air-fuel ratio in SI engines to an accuracy of 2.1%

[19]. Fuel properties and engine emissions with different fuels have been predicted successfully using ANNs [236, 237]. They have also been used in the supervision and control of injection in diesel engines [238, 239]. Traver et al. [240] used ANNs to predict NO_x and CO_2 emissions from a diesel engine using the in-cylinder pressure as input. Soot emissions, in-cylinder pressure, temperature and heat transfer have also been predicted using some simple variables such as engine speed, load, injection timing and injection pressure as inputs [241].

The Fast Artificial Neural Network (FANN) library [242] is used to train and test the neural networks considered in this study. The training algorithm used is resilient back-propagation (RPROP) [231] — this algorithm is considered to be a good compromise between speed, accuracy and robustness [243] and is therefore widely used in several fields utilising ANNs [244–248].

B.3 Prediction of engine-out torque

The prediction of torque is performed at fifteen engine operating conditions: eleven torque settings at 1600 RPM and four speed settings at 140 Nm. These are summarised in Table B.1. Four data sets of 180 cycles each were taken at each engine operating point. Each cycle consisted of ion current readings at 0.2 CAD intervals for 720 CAD, the entire engine cycle including the intake and exhaust strokes.

Table B.1: Engine operating points tested for prediction of engine speed and torque.

Speed (RPM)		Torque (Nm)
1200		140
1400		140
1600	12, 20, 30, 40, 60, 80, 100, 120, 140, 160, 180	
1800		140
2000		140

The training set for the ANN comprises three data sets of 180 consecutive engine cycles each, at each of the fifteen engine operating points — 540 engine cycles at each operating point are used to train the ANN. The performance of the ANN is tested over the remaining set of 180 cycles at each operating point. The prediction error e_y of the ANN is determined by the value of the RMS error in prediction of torque for a single cycle at each operating point. It is defined in Equation B.2.

$$e_y = \sqrt{\frac{\sum_{i=1}^{180} (y_i - Y)^2}{180}} / Y \quad (\text{B.2})$$

where y_i is the predicted torque for cycle i and Y is the measured torque at that engine operating point.

The ANN is defined with 3600 input nodes (720 CAD of ion current measurements at a resolution of 0.2 CAD) and one output node (engine-out torque). Two important variables that affect the performance of an ANN are its topology and the error to which it is trained, e_{TR} . The effects of these are explored in later sections.

Figure B.1 shows the error in prediction of engine torque at 1600 RPM with varying torque (a) and at 140 Nm with varying speed (b) for a network with 4 hidden layers with 20 nodes in each layer, $e_{TR} = 4.4\%$. It is observed that the error bears no significant relationship to torque, with errors of < 12 Nm observed across the torque range tested. A consequence of this is that the error is a large fraction of the predicted value at low values of torque. At idle (12 Nm), the prediction error reaches a maximum of 67%. Prediction accuracy also bears little relation to engine speed and is below 14% over the speed range tested.

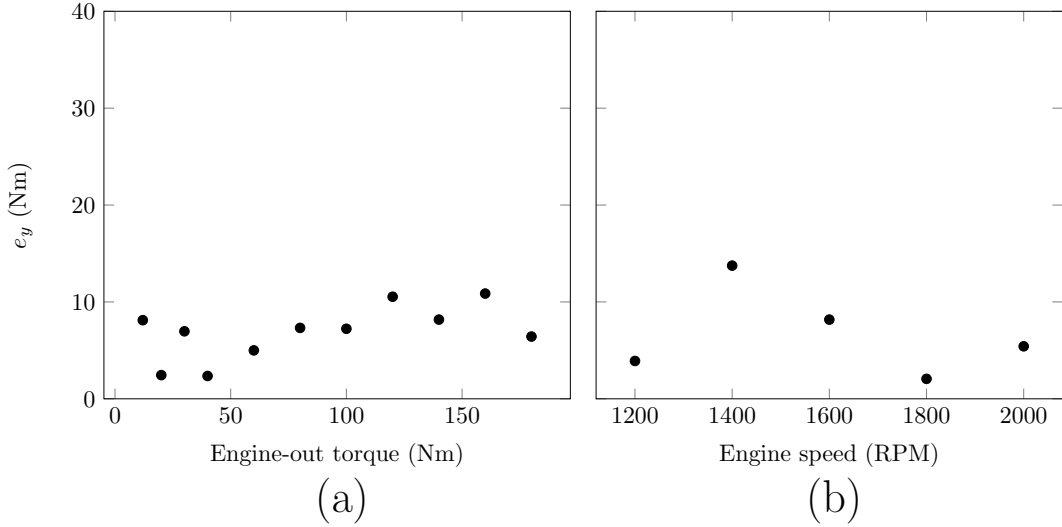


Figure B.1: Torque prediction error of a four layer, 20 neuron ANN at 1600 RPM, varying engine torque (a) and 140 Nm, varying engine speed (b) [2].

Prediction accuracy for an ANN depends on the strength of the relationship between the input and output signals. The strength of the relationship between the ion current and the engine-out torque is affected by two phenomena:

1. The engine-out torque is not directly related to the heat release, whilst the ion

current is. In the conversion of in-cylinder heat release to engine-out torque, several processes must occur that alter the amount of energy transferred to the flywheel of the engine: operation of the fuel, oil and water pumps, pumping losses from the transport of gases, driving of the camshaft and alternator and frictional losses in all moving components. These losses are non-linear and are not simple functions of torque or speed. If load is increased while speed is held constant, a greater fraction of energy from heat release is transferred to the flywheel. At high load, it would be expected that the relationship between the engine-out torque and the heat release (and therefore the ion current) would be strong. At very low load (such as idle), it would be expected that this relationship would be weak — losses account for nearly all of the heat release.

2. The engine-out torque is a measure of the performance of the engine as a whole. For multi-cylinder engines, therefore, it is an average of the performance of all cylinders. In this study, the torque is averaged over four cylinders, while the ion current is measured only in one. Constant differences between cylinders are implicitly modelled in the ANN approach; however, when the differences between cylinders vary with time, prediction errors can increase. Furthermore, given the significant rotating mass of the flywheel and crankshaft, the torque measured at the dynamometer is smoothed in time. Cycle-to-cycle variations in heat release may be observable in in-cylinder measurements but they will not manifest in torque measurements given the measurement technique used. However, given the extremely repeatable nature of the in-cylinder pressure signal, this effect is thought to be minor.

Point 1 above is illustrated by the dramatic increase in percentage prediction error at low values of torque.

It must be noted here that the use of an ANN requires the selection of initial weights for each node; these are usually chosen randomly, as here. The predictions, therefore, of two ANNs trained to the same error on the same training set are not necessarily identical, depending on the sensitivity to the initial choice of weights. In this study, high sensitivity of prediction error to the initial choice of weights was only observed for low values of torque (12–40 Nm). A comparison of the predictions for three values of torque (12 Nm, 100 Nm and 180 Nm) from ten ANNs with a different choice of initial weights but identical in topology and training error is shown in Figure B.2.

To mitigate the effect of randomly-chosen initial weights, prediction error was calculated as the mean prediction error of ten ANNs of the same topology and training error at each engine operating point.

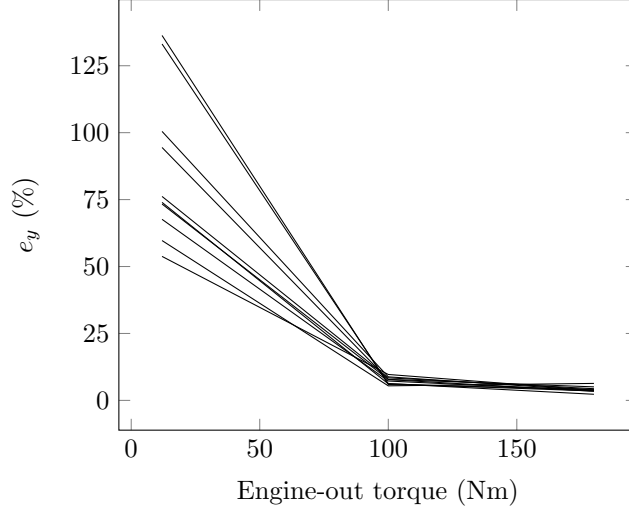


Figure B.2: Prediction errors of ten artificial neural networks with identical topologies and training errors for 12 Nm, 100 Nm and 180 Nm [2].

B.4 Prediction of in-cylinder measures of performance

For reasons described previously, the strength of the relationship between the ion current and torque depends on the load the engine is subjected to. The net indicated mean effective pressure (IMEP) P_i is an in-cylinder parameter that does not include several of the losses inherent in the torque measurement — power drawn by engine accessories and frictional losses. It would therefore be expected that the ion current would be better able to predict net IMEP than engine-out torque.

This approach can be extrapolated and the expansion work w_e , given by the area under the $P - v$ curve on the power stroke, calculated. This removes losses due to pumping work in the transport of gases and work done and heat lost on the compression stroke. It would be expected that the prediction error for w_e would be lower than that for either torque or net IMEP.

The prediction errors for these two quantities, e_P and e_w respectively, are calculated in the same way as that for torque (Equation B.2). Figure B.3 shows the prediction error for these quantities for varying engine-out torque. The results agree with expectations — as with e_y , e_P shows significantly increased error at idle but is much less dependent on torque than is e_y ; e_w is virtually independent of torque over the entire range tested.

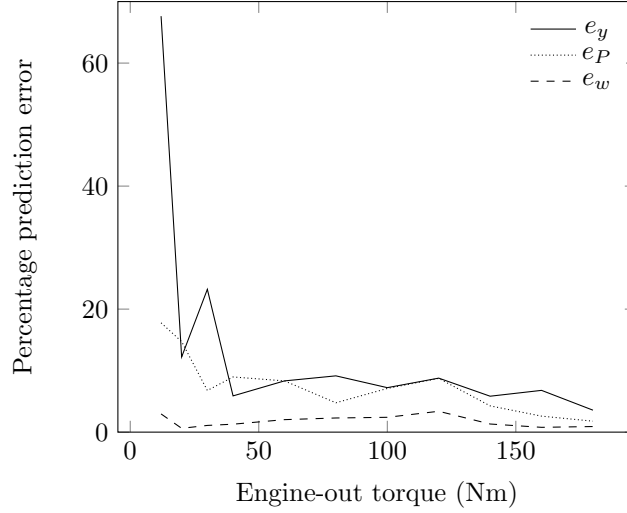


Figure B.3: Error in prediction of engine-out torque, net IMEP and expansion work when a four layer, 20 neuron ANN is used [2].

B.5 Analysis of ANN techniques for engine-related applications

This section provides a brief analysis of the user-defined variables affecting the performance of ANNs when used for prediction with the ion current, viz. the topology and the training error. For these studies, only the torque range 80–180 Nm was chosen for training and prediction.

B.5.1 Effect of ANN topology

ANN topologies vary widely with a variable number of hidden layers and hidden nodes. With an increasing number of hidden layers and nodes, the ANN gains degrees of freedom, enabling the more accurate fitting of a curve to the given training set. This, however, comes with two caveats:

- Any measurement noise or stochastic component of the signal is also fitted, leading to overfitting of the curve for input data where these form a large component of the signal.
- Extra complexity in ANN topology results in large increases in the time required for training and prediction. Small increases in training time are magnified when large training sets are used, as for most industrial applications to ensure robustness of predictions.

Four topologies of ANNs were used to determine the effect of changing complexity on the prediction accuracy — ANNs with three or four hidden layers, and 20 or 30 hidden nodes. The error in torque prediction for these four topologies at moderate-to-high torque settings is shown in Figure B.4 for $e_{TR} = 7.0\%$.

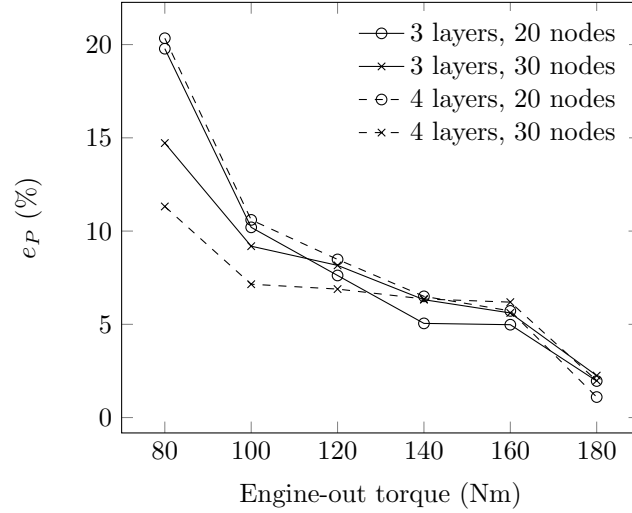


Figure B.4: Comparison of prediction performance of ANNs with different topologies at moderate-to-high torque settings. $e_{TR} = 7.0\%$. Figure taken from Rao & Honnery [2]

The percentage error can be seen to generally decrease with an increase in torque, as seen in Figures B.1 and B.3. A comparison of different numbers of hidden nodes shows that the 30-node networks produce lower error at low torque settings; this is to be expected given the additional degrees of freedom they possess over 20-node networks. Above 120 Nm, there is little difference between the four networks. There is no clear effect of changing the number of hidden layers.

B.5.2 Effect of training error

The objective of training an ANN is to minimise the error between predictions made on the basis of training set inputs and the actual training set outputs provided. Each training iteration involves the calculation of the error and the updating of the weight of each node to minimise the error. Training is complete when the calculated error is below the maximum permissible training error e_{TR} .

A lower value of e_{TR} would be expected to produce a lower average prediction error on the test data set, assuming the training set and test set are similar. This is found to hold true over the range of training errors tested in this study, as shown in Figure B.5, generated using a four-layer network with 20 nodes in each layer. The same trend

seen before of reducing error with increasing torque is also seen here. The minimum training error obtainable with this network was 4.4% — below this training failed to converge.

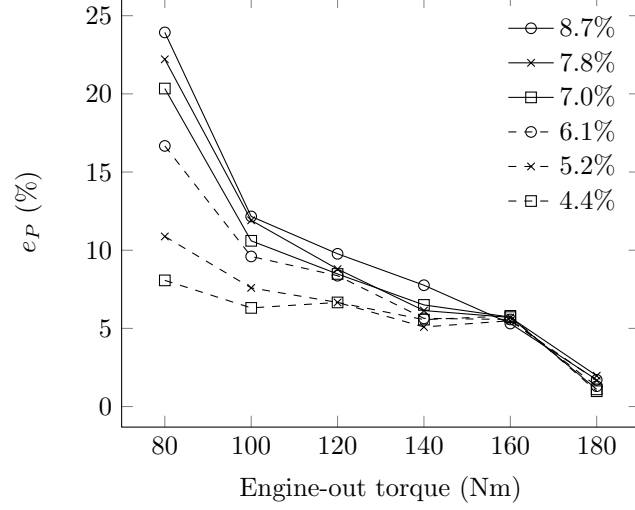


Figure B.5: Comparison of prediction performance of four layer, 20 node ANNs topologies at moderate-to-high torque settings with different training errors [2].

B.5.3 Convergence time

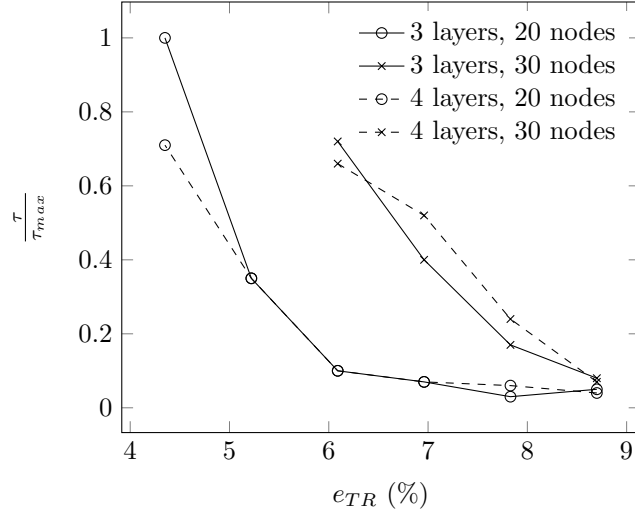


Figure B.6: Comparison of convergence time of ANN topologies over a range of training errors [2].

Figure B.6 shows the time taken for convergence τ normalised by the maximum time taken for convergence τ_{max} (that for the three-layer 20 node network at $e_{TR}=4.4\%$). Two factors affect the time taken to converge for any given value of training error:

1. Time taken to update weights and calculate errors for each iteration.
2. Number of iterations required.

Increasing the complexity of a network results in an increase in the first effect. However, the additional degrees of freedom available to a more complex network could result in a decrease in the number of iterations required in training. These competing effects mean the choice of network topology is not simple.

Figure B.6 illustrates this: at very high values of e_{TR} , there is little difference between networks of different topologies. At e_{TR} decreases, 30 node networks take significantly longer to train than 20 node networks, indicating that the first effect is stronger. At an e_{TR} of 6.1%, the 30 node network takes 7 times as long to converge as the 20 node network.

The 30 node networks were unable to converge at values of e_{TR} below 6.1%. Both 20 node networks are similar for values of e_{TR} of 5.2% and above; below this the 4 layer network converges in $0.71 \tau_{max}$, indicating dominance of the second effect.

B.6 Summary

The sensitivity of the ion current to engine load as described in Chapter 2 has been investigated further here. Given the complex relationship between the ion current and heat release, and further complexities of mechanical losses in the engine, artificial neural networks were employed to evaluate the ability of the ion current to predict engine-out torque.

Torque was predicted to < 11 Nm error over the entire torque range tested. At low values of torque, this forms a significant fraction of the predicted value. Further investigation of potential causes for high percentage error at low torque values was conducted by substituting first indicated mean effective pressure and then expansion work in place of torque — these measures showed far more prediction accuracy at low values of engine load. It is postulated that the error is related to the losses suffered between heat release in the cylinder and torque at the flywheel — these form a greater fraction of engine-out torque when the load is low. Expansion work is entirely unaffected by losses and its prediction accuracy was found to be torque-independent.

A brief study of artificial neural network topology and training was conducted to determine suitable networks for use in ion current statistical processing. Four layer

networks were found to be more suitable than three layer networks, and 20 hidden nodes per layer was preferred over 30, for reasons of both prediction accuracy and time taken for training.

Appendix C

Methane reaction mechanism

The Arrhenius coefficients presented here are used to calculate the forward rate of the chemical reaction via Equation C.1. The reverse reaction rate is calculated through equilibrium unless explicitly declared.

$$k_f = AT^\beta \exp\left(\frac{E_a}{RT}\right) \quad (\text{C.1})$$

Units for A are in terms of centimetre, second, Kelvin and moles.

Units for E_a are cal/mol.

Reaction	A	β	E_a	Source
$\text{O} + \text{CH}_4 = \text{OH} + \text{CH}_3$	1.02E+009	1.5	8600	[146]
$\text{H} + \text{CH}_2\text{OH} = \text{OH} + \text{CH}_3$	1.20E+013	0	0	[146]
$\text{H} + \text{CH}_2\text{O} + \text{M} = \text{CH}_2\text{OH} + \text{M}$	5.40E+011	0.454	3600	[146]
$\text{OH} + \text{CH}_3 = \text{CH}_2(\text{S}) + \text{H}_2\text{O}$	2.50E+013	0	0	[146]
$\text{CH}_3 + \text{H} + \text{M} = \text{CH}_4 + \text{M}$	8.00E+026	-3	0	[146]
$\text{CH}_2(\text{S}) + \text{N}_2 = \text{CH}_2 + \text{N}_2$	1.50E+013	0	600	[146]
$\text{CH} + \text{H}_2 = \text{H} + \text{CH}_2$	1.11E+008	1.79	1670	[146]
$\text{CH} + \text{H}_2\text{O} = \text{H} + \text{CH}_2\text{O}$	1.71E+013	0	-755	[146]
$\text{O} + \text{O} + \text{M} = \text{O}_2 + \text{M}$	1.20E+017	-1	0	[146]
$\text{O} + \text{CH}_3 = \text{H} + \text{CH}_2\text{O}$	8.43E+013	0	0	[146]
$\text{OH} + \text{CH}_2\text{O} = \text{HCO} + \text{H}_2\text{O}$	3.43E+009	1.18	-447	[146]
$\text{HCO} + \text{H}_2\text{O} = \text{H} + \text{CO} + \text{H}_2\text{O}$	2.24E+018	-1	17000	[146]
$\text{HCO} + \text{M} = \text{H} + \text{CO} + \text{M}$	1.87E+017	-1	17000	[146]
$\text{OH} + \text{CO} = \text{H} + \text{CO}_2$	2.40E+007	1.23	70	[146]

CH ₂ (S)+CO ₂ =CO+CH ₂ O	8.40E+013	0	0	[146]
H+O ₂ =OH+O	1.20E+017	-0.91	16514.9	[146]
Reverse Arrhenius coefficients	1.80E+013	0	0	[146]
O+H ₂ O=OH+OH	1.50E+010	1.14	17255.8	[146]
H+OH+H ₂ O=H ₂ O+H ₂ O	1.30E+024	-2	0	[146]
Reverse Arrhenius coefficients	1.60E+017	0	114242	[146]
CH+O=E-+CHO+	2.50E+011	0	14093.5	[149]
CHO++H ₂ O=H ₃ O++CO	1.00E+016	-0.0897	0	[56]
H ₃ O++E-=H ₂ O+H	2.29E+018	-0.5	0	[56]
E-+O ₂ +N ₂ =O ₂ -+N ₂	1.32E+017	-1	-164.9	[150]

Appendix D

Sensitivity analysis of CVC model

Figure D.1 shows predictions of chamber pressure for three meshes of differing average cell sizes, at initial pressure 3 bar and equivalence ratio 0.8. The size chosen in the study is 0.755 mm.

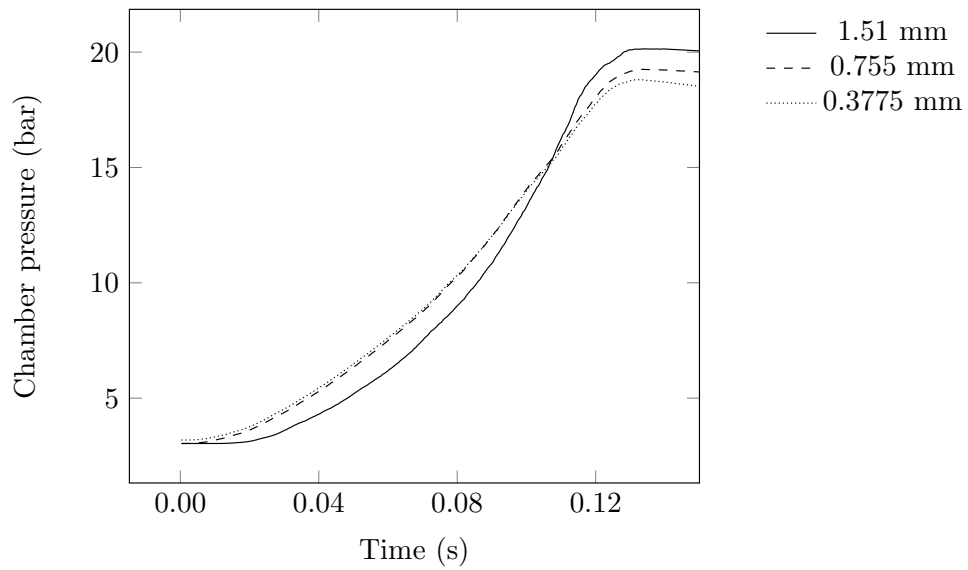


Figure D.1: Modelled chamber pressure at 3 bar and equivalence ratio 0.8 for different average cell sizes.

Figure D.2 shows predictions of chamber pressure for different values of time step, at initial pressure 3 bar and equivalence ratio 0.8. The time step chosen in this study is 2.5×10^{-4} s.

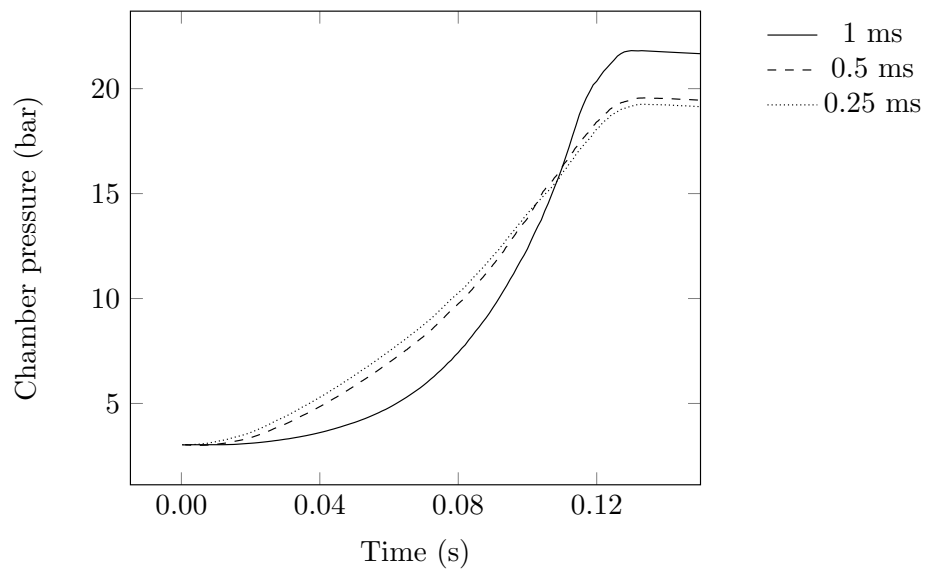


Figure D.2: Modelled chamber pressure at 3 bar and equivalence ratio 0.8 for different values of time step.

Appendix E

Further engine modelling results

E.1 Introduction

This appendix contains outputs from sub-models of the phenomenological diesel engine model presented in Chapter 5. Much like data presented in Appendix A, most of this data is not directly relevant to the prediction of cylinder pressure, heat release or the ion current, but is useful as measures of the performance of sub-models that are relevant to these predictions. This data is presented in Section E.2.

Comparisons of predictions of cylinder pressure and ion current to those measured in the experiment can be seen in Section E.3. Section E.4 presents a sensitivity analysis of pressure, NO_x and ion current predictions to several assumptions made in the model.

E.2 Outputs from sub-models

E.2.1 Injection

The modelled pressure drop and injection profile across the injector at 1600 RPM and two values of torque, 80 Nm and 180 Nm is shown in Figure E.1.

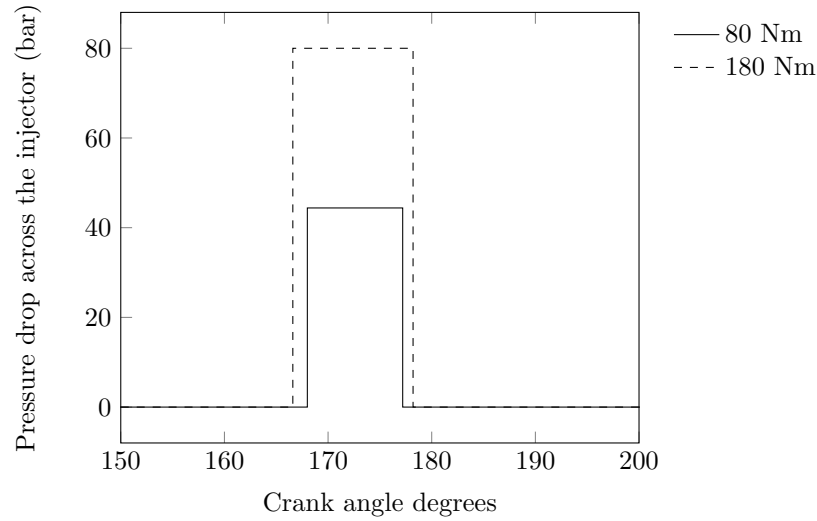


Figure E.1: Modelled pressure drop across the injector at 1600 RPM, 80 Nm and 1600 RPM, 180 Nm.

E.2.2 Spray

The variables of interest in the spray model are spray penetration, velocity, breakup time and breakup length.

Figures E.2 (a) and (b) show the spray tip penetration and velocity along the spray centreline for two values of engine-out torque, 80 Nm and 180 Nm, at 1600 RPM.

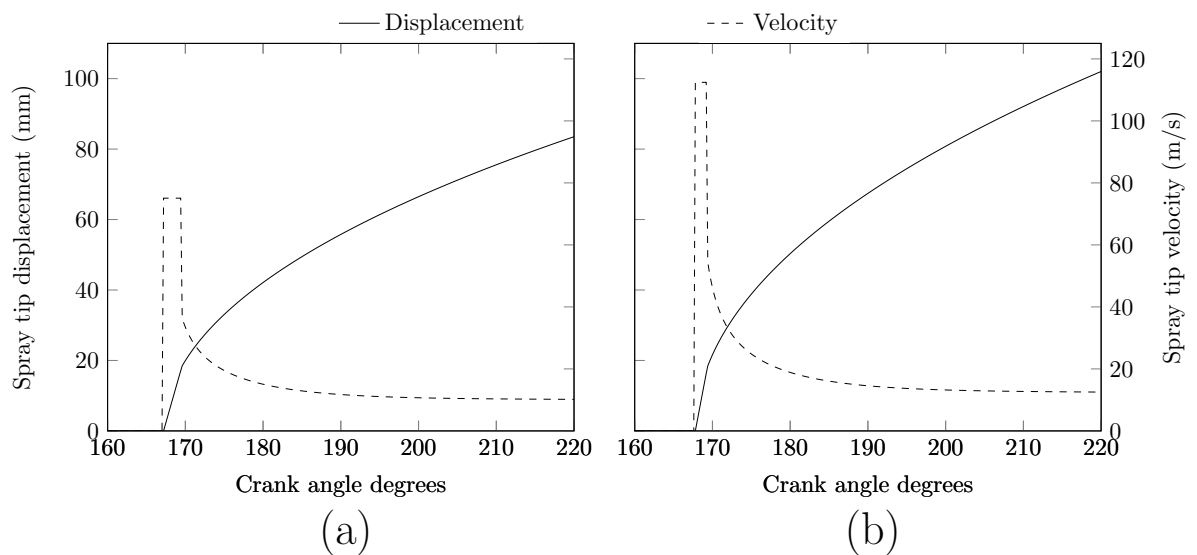


Figure E.2: Spray tip penetration and velocity at 1600 RPM, 80 Nm (a) and 1600 RPM, 180 Nm (b).

The mass of fuel injected depends on the torque setting used; the torque therefore also

affects the mass flow rate of fuel, via the injection period as described in Appendix A. The initial spray velocity is affected by the mass flow rate of fuel, and therefore the torque.

After injection begins, the spray velocity remains constant for a short time, then sharply decays around 170 CAD, marking the breakup of the spray. From this point onwards, the spray decelerates.

Before the breakup of the spray and the consequent sudden decrease in tip velocity, the spray exists as a continuous liquid jet. Figure E.3 shows the breakup time and the length of the liquid jet for the spray at different values of engine-out torque at 1600 RPM. The breakup time can be seen to decrease slightly as torque increases, due to an increase in the pressure drop across the injector. The distance travelled before spray breakup is fairly constant due to the greater initial spray velocity at higher values of torque. These results are similar to those found by Yule & Filipovic [249] and Rao [64].

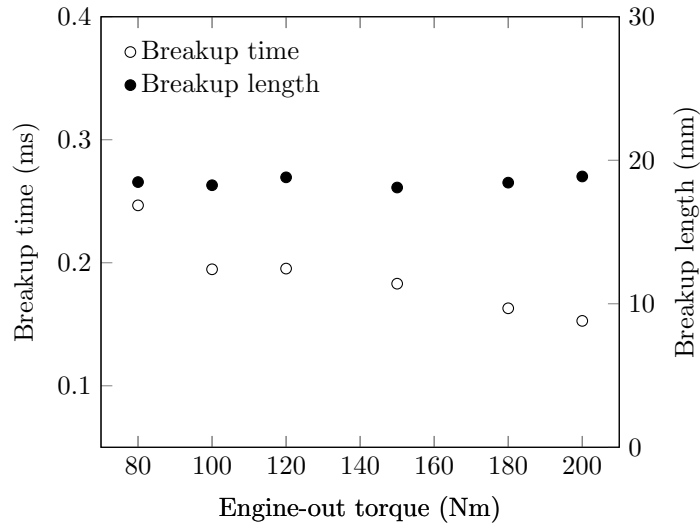


Figure E.3: Spray breakup time and length for 1600 RPM, 80 Nm (a) and 1600 RPM, 180 Nm (b).

E.2.3 Air entrainment

Results from the air entrainment model are shown in Figure E.4 at 1600 RPM and 80 Nm (a) and 1600 RPM and 180 Nm (b). Air entrainment can be seen to be intrinsically linked to the decay in spray tip velocity. The effect of initial spray velocity can be seen in the large difference in air entrainment between the two values of engine-out torque. At 220 CAD, 0.33 g of air has been entrained into the spray at 80 Nm, compared to

0.62 g at 180 Nm.

By the end of the combustion process, not all the air in the combustion chamber is entrained into the spray, even at high values of engine torque. This finding disagrees with the entrainment model used by Rao [64] on the same engine; that study found much higher rates of air entrainment.

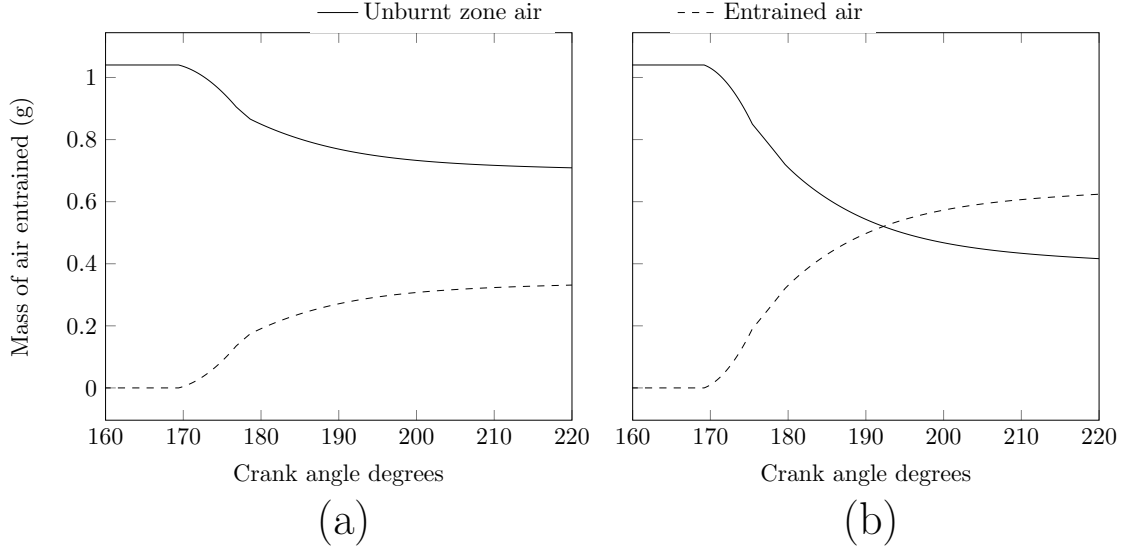


Figure E.4: Air entrainment characteristics for 1600 RPM, 80 Nm (a) and 1600 RPM, 180 Nm (b).

E.2.4 Fuel evaporation

Figure E.5 shows the mass of fuel injected and that evaporated for engine operating conditions 1600 RPM, 80 Nm (a) and 1600 RPM, 180 Nm (b). Evaporation of the fuel evidently occurs in a very short time. The evaporation rates shown here agree well with those found by Rao [64].

E.2.5 Combustion & heat release

Figure E.6 shows the temperatures of the burnt and unburnt zones and also the mass-weighted cylinder average temperature at 1600 RPM, 80 Nm (a) and 1600 RPM, 180 Nm (b). The burnt zone temperature depends on overall equivalence ratio in the burnt zone, which depends both on the mass of fuel introduced and the mass of air entrained. Both of these quantities increase with an increase in torque, however the mass of air entrained increases at a slower rate than the mass of fuel injected — the

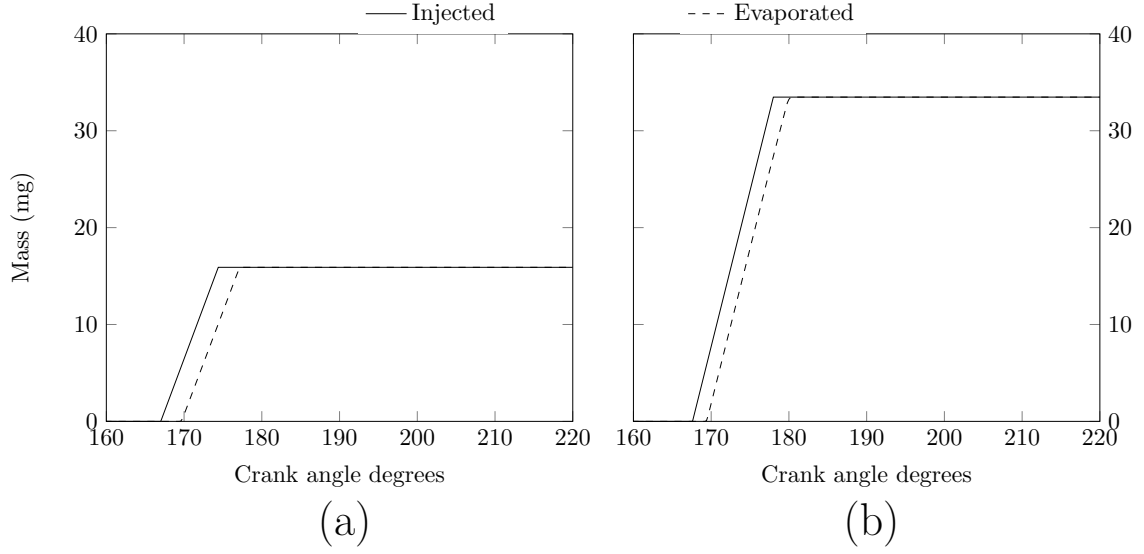


Figure E.5: Mass of fuel injected and mass of fuel vapour at 1600 RPM, 80 Nm (a) and 1600 RPM, 180 Nm (b).

mass of air entrained depends on the initial spray velocity and the increase in injection period at higher values of torque results in initial spray velocity increasing slower than the fuel mass injected.

These competing effects result in the burnt zone being more fuel-rich at higher values of torque than at lower values, where the equivalence ratio is closer to 1. The burnt zone temperature is therefore slightly higher at low values of torque. A similar phenomenon was also predicted by Rao [64].

The cylinder average temperature is higher for the high load case than for the low load case due to a greater mass of the burnt zone at high load, caused by higher air entrainment.

E.3 In-cylinder pressure and ion current predictions

Figures E.7–E.14 compare measured and predicted values for in-cylinder pressure and ion current over a range of engine speeds and loads.

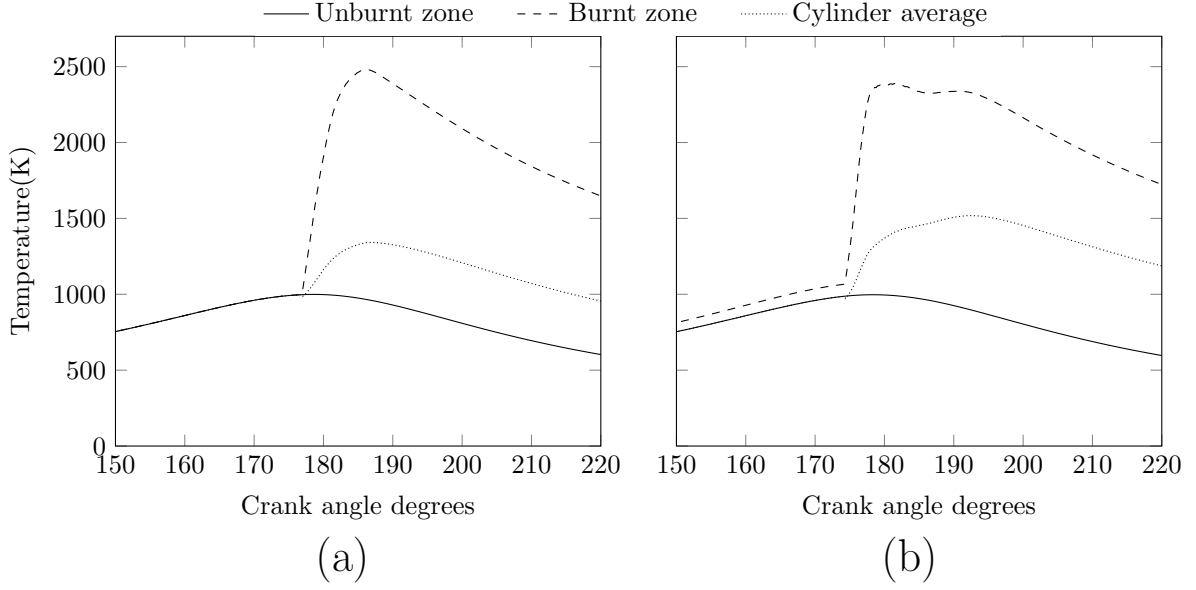


Figure E.6: Modelled temperatures of burnt and unburnt zones and cylinder average at 1600 RPM, 80 Nm (a) and 1600 RPM, 180 Nm (b).

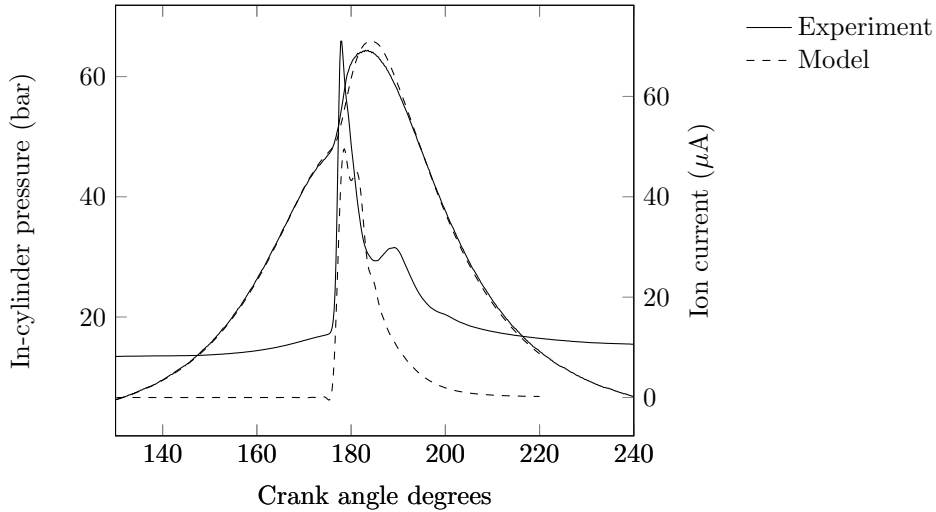


Figure E.7: Measured and predicted in-cylinder pressure and ion current at 1600 RPM, 80 Nm.

E.4 Sensitivity analysis

All phenomenological models use empirical constants in their various submodels. The choice of these empirical constants in this study is based either on established models or on the requirements to calibrate the in-cylinder pressure curve against that obtained from experiment as described in Section 5.2.8. This section presents the sensitivities of predicted values of cylinder pressure, NO_x emissions and ion current to the choice of these constants. The engine operating point chosen for all sensitivity analyses is

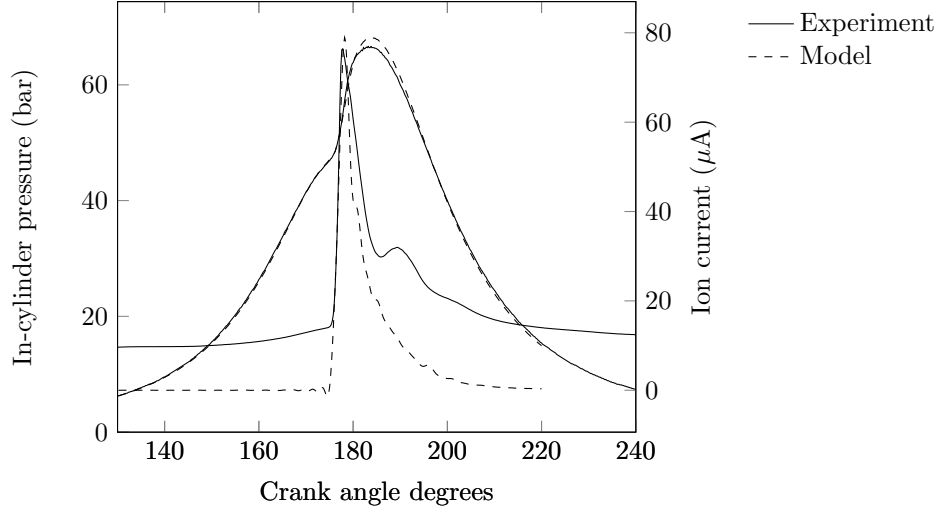


Figure E.8: Measured and predicted in-cylinder pressure and ion current at 1600 RPM, 100 Nm.

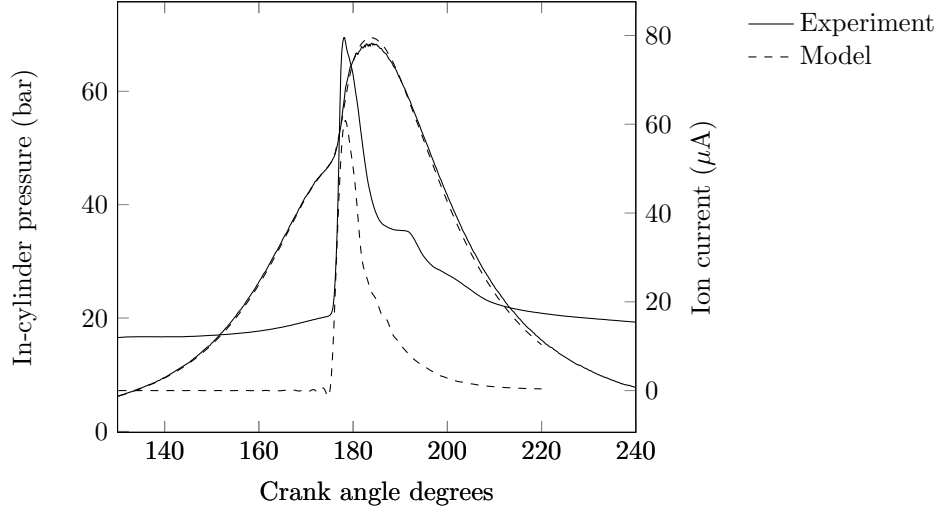


Figure E.9: Measured and predicted in-cylinder pressure and ion current at 1600 RPM, 120 Nm.

1600 RPM, 140 Nm.

E.4.1 Time step size

Jung & Assanis [176] found numerical instabilities for time steps smaller than 0.5 CAD and recommended time steps of 0.5 CAD or 1 CAD to ensure stability. Rao [64] found that time steps of 0.2 CAD and above exhibited sufficient numerical stability for use in their model, but found smaller time steps to be unstable. In this study, a time step of 0.2 CAD has been used for all data hitherto presented. Figure E.15 shows the

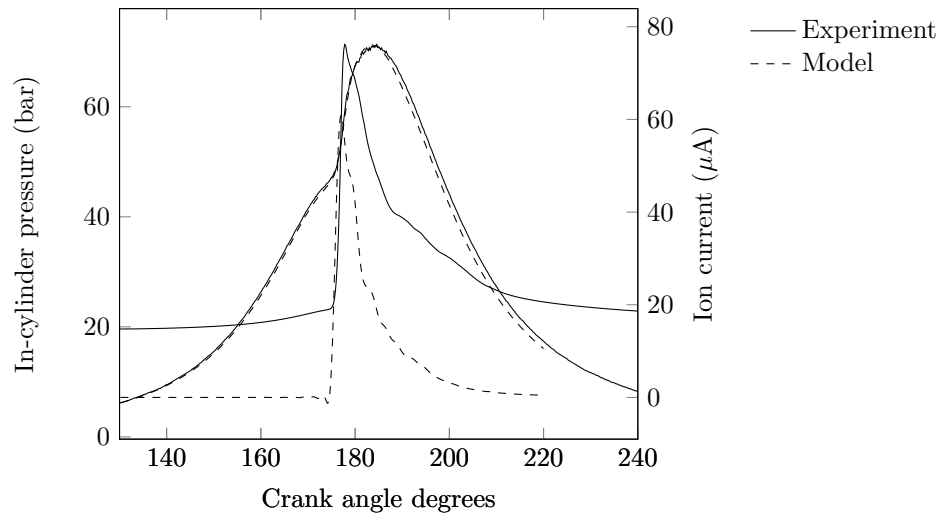


Figure E.10: Measured and predicted in-cylinder pressure and ion current at 1600 RPM, 140 Nm.

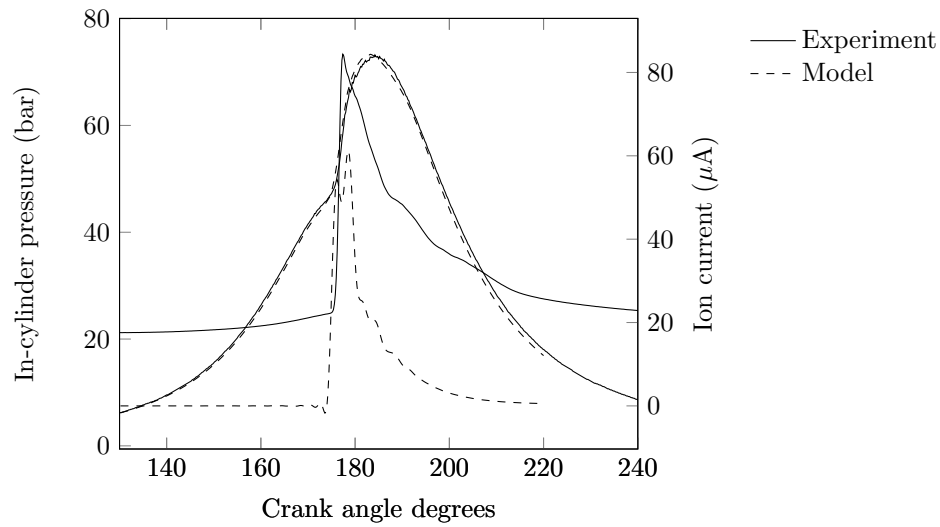


Figure E.11: Measured and predicted in-cylinder pressure and ion current at 1600 RPM, 160 Nm.

sensitivity of cylinder pressure prediction to time step chosen. There is little difference in the in-cylinder pressure at time steps below 0.4 CAD.

Figures E.16 and E.17 show the sensitivities of NO_x and ion current predictions to time step size; time steps of 0.2 and 0.4 CAD show little difference.

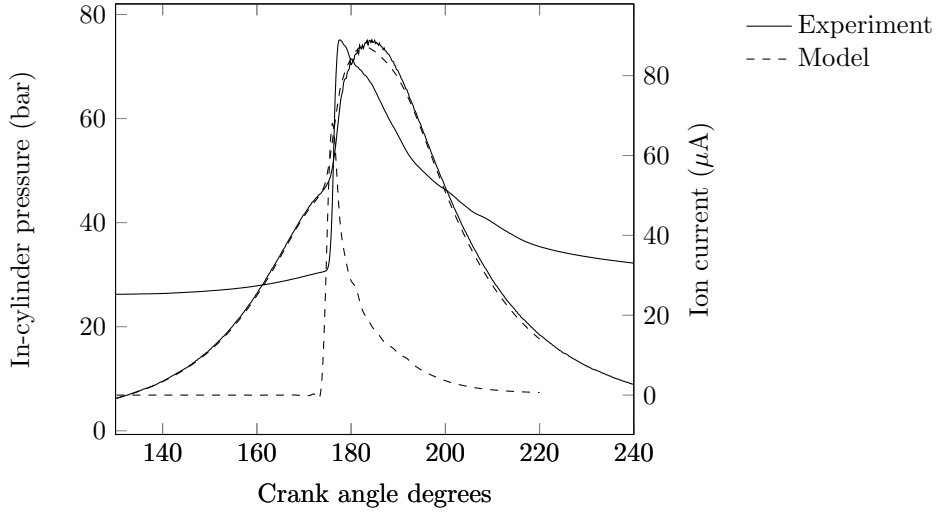


Figure E.12: Measured and predicted in-cylinder pressure and ion current at 1600 RPM, 180 Nm.

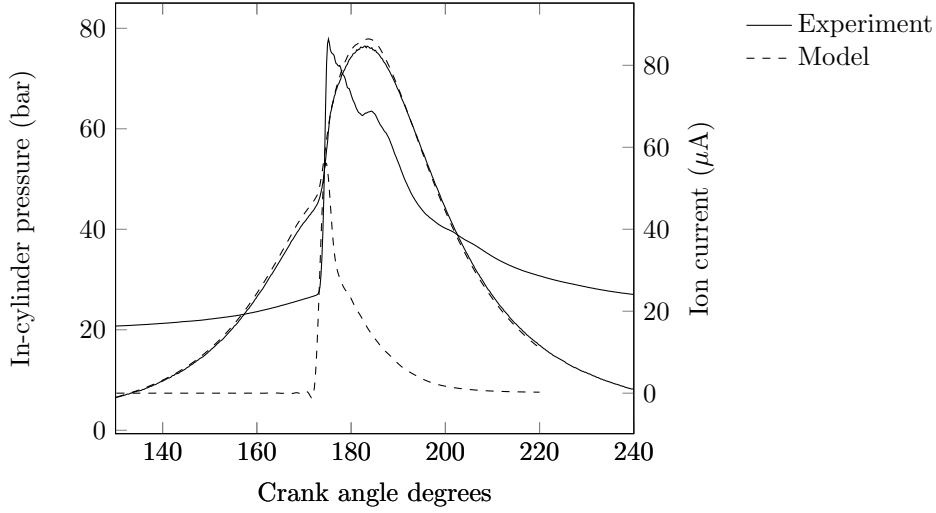


Figure E.13: Measured and predicted in-cylinder pressure and ion current at 1200 RPM, 140 Nm.

E.4.2 Spray division

The number of radial packets in the spray (n_R) is user-defined; sensitivity to this value was examined. Predictions of in-cylinder pressure, NO_x and ion current for different numbers of radial packets are shown in Figures E.18, E.19 and E.20. The in-cylinder pressure shows very little variation across the range of n_R tested, but NO_x and the ion current require 9 or more radial packets to be insensitive to the choice of n_R . In previous studies, Rao [64] used 10 radial packets, while Jung & Assanis [176] found that 5 was the minimum number required for convergence of predictions of NO_x .

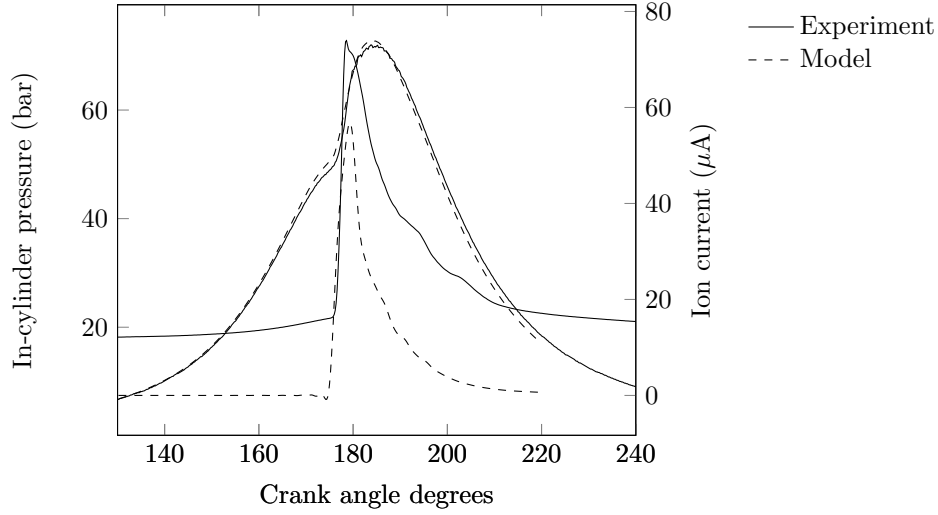


Figure E.14: Measured and predicted in-cylinder pressure and ion current at 1800 RPM, 140 Nm.

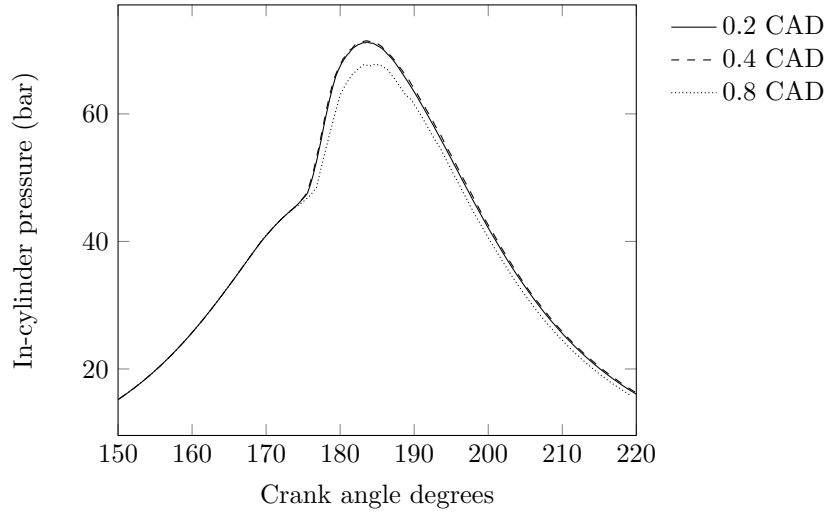


Figure E.15: Sensitivity of in-cylinder pressure predictions to time step size.

E.4.3 Nozzle discharge coefficient

The choice of nozzle discharge coefficient affects the pressure drop across the injector and therefore the spray penetration after breakup (Equation 5.1). This is therefore an important parameter in the evaluation of air entrainment. Rao [64] found the in-cylinder pressure to depend to a great extent on the choice of the discharge coefficient. It follows that the average cylinder temperature and therefore the ion current and NO_x would be similarly affected.

Spray penetration after breakup and therefore spray velocity vary as $C_d^{-0.5}$. Therefore, given that the effect of nozzle discharge coefficient is to uniformly change air entrain-

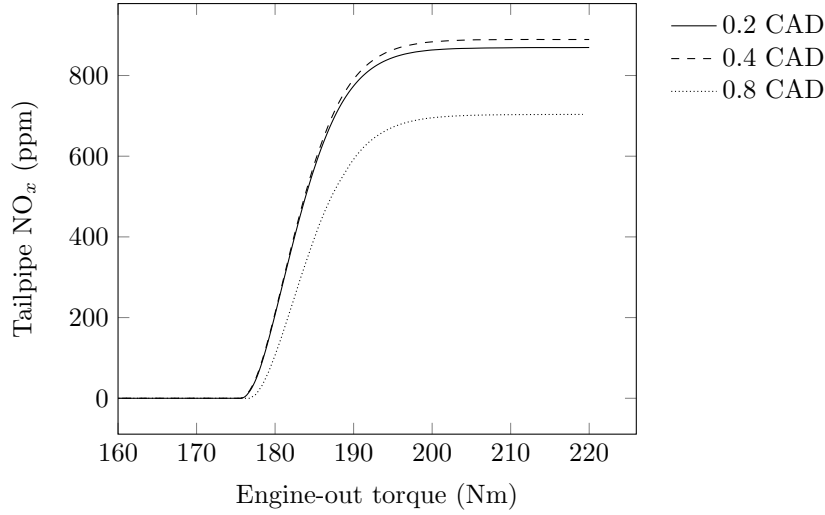
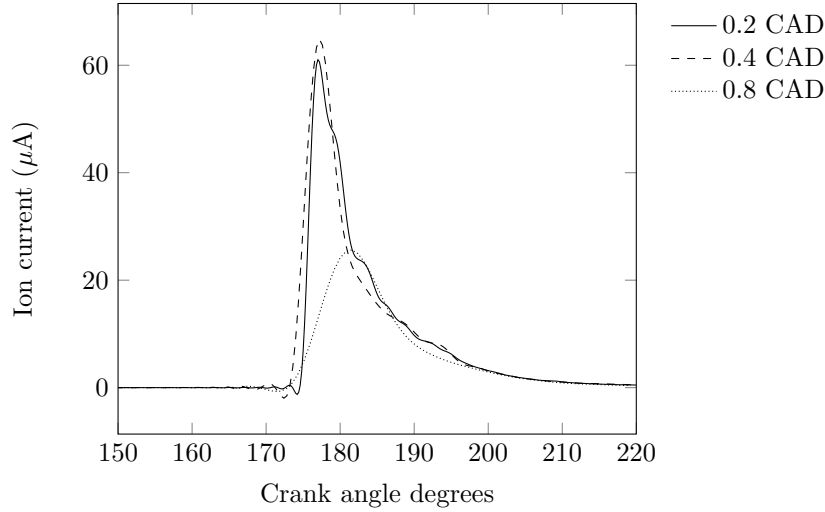
Figure E.16: Sensitivity of NO_x predictions to time step size.

Figure E.17: Sensitivity of ion current predictions to time step size.

ment, sensitivity to nozzle discharge coefficient is accounted for in the calibration of the air entrainment constants and is discussed in the following section.

E.4.4 Air entrainment constants

Phenomenological models are necessarily sensitive to the air entrainment constants as accurate modelling of the combustion process is reliant on the production of an accurate distribution of packets within the temperature-equivalence ratio space. The spray and entrainment models are integral to the production of this distribution. It is therefore expected that predictions from the model will depend heavily on the choice of these constants, which is the reason they must be calibrated. As discussed in Chapter

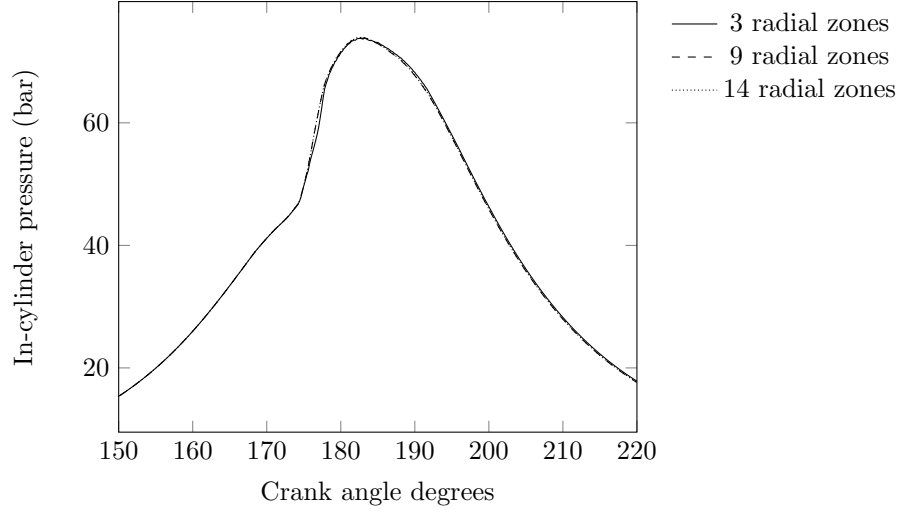


Figure E.18: Sensitivity of in-cylinder pressure predictions to number of radial zones.

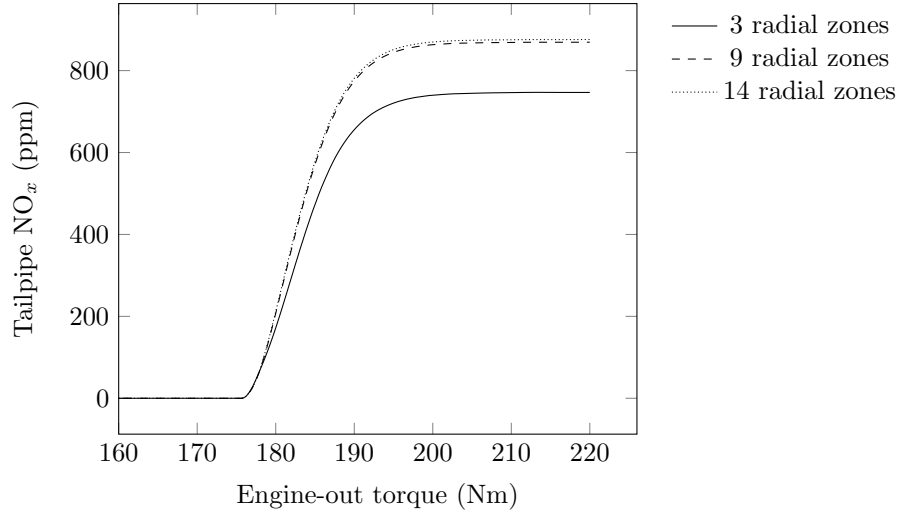


Figure E.19: Sensitivity of NO_x predictions to number of radial zones.

5, these constants can be calibrated against various engine performance parameters of interest, such as cylinder pressure (as here), heat release and NO_x emissions. The choice of these constants is therefore somewhat arbitrary and specific to each engine.

Figures E.21 (a) and (b) show the sensitivity of in-cylinder pressure to the choice of the entrainment constant before impingement of the spray on the piston crown, $F_{e,1}$, and to the choice of the entrainment constant after impingement, $F_{e,2}$. The default values for these constants are 1.9 and 1.0 respectively. Changes to either entrainment constant produce a significant difference in predicted pressure, indicating the importance of accurate calibration of these constants for a particular model of engine used in experiments. These results suggest that NO_x and the ion current signal will also be sensitive to the values of the air entrainment constants.

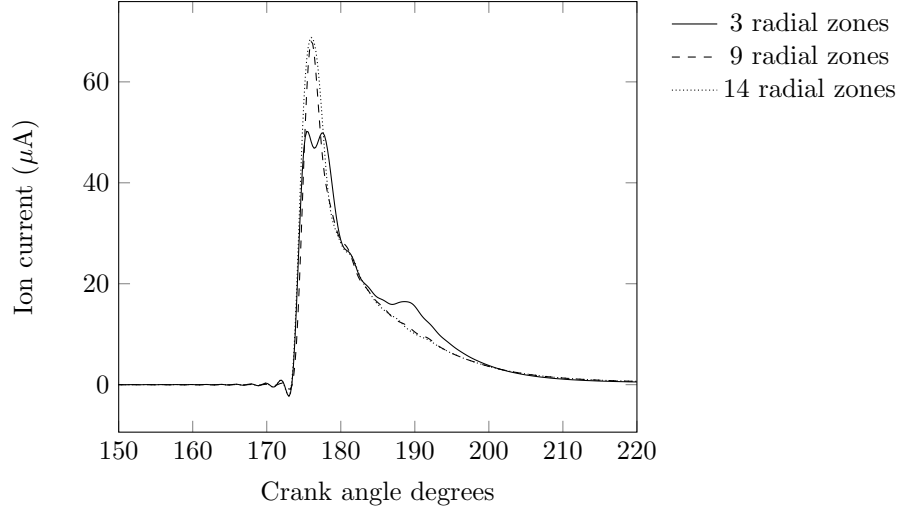


Figure E.20: Sensitivity of ion current predictions to number of radial zones.

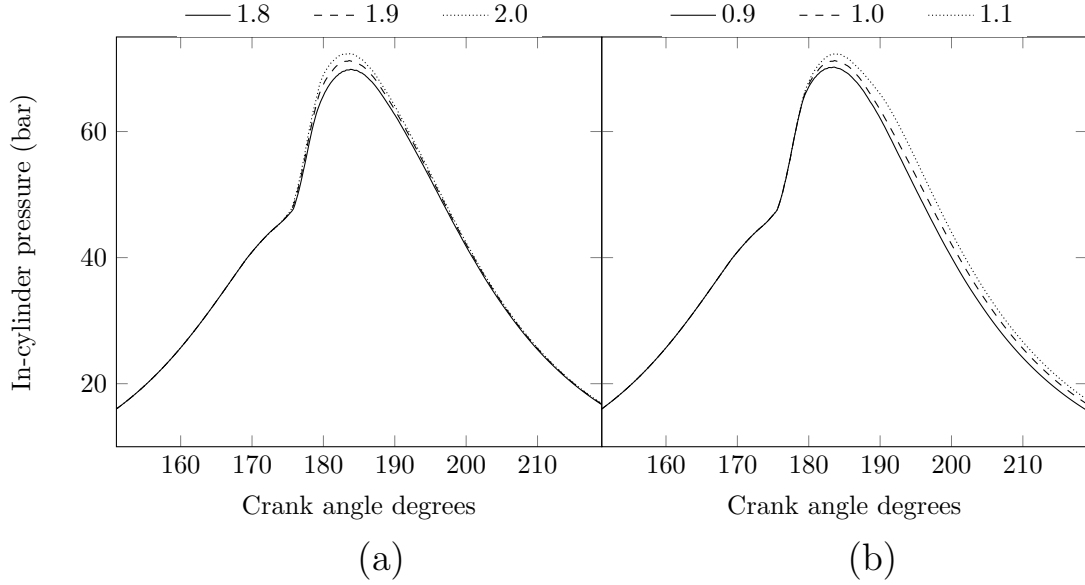


Figure E.21: Sensitivity of in-cylinder pressure prediction to air entrainment factor before impingement (a) and after impingement (b).

E.4.5 Fuel evaporation constant

Sensitivities of predictions of in-cylinder pressure, NO_x and ion current to the value of the empirical evaporation constant K_{evap} are shown in Figures E.22, E.23 and E.24. There is no sensitivity in predicted pressure, small sensitivity in NO_x predictions and significant sensitivity in ion current peak for values below 5.0, which is the value used in this study.

The sensitivity in the ion current peak is due to its early development in the engine

cycle. Combustion in diesel engines first begins in fuel-rich packets. When evaporation rates are set to be low, the decrease in mass of gaseous fuel in each packet results in an equivalence ratio closer to 1. As seen in Chapter 3, the ion current is sensitive to changes in equivalence ratio and is maximum at an equivalence ratio of 1.0.

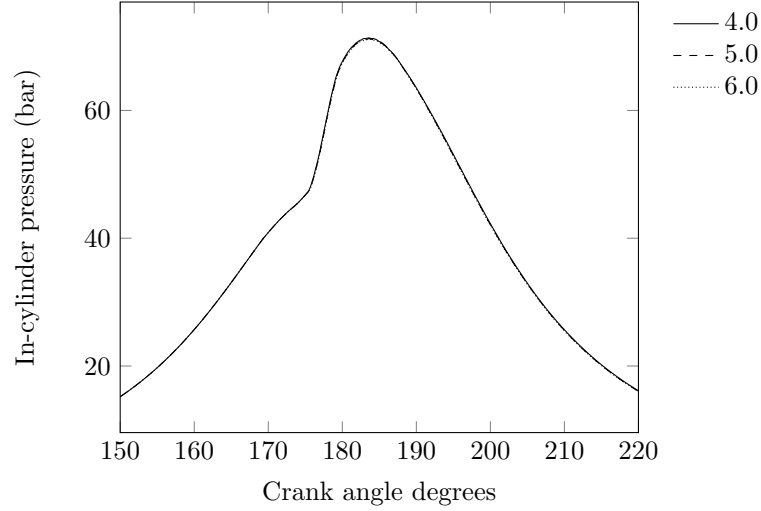


Figure E.22: Sensitivity of in-cylinder pressure prediction to evaporation constant.

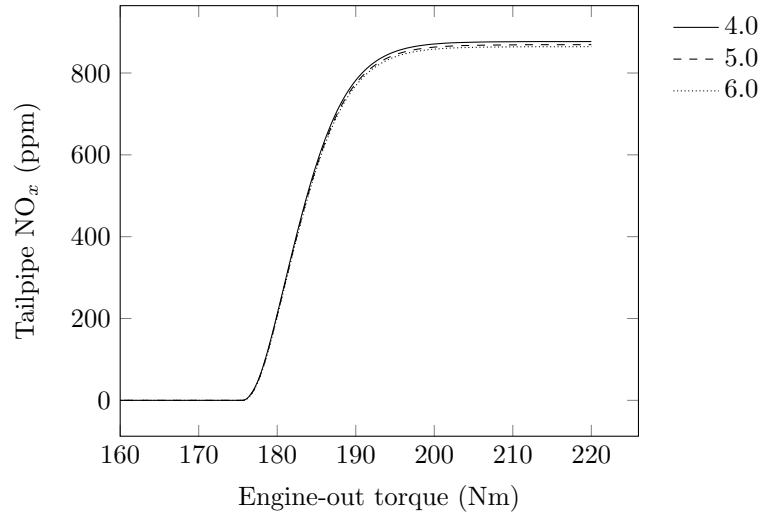


Figure E.23: Sensitivity of NO_x prediction to evaporation constant.

E.4.6 Cylinder wall temperature

As described in Section 5.2.6, the cylinder wall temperature T_w chosen in this study was 450 K. It is well known that NO_x production is highly temperature-dependent, indicating that the choice of T_w could affect the predicted tailpipe NO_x . Figures E.25 shows the minimal sensitivity of pressure to this value. NO_x and ion current peaks

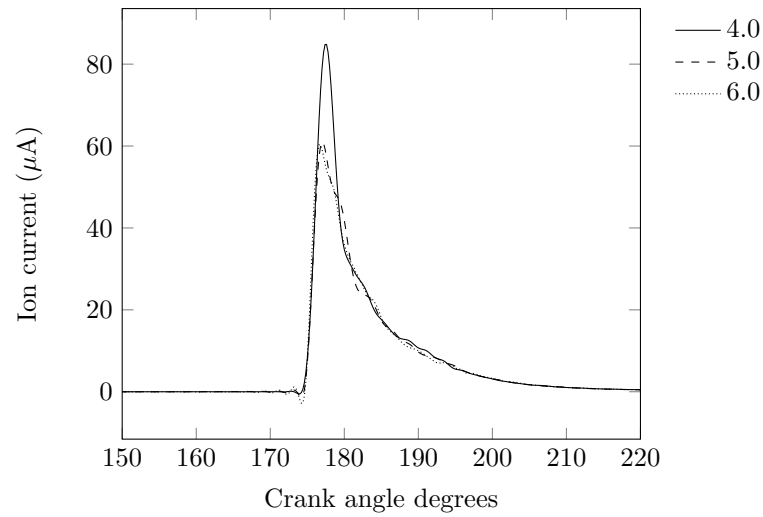


Figure E.24: Sensitivity of ion current prediction to evaporation constant.

show larger sensitivity to the assumed wall temperature (Figures E.26 and E.27); 450 K is assumed here as has been done in several studies [1, 3, 5, 211].

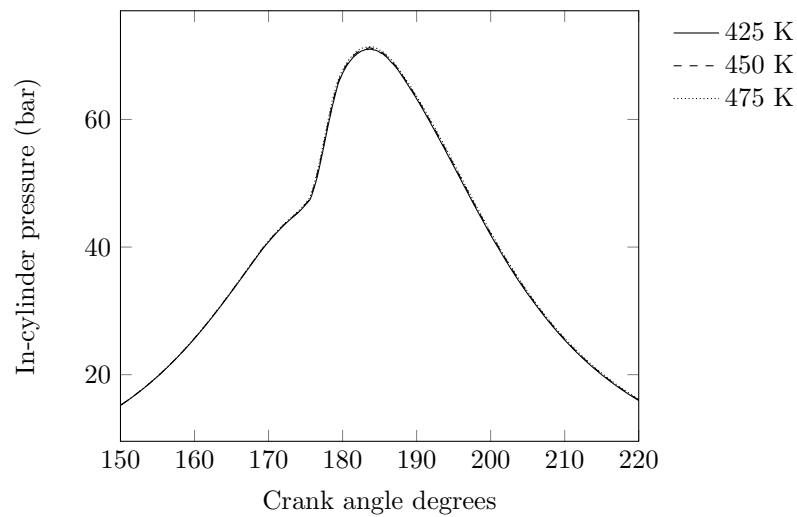


Figure E.25: Sensitivity of in-cylinder pressure prediction to cylinder wall temperature.

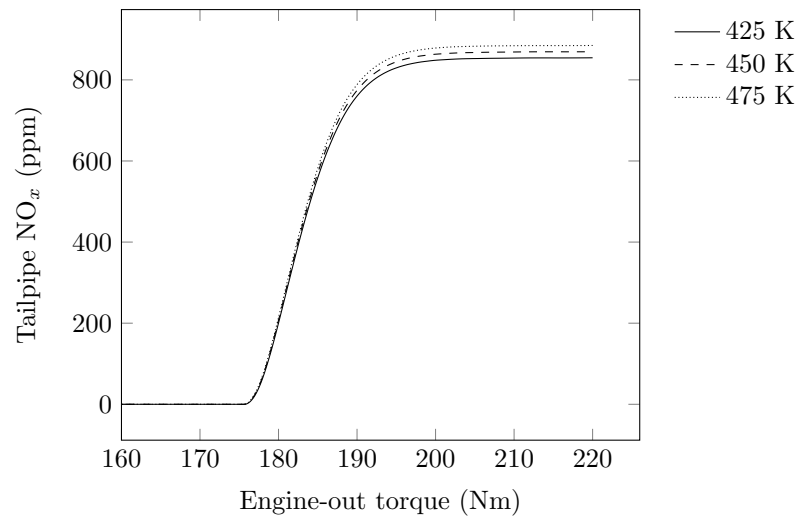


Figure E.26: Sensitivity of NO_x prediction to cylinder wall temperature.

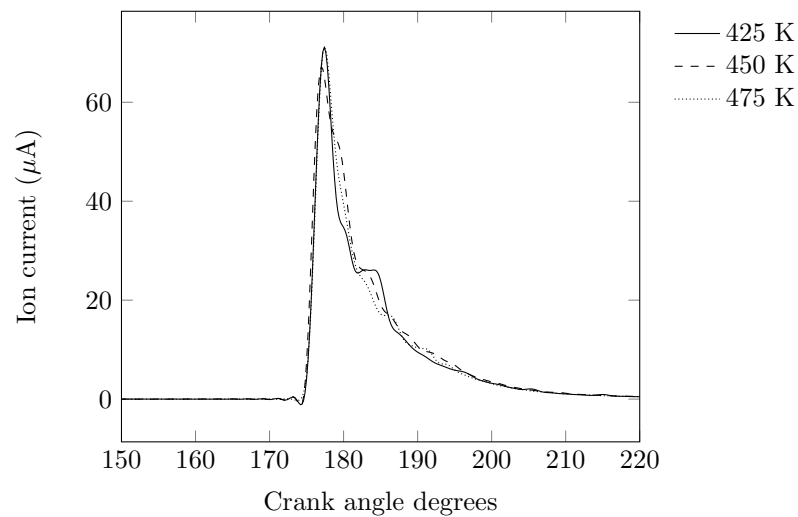


Figure E.27: Sensitivity of ion current prediction to cylinder wall temperature.

Appendix F

n-Heptane reaction mechanism

The Arrhenius coefficients presented here are used to calculate the forward rate of the chemical reaction via Equation F.1. The reverse reaction rate is calculated through equilibrium.

$$k_f = AT^\beta \exp\left(\frac{E_a}{RT}\right) \quad (\text{F.1})$$

Units for A are in terms of centimetre, second, Kelvin and moles.

Units for E_a are cal/mol.

Reaction	A	β	E_a	Source
NC7H16+H =C7H15-2 +H2	4.380E+07	2	4760	[205]
NC7H16 + OH = C7H15-2 + H2O	9.700E+09	1.3	1690	[205]
NC7H16 + HO2 = C7H15-2 + H2O2	1.650E+13	0	16950	[205]
NC7H16 + O2 = C7H15-2 + HO2	2.000E+15	0	47380	[205]
C7H15-2 + O2 = C7H15O2	1.560E+12	0	0	[205]
C7H15O2 + O2 = C7KET12 + OH	4.500E+14	0	18232.712	[205]
C7KET12 = C5H11CO + CH2O + OH	9.530E+14	0	4.11E+04	[205]
C5H11CO = C2H4 + C3H7 + CO	9.84E+15	0	4.02E+04	[205]
C7H15-2 = C2H5 + C2H4 + C3H6	7.045E+14	0	3.46E+04	[205]
C3H7 = C2H4 + CH3	9.600E+13	0	30950	[205]
C3H7 = C3H6 + H	1.250E+14	0	36900	[205]
C3H6 + CH3 = C3H5 + CH4	9.000E+12	0	8480	[205]
C3H5 + O2 = C3H4 + HO2	6.000E+11	0	10000	[205]
C3H4 + OH = C2H3 + CH2O	1.000E+12	0	0	[205]
C3H4 + OH = C2H4 + HCO	1.000E+12	0	0	[205]

$\text{CH}_3 + \text{HO}_2 = \text{CH}_3\text{O} + \text{OH}$	5.000E+13	0	0	[205]
$\text{CH}_3 + \text{OH} = \text{CH}_2 + \text{H}_2\text{O}$	7.500E+06	2	5000	[205]
$\text{CH} + \text{H}_2 = \text{H} + \text{CH}_2$	1.11E+08	1.79	1670	[146]
$\text{CH} + \text{H}_2\text{O} = \text{H} + \text{CH}_2\text{O}$	1.71E+13	0	-755	[146]
$\text{CH}_2 + \text{O}_2 = \text{HCO} + \text{OH}$	4.300E+10	0	-500	[205]
$\text{CH}_2 + \text{O}_2 = \text{CO}_2 + \text{H}_2$	6.900E+11	0	500	[205]
$\text{CH}_2 + \text{O}_2 = \text{CO} + \text{H}_2\text{O}$	2.000E+10	0	-1000	[205]
$\text{CH}_2 + \text{O}_2 = \text{CO}_2 + \text{H} + \text{H}$	1.600E+12	0	1000	[205]
$\text{CH}_2 + \text{O}_2 = \text{CO} + \text{OH} + \text{H}$	8.600E+10	0	-500	[205]
$\text{CH}_3\text{O} + \text{CO} = \text{CH}_3 + \text{CO}_2$	1.570E+14	0	11800	[205]
$\text{CO} + \text{OH} = \text{CO}_2 + \text{H}$	8.987E+07	1.38	5232.877	[205]
$\text{O} + \text{OH} = \text{O}_2 + \text{H}$	4.000E+14	-0.5	0	[205]
$\text{H} + \text{HO}_2 = \text{OH} + \text{OH}$	1.700E+14	0	875	[205]
$\text{OH} + \text{OH} = \text{O} + \text{H}_2\text{O}$	6.000E+08	1.3	0	[205]
$\text{H} + \text{O}_2 + \text{M} = \text{HO}_2 + \text{M}$	3.600E+17	-0.72	0	[205]
$\text{H}_2\text{O}/21./ \text{CO}_2/5.0/ \text{H}_2/3.3/ \text{CO}/2.0/$				
$\text{H}_2\text{O}_2 + \text{M} = \text{OH} + \text{OH} + \text{M}$	1.000E+16	0	45500	[205]
$\text{H}_2\text{O}/21./ \text{CO}_2/5.0/ \text{H}_2/3.3/ \text{CO}/2.0/$				
$\text{H}_2 + \text{OH} = \text{H}_2\text{O} + \text{H}$	1.170E+09	1.3	3626	[205]
$\text{HO}_2 + \text{HO}_2 = \text{H}_2\text{O}_2 + \text{O}_2$	3.000E+12	0	0	[205]
$\text{CH}_2\text{O} + \text{OH} = \text{HCO} + \text{H}_2\text{O}$	5.563E+10	1.095	-76.517	[205]
$\text{CH}_2\text{O} + \text{HO}_2 = \text{HCO} + \text{H}_2\text{O}_2$	3.000E+12	0	8000	[205]
$\text{HCO} + \text{O}_2 = \text{HO}_2 + \text{CO}$	3.300E+13	-0.4	0	[205]
$\text{HCO} + \text{M} = \text{H} + \text{CO} + \text{M}$	1.591E+18	0.95	56712.329	[205]
$\text{CH}_3 + \text{CH}_3\text{O} = \text{CH}_4 + \text{CH}_2\text{O}$	4.300E+14	0	0	[205]
$\text{C}_2\text{H}_4 + \text{OH} = \text{CH}_2\text{O} + \text{CH}_3$	6.000E+13	0	960	[205]
$\text{C}_2\text{H}_4 + \text{OH} = \text{C}_2\text{H}_3 + \text{H}_2\text{O}$	8.020E+13	0	5955	[205]
$\text{C}_2\text{H}_3 + \text{O}_2 = \text{CH}_2\text{O} + \text{HCO}$	4.000E+12	0	-250	[205]
$\text{C}_2\text{H}_3 + \text{HCO} = \text{C}_2\text{H}_4 + \text{CO}$	6.034E+13	0	0	[205]
$\text{C}_2\text{H}_5 + \text{O}_2 = \text{C}_2\text{H}_4 + \text{HO}_2$	2.000E+10	0	-2200	[205]
$\text{CH}_4 + \text{O}_2 = \text{CH}_3 + \text{HO}_2$	7.900E+13	0	56000	[205]
$\text{OH} + \text{HO}_2 = \text{H}_2\text{O} + \text{O}_2$	7.50E+12	0	0	[205]
$\text{CH}_3 + \text{O}_2 = \text{CH}_2\text{O} + \text{OH}$	3.80E+11	0	9000	[205]
$\text{CH}_4 + \text{H} = \text{CH}_3 + \text{H}_2$	6.600E+08	1.6	10840	[205]
$\text{CH}_4 + \text{OH} = \text{CH}_3 + \text{H}_2\text{O}$	1.600E+06	2.1	2460	[205]
$\text{CH}_4 + \text{O} = \text{CH}_3 + \text{OH}$	1.020E+09	1.5	8604	[205]
$\text{CH}_4 + \text{HO}_2 = \text{CH}_3 + \text{H}_2\text{O}_2$	9.000E+11	0	18700	[205]
$\text{CH}_4 + \text{CH}_2 = \text{CH}_3 + \text{CH}_3$	4.000E+12	0	-570	[205]
$\text{C}_3\text{H}_6 = \text{C}_2\text{H}_3 + \text{CH}_3$	3.150E+15	0	85500	[205]

$\text{N} + \text{NO} = \text{N}_2 + \text{O}$	2.700E+13	0	355	[208]
$\text{N} + \text{O}_2 = \text{NO} + \text{O}$	9.000E+09	1	6500	[208]
$\text{N}_2\text{O} + \text{O} = 2\text{NO}$	2.900E+13	0	23150	[208]
$\text{N}_2\text{O} + \text{OH} = \text{N}_2 + \text{HO}_2$	2.000E+12	0	21060	[208]
$\text{N}_2\text{O} (+\text{M}) = \text{N}_2 + \text{O} (+\text{M})$	7.910E+10	0	56020	[208]
LOW / 6.370E+14 0 56640.00/				
H2/2.00/ H2O/6.00/ CH4/2.00/ CO/1.50/ CO2/2.00/ C2H6/3.00/				
$\text{HO}_2 + \text{NO} = \text{NO}_2 + \text{OH}$	2.110E+12	0	-480	[208]
$\text{NO} + \text{O} + \text{M} = \text{NO}_2 + \text{M}$	1.060E+20	-1.41	0	[208]
H2/2.00/ H2O/6.00/ CH4/2.00/ CO/1.50/ CO2/2.00/ C2H6/3.00/				
$\text{NO}_2 + \text{O} = \text{NO} + \text{O}_2$	3.900E+12	0	-240	[208]
$\text{NO}_2 + \text{H} = \text{NO} + \text{OH}$	1.320E+14	0	360	[208]
$\text{CH} + \text{O} = \text{CHO}^+ + \text{E}^-$	2.51E11	0	1695	[149]
$\text{CHO}^+ + \text{H}_2\text{O} = \text{H}_3\text{O}^+ + \text{CO}$	1.00E16	-0.1	0	[56]
$\text{CHO}^+ + \text{NO} = \text{NO}^+ + \text{HCO}$	7.23E13	0	0	[63]
$\text{CHO}^+ + \text{E}^- = \text{CO} + \text{H}$	1.32E17	0	0	[56]
$\text{H}_3\text{O}^+ + \text{E}^- = \text{H}_2\text{O} + \text{H}$	2.29E18	-0.5	0	[56]
$\text{H}_3\text{O}^+ + \text{E}^- = \text{OH} + \text{H} + \text{H}$	7.95E21	-1.4	0	[56]
$\text{N} + \text{O} = \text{NO}^+ + \text{E}^-$	4.80E10	0.5	64250	[209]
$\text{N}^+ + \text{NO} = \text{NO}^+ + \text{N}$	7.05E14	0	0	[210]
$\text{N}^+ + \text{O}_2 = \text{NO}^+ + \text{O}$	4.77E14	0	0	[210]
$\text{N}^+ + \text{CH}_2\text{O} = \text{CHO}^+ + \text{NH}$	1.75E15	0	0	[210]
